Suspended sand concentrations and bedform evolution under irregular waves

UNIVERSITY OF LIVERPOOL

Thesis submitted in accordance with the requirements of the University of Liverpool for the degree of Doctor in Philosophy

by

Rory Benedict O'Hara Murray

February 2011

Suspended sand concentrations and bedform evolution under irregular waves

Rory B. O'Hara Murray, February 2011

Abstract

Within the nearshore zone and shallow continental shelf the (i) hydrodynamic forcing, (ii) seabed and (iii) sediment suspensions form a dynamic and interacting sediment transport triad that operates over a wide range of spatial and temporal scales. The study of these flow-deposit-suspension interactions in a field environment is complicated. This work examines the triad over a variety of timescales under irregular free surface waves, typical of the natural environment, generated in a large field scale flume. A series of experiments were conducted over a bed composed of fine-medium-grained sand and a bed composed of upper-medium-grained sand. The significant wave height was systematically stepped up and down to simulate the passing of a storm event and to enable the sediment transport triad to be observed during a number of sediment transport regimes. The acoustic technology used, enabled high resolution measurements to be made of the oscillatory wave induced flow, bedforms and suspended sediments simultaneously in a nonintrusive manner.

The initial entrainment of sediment from the bed is largely an intra-wave process ($<$ 10 seconds) depending on the characteristics of individual waves and the bedforms. Intra-wave measurements of the suspended sediment concentration (SSC) field above steep ripples were made in order to examine the coherence and repeatability of sediment entrainment via vortices beneath irregular waves. The results demonstrate the existence of a clear suspended sediment structure consistent with vortex entrainment, previously observed under regular waves. This process was found to be intermittent, however, with vortex entrainment occurring when the orbital diameter was $>$ 1.2 times the ripple wavelength. The SSC close to the bed, entrained via intra-wave processes, was found to vary with the wave forcing and bedforms and at intra-wave timescales.

This near bed SSC influenced the SSC at higher elevations at wave group timescales ($<$ 2 minutes). During the passage of wave groups suspended sediments typically confined to the near bed layer were transported vertically due to the continual injection of turbulence. The character of wave groups is considered to control this vertical sediment transport, and those groups with abrupt terminations were found to strongly influence this process.

The sediment transport regimes that emerged during the course of the experiments (each lasting 25 minutes) included (i) quiescent wave forcing above plane beds and ripples with low steepness, (ii) vortex entrainment above steep ripples and (iii) strong wave forcing above large bedforms with three-dimensional plan-form geometries, hummocks and plane beds. The vertical decay of time mean SSC above bedforms was exponential within a near bed layer approximately equal in thickness to two times the exponential decay length scale, the mixing length. The mixing length was found to be strongly controlled by the hydraulic roughness and the presence of inherited bedforms, with contributions from vortex ripple and sheet flow processes. This offers a simplified framework to unite a number of sediment transport processes. Such an integrated approach is necessary in order to improve understanding and modelling of sediment transport across different timescales in the coastal zone.

To Louise,

Joanna and Robin,

and the loving memory of Sheila and Franz.

Acknowledgements

I would first like to thank my primary supervisors Dave Hodgson at the University of Liverpool, and Pete Thorne at the National Oceanography Centre, Liverpool, previously the Proudman Oceanographic Laboratory (POL). Dave and Pete have different academic backgrounds and yet their work has led them towards a common interest in sediment dynamics. It is their enthusiasm and drive in uncovering the nature of small scale sediment transport processes that has motivated me throughout this project. Dave and Pete's respective backgrounds have made the project very diverse. I now have an understanding of how sound interacts with marine sediments and an appreciation of how the study of present day processes can be used to infer great details about the past. I have learnt a great deal from Dave and Pete, and look forward to carrying these skills and ideas with me into the future. So, thank you Dave and Pete for inspiring me, showing great interest in the project, funding the project and of course proof reading countless abstracts and paper drafts.

I would next like to thank Alan Davies at the School of Ocean Sciences, Bangor University, for showing such a strong interest in this work. After chance meetings at conferences or more formal discussions with Alan, I have always come away feeling inspired and motivated. I will always remember Alan's advice to 'never underestimate the individual wave' as it reminds me to pay attention to detail. I also have to acknowledge Alan's involvement in sparking an interest in sediment transport processes during my time as an MSc student at Bangor.

Steve Flint at the University of Liverpool is my final supervisor I would like to thank. Despite being very busy with countless other commitments, he has always shown enthusiasm and interest in what I do. I had great fun with him and Rhodri in Kentucky and felt very privileged to have a one-on-one field tutorial on tidal rhythmites.

I have really enjoyed hanging out with Ben and Richard at POL over the last four years. We've been lucky enough to go to some interesting conferences in Greece, but we've mainly spent time together in the small cold sediments laboratory fishing for ballotini in the sediment tank. Ben has always listened to my ideas and through interesting discussions has helped develop my understanding of sound and sediments a great deal. This leads me on to thank Paul Bell at POL and all those, including Peter Thorne and John Williams, who were involved with the Deltaflume experiments and data collection. It was a privilege to work on these data which, even after almost ten years, form an extremely comprehensive and innovative dataset. There is plenty more scope for new research using these data. I also wish all those involved in the FORMOST project and future collaborations the best, and hope that I can work with you all in the future at some point. I would also like to thanks Jaco Baas at the School of Ocean Sciences, Bangor University, and Andy Plater within the School of Environmental Sciences, University of Liverpool, for an interesting, enjoyable and constructive viva.

Throughout my time in Liverpool I have felt very welcomed by all the Department of Earth and Ocean Sciences staff members, PhD students and those I know at BODC. I would especially

like to thank the entire STRAT group including those who have moved on to do other research including Claudio, Rowena, Ajay, Laura and Becky. Two very *special* people in the Department are my office mates, Amandine and Rhodri, who have been a great source of fun, enthusiasm, anguish, frustration, annoyance, stupidity and support over the last four years. I know we'll be life long friends, and that I will forever be a source of mitigation between the poor shivering Rhodri and perspiring Amandine – all because the window was open or closed or somewhere in between which was wrong...

All my friends who don't live in Liverpool have been reality checks, distractions and not least great encouragement. I love all you guys to bits and really treasure our time by the camp fire, hanging off cliffs, peddling frantically up hills or in the pub. You guys all inspire me so much and by doing what we do together you help me strive to understand our natural world a little more. I would especially like to thank Jonny, Jenny W, Marija, Emma, Jane, Kara, Dave H, Kerry, Jenny B, Chris, Mike, Lewis, Dave S and Luke.

I would finally like to thank those closest to me. First my mother, father and sister, Joanna, Robin and Lucy, who are the most supportive, understanding and accepting people in the world. You have helped distil in me a great love of nature through messing about in boats and rock pools, and striding up mountains. It is my love of nature, and her workings, which motivates me in my work. It is this deep routed respect and intrigue that is most valuable and useful to me, much more than matlab and the access to numerous journals – although they do help a bit. I also owe a lot to all my other family members, including Brigid, Ruth, Michale, Joan and Arthur, who have helped bring me up and still help support and motivate me today. Finally, I want to express my heartfelt gratitude to Louise without who this work would never have happened. Louise has selflessly supported me over the last few years and has always helped to remind me why I love doing what I do. Louise shares with me an admiration for the world in which we live, and the time we have spent shivering in tents and cycling around Liverpool is extremely precious to me.

Contents

Notation

Abbreviations

ABS	Acoustic Backscatter System
ARP	Acoustic Ripple Profiler
PDF	Probability Density Function
PSD	Power Spectral Density
RMS	Root Mean Square
SSC	Suspended Sediment Concentration
SSS	Sector Scanning Sonar

Symbols List

Symbol	Description [dimensions] (typical units)
a_i	Grain radius of the i^{th} class interval [L] (μm)
a_s	Grain radius of the particle number distribution [L] (μm)
$a_s\prime$	Grain radius of the particle mass distribution [L] (μm)
$< a_s >$	Mean radius of the particle number size distribution [L] (μm)
$< a_s' >$	Mean grain radius of the mass distribution [L] (μm)
B	Wave asymmetry parameter [-]
c	Speed of sound in water [L T^{-1}] (m/s)
$< c_0(\phi)/\overline{c_0(\phi)} >$	Phase ensemble averaged normalised intra-wave reference concentration [-]
$\overline{c_0(\phi)}$	Cycle mean reference concentration [M L^{-3}] (kg m^{-3})
C_0	Time averaged mass reference concentration at bed level [M L^{-3}] (kg m^{-3})
$C_0(t)$	Instantaneous reference concentration as a function of time, t, [M L^{-3}] (kg m^{-3})
$C_0(\phi)$	Instantaneous reference concentration as a function of phase, ϕ, [M L^{-3}] (kg m^{-3})
C_1	Time averaged mass reference concentration 1cm above bed [M L^{-3}] (kg m^{-3})
C_A	SSC obtained from the ABS at the pumped sampled bin ranges [M L^{-3}] (kg m^{-3})
C_P	SSC obtained from the pumped samples [M L^{-3}] (kg m^{-3})
C_r	Time averaged mass reference concentration at $z = r$ [M L^{-3}] (kg m^{-3})
$C(z)$	Time average SSC profile [M L^{-3}] (kg m^{-3})
d_0	Wave orbital excursion diameter [L] (m)
$d_0/2k_s$	Relative roughness [-]
d_s	Significant wave orbital excursion diameter [L] (m)
D_i	Grain diameter for which i% of sediment is finer than [L] (μm)
D_{s50}	Median grain diameter of mass size distribution [L] (μm)
$\overline{D_{s50}}$	The mean of D_{s50} over the pumped sampled measurement bins [L] (μm)
D_*	Dimensionless grain size [-]
f	Form function [-]
$f_{2.5}$	Wave friction factor based on $k_s = 2.5D_{50}$ [-]
f_i	Frequency of the i^{th} frequency interval [T^{-1}] (Hz)
g	Acceleration due to gravity [L T^{-2}] (m s^{-2})

Symbols list continued over leaf.

Symbols List (continued)

Symbol	Description [dimensions] (typical units)
h	Water depth [L] (m)
H_s	Significant wave height [L] (m)
I_{dB}	Backscattered intensity [-] (dB)
k	Wavenumber, of sound for example, [L^{-1}] (m^{-1})
k_p	Wavenumber obtained by solving the dispersion equation using the peak spectral wave period, T_p, [L^{-1}] (m^{-1})
k_s	Equivalent roughness [L] (m)
K_t	ABS system constant [-]
K_s	Equivalent bed roughness [L] (m)
L	Vertical decay length scale [L] (m)
L_z	Near bed mixing layer thickness [L] (m)
m_0	Variance of the water surface elevation [L^2] (m^2)
$M = M(r)$	Mass concentration of sediment as a function of range, r, [M L^{-3}] (kg m^{-3})
$\overline{M}$	Mean sediment mass concentration, M, over two or more channels [M L^{-3}] (kg m^{-3})
$n(a_i)$	Probability density as a function of grain radius [-]
r	Range from the ABS transceivers [L] (m)
r_r	The reference range at which the sediment mass concentration is known [L] (m)
s	Ratio of sediment density to water density [-]
t	Time [T] (s)
T	Wave period [T] (s)
T_p	Peak spectral wave period [T] (s)
$u_{*2.5}$	Shear velocity (skin friction) calculated using $f_{2.5}$ [L T^{-1}] (m s^{-1})
$u(t)$	Velocity time-series as a function of time [L T^{-1}] (m s^{-1})
$< u >$	Phase ensemble averaged intra-wave velocity [L T^{-1}] (m s^{-1})
U_1	First harmonic of the equivalent Stokes second order wave [L T^{-1}] (m/s)
U_2	Second harmonic of the equivalent Stokes second order wave [L T^{-1}] (m/s)
U_0	Wave orbital velocity amplitude [L T^{-1}] (m s^{-1})
U_{on}	Onshore wave orbital velocity amplitude [L T^{-1}] (m s^{-1})
U_{off}	Offshore wave orbital velocity amplitude [L T^{-1}] (m s^{-1})
$\overline{U_{on}}$	Mean of the onshore wave orbital velocity amplitudes [L T^{-1}] (m s^{-1})
$\overline{U_{off}}$	Mean of the offshore wave orbital velocity amplitudes [L T^{-1}] (m s^{-1})
U_s	Significant wave orbital velocity amplitude [L T^{-1}] (m s^{-1})
$U_{s\Gamma}$	Significant wave orbital velocity amplitude from the surface elevation [L T^{-1}] (m s^{-1})
V_{rms}	Root mean square backscattered voltage [M L^2 T^{-2} Q^{-1}] (Volts)
w_s	Sediment settling velocity [L T^{-1}] (m s^{-1})
$x = ka_s$	The product of the wavenumber and grain radius [-]
x_0	The arithmetic mean of the particle number PDF as a function of x [-]
z	Height above bed [L] (m)
z_A	Height of ADV above the bed [L] (m)

Symbols list continued over leaf.

Symbols List (continued)

Symbol	Description [dimensions] (typical units)
α_s	Sediment attenuation [L^{-1}] (m^{-1})
α_w	Water attenuation [L^{-1}] (m^{-1})
γ	JONSWAP peak enhancement factor [-]
Γ	Water surface elevation [L] (m)
η	Cross-sectional ripple height [L] (m)
η_0	Temporally averaged height of the ripple below the ARP [L] (m)
$\overline{\eta}$	Spatial and temporal mean cross-sectional ripple height [L] (m)
η/λ	Cross-sectional ripple steepness [-]
η_0/λ_0	Temporally averaged steepness of the ripple below the ARP [-]
$\overline{\eta/\lambda}$	Spatial and temporal mean cross-sectional ripple steepness [-]
θ	Skin friction Shields parameter [-]
$\theta_{2.5}$	Grain roughness Shields parameter based on $k_s = 2.5D_{50}$ [-]
θ_r	Ripple modified Shields parameter [-]
$\overline{\theta}_r$	Cycle mean ripple modified Shields parameter [-]
λ	Cross-sectional ripple wavelength [L] (m)
λ_0	Temporally averaged wavelength of the ripple below the ARP [L] (m)
$\overline{\lambda}$	Spatial and temporal mean cross-sectional ripple wavelength [L] (m)
ξ	Sediment attenuation coefficient [L^2 M^{-1}]
ρ_s	sediment density [M L^{-3}] (kg m^{-3})
$\sigma(...)$	Standard deviation of the quantity in the brackets
σ_M	Standard deviation of the sediment mass concentration, M, [M L^{-3}] (kg m^{-3})
σ_x	Standard deviation of the particle number PDF as a function of x [-]
ς	Trapping efficiency of pumped sampling nozzles [-]
υ	Kinematic viscosity of water [L^2 T^{-1}] (m^2 s^{-1})
ϕ	Phase angle (degrees). Peak onshore velocity of the i^{th} wave cycle is defined to occur at $\phi = 360(i\text{-}1)$
χ	Normalised total scattering cross-section [-]
ψ	Near field correction to spherical spreading [-]

Chapter 1

Introduction

1.1 Background

The coastal zone is dynamic with changes occurring at different timescales both naturally and because of human interference. With the human population living in coastal regions growing, the coastlines and nearshore zones are becoming increasingly influenced by both industry and leisure activities. These activities are not necessarily confined to the nearshore, with the energy industry looking to deeper waters for oil and gas exploration, as well as the development of offshore renewable energy schemes. Any development of the coastal zone and continental shelf relies on the assessment of local sediment transport mechanisms, and can often lead to changes in such mechanisms. There is therefore an increasing need to make reliable predictions of the movement of coastal sediments over a number of temporal and spatial scales. In order to do this, sediment transport processes can be split into the (i) hydrodynamic forcing, (ii) bedforms and (iii) sediment suspensions which together form a *sediment transport triad.*

1.2 Thesis layout

This thesis includes three independent manuscripts as three core chapters that have been, or are intended to be, submitted to peer-reviewed journals. These three papers examine the sediment transport triad in the Deltaflume over different timescales. Chapter 5, the first paper, examines *intra-wave* sediment entrainment processes above ripples and under irregular waves, the shortest of the timescales considered (<10 seconds). Chapter 6 then examines the character of sediment suspensions on *intra-wave*, *wave* and *wave group* timescales (<2 minutes) under a variety of wave forcing conditions and over a variety of bedform types. The last of the three papers, Chapter 7, examines the sediment transport triad during the simulated passing of a storm. In this last paper, each measurement burst during the storm is considered in a time average sense (25 minutes).

Chapter 1 provides an introduction to this study including thesis layout, research objectives

and the author contribution to paper manuscripts.

Chapter 2 presents a concise background to the topic of sand transport processes and bedforms under oscillatory flow. Together, the hydrodynamic forcing, bed and suspended sediments form a dynamic and interacting process triad (Thorne and Hanes, 2002). This chapter reviews these three components in the context of oscillatory flow, and highlights some of the interactions between them.

Chapter 3 describes the Deltaflume facility, the experiments conducted and details the analysis of the bed sediments and the instruments deployed in the flume. Apart from the analysis of the bed sediments, there are no data analysis details given as these are included in the following chapters.

Chapter 4 provides details of the methodology employed to gain reliable measurements of the suspended sediments. Measurements of the suspended sediments were made using a pumped sampling technique and acoustically using the acoustic backscatter system. These two measurement techniques are compared in order to validate the methods used and to determine their accuracy.

Chapter 5 - *Intra-wave observations of sediment entrainment processes above sand ripples under irregular waves* - is a paper published in the Journal of Geophysical Research–Oceans. This paper focuses on the intra-wave process of sediment suspension over rippled beds and under irregular waves, the shortest timescales considered in the three papers. Such small scale processes heavily influence the initial entrainment of sediment which can lead to substantial near bed sediment concentrations. These processes have received a considerable amount of attention, due to their influence on net suspended sediment transport, under regular oscillatory flow. This work is novel because it studies the intra-wave ensemble average suspended sediment field under irregular free surface waves, more typical than regular waves in the field. Whether sediment entrainment occurs repeatedly, as is the case beneath regular waves, under irregular waves is investigated.

Chapter 6 - *Wave groups and the character of sediment resuspension over an evolving sandy bed* - is a manuscript intended for submission to Continental Shelf Research and studies the suspension of sediment on intra-wave, wave and wave group time-scales over a number of fine and medium-grained bedform types. This is done by examining high resolution time-series of water velocity and suspended sediment concentration in both the time and frequency domain. This chapter studies the character of the wave groups and ends by considering the implications of wave groups rather than individual waves in the modelling of coastal sediment transport.

Chapter 7 - *A stormy inheritance: the interaction of irregular wave forcing, bedforms and sus-*

pended sediment concentrations in an experimental waxing and waning hydrodynamic regime - is a manuscript intended for submission to the Journal of Geophysical Research–Earth Surface - and studies the evolution of bedforms and changes in the time average suspended sediment concentrations during the simulated passing of a storm event in the Deltaflume. The emphasis of this work is on the interaction between the wave forcing, bedforms and suspended sediment concentrations at each stage of the storm sequence. An expression was found relating sediment suspensions to the bed roughness. Crucially this bed roughness was not only due to the bed morphology, but was enhanced by contributions from a moving sand layer at high flow velocities. The questions of bedform inheritance and their influence on sediment suspensions are also addressed.

Chapter 8 is an extended discussion drawing together the work in the previous chapters. The research questions laid out below form the basis of this discussion.

1.3 Research questions

The major questions that have framed this research of sediment suspensions over sandy bedforms in the Deltaflume under irregular waves are presented below with their rationale. These questions are addressed in the final chapter using results and interpretations from core chapters where applicable.

Question 1. ***Can the sediment entrainment process of vortex formation and shedding be identified under irregular waves and how does it contribute to the intra-wave sediment suspension field?***

Rationale: The suspension of sediment via vortices generated through flow separation above steep sided ripples is well documented (e.g. Bagnold, 1946; Bijker et al., 1976; Nakato et al., 1977; Davies and Thorne, 2005; Van der Werf et al., 2007). This can have a significant effect on net cross-shore sediment transport as vortices generated in the first wave half cycle are vertically-advected and transported in the second wave half cycle (Bijker et al., 1976). Most quantitative work is based on observations made under regular oscillatory flow in the laboratory. Whilst observations have been made in the field and under irregular waves (Osborne and Vincent, 1996; Villard and Osborne, 2002), there is little quantitative information regarding the extent to which this process occurs in the field. The theoretical work of Malarkey and Davies (2002, 2004) suggests that for vortex shedding to occur, the ripples must be steep sided and the orbital excursion diameter must be at least as long as the ripple wavelength. One hypothesis therefore is that vortices form only under a fraction of irregular waves.

Question 2. ***What is the character of the sediment suspensions under wave groups?***

Rationale: The initial entrainment of sediment is largely an intra-wave process dependant on the properties of individual incident waves (Vincent and Hanes, 2002) and of the bedforms (Ribberink and Al-Salem, 1994). Fluctuations in the suspended sediment concentrations have, however, been observed not only to occur at these intra-wave frequencies but also at lower frequencies associated with wave groups (Hanes, 1991; Villard et al., 2000; Vincent and Hanes, 2002). The height to which sediment can be entrained by intra-wave processes is generally limited to the near bed mixing layer, but wave-groups enable a continual injection of turbulence, with turbulence production being greater than dissipation, and allows for the further entrainment of sediment beyond the intra-wave near bed mixing layer. There are often time lags between peaks in sediment concentration close to and far away from the bed (Vincent and Hanes, 2002). Models based purely on intra-wave entrainment, and under regular waves, are therefore unlikely to predict high sediment concentrations high up from the bed. It is therefore important to characterise the suspension patterns under wave groups in differing hydrodynamic and bedform conditions.

Question 3. ***How do sandy beds respond to changes in wave forcing and what is the influence of inherited bedforms?***

Rationale: There are many parameters that influence the development of ripples in oscillatory flow. One dominant control is the orbital excursion diameter, and ripples are often described by how their cross-sectional wavelength compares with the orbital diameter (Clifton, 1976; Wiberg and Harris, 1994). As the wave steepness increases the orbital diameter increases and influences bedform development. There are a number of schemes that can be used to predict the cross-sectional dimensions of ripples depending on the orbital diameter (e.g. Wiberg and Harris, 1994; Soulsby and Whitehouse, 2005). Many of these schemes are based on a large number of different field and laboratory studies, together covering a large range of dynamic parameters. In the field there are many parameters influencing bedform development and it is difficult to select, and systematically vary, a suitable dynamic variable. Laboratory experiments, however, offer more control over the dynamic variable but are often simplified in many ways. One such simplification is that sediment beds are often laid out smooth with no relict structures from, for example, bioturbation or previous flow regimes. In recent years there have been a number of studies conducted in large scale flumes (Williams et al., 2005) or oscillatory flow tunnels (O'Donoghue and Clubb, 2001; O'Donoghue et al., 2006). Many of these studies have however focused on regular oscillatory flow and there are knowledge gaps concerning the development of ripples beneath irregular field scale free-surface waves and in a variety of different sediment transport regimes.

Question 4. ***How do time average suspended sediment concentration profiles respond to changes in the wave forcing and bed conditions?***

Rationale: The intra-wave suspension of sediment is strongly dependant on the strength of the oscillatory flow and the type of bedforms present (Ribberink and Al-Salem, 1994; Vincent et al., 1999; Grasmeijer and Kleinhans, 2004). This is reflected in time average suspended sediment concentration profiles. It is important to predict the wave related contribution to sediment suspensions in a time average sense as it can contribute greatly to net transport in many coastal settings (Nielsen, 1992). Therefore it is important to parameterise such suspensions over a variety of bedform and flow conditions for use in simplified time average numerical modelling. The presents of relict bedforms can influence sediment suspensions in ways that are not normally associated with certain hydraulic regimes. It is important therefore to consider when relicts may be present and what influence they have on suspended sediment concentrations.

Question 5. ***Over what timescales do sediment suspension processes operate under irregular waves and what implications does this have for future observations and modelling?***

Rationale: The previous questions address sediment transport process acting (i) at high frequency intra-wave timescales, (ii) at lower frequency 'wave-group' timescales and (iii) in a time average sense. It is important to consider the relative importance of the different timescales and how they interact to influence sediment transport. Understanding the character of sediment transport over different timescales could have an impact on experimental design, observations, measurements and modelling.

1.4 Author contribution and status of manuscripts

Chapter 5: *Intra-wave observations of sediment entrainment processes above sand ripples under irregular waves.* Published in Journal of Geophysical Research - Oceans.

Citation: O'Hara Murray, R. B., P.D. Thorne and D. M. Hodgson (2011), Intrawave observations of sediment entrainment processes above sand ripples under irregular waves, J. Geophys. Res., 116, C01001, doi: 10.1029/2010JC006216.

Author contributions: (i) **O'Hara Murray, R. B.** was the principle investigator and main author and performed all the processing and data analysis. (ii) **Thorne, P. D.** was involved with the design of the Deltaflume experiments and with the collection of data. He instigated many discussions regarding the ABS data analysis, and its validation, and the interpretation of results. He also reviewed the manuscript making in-depth and detailed comments. (iii) **Hodgson, D. M.** was involved with in depth discussions regarding the results and reviewed the manuscript.

Chapter 6: *Wave groups and the character of sediment resuspension over an evolving sandy bed.* Intended for submission to Continental Shelf Research.
Author contributions: (i) **O'Hara Murray, R. B.** was the principle investigator and main author and performed all the processing and data analysis. (ii) **Hodgson, D. M.** instigated and encouraged in-depth discussions, provided assistance with the interpretation and extensively reviewed the manuscript. (iii) **Thorne, P. D.** was involved with the design of the Deltaflume experiments and with the collection of data. He has also been involved in discussions regarding the ABS data analysis.

Chapter 7: *A stormy inheritance: the interaction of irregular wave forcing, bedforms and suspended sediment concentrations in an experimental waxing and waning hydrodynamic regime.* Intended for submission to Journal of Geophysical Research–Earth Surface.
Author contributions: (i) **O'Hara Murray, R. B.** was the principle investigator and main author and performed all the processing and data analysis. (ii) **Hodgson, D. M.** has instigated in-depth discussions regarding results, assisted with interpretation and reviewed the manuscript. (iii) **Thorne, P. D.** was involved with the design of the Deltaflume experiments and with the collection of data. He has participated and instigated many discussions regarding the ABS data analysis and interpretation of results as well as providing detailed manuscript review. (iv) **Davies, A. G.** has been involved in a number of discussions and reviewed the manuscript.

Chapter 2

Sand transport processes in oscillatory flow

Sediment transport processes can broadly be considered to include three components: (i) the hydrodynamic forcing of the waves and tides, (ii) the seabed characteristics and bed morphology and (iii) the sediments suspended in the water. These three components interplay with one another and commonly there are complicated and dynamic feedbacks (Thorne and Hanes, 2002). For example, bedforms are generated by the interaction of the flow with the bed sediments, and these bedforms in turn influence the flow within the boundary layer and the entrainment of sediment from the bed. This sediment entrainment can in turn influence ripple growth, migration or erosion. Figure 2.1 depicts these three components as an interacting triad. These three components are considered below in the context of oscillatory flow. In addition, the bottom boundary layer, resulting from an interaction of the bed and the hydrodynamics, is considered.

Sediment transport processes are of interest to workers within a variety of disciplines including oceanography, coastal and ocean engineering, process sedimentology, and stratigraphy. Coastal scientists and engineers are interested in predicting the transport of sediment over a number of timescales. Applications include coastal engineering impact assessments in terms of sediment transport pathways. For example, interference often leads to net accretion or erosion in other, often unpredicted, locations. Predictions can also be made to inform policy decisions such as coastal defence, waterway maintenance such as dredging and marine environmental management. Commonly, sedimentologists study preserved bedforms from which the process leading to their development can be inferred, which in turn can lead to the inference of the palaeoenvironmental conditions (Komar, 1974).

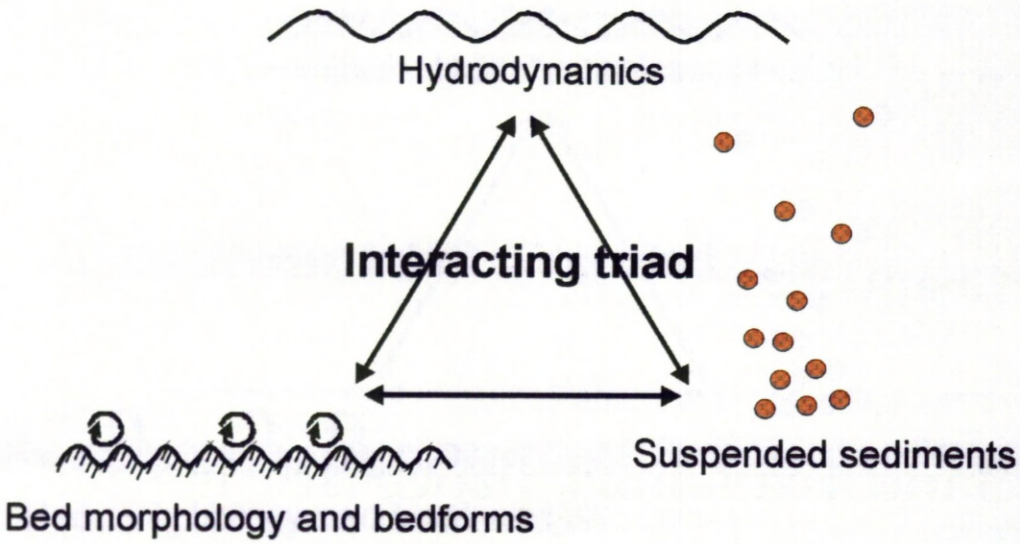

Figure 2.1: An illustration of the sediment transport triad with interactions and feedbacks.

2.1 Hydrodynamic forcing

The motion of water particles under waves can be described by linear wave theory where a number of simplifications are made in order to solve the hydrodynamic continuity equation and kinematic boundary conditions. The solution is a sinusoidal wave describing the water surface elevation in space and time. Such *Airy waves* have a fixed height and wavelength and are symmetrical. Other wave theories result in asymmetrical *Stokes*, *cnoidal* or *solitary* waves which describe the steepening of wave crests that can occur in shallow water. These theoretical monochromatic waves are idealised, in that they have a constant height and period, and are termed *regular waves*. Naturally occurring surface waves have, however, a broad distribution of heights and periods, and are termed *irregular waves*.

The water particle paths under regular symmetric waves are circles which elongate into ellipses with depth (Dean and Dalrymple, 1991). Using linear wave theory, the horizontal velocity component of the water particles, u, parallel to the direction of wave propagation, can be expressed as (Dean and Dalrymple, 1991)

$$u = \frac{H\pi \cosh k(h+z)}{T \sinh kh} \cos(kx - \omega t), \tag{2.1}$$

where x and z are horizontal and vertical positions of the particle, h is the water depth, t is time, H is the wave height and T is the wave period. Thus close to the bed, just above the wave boundary layer, the velocity amplitude, U_0, and excursion diameter, d_0, are given by

$$U_0 = \frac{\pi\ H}{T \sinh kh} \tag{2.2}$$

$$d_0 = U_0 T/\pi. \tag{2.3}$$

The distribution of irregular wave heights and periods can be described by spectral energy functions, such as the JONSWAP spectrum (Carter, 1982). When modelling sediment transport it is often convenient to parameterise the irregular wave spectrum with the wave height and period of an *equivalent* regular wave. Some workers use the root mean square wave height (Fredsoe and Deigaard, 1992; Soulsby, 1997) and others have found that parameterisations such as the mean of the highest one tenth orbital velocity amplitudes is more suitable in some sediment transport applications (O'Donoghue et al., 2006). One widely used parameterisation is the peak spectral period and significant wave height (e.g. Thorne et al., 2002; Williams et al., 2004). The significant wave height, H_s, is defined as the mean of the highest one third waves in a record and can be easily calculated using (e.g. Soulsby, 1997)

$$H_s = 4\sigma(\Gamma), \tag{2.4}$$

where $\sigma(\Gamma)$ is the standard deviation of the water surface elevation time-series, Γ. Section 7.4 details methods for calculating H_s from the water elevation power spectrum and water particle velocity measurements.

2.2 Bedforms

The seabed in the near-shore zone is rarely flat and smooth. Sedimentary structures such as ripples, dunes, hummocks and ribbons tend to form, due to the constant transport and sorting of sediment by currents and waves. Wave generated ripples are oscillatory, or bidirectional, bedforms that form as a result of the orbital excursions of fluid particles near the bed. Early laboratory experiments showed that oscillatory ripples broadly fall into two categories: rolling grain and vortex ripples (Bagnold, 1946). Rolling grain ripples are the first to form on a lower-stage plane bed after the initiation of sediment movement. In faster flows, ripples are steeper and force the boundary layer flow to separate and form vortices that can trap and entrain bed sediment. As the flow gets faster still the vortex ripple regime is replaced by sheet flow processes and the bed becomes an upper-stage plane bed. These bedform stages, or phases, were presented by Allen (1979) in the form of a bedform phase diagram, Figure 2.2, where the type of ripples present on the bed is a function of the diameter of the bed sediment and the orbital velocity amplitude of the oscillations.

The process of bedform development is more complicated in field environments where there are additional processes disturbing the bed, such as bioturbation, and there often remain relict bedforms from previous flow regimes (Nielsen, 1992; Hanes et al., 2001). Clifton (1976) and Wiberg and Harris (1994) categorised wave generated ripples as either orbital, suborbital or anorbital, depending on how their cross-sectional wavelengths compare to the wave orbital diameter, d_0. (i) Orbital ripples have wavelengths that scale with d_0 and sharp well defined trochoidal shaped crests. (ii) Anorbital ripples are less steep than orbital ripples and have

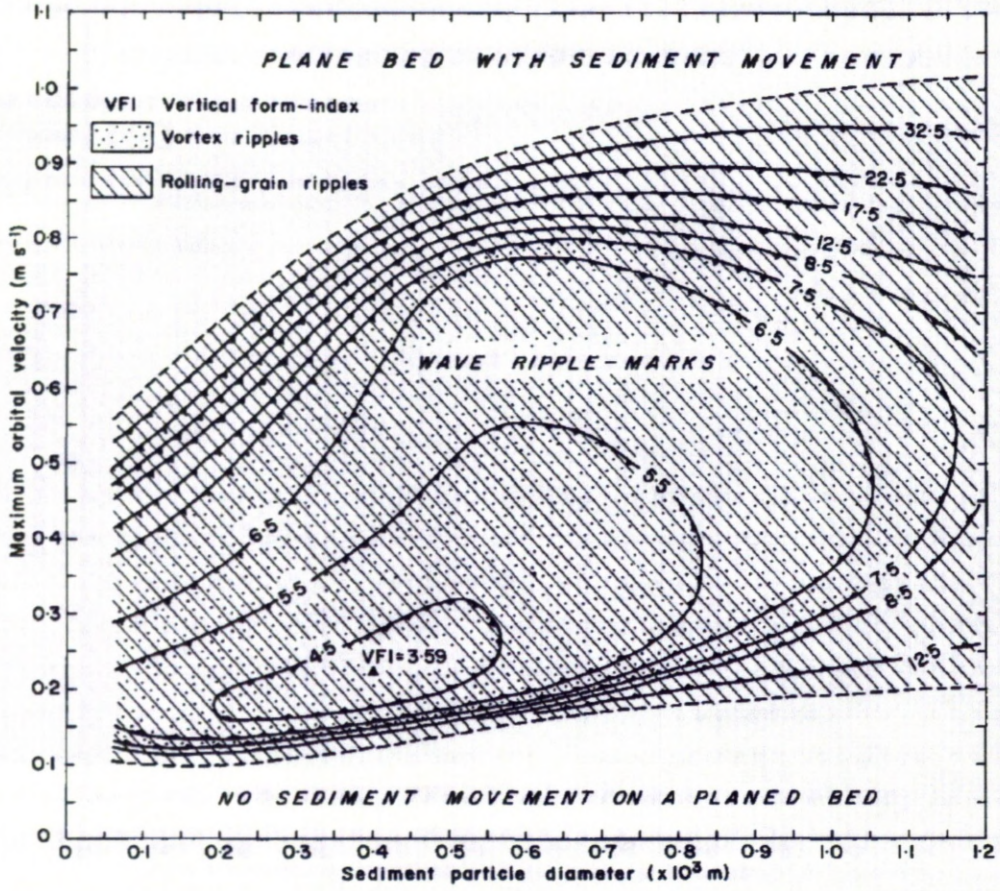

Figure 2.2: The bedform phase diagram of Allen (1979) for oscillatory flow.

wavelengths that, rather than scaling with the d_0, depend on the median diameter of the bed sediment. (iii) Suborbital ripples are an intermediate type and have wavelengths shorter than those of orbital ripples but still show some dependence on d_0. Another consideration is the plan-form geometry of wave ripples. One recently documented terminology is that of Pedocchi and Garcia (2009) who defined ripples as either (i) two-dimensional (2D) with long straight crests perpendicular to the flow, (ii) three-dimensional (3D) with irregular and short crests or (iii) almost two-dimensional (quasi-2D) with crests perpendicular to the flow but with shorter and more sinuous crests than those of 2D ripples. More details on the classification of wave generated ripples in terms of their cross-sectional and plan-form geometries are given in Section 7.2.

Many of the ripple prediction schemes assume the bed to have adjusted to recent changes in the hydrodynamics and to be in equilibrium. The equilibrium simplification is valid in environments where there are dominant hydrodynamic conditions over long timescales. Close to the shore, however, there can be continual changes in the hydrodynamics, especially in the surf zone where there are great changes through tidal cycles (Austin et al., 2007), and due to weather events such as storms. The equilibrium assumption can be valid though, as the bed can adjust quickly to changes in the hydrodynamics and form a new equilibrium state. Nevertheless, there are transient states where ripples adjust to the new flow conditions (Davis et al., 2004; Doucette and O'Donoghue, 2006). Rolling grain ripples are an example of a transient bedform that tend to be observed in flume tanks. In the field they may exist, but only for very short periods of time before being replaced by low steepness ripples conforming more to the definition of vortex ripples (Andersen, 2001).

2.2.1 Hydraulic bed roughness

Bedforms, formed by the interaction of the hydrodynamics with the bed sediment, in turn influence the hydrodynamics by contributing to the hydraulic bed roughness, k_s. Over flat beds, the Nikuradse grain roughness, due to skin frictional forces on the individual grains (Nielsen, 1992), is a function of the median grain diameter of the bed sediment, D_{50}, and is typically given by (e.g. Soulsby, 1997)

$$k_s = 2.5 D_{50}. \tag{2.5}$$

When bedforms are present, the dominant contribution to the roughness is due to form drag forces that act on the ripple profile (Nielsen, 1992; Van Rijn, 2007) and k_s is often expressed in terms of the ripple dimensions. One commonly used form for k_s above a rippled bed is (Grant and Madsen, 1982; Nielsen, 1992; Styles and Glenn, 2002; Davies and Thorne, 2008)

$$k_s = \alpha \, \eta \, (\eta/\lambda), \tag{2.6}$$

where η and λ are respectively the cross-sectional height and wavelength of the ripples present on the bed and α is a constant. The concept of hydraulic roughness is further outlined in Section 5.2 which also outlines the development of ripples and a simple modelling framework (Davies and Thorne, 2008) in this context.

2.2.2 The prediction of ripple geometry

The hydraulic roughness above ripples is often a function of the ripples' cross-sectional geometry (e.g. Grant and Madsen, 1982; Davies and Thorne, 2008). Thus there have emerged a number of schemes that predict the cross-sectional dimensions of ripples (e.g. Nielsen, 1981; Mogridge et al., 1994; Wiberg and Harris, 1994; Soulsby and Whitehouse, 2005). These prediction formulae are typically functions of a non-dimensional dynamic variable that captures all the information regarding the flow and bed sediment that influence ripple formation. One such variable is the grain roughness Shields parameter (e.g. Nielsen, 1992)

$$\theta_{2.5} = \frac{f_{2.5} U_0^2}{2(s-1) g D_{50}}, \tag{2.7}$$

where s is the ratio of sediment density to water density (s=2.65 for quartz sand), g is the acceleration due to gravity and $f_{2.5}$ is the grain roughness wave friction factor (skin friction) based on the equivalent Nikuradse grain roughness, $k_s = 2.5 D_{50}$, which can be calculated using (Soulsby, 1997)

$$f_{2.5} = 0.237 (d_0 / 5 D_{50})^{-0.52}. \tag{2.8}$$

A somewhat simplified parameter is the mobility number (e.g. Nielsen, 1981)

$$\Psi = \frac{U_0^2}{(s-1) g D_{50}}. \tag{2.9}$$

These two parameters, $\theta_{2.5}$ and Ψ, represent the balance between disturbing and stabilising forces acting on the sediment grains. A much simpler parameter is d_0/D_{50} which does not include the influence of the sediment density or gravity, which are often relatively constant.

The issue of the prediction of plan-form ripple geometry was addressed by Pedocchi and Garcia (2009) who reviewed the limited number of criteria defining a transition from 2D to 3D ripples and also developed new criteria. The development of 3D ripples is associated with turbulent three-dimensional motions. Generally, finer sands tend to form 3D ripples before coarser sands: coarser sands can resist the turbulent three-dimensional motions. The criteria for the transition from 2D to 3D ripples proposed by Pedocchi and Garcia (2009) are functions of a dimensionless particle size given by $\sqrt{g(s-1)D_{50}} D_{50}/\nu$, where ν is the kinematic viscosity of the water, and the wave Reynolds number given by $Re = U_0 d_0 / 2\nu$.

2.3 The oscillatory bottom boundary layer

The oscillatory bottom boundary layer is that part of the flow close to the bed heavily influenced by the bed (Nielsen, 1992). Oscillatory bottom boundary layers can be classified in terms of the wave Reynolds number, Re, and the relative roughness, $d_0/2k_s$. Properties of laminar and hydraulically smooth turbulent boundary layers heavily depend on Re, whereas the properties of hydraulically rough boundary layers depend on $d_0/2k_s$ (e.g. Jonsson, 1980). In turbulent oscillatory boundary layers, an important contribution of turbulence to sediment resuspension is its anisotropic nature. One manifestation of this is the bursting phenomenon (e.g. Heathershaw, 1974) including irregularly occurring upward *ejections* and downward *sweeps* of fluid. The anisotropic nature of turbulence is often compared with the Brownian motion of molecules, resulting in Fick's law of diffusion where the flux of a substance is proportional to its concentration gradient. Drawing an analogy with such behaviour results with the definition of the eddy viscosity, K, as a constant of proportionality between the turbulent shear stress, τ, which is a momentum flux, and the velocity shear, dU/dz:

$$\tau = \rho K \frac{dU}{dz} \tag{2.10}$$

where ρ is the fluid density.

2.4 Suspended sediments

2.4.1 Intra-wave sediment suspension processes above ripples

When steep sided ripples are present on the bed, the wave boundary layer can separate in the lee of ripple crests and form vortices which are ejected into higher parts of the flow around flow reversal. Vortices can trap sediment which is advected both horizontally and vertically after being shed from the crest of a ripple (Bijker et al., 1976; Hansen et al., 1994). The generation of vortices can actually impose some spatial and temporal order on turbulence effects, because they can be generated in a coherent manner each wave half cycle. For these reasons the entrainment of sediment via vortices is often referred to as a convective, rather than a diffusive, process (e.g. Nielsen, 1992; Thorne et al., 2002, 2009a).

Figure 2.3 shows a schematic of the vortex entrainment process from Thorne et al. (2003). Figure 2.3(a) shows the growth of the vortex, V_1, in the lee of the ripple during the onshore phase of the wave cycle. Figures 2.3(b and c) show the V_1 vortex being advected over the crest of the ripple at flow reversal. In Figure 2.3(d) the offshore directed flow is at a maximum and the V_1 vortex is being advected offshore. At the same time in Figure 2.3(d) a new vortex, V_2, is being generated in the ripple lee. Figures 2.3(e and f) show the V_1 vortex growing in size as it is directed offshore and the V_2 vortex being advected over the ripple crest as the flow changes direction. Thus it can be seen that whilst the V_1 vortex was generated during the

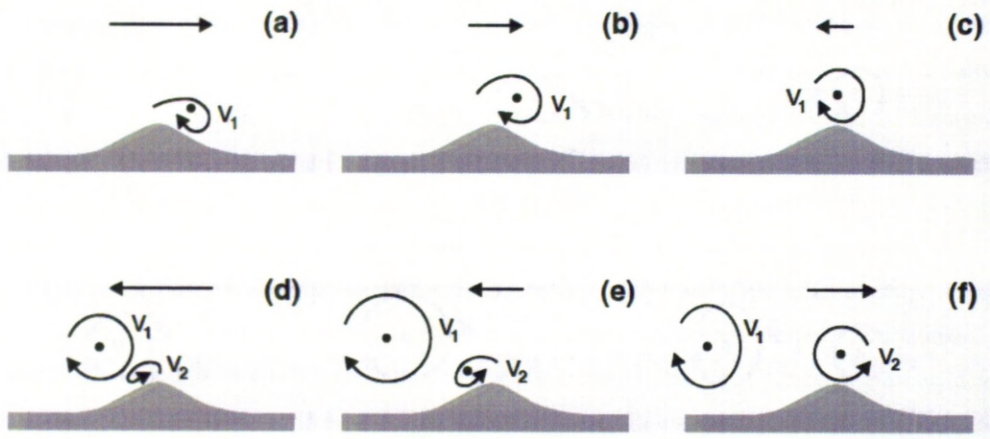

Figure 2.3: A schematic drawing depicting the process of vortex entrainment of sediment (from Thorne et al. 2003). The arrow at the top of each figure represents the near bed horizontal velocity vector and the direction of wave propagation is from left to right.

onshore phase of the wave cycle, it is in fact transported offshore. Asymmetric waves, with the onshore orbital velocity amplitude being larger than the offshore velocity amplitude, can lead to the V_1 vortex being larger than the V_2 vortex. Thus, despite the larger onshore velocity amplitudes, net sediment transport can be in the offshore direction under asymmetrical waves. This is often termed offshore sediment pumping.

Some of the earliest observations of vortex entrainment of sediment were by Bagnold (1946) and Bijker et al. (1976) but some of the first intra-wave measurements of the suspended sediment concentration were made by Nakato et al. (1977). More recently, detailed intra-wave measurements have been made of suspended sediment concentration fields in large scale facilities using acoustic instrumentation (Thorne et al., 2003; Davies and Thorne, 2005; Van der Werf et al., 2007). During these measurements the ripples migrated beneath the acoustic instrumentation allowing measurements to be made across the whole cross-sectional ripple profile. A coherent phenomenon consistent with the entrainment of sediment in a lee-wake vortex shed at flow reversal was identified.

Process-based numerical 'research' models (Davies et al., 2002) can accurately predict the vertical and temporal structure of sediment suspensions on intra-wave timescales, and can lead to further understanding of the fundamental processes of sediment entrainment. The accurate measurement of the intra-wave velocity and sediment suspension fields are therefore necessary to validate and further develop such models.

2.4.2 time average suspended sediment concentrations

Research models can be highly successful at predicting intra-wave suspensions but are often limited to certain flow and bedform regimes (Davies et al., 2002). Whilst the prediction of net time average concentrations and fluxes is possible with such models, they can be slow to run

and not necessarily stable over wide parameter ranges. Therefore, there is a need to develop practical models that do not necessarily resolve the detailed spatial and temporal structure of velocity and sediment suspension fields (Davies et al., 2002). The modelling of time average suspended sediment concentration profiles in the one-dimensional vertical is an example of such practical modelling techniques. One simplified approach is to assume that in the steady state the downward flux of sediment via settling is equal to the upward flux due to diffusion. Thus, the time average sediment diffusion equation is given by

$$w_s C + \varepsilon_s \frac{dC}{dz} = 0, \tag{2.11}$$

where $C = C(z)$ is the sediment concentration with height, z, above the bed, w_s is the sediment settling velocity and ε_s is the sediment diffusivity. The upward flux of sediment is often contributed to convective, as well as diffusive, processes, such as the upward advection of sediment via vortices. In these cases the diffusion equation can be modified to include terms representing the upward convection of sediment. One example of a sediment convection-diffusion equation is (Nielsen, 1992; Lee and Hanes, 1996)

$$w_s C + \varepsilon_s \frac{dC}{dz} - w_s C_0 F(z) = 0, \tag{2.12}$$

where $F(z)$ is termed the convective-entrainment function and describes the probability of a particle reaching the height z above the bed. The solution to equations (2.11) and (2.12) can generally be expressed as

$$C(z) = C_r \, \Phi(z) \tag{2.13}$$

where $C_r = C(z = r)$ is the concentration magnitude at a specific near-bed elevation and is termed the reference concentration and $\Phi(z)$ is the distribution of suspended sediment with height, z, above the bed, often termed the shape function. Section 7.2.3 outlines the basis behind a number of simple solutions to equation (2.11) including expressions for the sediment diffusivity. Section 7.2.3 also reviews a number of empirical expressions for C_r, which are typically functions of the Shields parameter.

Chapter 3

The Deltaflume experimental storm sequence and instrumentation

3.1 Introduction

The Deltaflume of Deltares Delft Hydraulics, the Netherlands, is a large scale flume, 230m long, 5m wide and 7m deep, which enables sediment transport processes to be monitored at field scale. At one end there is a wave paddle for generating waves and at the other end a sloping surface designed to dissipate the wave energy, preventing wave reflection. Figure 3.1 is a view looking along the length of the Deltaflume towards the wave paddle. Irregular waves were generated in a series of experiments during which the significant wave height, H_s, was systematically stepped up and then back down in order to simulate the waxing and waning of a storm sequence. During the course of the experiments there were no steady currents generated and the peak spectral wave period was held constant at approximately 6 seconds such that the surface wave steepness increased with H_s. The systematic stepping up and down of H_s, in approximate 0.2m step sizes, is here termed the experimental sequence. Similarly, the experiments during which H_s was stepped up are termed the waxing phase of the storm sequence and the experiments during which H_s was stepped down are termed the waning phase of the storm sequence. The experimental sequence was conducted twice: first over a fine-medium-grained sand bed and then over an upper-medium-grained sand bed. These two sediment beds are here referred to as the fine-grained and the medium-grained beds for brevity. In each case, a 0.7m deep sediment bed was laid down in the centre of the flume in a 30m long region spanning the width of the flume. The sand beds were initially flat and were not flattened between experiments such that each experiment inherited the bed morphology formed during the previous experiment (Bell and Williams, 2002). After the sediment beds were laid down, the flume was filled to a nominal

Figure 3.1: The Deltaflume of Deltares Delft Hydraulics, the Netherlands, looking towards the wave paddle from which the waves propagate. This large scale flume facility is 230m long, 5m wide and 7m deep.

depth of 4m using water from the nearby canal. Over the fine-grained bed 16 experiments were conducted and are referred to here as F01, F02, ..., F16. Similarly, over the medium-grained bed 17 experiments were conducted, referred to here as M01, M02, ..., M17. During the majority of experiments there were two 25 minute measurement bursts, distinguished here by _1 and _2, such as M01_1 and M01_2. The first measurement burst started one minute before the waves commenced and the second measurement burst started after the waves had been running for one hour. This way measurements were made both with the bedforms in a state of non-equilibrium and equilibrium with the flow (Marsh et al., 1999). Bell and Williams (2002) provided detailed documentation of the experiments conducted, the research objective and the experimental instrumentation.

3.2 Bed sediment grain size analysis

Sediment cores were taken from a variety of locations on the bed (Bell and Williams, 2002) and their volume size distributions analysed using a Coulter Laser Granulometer. Samples of the bed sediment were also sieved by Delft Hydraulics in order to determine the mass size distribution. Samples of sediment laden water were taken through pumped sampling (see Chapter 4) and on a number of occasions the lower most pumped sampling nozzle was buried in the bed sediment. These provided a third set of bed sediment samples and were analysed using laser granulometry.

Figure 3.2 shows the cumulative grain size distributions from sieving and laser graulometry of (a) the fine-grained and (b) the medium-grained bed sediment. In Figure 3.2, the data labelled 'Laser 1' and 'Laser 2' correspond to the samples obtained from the pumped samples of the

	$\overline{D}_{10}$ (μm)	$\sigma(\overline{D}_{10})$ (μm)	$\overline{D}_{50}$ (μm)	$\sigma(\overline{D}_{50})$ (μm)	$\overline{D}_{90}$ (μm)	$\sigma(\overline{D}_{90})$ (μm)
Fine-grained Laser	161.4	15.4	258.0	16.7	407.8	20.3
Fine-grained Sieved	156.7	03.3	221.1	04.1	290.6	07.1
Medium-grained Laser	242.7	19.6	374.9	29.8	576.6	46.8
Medium-grained Sieved	246.4	06.6	348.8	00.1	473.2	18.4

Table 3.1: Grain diameters for which 10%, 50% and 90% of the sediment is finer than, determined from the sieving and laser granulometry results of the fine and medium-grained bed sediments.

bed and the sediment cores respectively. These two 'laser' results were analysed using laser granuolmetry to determine the volume size distribution. Assuming the sediment density to be uniform with size, the mass size distributions from the sieving and the volume size distributions from laser granulometry are equivalent in terms of 'fraction finer than' cumulative distribution. For each of the three sampling/analysis methods, a number of samples were analysed and Figure 3.2 presents the mean (symbols) and standard error (error bars). The one exception was the medium-grained Laser 2 results, where only one sample was analysed. Lognormal grain size distributions were fitted to the Sieved and Laser 1 results and are shown by the lines in Figure 3.2. For each of the two size distributions there is a high level of agreement between the different methods at the smaller grain diameters less than a fraction of 0.2. There is, however, a discrepancy between the sieved and laser results at the larger grain diameters. By comparison, there is a high agreement between the two Laser results. For natural sediments, the size of a particle is not uniquely defined and size depends on the method of measurement (Syvitski et al., 1991). For example, Allen (1968) defined a number of definitions including surface diameter, volume diameter, drag diameter, sieved diameter and Stokes diameter. The difference between the volume diameter obtained by laser granulometry and the sieved diameter is clear from Figure 3.2.

Table 1 lists grain diameters for which 10%, 50% and 90% of the sediment is finer than, determined from the sieving and laser granulometry results. The mean of the different samples is shown, $\bar{D}_i$ where i is the percent finer than, along with the standard deviation, $\sigma(\bar{D}_i)$. In this work the the results from the laser grain size analysis are used so that they can be compared with the grain size results from the pumped samples of the suspended sediments.

3.3 Description of the instrumentation deployed

Figure 3.3 shows (a, b) images of the instruments frame that was aligned to one side of the Deltaflume and in the centre of the sandy bed, and (c, d) a schematic of the instruments on the frame, which are used in this study. The instrumentation has previously been described by Williams et al. (2004, 2005); Bell and Williams (2002). The two Nortek Acoustic Doppler Velocimeters (ADV-1 and ADV-2) measured three components of the flow: horizontal along-flume (cross-shore), horizontal across-flume (along-shore) and vertical. ADV-1 was mounted at

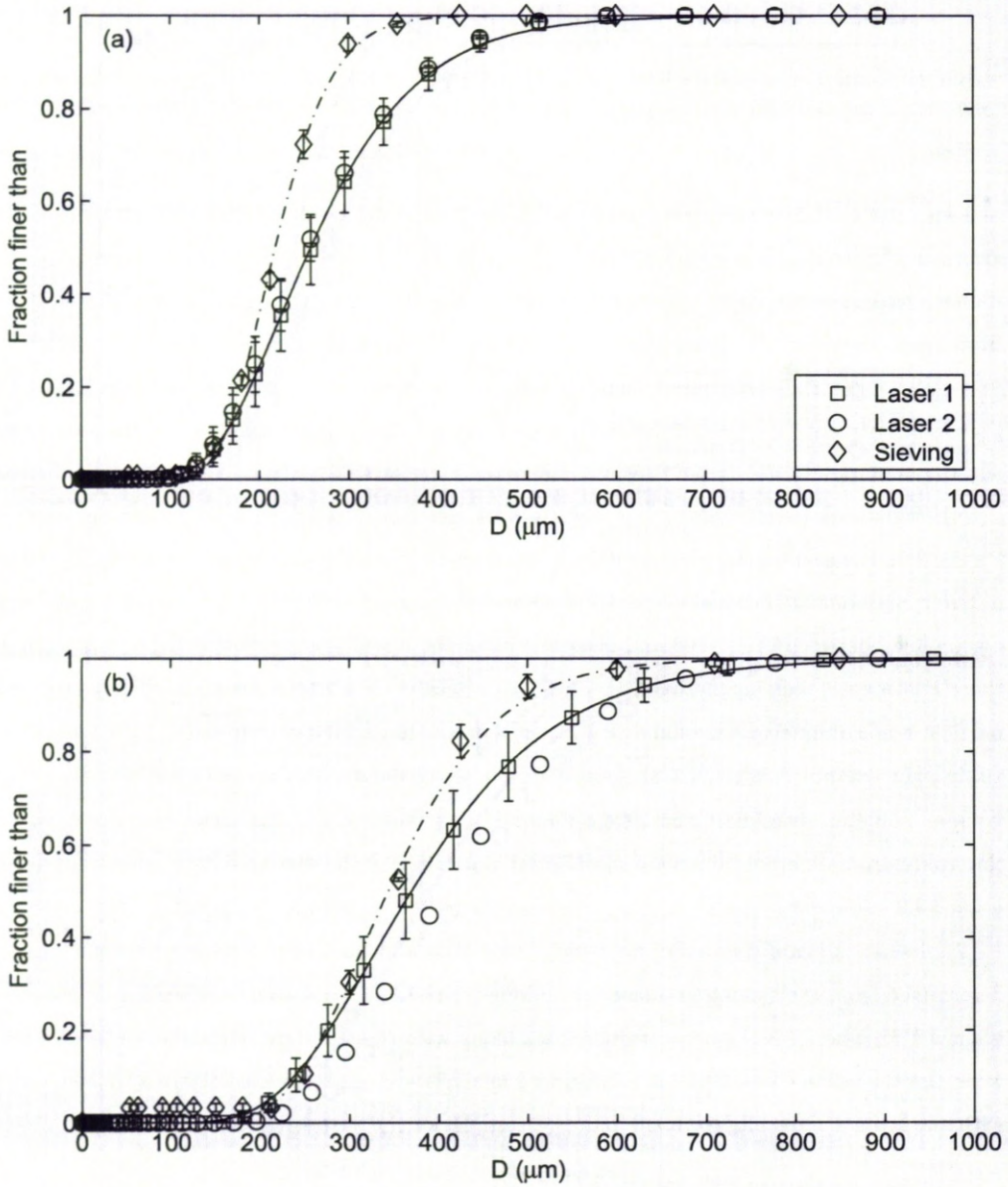

Figure 3.2: Cumulative grain diameter, D, distributions of the bed sediment obtained through sieving (diamonds) and laser grain size analysis of the pumped samples (Laser 1, squares) and sediment cores (Laser 2, circles). The mean of a number of samples is indicated in each case, along with their standard errors as error bars. Lognormal size distributions fitted to the Sieved ($- \cdot -$) and Laser 1 ($-$) results are shown.

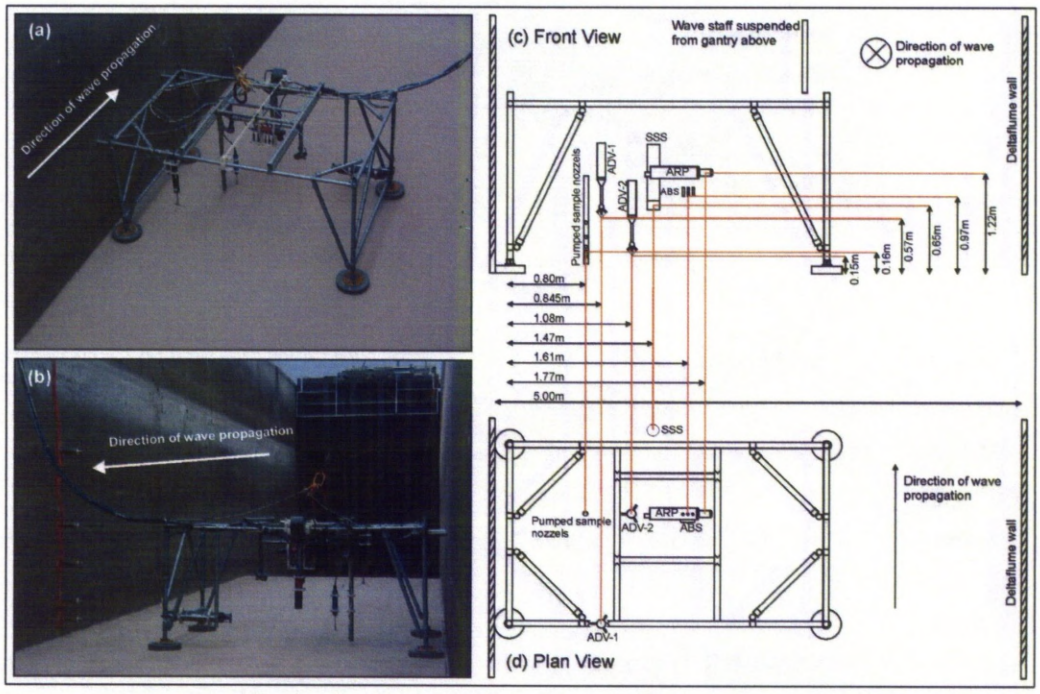

Figure 3.3: The instrument frame deployed in the Deltaflume. The wave paddle is clearly visible in (b). (c) and (d) show a schematic of the frame and instruments used in this study including the two Acoustic Doppler Velocimeters (ADV), Sector Scanning Sonar (SSS), Acoustic Ripple Profiler (ARP), Acoustic Backscatter System (ABS), wave staff and pumped sampling equipment.

the offshore end of the instrument frame with the measuring volume 0.57m above the base of the frame. ADV-2 was mounted in the centre of the instrument frame and with the measuring volume 0.15m above the base of the frame. The bedforms were monitored using the Acoustic Ripple Profiler (ARP) and Sector Scanning Sonar (SSS) which were mounted in the centre and at the onshore end of the frame respectively. The 2.0MHz ARP, shown in Figure 3.4(a), scanned a 4m across-shore transect of the bed approximately once a minute at centimetre horizontal resolution and sub-centimetre vertical resolution providing a cross-sectional profile of the bed, and how it changed with time. Figure 3.4(b) is an illustration of the ARP scanning a 4m transect. The 1.2MHz SSS, shown in Figure 3.4(c), mechanically scanned through 400 angular steps during each revolution taking $\sim$ 60s (Williams et al., 2004) and provided plan-form images of the bed.

The suspended sediments were measured through direct pumped sampling and by the Acoustic Backscatter System (ABS). Pumped sampling, otherwise known as transverse suction, was described by Bosman et al. (1987) and enables samples of sediment laden water to be taken at a number of heights above the bed. The pumped sampling equipment was positioned in the centre of the instrument frame and consisted of a metal pipe with 5 nozzles at different heights. Attached to each nozzle was a flexible tube that ran up the metal pipe and out of the flume. Figure 3.5 shows (a) the pumped sampling equipment deployed in the flume and (b) the samples of sediment laden water being gathered in buckets by the side of the flume.

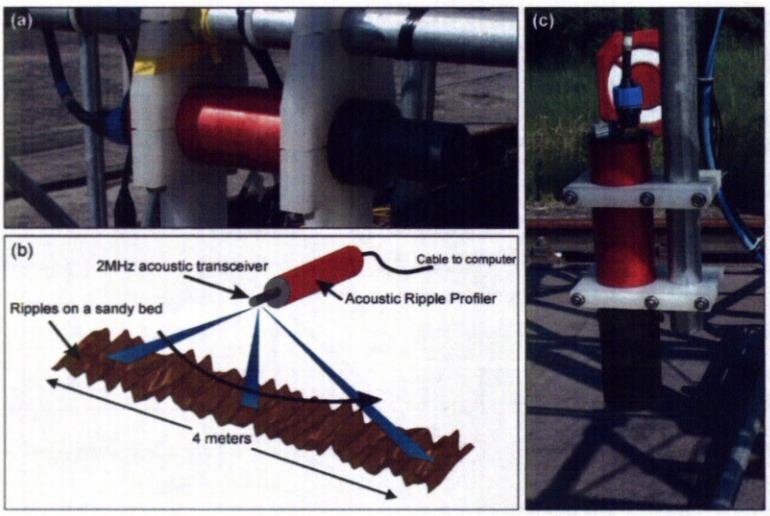

Figure 3.4: The (a, b) 2.0MHz Acoustic Ripple Profiler and (c) 1.2MHz Sector Scanning Sonar were used to study the cross-sectional and plan-form bedform geometries in the Deltaflume.

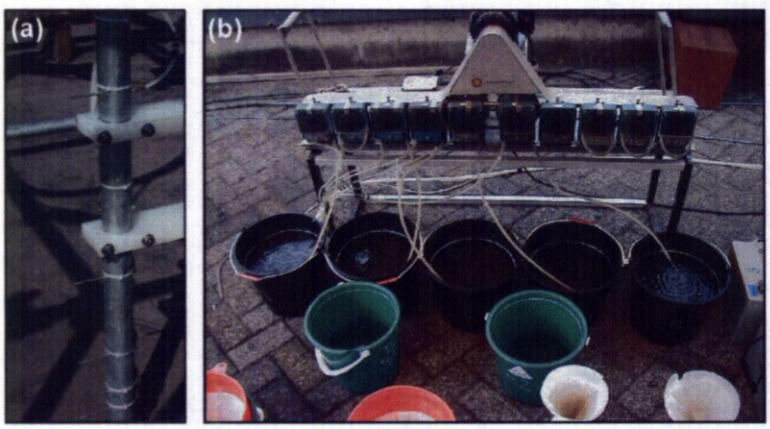

Figure 3.5: The (a) pumped sampling equipment deployed in the Deltaflume and (b) samples of sediment laden water being gathered in buckets by the side of the Deltaflume.

The ABS comprised three transceivers operating at 1.0, 2.0 and 4.0 MHz aligned perpendicular to the flow (along-shore), 0.05m apart and with nominal radiating aperture radii of 0.0058, 0.0050 and 0.0050 m respectively. Each of these three channels recorded backscatter profiles at $\sim$ 1cm vertical resolution at 128Hz, which were subsequently block averaged in order to improve the statistical reliability of the results to produce backscatter profiles at 4Hz. The oscillating frequency of the ABS electronics was 75kHz. Figure 3.6 is an illustration of the ABS and how it functions by emitting and receiving acoustic pulses which are scattered by the sediments in the water column. The ABS and the theory behind inverting the backscattered sound intensity to suspended sediment concentration are detailed in Chapter 4. Chapter 4 also details the pumped sampling methodology and data analysis and compares the measurements of suspended sediment concentration from the pumped samples and ABS.

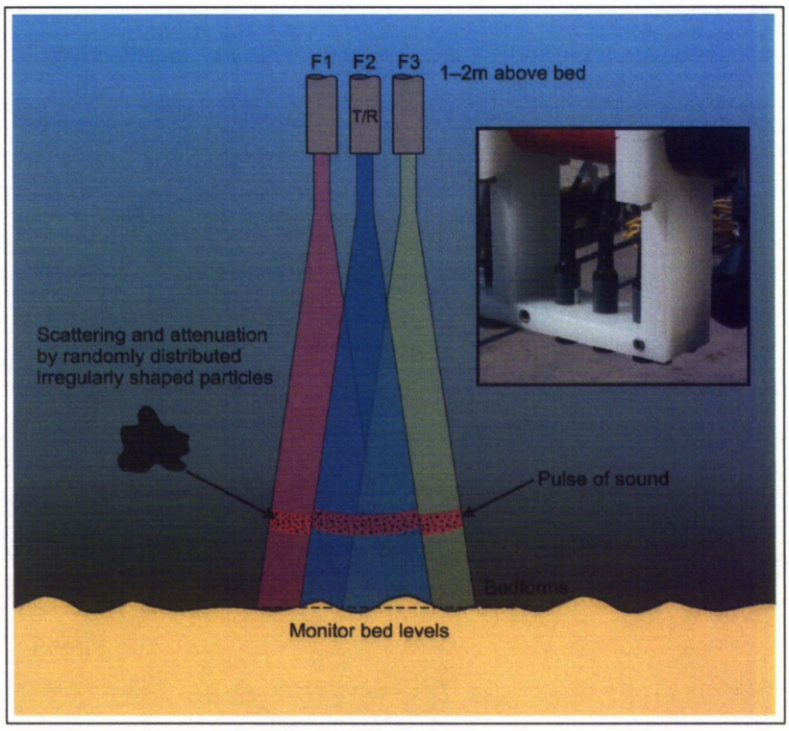

Figure 3.6: An illustration of the ABS. In the Deltaflume the ABS comprised three transceivers, mounted approximately 1m above the bed, operating at 1.0, 2.0 and 4.0 MHz.

The ABS, ADV-2, ARP and pumped sampling equipment were mounted on an along-shore line in the centre of the frame on a sliding trolley. The sliding trolley was driven by an electric motor such that the equipment could be translated up to $\sim$ 0.5m across-shore. During a number of experiments, the trolley was used to translate the instruments between 0.1 – 0.4m, aligning them with the crest of a ripple. Whilst this was advantageous in many respects, it meant that there were sudden relative bed level changes of a few centimetres, equal to the height of the ripple below the ABS, during some of the measurement bursts that could be accounted for during data analysis.

The water surface elevation was measured at 25Hz by three wave staffs mounted on gantries above the flume, as shown in Figure 3.7. These staffs physically moved up and down with the water surface displacement due to the waves. In this study, the water surface elevations from the centre of the three staffs, which was closest to the instrument frame, were used to calculate the significant wave height and peak spectral wave period for each experiment (Chapter 5).

Figure 3.7: A wave staff suspended from a gantry above the Delaflume.

Chapter 4

Suspended sediments and ABS inversion and validation

4.1 Introduction

A key element of this study is the examination of the suspended sediments in the Deltaflume over a variety of different time scales. Measurements of the suspended sediments were made by collecting direct samples of the sediment laden water using pumped samples, and indirectly using the Acoustic Backscatter System (ABS). The pumped samples provided time average measurements of the sediment concentrations and the grain size distributions at up to five heights above the bed. In contrast, the ABS offered non-intrusive measurements of the suspended sediments at a higher spatial and temporal resolution. Each of these two methods had their advantages and disadvantages but together they offered comprehensive measurements of the suspended sediment concentration (SSC) and grain size distribution across the series of experiments conducted in the Deltaflume.

This chapter starts by reviewing the ABS, the theory describing the sound scattering characteristics of suspended sediment and a number of different inversion methodologies in Section 4.2. In Section 4.3 acoustic measurements made in a sediment tower are used to test the different inversion methodologies outlined in Section 4.2.2. The sediment tower provided a homogenous suspension of a known sediment concentration and size distribution (Thorne and Buckingham, 2004; Betteridge et al., 2008). The pumped sampling method was briefly outlined in Chapter 3. Section 4.4 here describes the methodology in more detail and outlines the subsequent data analysis. In Sections 4.5 – 4.7 the methodology adopted for the inversion of the Deltaflume ABS data at a variety of different temporal resolutions is described. In these final sections the independent measurements of the SSC made by the ABS and pumped sampling are compared in order to validate the methods used and to determine their accuracy to measure suspended sediments.

4.2 Acoustic backscatter systems

Acoustic backscatter systems (ABS) are high frequency acoustic devices used to make measurements of primarily the concentration profile, but also the particle size, of suspended sediments above sandy beds. ABSs work on the principle that marine sands can significantly scatter underwater sound, and that the backscattered intensity is a function of the suspension concentration and size distribution (Hay and Sheng, 1992; Moate and Thorne, 2009). ABSs typically comprise three transceivers operating at different frequencies; transmitting and receiving acoustic pulses. For each of the three channels, the backscattered sound, with range from the transceivers, is recorded in the form of a voltage. In order to extract the unknown parameters of the suspended sediment, an inversion is performed on the recorded voltages. In theory, the use of three channels enables three suspended sediment parameters to be quantified from the acoustic inversion, such as the sediment concentration and two parameters describing the size distribution. However, the inversions are sensitive to small variations in the backscatter intensity and the sediment size response is nonlinear (Thosteson and Hanes, 1998). Typically, therefore, only two parameters are inverted for at each range from the transceivers – concentration and mean particle size.

The voltages recorded by each channel can be expressed in terms of the backscatter pressure which in turn can be modelled by theory describing how sound is scattered from the particles in suspension. For regularly shaped particles, such as spheres, exact algebraic expressions exist describing the scattering characteristics of sound (e.g. Gaunaurd and Uberall, 1983). However, there is no such solution to the problem of how sound is scattered from irregularly shaped particles such as marine sands. One commonly used approach is to make direct observations of the scattering properties of marine sands and to use the sphere scattering models to interpret and represent the observations (Thorne and Meral, 2008).

4.2.1 Acoustic scattering properties of the suspended sediments

The ABS transceivers both emit and receive sound pulses. These pulses of sound are subject to attenuation by the water and the suspended sediments during (i) the outgoing propagation of the signal and (ii) the backscattered propagation. Therefore an accurate description of the attenuation and backscattering characteristics of the suspended sediment is essential in order to model the backscattered pressure at the transceivers. The attenuation intrinsic to suspended particles can be described by their normalised total scattering cross-section, χ, quantifying the total scattering over all angles. Similarly, the intrinsic backscatter characteristics can be described by their form function, f. χ and f are non-dimensional quantities and vary with the wavelength of the sound, λ, and the radius of the particles in suspension, a_s. Because of this dependence on two parameters it is common to express χ and f in terms of a single non-dimensional parameter $x = ka_s$, where k is the wave number, $k = 2\pi/\lambda$.

It is important to consider the particle size distribution of the sediments in suspension. χ and

f describe the scattering properties of a narrowly sieved sand suspension. In the presence of a broader size distribution, the ensemble scattering properties of the sediment can be determined theoretically by integrating the intrinsic scattering properties (χ and f) over the probability density function (PDF) describing the particle number size distribution present. The ensemble scattering properties, $< \chi >$ and $< f >$, are thus given by (Sheng and Hay, 1988; Thorne and Campbell, 1992)

$$< \chi(x_0) >= \frac{\int_0^\infty xP(x_0,x)dx \int_0^\infty x^2\chi(x)P(x_0,x)dx}{\int_0^\infty x^3P(x_0,x)dx} \tag{4.1a}$$

$$< f(x_0) >= \left(\frac{\int_0^\infty xP(x_0,x)dx \int_0^\infty x^2f^2(x)P(x_0,x)dx}{\int_0^\infty x^3P(x_0,x)dx} \right)^{1/2} \tag{4.1b}$$

where $P(x_0,x)$ is the particle number PDF. $P(x_0,x)$ is a function of $x = ka_s$, a function of the arithmetic mean of the PDF, x_0, and satisfies $\int_0^\infty P(x_0,x)dx = 1$. The width of $P(x_0,x)$ is defined by its standard deviation, σ_x, which is typically expressed as a constant fraction of x_0, such that σ_x/x_0 is constant for all x_0. The intrinsic scattering properties (χ and f) of a suspension of spheres can be expressed algebraically and substituted into equations (4.1a) and (4.1b). No such theoretical expressions exist, however, for irregularly shaped particles. Sheng and Hay (1988) used a rigid mobile sphere model and compared it with observations of sediment attenuation and constructed heuristic expressions for the form factor and attenuation coefficient (related to χ) that agreed well with the data. Following this approach, Thorne and Meral (2008) compiled a large number of measurements of the intrinsic scattering properties of suspensions of natural sandy sediments and developed heuristic expressions for χ and f that agree well with the data. Figure 4.1 shows how $< \chi >$ and $< f >$ vary as a function of x_0 for three widths of normal and lognormal size distributions. The three widths of particle number size distributions shown in Figure 4.1 correspond to narrowly sieved (nominally single sized) sand and moderately-broad and broad distributions of sand with σ_x=0.5x_0 and σ_x=1.0x_0 respectively. Regardless of the distribution type, broadening the size distribution by increasing σ_x/x_0 increases the size of both $< \chi >$ and $< f >$ within the Rayleigh regime, $x_0 << 1$. The opposite is true within the geometric scattering regime, $x_0 >> 1$, where the size of $< \chi >$ and $< f >$ decrease with σ_x/x_0. The effect of the size distributions type, normal and lognormal, is also shown in Figure 4.1. The lognormal distribution has larger values of $< \chi >$ and $< f >$ within the Rayleigh regime than the normal distribution, and smaller values within the geometric regime. Also, the distribution width has a stronger influence on the size of $< f >$ and $< \chi >$ when the particle sizes have a lognormal distribution, as apposed to a normal distribution. These effects of size distribution on $< f >$ and $< \chi >$ were discussed in more detail by Moate and Thorne (2009).

Size distributions

The PDF, $P(x_0,x)$, in equations (4.1a) and (4.1b) describes the particle number size distribution. However, sedimentologists often describe grain size distributions in terms of mass or volume. Thus it is important to be able to relate particle number size distributions to mass

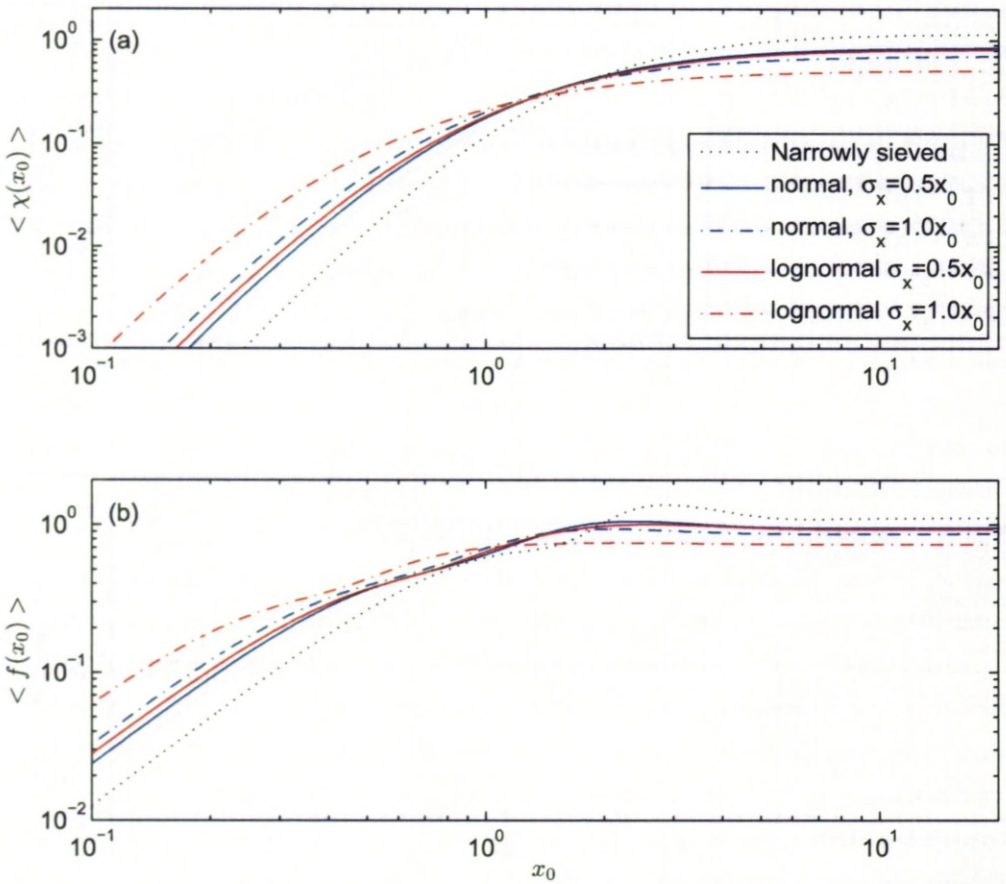

Figure 4.1: Average total scattering cross sectional area, $< \chi >$, and form function, $< f >$, for narrow, moderately-broad ($\sigma_x = 0.5x_0$) and broad ($\sigma_x = 1.0x_0$), normal and lognormal size distributions.

size distributions. The number, N_i, of uniformly sized particles, with total mass M_i, within a class interval, i, with a density ρ_s and radius a_i is given by

$$N_i = \frac{3M_i}{4\pi\rho_s\, a_i^3}. \tag{4.2}$$

Hence each grain size class within a mass distribution can be converted to a class within a particle number distribution, and vice versa. The probability density, $n(a_i)$, of each class, within say a particle number distribution, can then be calculated using (Moate and Thorne, 2009)

$$n(a_i) = \frac{N_i}{N_T \Delta a_i} \tag{4.3}$$

where $\Delta a_i = a_i - a_{i-1}$ and N_T is the total number of particles within the distribution. Figure 4.2 shows (a) the lognormal PDF of a particle numbers size distribution and (b) the equivalent mass size distribution. In Figure 4.2(a) the particle number PDF has an arithmetic mean radius of $< a_s >= 100\mu$m and standard deviation of $\sigma(a_s) = 0.2 < a_s >= 20\mu$m. The corresponding parameters of the mass size distribution, Figure 4.2(b), are $< a_s' >= 112.5\mu$m and $\sigma'(a_s) = 22.5\mu$m. The particle number distribution is shifted towards the fine particle sizes, relative to the mass size distribution. This is because a given number of small particles weighs less than the same number of large particles. It is of interest to note that the ratio of standard deviation to mean for each distribution are the same, i.e. $\sigma(a_s)/ < a_s >= \sigma'(a_s)/ < a_s' >$ (=0.2 here). This is true for lognormal distributions regardless of their mean and standard deviation.

The ratio of the standard deviation to the mean of the particle size distribution defines how $< \chi >$ and $< f >$ vary with the mean particle size of the distribution. Therefore, this ratio must be measured in order to accurately describe the scattering characteristics of the suspended sediments. Section 4.4 examines the volumetric grain size distributions of suspended sediment from the Deltaflume. It is important however, to consider particle number size distributions for acoustical applications, and this can be achieved using equations (4.2) and (4.3) and assuming the density to be uniform across all sizes.

4.2.2 Inversion theory

The root mean square (RMS) backscattered voltage from the ABS can be expressed as (Thorne and Hanes, 2002)

$$V_{rms} = \frac{K_s K_t}{\psi\, r} M^{1/2} \mathrm{e}^{-2r(\alpha_w + \alpha_s)} \tag{4.4}$$

where ψ accounts for the departure from spherical spreading in the near field of the transceivers (Downing et al., 1995), r is the range from the transceivers, M is the mass concentration of the sediment, K_t is the ABS system constant, K_s describes the backscattering characteristics of the sediments and α_w and α_s are the attenuation coefficients of the water and sediment

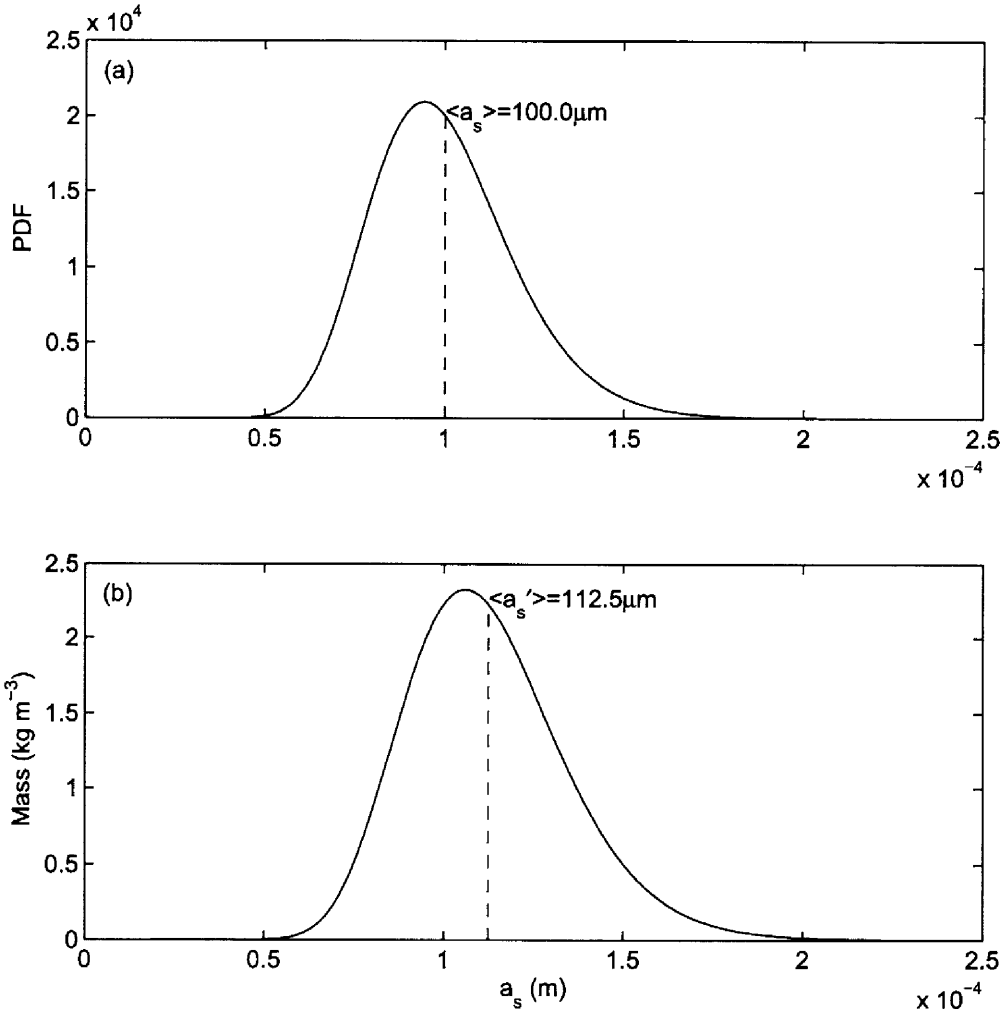

Figure 4.2: Lognormal grain size distribution in terms of (a) particle number probability density function (PDF) and (b) mass. a_s is the particle radius, $< a_s >$ is the mean of the particle number PDF and $< a_s' >$ is the mean of the mass distribution.

respectively. The attenuation due to the sediment can be described by

$$\alpha_s = \frac{1}{r}\int_0^r \xi(r)M(r)dr \tag{4.5}$$

where ξ is known as the sediment attenuation coefficient (Thorne and Hanes, 2002). ξ and K_s are functions of the ensemble total scattering cross sectional area, $< \chi >$ given by equation (4.1a), and ensemble form function, $<f>$ given by equation (4.1b), respectively, and can be expressed as

$$\xi = \frac{3 < \chi >}{4 < a_s > \rho_s} \tag{4.6}$$

$$K_s = \frac{< f >}{\sqrt{< a_s > \rho_s}} \tag{4.7}$$

where $< a_s >$ is the mean grain radius of the particle number size distribution and ρ_s is the sediment density. If any of the parameters in equations 4.6 and 4.7 vary with range from the transceiver, i.e. $< a_s >=< a_s(r) >$, then ξ and K_s become range dependent.

Equation (4.4) is a forward model of the voltage recorded by the transceivers and is a function of the unknown parameters describing the suspended sediment, M and $< a_s >$. Therefore, to solve for M and $< a_s >$, an inversion of equation (4.4) is required. A number of inversion methods have been developed and an extensive review of these methods was conducted by Thorne and Hanes (2002). If the two unknowns of $M(r)$ and $< a_s(r) >$ are sought then at least two measurements of V_{rms}, from two transceivers, are required. Alternatively, if the size profile, $< a_s(r) >$, is known or assumptions made about its form are made, and only $M(r)$ is sought, then only the signal from one transceiver is required.

4.2.3 Empirical one parameter, explicit, ABS inversion

The inversion of equation (4.4) for $M(r)$ relies on knowledge of the ABS system constant, K_t, for each channel. Lee and Hanes (1995), however, developed a one parameter ABS inversion relying on an independent measurement of the suspend sediment mass concentration at one point above the bed, rather than K_t. This empirical one parameter inversion is commonly referred to as an 'explicit' inversion (Thorne and Hanes, 2002). An additional requirement of this inversion method is for the grain size profile, $< a_s(r) >$, to be known so that $\xi(r)$ and $K_s(r)$, equations (4.6) and (4.7), can be calculated. Assuming K_t to be constant with range, equation (4.4) can be manipulated to give (Thorne and Hanes, 2002)

$$M(r) = \frac{\beta^2(r)}{\beta^2(r_r)/M(r_r) - 4\int_{r_r}^{r}\beta^2(r)\xi(r)dr}, \tag{4.8}$$

where $\beta(r) = V_{rms}(r)\ r\ \psi(r)\ K_s^{-1}(r)\ \mathrm{e}^{2\alpha_w r}$ and r_r is the reference range at which M is known. Given the knowledge of $M(r_r)$, $\xi(r)$ and $K_s(r)$, equation (4.8) can be evaluated for all r, and does not require knowledge of the system constant, K_t.

4.2.4 Semi-analytical, implicit, ABS inversion

Semi-analytical ABS inversions, commonly referred to as 'implicit' inversions (Thorne and Hanes, 2002), require no independent measurements of mass concentration, M, and both $M(r)$ and $< a_s(r) >$ can be solved for. Whilst implicit inversions are primarily two parameter inversions, in some cases $< a_s(r) >$ is known or assumed and only $M(r)$ is solved for. Equation (4.4) can be rearranged to give

$$M = M_0 \mathrm{e}^{4r\alpha_s} \tag{4.9}$$

where

$$M_0 = (V_{rms}\psi\, r/K_s K_t)^2 \mathrm{e}^{4r\alpha_w}. \tag{4.10}$$

In equation (4.9), M is present both on the LHS and on the RHS in the sediment attenuation coefficient (equation (4.5)) and must therefore be solved for using an iterative method. Because α_s is calculated by integrating the result for M over all previous range bins, each range bin from the transceivers is stepped through in turn and M is calculated in each case. At each range bin in turn, M_0 is calculated and M_1 is calculated using the M_0 profile in the calculation of α_s. M_2 is then calculated using the profile of M_1 in the calculation for α_s. This iterative process is repeated until M_n and M_{n+1} are convergent.

If $< a_s(r) >$ is not known then the above iteration can be performed, but for a range of particle sizes and using more than one ABS channel. For each range bin in turn, M is found for a range of particle sizes, $< a_s >$, and how M varies with $< a_s >$ at each channel is compared. The $< a_s >$ value at which the M values obtained using each channel agree is chosen as the $< a_s >$ value for that range bin. For example Figure 4.3(a) shows the results for the inverted mass concentrations at a single range bin, for a number of possible particle sizes and from three frequency channels. The results from the 1 and 2 MHz channels agree at three different particle sizes - approximately 140, 240 and 360μm. These results only agree, however, with the results from the 4 MHz channel at 140μm. In this example, therefore, the mean particle size is 140μm. There are a number of methods for determining the correct mean size, and there is a certain amount of ambiguity with each method. One method, used by Hay and Sheng (1992), involves calculating the ratio of the measured form function at one channel with that at another, for a range of particle sizes, and comparing it with a theoretical ratio where the form function is calculated using equation (4.1b). Another method, described by Thorne et al. (2007), calculates the mean, $\bar{M}$, and standard deviation, σ_M, of the mass concentration across two or more channels. This is done for a range of $< a_s >$ so that $\sigma_M/\bar{M}$ can be plotted against $< a_s >$. The minimum in this curve is where the estimates of M at each channel agree most and is therefore a suitable choice for $< a_s >$. For example, Figure 4.3(b) shows $\sigma_M/\bar{M}$ calculated from the 1 and 2; 1 and 4; and 2 and 4 MHz channels. The only point where all three lines are at a minimum is $< a_s > \sim 140\mu$m, the size of the sediment suspension.

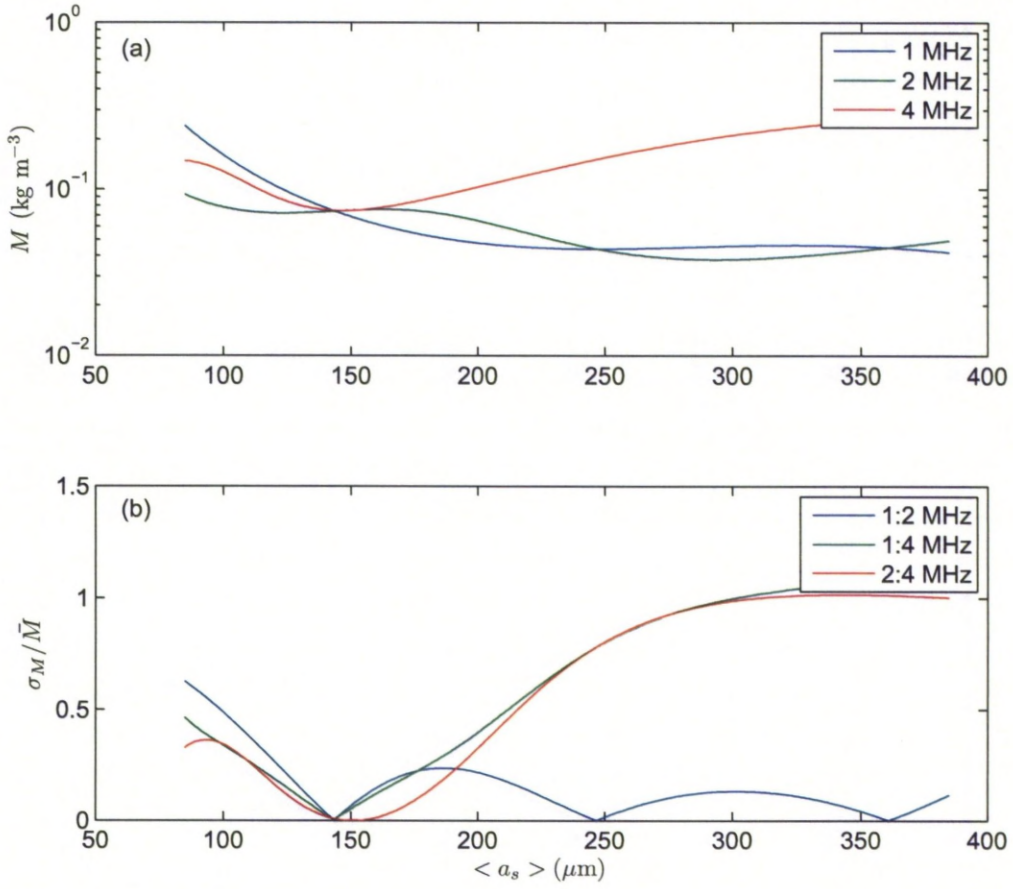

Figure 4.3: (a) Inverted sediment mass concentration, M, for a number of possible particle sizes, $< a_s >$, for three ABS channels operation at different frequencies. (b) The ratio of the standard deviation and mean sediment mass taken over two ABS channels, σ_M and $\bar{M}$ respectively.

4.2.5 Acoustic inversion uncertainties

There are a number of factors that limit the accuracy of sediment concentrations inverted from acoustic backscatter including (i) calibration accuracy, (ii) uncertainties in the ensemble scattering properties of the suspended sediments, (iii) feedbacks incurred from an inaccurate description of the particle size during the inversion and (iv) other ancillary parameters affecting inversions. These four limitations are discussed separately below.

(i) The semi-analytical, implicit, inversion outlined in Section 4.2.4 requires knowledge of the ABS system constant, K_t, for each channel, determined from an ABS system calibration (Betteridge et al., 2008). This calibration procedure can be time consuming, however, and requires specialist laboratory equipment. The methodology and expertise has also only recently become available (Betteridge et al., 2008). The ABS system constants required regular calibration to check system continuity. When the K_t values of a system are not known then empirical inversions, such as the explicit inversion outlined in Section 4.2.3, can be used in conjunction with an independent measurement of sediment concentration (Thorne and Hanes, 2002; Thorne et al., 2007). This removes the need to calibrate the system but limits the accuracy of the acoustic inversion to that of the independent measurement.

(ii) The uncertainties in the ensemble scattering properties arise from uncertainties in the intrinsic scattering properties and size distribution of the suspended sediment (Moate and Thorne, 2009). The intrinsic scattering properties of a sediment suspension depend on the shape and density of the sediment typically associated with different mineralogy. Quartz sand is a common coastal mineralogy, but until recently there was no clear consensus as to its intrinsic scattering properties (Thorne and Meral, 2008). In addition to the intrinsic scattering properties it is important to characterise the size distribution of the sediment suspension. Typically, coastal sediments are lognormal but it is important to know the width and mean size of the distribution. Moate and Thorne (2009) considered the impact of inaccurately describing the width of broad size distributions on acoustic inversions for mean size and concentration. They found that underestimating the size distribution width led to overestimates of the mean size, and vice versa.

(iii) Uncertainties in the mean size of a suspension can have a strong impact upon inversions for concentration. This is mainly through inaccurate calculations of the sediment attenuation coefficient, ξ, which is inversely proportional to the mean size in equation (4.6). Such errors are particularly pronounced at large ranges from the transceivers because the sediment attenuation, α_s, is calculated by integrating through all the previous range bins, the propagation path, equation (4.5). Underestimating the mean size leads to an overestimate of ξ and α_s, and this can lead to an overestimate in the concentration. This in turn leads to overestimates of α_s at subsequent ranges from the transceivers. Such positive feedbacks can lead to substantial errors in the sediment concentrations, especially at large ranges and sediment concentrations typical close to the bed. This is one major disadvantage with full implicit inversions for mean size and concentration. When independent measurements of the mean size and concentration at one

point in the ABS profile have been made, then the explicit approach offers a much more stable inversion.

(iv) Ancillary parameters affecting the inversions include the speed of sound in the water and the radiating aperture of the transceivers. The speed of sound in water is a function of temperature, depth and salinity (Mackenzie, 1981) and is important because it defines the sounds wavelength and wave number involved in the calculation of intrinsic scattering properties. The radiating transceiver aperture effects corrections applied to the transceivers near field which effects the integration of attenuation along the propagation path.

4.3 Sediment tank validation of ABS inversion methods

Section 4.2.2 introduced two main inversion methods: explicit, relying on an independent measurement of the suspended sediment concentration, and implicit. This section examines the results from two inversions for sediment concentration, explicit and implicit, and the result from one implicit inversion for both sediment concentration and mean size. The ABS backscatter examined is that of Moate and Thorne (2009) from an indoor tank with a homogeneous lognormal sand suspension with a concentration of ~0.87 kg m^{-3}. The median grain diameter of the mass distribution was $D_{s50} = 144\mu$m and the mean size and standard deviation of the particle number size distribution were $< a_s >= 50\mu$m and $\sigma(a_s) = 20\mu$m respectively. The particle number size distribution, $n(a_s)$, was calculated from the mass distribution using equations (4.2) and (4.3) and $< a_s >$ and $\sigma(a_s)$ were calculated using

$$< a_s >= \sum_{i=1}^{N} (a_i - a_{i-1})\, a_i\, n_i(a_i) \tag{4.11a}$$

$$\sigma(a_s) = \sqrt{\sum_{i=1}^{N} (a_i - a_{i-1})\, (a_i - < a_s >)^2\, n_i(a_i)} \tag{4.11b}$$

were a_i and $n_i(a_i)$ are the mean radius and probability density of the class interval i and N is the total number of class intervals in the distribution.

Here, the ABS backscatter from three transceivers, with apertures of nominal radii 0.0090, 0.0048 and 0.0100m, which operated at 1.015, 2.015 and 0.500 MHz is examined. The ensemble scattering properties of the homogenouse suspensions were calculated using equations (4.1a) and (4.1b) and a lognormal size distribution described by $\sigma(a_s)/ < a_s >= 0.4$. A correction was made to the backscatter from the near field of the transceivers to account for the departure from spherical spreading (Downing et al., 1995), the speed of sound was taken as 1487.7m/s and the ABS bin size as 0.01m. The ABS system constants are those obtained from calibration using the method of Betteridge et al. (2008).

Figure 4.4 shows the results from (a) an explicit and (b) an implicit inversion for sediment mass using the ABS backscatter from the three ABS channels. Pumped samples were taken and the open circles indicate the resulting sediment concentrations. In the case of the explicit

inversion, the pumped sampled result from $r = 0.46$m was used to aid the inversion which is why the results from the three frequencies pass through that point. In these inversions a height constant grain size profile of $< a_s >= 50\mu$m was used. In Figure 4.4(a) the results from the explicit inversion of the backscatter from the 1MHz and 2MHz transceivers are within the $\pm 20\%$ error suggested by Moate and Thorne (2009) as the typical uncertainty of the pumped samples. The result from the 0.5MHz transceiver is comparatively more variable through the water column, especially above 0.3m, but is still, with the exception of the first 0.3m, generally within a factor of two. The reason for the fluctuation in the results from the 0.5MHz transceiver is most likely associated with reverb from the sides of the tank and the poor signal to noise ratio of the 0.5MHz channel (personal communication, B. Moate 2010). The sand suspension was known to be homogeneous from the pumped samples, which the results from the 1 and 2 MHz transceivers confirm. The results in Figure 4.4(b) from the implicit inversion of the 1 and 2MHz data are typically 15% larger than the results from the explicit inversion, Figure 4.4(a). This is because instead of being fixed to a pumped sampled result the inversion required the system constant, K_t, for each frequency channel obtained by calibration. Any uncertainties in K_t are therefore likely to be manifest in the resulting concentrations. However, the results are generally within the 20% error on the pumped samples.

Figure 4.5 shows the results from an implicit inversion for (a) mean size and (b) sediment mass concentration. The mean size profile, Figure 4.5(a), results from a comparison of the mass concentration results from the 1 and 2MHz transceivers, at each range bin, which is why there is only one result. This mean size profile is highly in agreement with the mean of the size distribution present in the water tank, 50μm. The results in Figure 4.5(b) show the sediment mass concentration inverted from the backscatter at each frequency channel using the mean size obtained from the inversion, shown in Figure 4.5(a). The 1 and 2MHz results are $\sim 25\%$ larger than the first two pumped samples but are within the 20% error on the third pumped sample. It is interesting to note the effect of the different size profiles used in the two implicit inversions, the results of which are shown in Figures 4.4(b) and 4.5(b). The 5μm – 6μm smaller sizes at $r \sim 0.1 - 0.5$m in Figure 4.5(a) force the concentrations in Figure 4.5(b) to generally be larger than those in Figure 4.4(b) where $< a_s >= 50\mu$m was used throughout the water column.

4.4 Pumped samples of suspend sediment

During the Deltaflume experiments, samples of sediment laden water were taken at a number of heights above the bed. The process by which this was done is known as transverse suction or pumped sampling and is described by Bosman et al. (1987). Samples of the sediment laden water were taken over a period of approximately 10 minutes during the middle of many of the Deltaflume experiments (Williams and Bell, 2006). The sediment was filtered from the water sample, dried and then and weighed to give a concentration (mass per unit volume). A Coulter Laser Granulometer was used to determine the grain size distribution of the suspended sedi-

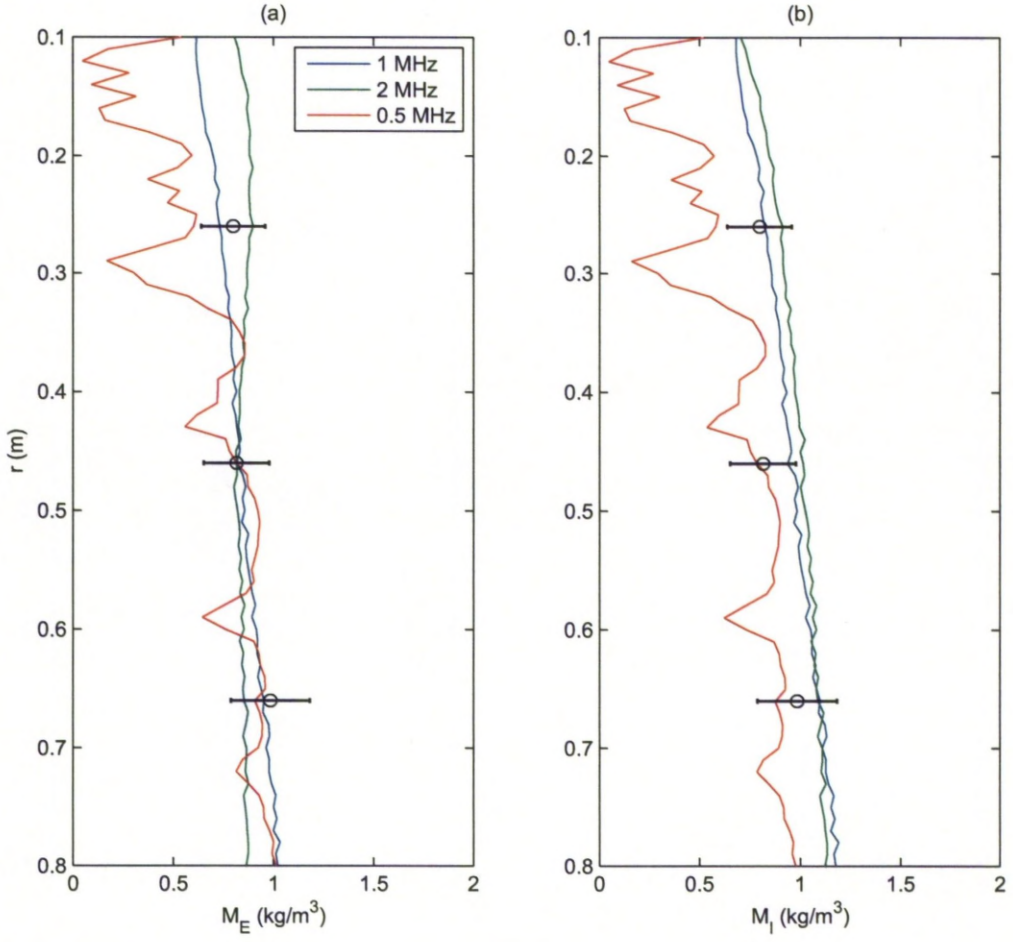

Figure 4.4: Results from acoustic inversions for sediment mass using (a) an explicit method (M_E) and (b) an implicit method (M_I). r is the range from the ABS transceivers and the results from three transceivers operating at 1, 2 and 0.5 MHz are shown. The pumped sampled results are shown (o) with $\pm 20\%$ error bars. In each inversion a height constant grain size profile of $< a_s >= 50\mu$m was used.

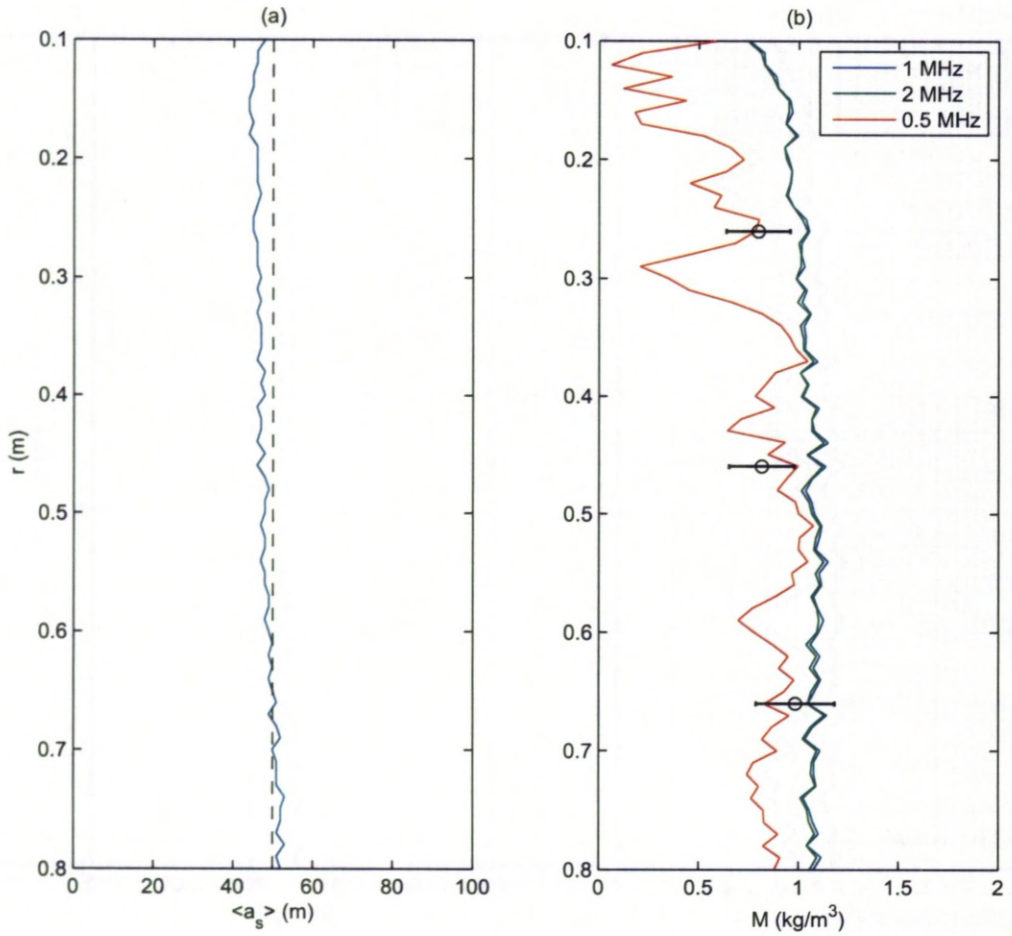

Figure 4.5: Results from an acoustic inversion for (a) mean size ($< a_s >$) and (b) sediment mass concentration (M) with range (r) from the three transceivers operating at 1, 2 and 0.5 MHz.

ment, via laser diffraction grain size analysis. Pumped samples were taken during most of the Deltaflume experiments, both over the fine and medium-grained sand beds and the concentration measurements taken represent time average concentrations. Next to in-situ water bottle sampling, the method of pumped sampling is one of the most direct methods of measuring the concentration. The only calibration required is to take into account the sediment trapping efficiency of the system (Bosman et al., 1987). In the Deltaflume, each pumped sample represents a time average concentration over roughly 100 wave cycles.

4.4.1 The pumped sampling method

The pumped sampling apparatus deployed in the Deltaflume consisted of a tube containing five nozzles approximately logarithmically spaced vertically, mounted on a sliding trolley on the instrument frame and aligned normal to the flow (Bell and Williams, 2002), see Figure 3.5. During the majority of the experiments the nozzles were positioned at heights of 0.12, 0.16, 0.24, 0.40 and 0.72 m above the base of the instrument frame. By experiment M10_1 the instrument frame had settled into the bed sediment such that the bottom of the pumped sampling apparatus was within the bed. Subsequently, the drive chain on the sliding trolley was damaged and the flume was emptied for repairs. After this, the pumped sampling instrumentation was moved vertically upwards 0.09m such that during M10_2, and all subsequent experiments, the nozzles were position at heights of 0.21, 0.25, 0.33, 0.49 and 0.81 m above the instrument frame base. Typically, 8 litres of water were pumped into buckets over an approximate 10 minute period. These pumped samples were then left to stand for a few minutes before emptying the excess water off and filtering out the sand which was subsequently dried and weighed.

Because the bed level relative to the instrument frame varied from experiment to experiment, occasionally the bottom most one or two pumped sampling nozzles went very close to, or beneath, the bed level (as in M10). In these cases the results represent the bed sediment and were presented in Section 3.2 and are hence omitted from the analysis of the suspended sediments here. The ABS provided accurate bed detection, as the bed produced a large backscatter. The root mean square time average of the ABS profile of backscattered signal (voltages), V_{rms}, was taken over the measurement burst. Approximate bed levels were taken as the maximum in V_{rms} multiplied by the gradient of V_{rms} for each frequency channel. These approximate bed levels were then examined in conjunction with the V_{rms} profiles, and their gradients, to determine whether they were chosen accurately. Thus it was possible to determine which of the pumped sample nozzles were above the bed for the analysis of the pumped sample data. More accurate bed detection was performed prior to the ABS inversion to sediment concentration (Section 4.6.1).

4.4.2 Measurements of suspended sediment grain size distribution

A laser diffraction grain size analysis of each pumped sample was performed. Laser diffraction particle size analysis is based on the principle that the angle at which the laser beam is scattered by a particle is directly related to the particle radius, a_s, with the angle increasing as a_s decreases (Ramaswamy and Rao, 2006), and the scattering intensity diminishing with particle volume. The expression for intensity in terms of the scattering angle and a_s, is inverted to obtain a_s based on measurements of the scattering angle and the intensity. The result is that a volume distribution of grain sizes is obtained. The results obtained from the laser diffraction grain size analysis gave the percent of total volume of 100 grain size class intervals between 0.01 and 10,000 μm.

The volumetric grain size distributions of the pumped samples of the suspended sediment were generally lognormal in form. Assuming the sediment density to be uniform with size, the volumetric distributions are equivalent to mass size distributions. Figure 4.6 shows the cumulative grain size distributions obtained from the five pumped sample nozzles during the M06_2 Deltaflume experiment. A lognormal cumulative distribution function (CDF) was fitted to the data from each sampling bin, and is shown by the solid lines in Figure 4.6. Particle number CDFs were constructed using equation (4.2), and are shown by the dashed lines in Figure 4.6. In the example shown in Figure 4.6, the median grain diameters of the mass distributions, D_{s50}, decreased from 322μm in Figure 4.6(a) to 247μm in Figure 4.6(e). The median grain diameters of the CDFs optimised to fit the data, D'_{s50}, compare favorably to the D_{s50} values at the first four bins. At the fifth pumped sample bin, Figure 4.6(e), $D_{s50} \sim 1.2D'_{s50}$ and $D_{s50} \sim 32D_{s50N}$, where D_{s50N} is the median diameter of the particle number distribution. This discrepancy corresponds to the size distribution at the fifth bin being dominated by very-fine-grained sediment (wash-load) and the size distribution not being lognormal in form, as was the case in the lower bins. It was unlikely that the wash-load produced any detectable acoustic backscatter relative to the backscatter produced by the sand (Vincent and Hanes, 2002; Vincent, 2007). Therefore the particle number distributions dominated by wash-load were not used to parameterise any acoustic inversion of the ABS data, and the pumped samples where D_{s50} and D'_{s50} and/or D_{s50} and D_{s50N} strongly differed were excluded from the pumped sample analysis.

For each experiment, the median grain diameter of the pumped samples at each measurement bin above the bed were averaged to give $\overline{D_{s50}}$, and the results are listed in Table 4.1. Similarly, the mean sizes of the particle number size distribution, and their relative standard deviations, were averaged over the measurement bins to give $\overline{< a_s >}$ and $\overline{\sigma(a_s)/ < a_s >}$ in Table 4.1.

The size distributions obtained from the pumped samples provided valuable insight into the sound scattering characteristics of the sediments needed for the ABS inversions. The pumped samples did not, however, form a complete record through all the experiments. The mean sizes, $\overline{< a_s >}$, and relative standard deviations, $\overline{\sigma(a_s)/ < a_s >}$, were found to vary with the grain roughness Shields parameter defined by $\theta_{2.5} = f_{2.5}U_s^2/(2(s-1)gD_{50})$ where $f_{2.5}$ is the grain roughness wave friction factor, U_s is the significant orbital velocity amplitude, s is the relative

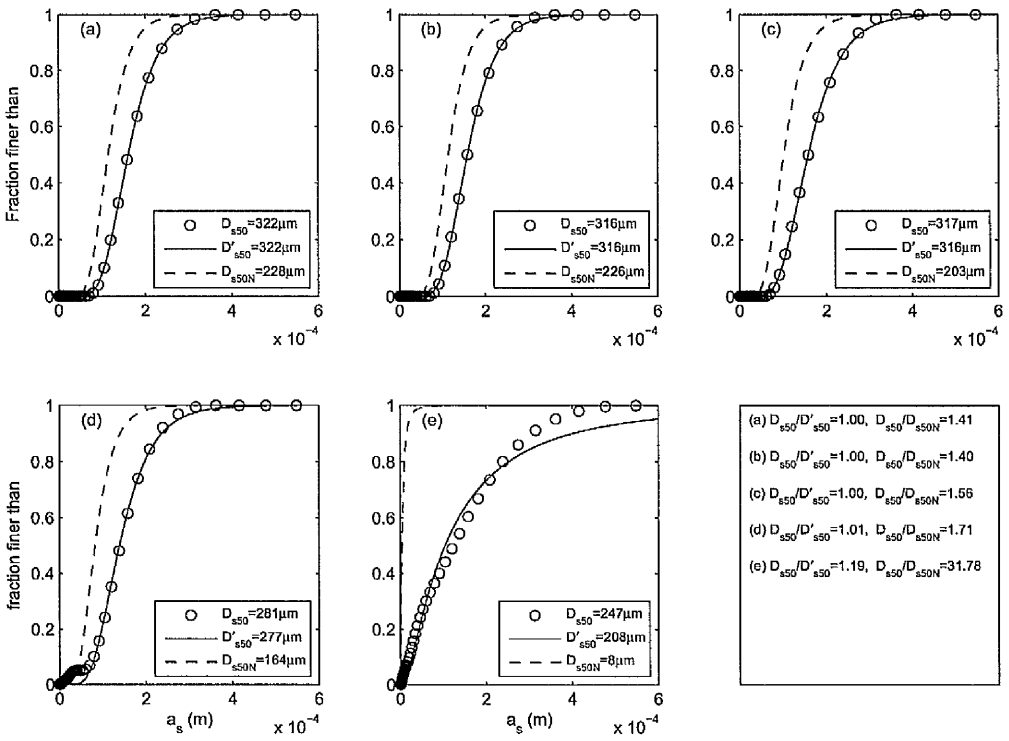

Figure 4.6: Cumulative grain size (radius, a_s) mass distributions (o) obtained during M06_2 from (a) the pumped sample nozzle closest to the bed to (e) the pumped sample nozzle furthest away from the bed. The median grain diameter of these distributions, D_{s50}, is indicated in each case. The optimised fit of a cumulative distribution function made to the data (−) is shown, with their corresponding median grain diameters D'_{s50}, in each case along with the particle number distribution (−−), and their corresponding median grain diameters $D_{s50,N}$. The D_{s50}:D'_{s50} ratios at each pumped sample bin are indicated in the lower right hand side of the figure.

EXP.	H_s (m)	Concentration of suspended load (kg m^{-3}) bin 1	bin 2	bin 3	bin 4	bin 5	$\overline{D_{s50}}$ (μm)	$\overline{< a_s >}$ (μm)	$\overline{\sigma(a_s)/ < a_s >}$
F07_1	1.28			0.3137			253.38	74.88	0.48
F07_2	1.26		0.3437	0.2062			260.96	85.10	0.43
F08_1	1.44			0.2485	0.0670	0.0476	254.23	81.98	0.44
F10_1	1.26			0.2045	0.1851		259.55	82.27	0.45
F10_2	1.24	0.7385					261.44	98.01	0.35
F11_1	1.16			0.2609	0.1674		257.71	78.62	0.47
F11_2	1.16			0.2820			273.10	96.33	0.39
F12_1	1.06			0.2661	0.2027		259.81	85.57	0.43
F13_1	0.72			0.1410	0.2027	0.1199	240.82	75.21	0.46
F13_2	0.85				0.3402		260.81	86.70	0.42
F14_1	0.64			0.1851	0.1357		234.27	69.55	0.48
M03_1	0.55	0.1126					322.32	83.70	0.55
M03_2	0.54	0.1251	0.0929	0.0447			315.72	85.77	0.53
M04_1	0.65	0.1645	0.1359				303.42	96.35	0.45
M04_2	0.64	0.1823	0.1359				294.51	67.46	0.61
M05_1	0.85	0.3736	0.2252	0.0912			305.66	103.92	0.41
M05_2	0.86	0.3450	0.1931	0.0840			292.31	86.88	0.49
M06_1	1.07	0.4129	0.2592	0.1627			302.47	97.22	0.44
M06_2	1.06	0.6614	0.3593	0.1913	0.0679		307.64	109.84	0.38
M07_1	1.27	0.8866	0.5327	0.2503			317.56	108.63	0.41
M07_2	1.29		0.5255	0.3986	0.1376		328.71	123.13	0.35
M08_1	1.49		1.0761	0.5309	0.1491	0.0286	329.14	111.01	0.43
M08_2	1.49		1.4926	0.7418	0.2538	0.0375	335.13	120.70	0.38
M09_1	1.64		0.7418	0.4719	0.2091		341.68	126.35	0.36
M09_2	1.62		1.1798	0.6095	0.2485	0.0769	340.28	118.30	0.40
M10_1	1.82			1.0494	0.3232	0.0744	341.15	114.57	0.42
M10_2	1.72	0.6185	0.4415	0.2932	0.1073	0.0697	326.93	113.53	0.40
M11_1	1.61	1.2530	0.8777	0.1287	0.0947	0.0286	329.35	109.64	0.43
M11_2	1.59		0.4379	0.2270	0.1090		306.57	100.92	0.44
M12_1	1.42		0.5434	0.2628	0.1108		322.19	103.32	0.45
M12_2	1.45		0.5649	0.3289	0.0751		340.62	120.54	0.39
M13_2	1.24	1.0654	0.5792	0.3057	0.1305		336.81	127.47	0.34
M14_1	1.06	0.8133	0.4219	0.2074			333.55	126.93	0.34
M14_2	1.08	0.7829	0.3843	0.1662	0.0447		327.99	123.88	0.35
M15_1	0.87	0.5166	0.2592	0.1251			315.16	111.41	0.39
M15_2	0.86		0.3289	0.1519	0.0608		307.82	113.85	0.36
M16_1	0.65		0.1734	0.1001			344.92	123.65	0.38
M16_2	0.65		0.2295	0.0953			335.42	125.07	0.35

Table 4.1: Results of the pumped sample analysis. The concentration of suspended sediment at each pumped sample bin above the bed is listed together with the median grain diameter, $\overline{D_{s50}}$, and mean size of the particle number distributions, $\overline{< a_s >}$, averaged over the measurement bins, $\overline{< a_s >}$. The standard deviation to mean ratio of the particle size distributions, averaged over the measurement bins, $\overline{\sigma(a_s)/ < a_s >}$, are also listed. A number of results have been excluded because they were (i) beneath the bed level or (ii) classified as wash-load.

sediment density taken to be $s = 2.65$, g is the acceleration due to gravity and D_{50} is median grain diameter of the bed sediment. Figure 4.7 shows $\overline{< a_s >}$ and $\overline{\sigma(a_s)/ < a_s >}$ plotted against $\theta_{2.5}$ for all the fine and medium-grained experiments. Linear regressions were made on $\overline{< a_s >}$ and $\theta_{2.5}$ and gave

$$< a_s > /\hat{a}_s = (29.7 \pm 23.8)\theta_{2.5} + (71.9 \pm 9.4) \tag{4.12a}$$

for the fine-grained sand and

$$< a_s > /\hat{a}_s = (40 \pm 17)\theta_{2.5} + (95 \pm 6) \tag{4.12b}$$

for the medium-grained sand, where $\hat{a}_s = 1\mu$m and the errors indicated are the standard deviations. Similarly, a linear regression was made on $\overline{\sigma(a_s)/ < a_s >}$ and $\theta_{2.5}$ which gave

$$\sigma(a_s)/ < a_s >= -(0.12 \pm 0.06)\theta_{2.5} + (0.46 \pm 0.02) \tag{4.13}$$

for both fine and medium-grained sands.

4.4.3 Measurements of suspended sediment concentration

The total suspended sediment concentration, SSC, of each pumped sample was obtained by weighing the dried sediment and the filter paper on which it was stored. The average weight of the filter paper (0.0059±0.000015 kg) was then subtracted. Bosman et al. (1987) described the method of pumped sampling via transverse suction under currents alone and under waves. Detailed measurements of the trapping efficiency of the nozzles, ζ, were made. ζ is a constant calibration factor which the measured sediment concentrations should be multiplied by. Under both currents and/or waves the trapping efficiency was found to vary with the median grain size of the suspended sediment, D_{s50}, as (Bosman et al., 1987)

$$\zeta = 1 + \frac{1}{3}\arctan(D_{s50}/D_r) \tag{4.14}$$

where $D_r = 0.090$mm. The grain size analysis in Section 4.4.2 revealed the grain size of the pumped samples to vary from $D_{s50} = 215\mu$m – 273μm and $D_{s50} = 262\mu$m – 373μm for the fine and medium-grained sands respectively. On the basis of these findings, correction factors of ζ=1.41 and 1.43 were applied to the weighed pumped samples from the fine and medium-grained sands respectively. Table 4.1 includes the results of the analysis of the pumped sampled sediment concentrations. The total concentrations of the suspend load, with the ζ correction factors applied, at each pumped sample bin are listed.

4.4.4 Uncertainties surrounding the pumped samples

Moate and Thorne (2009) suggested that the pumped samples obtained from the sediment tower were accurate to within ±20%. The uncertainties surrounding the pumped samples taken in

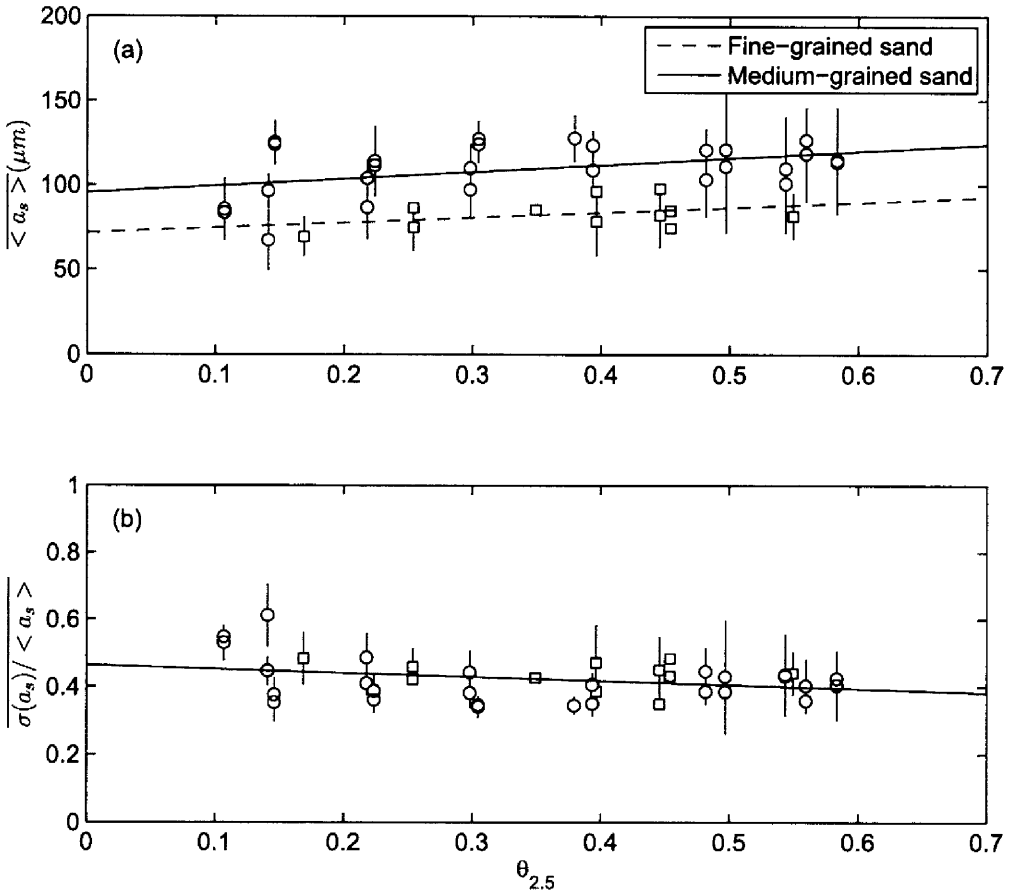

Figure 4.7: Height mean sizes of the suspended sediment, $\overline{< a_s >}$, and standard deviation to mean ratios, $\overline{\sigma(a_s)/ < a_s >}$, plotted against the grain roughness Shields parameter, $\theta_{2.5}$, from the fine (squares) and medium-grained (circles) Deltaflume experiments.

the Deltaflume are likely to be somewhat larger for the following reasons.

(i) On occasion, the pumped sampling tubes or nozzles got blocked with sediment and/or algae (Bell and Williams, 2002). It may be possible that some of the resulting sediment samples were contaminated with algae.

(ii) Uncertainty in the volume of water taken. A standard 8 litre bucket was used. Should the sampling volume have become blocked this water column could have been reduced.

(iii) Both the dried sediment and filter paper were weighed and the weight of an average filter paper was subtracted. The filter paper weight was later found to vary by up to 15mg. The resulting uncertainties were inversely proportional to the weight of sediment collected.

(iv) When the sampling nozzles were close to the bed it is possible that sediment was sampled directly from the bed. Samples taken within 1cm of the ABS detected bed level were therefore excluded from the analysis.

(v) The efficiency of sediment trapping by the nozzles under the irregular waves was estimated using the formula of Bosman et al. (1987). However, this trapping efficiency is likely to vary between instruments and during the strong variation in wave forcing conditions experienced both during and between experiments.

All the medium-grained experiments were conducted in pairs, and this allowed for an assessment of the maximum uncertainty in the Deltaflume pumped sample concentration measurements as follows. The successful pumped sampled concentration measurements made during the first of each pair were compared with those from the second of each pair. For example the measurements taken during M05_1 were compared with those taken during M05_2. The mean average of the resulting uncertainties was approximately ±30%, which, as expected, is somewhat larger than the uncertainty found by Moate and Thorne (2009).

4.5 ABS data analysis prior to inversion and inversion preliminaries

There is inherent variability in the ABS backscattered signal due to the random, Rayleigh distributed, phasing of the acoustic returns (Thorne et al., 1993). Such variability can be reduced significantly by root mean square (RMS) averaging over a number of independently measured profiles. The standard error on an average of N measurements is approximately given by $V_{rms}/(2\sqrt{N})$ (Thorne and Hanes, 2002). The ABS operated at 128Hz and RMS averaging was performed over every 32 measurements, reducing the error on the V_{rms} profile recorded at 4Hz by a factor of $\sqrt{32}$. The raw digitalised voltage output from the ABS was calibrated after deployment. Figure 4.8 shows the raw digitalised output from each transceiver plotted against the received backscatter in decibels, I_{dB}. A least squares fit was made to the data from each frequency channel and these used to convert the recorded output from the ABS to decibels, which were subsequently linearised to a voltage divided by a reference, V/V_0, using the *20 log*

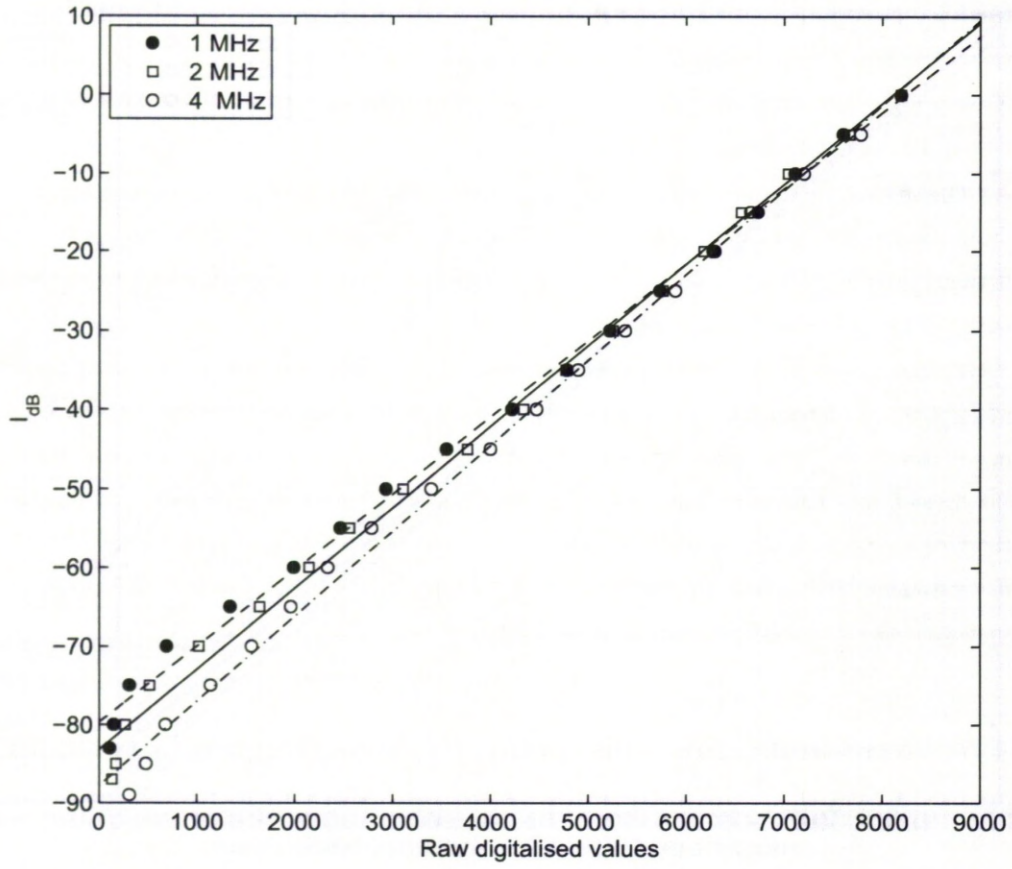

Figure 4.8: Raw digitalised ABS output plotted against sound intensity in decibels, I_{dB}, for each ABS frequency. Least squares were made to 1 MHz (−), 2 MHz (−−) and 4 MHz (− · −) data.

rule:

$$I_{dB} = 10\log_{10}(V^2/V_0^2) = 20\log_{10}(V/V_0). \tag{4.15}$$

The Deltaflume experiments were conducted in pairs. During the first experiment of each pair, the acoustic instrumentation recorded for approximately one minute prior to the initialisation of the waves. These one-minutes ABS backscatter recordings prior to each experiment are effectively *still water* readings which were used as *background* readings and subtracted from subsequent ABS backscatter recorded during each experiment.

The first 10-12 bins (approximately 10-12cm from the transceivers) of the ABS backscatter profiles were dominated by transmit breakthrough. These recordings are not due to the backscatter close to the transceiver. Thus, for each profile of the ABS backscatter (at 4Hz) a linear least squares fit was made to the backscatter data from bins 13-18 (approximately 13-18cm from the transceivers) and the backscatter from the first 12 bins were extrapolated from these least squares fits.

The speed of sound in water, c, is an important parameter in the acoustic inversion. This is because the scattering properties of the sediment, f and χ, are described in terms of the wave number of the sound, but also because it determines the ABS bin size. The speed of sound in water is a function of salinity, S, temperature, T, and depth, D, and was empirically determined by Mackenzie (1981) as

$$\begin{aligned} c = {} & 1448.96 + 4.591T - 5.304\times10^{-2}T^2 + 2.374\times10^{-4}T^3 + 1.340(S-35) + 1.630\times10^{-2}D \\ & + 1.675\times10^{-7}D^2 - 1.025\times10^{-2}T(S-35) - 7.139\times10^{-13}TD^3. \end{aligned} \tag{4.16}$$

The water in the Deltaflume came from the nearby canal and was assumed here to be fresh (S=0). The Vector ADV had a temperature sensor on board and the depth of the ABS was determined from the pressure sensor on the instrument frame. Thus for each Deltaflume experiment, the speed of sound at the ABS transceivers was accurately determined, and was typically 1457m/s. Whilst the speed of sound did vary with range from the ABS, this variation was negligible, hence for each Deltaflume experiment a height constant speed of sound was used. The oscillatory sampling frequency of the electronics was 75kHz. Thus, the range to a bin, b, from the transceivers was given by $bc/(2\times75,000)$ and the bin size was typically found to be 0.97cm.

The acoustic waveforms emitted from the ABS transceivers generally spread out spherically. This is not true for the near-field of the transceivers and a correction, Ψ, was applied (Downing et al., 1995):

$$\Psi = \frac{1 + 1.35z + (2.5z)^{3.2}}{1.35z + (2.5z)^{3.2}} \tag{4.17}$$

where $z = r\lambda/b^2$ is a the normalised range from the transceiver, r is the range, λ is the wavelength of the sound and b is the radius of the transceiver radiating aperture. The attenuation due to water was taken as $\alpha_w = 31\times10^{-15}c^2\lambda^{-2}$ (Kaye and Laby, 1986) and the transceiver

aperture radii were 0.0058, 0.0050 and 0.0050 m for the 1, 2 and 4 MHz transceivers respectively.

4.6 time average acoustic inversions and ABS validation

This section outlines the inversion methods employed to invert the acoustic backscatter from each experiment to time average suspended sediment concentration (SSC) profiles using the explicit inversion methodology. These time average SSC profiles are then compared with the pumped samples, representing the time average SSC, taken during each experiment. This comparison of two independent measurements of the SSC at a number of heights above the bed enables the validation of the two methods.

The explicit inversion requires the sediment concentration at one range bin, the reference range, r_r, to be known. Generally, the pumped sample taken at the second successful height range above the bed level was used. In the cases where only one pumped sample was successful, this was used as the reference. During approximately half of the fine-grained bed experiments, the pumped sampling at all heights above the bed was not successful. In contrast, almost all the medium-grained bed experiments had at least two successful pumped samples. Only the acoustic results from the Deltaflume experiments where at least one pumped sample was successful, listed in Table 4.1, were inverted using the explicit inversion method for comparison with the pumped samples.

4.6.1 Explicit inversions with height constant grain size profiles

One simplistic ABS inversion scenario is where the scattering and attenuation properties of the suspended sediments do not vary with range from the transceivers, in which case $< f >$ and $< \chi >$ are held constant, for each transceiver frequency, with range. Such height constant profiles in $< f >$ and $< \chi >$ are characteristic of sediment suspensions homogenous in terms of particle size distribution. If, however, the suspended sediment distribution strongly varies, in terms of its mean size or width, with range, then profiles of $< f >$ and $< \chi >$ must be calculated for the inversion. The assumptions made about the distribution and mean size profile of the suspended sediment can strongly influence the outcome of the acoustic inversion for sediment concentration (Moate and Thorne, 2009).

The ABS data were inverted using the explicit method outlined in Section 4.2.3 with a height constant particle size profile assumed. Table 4.1 lists the mean size of the particle number size distributions, mean averaged over the five pumped samples at different heights, $< a_s >$, for each experiment. It was assumed that the sediment suspensions are composed of quartz sand with this size, at all ranges from the transceivers.

The ensemble scattering and attenuation properties of the suspended sediment were calculated by averaging the intrinsic properties over the size distribution present, as described in Section 4.2.1, using equations (4.1a) and (4.1b) to gain $< \chi >$ and $< f >$. The particle number size distribution PDFs were described using the $\sigma / < a_s >$ listed in Table 4.1 for each

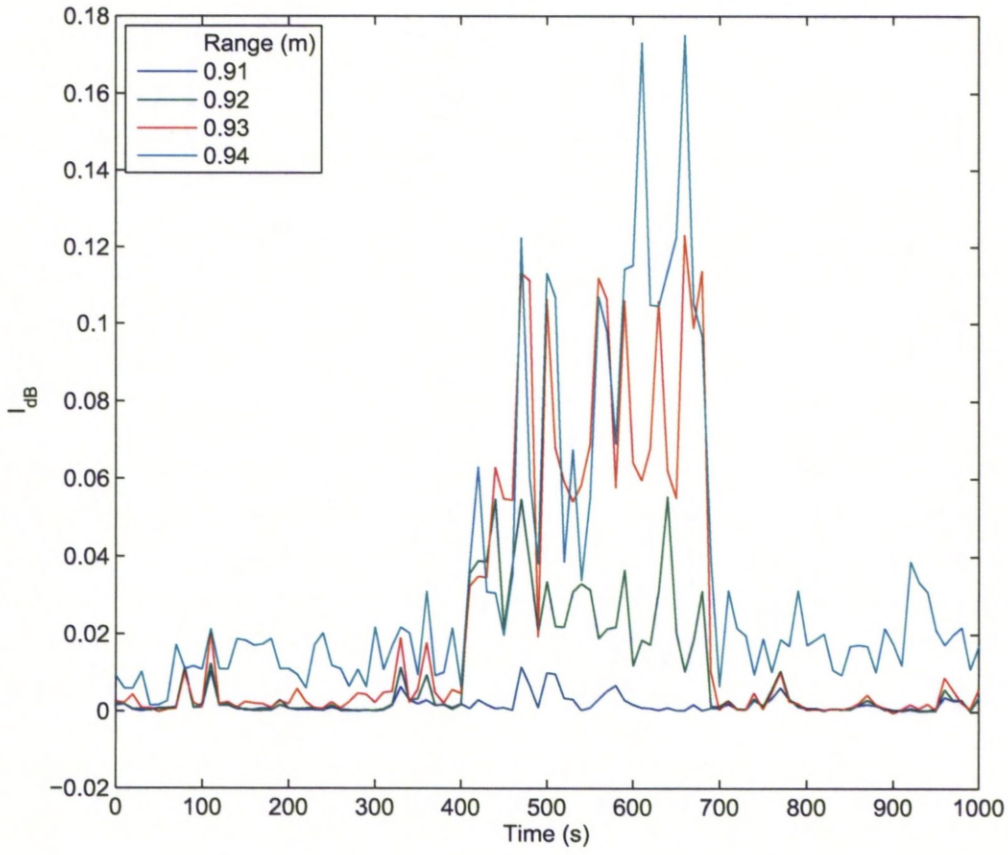

Figure 4.9: Linearised backscattered intensity, I_{dB}, at four ranges from the ABS transceivers, recorded by the 1MHz ABS channel during $\sim$ 15 minutes in M03_2.

experiment. For each experiment and ABS channel, the sediment concentration was calculated at all ranges from the transceivers using equation (4.8). This was done by starting at the reference range (r_r) and evaluating equation (4.8) at each range bin above r_r in turn, and then at each range bin below r_r in turn. The result for each experiment was three profiles of sediment concentration – one from each ABS channel – which were then mean averaged to give a single profile with error bars.

Determination of bed levels and calculation of reference concentrations

The time-series of near bed backscatter signal from each ABS channel was examined in order to accurately track bed level variations in each measurement burst and to identify nominal time average bed levels. Figure 4.9 shows the backscattered intensity, in dB, recorded by the 1MHz ABS channel, at four range bins, as a function of time. The signal has been smoothed to 0.1Hz using linear interpolation in order to see bed level variations more clearly. At the range of 0.91m from the transceivers the backscattered intensity is relatively low throughout the $\sim$ 15 minute bursts shown, with a number of small spikes most likely associated with short lived suspension events close to the bed. At the range of 0.92m, the backscatter is again low for the majority of

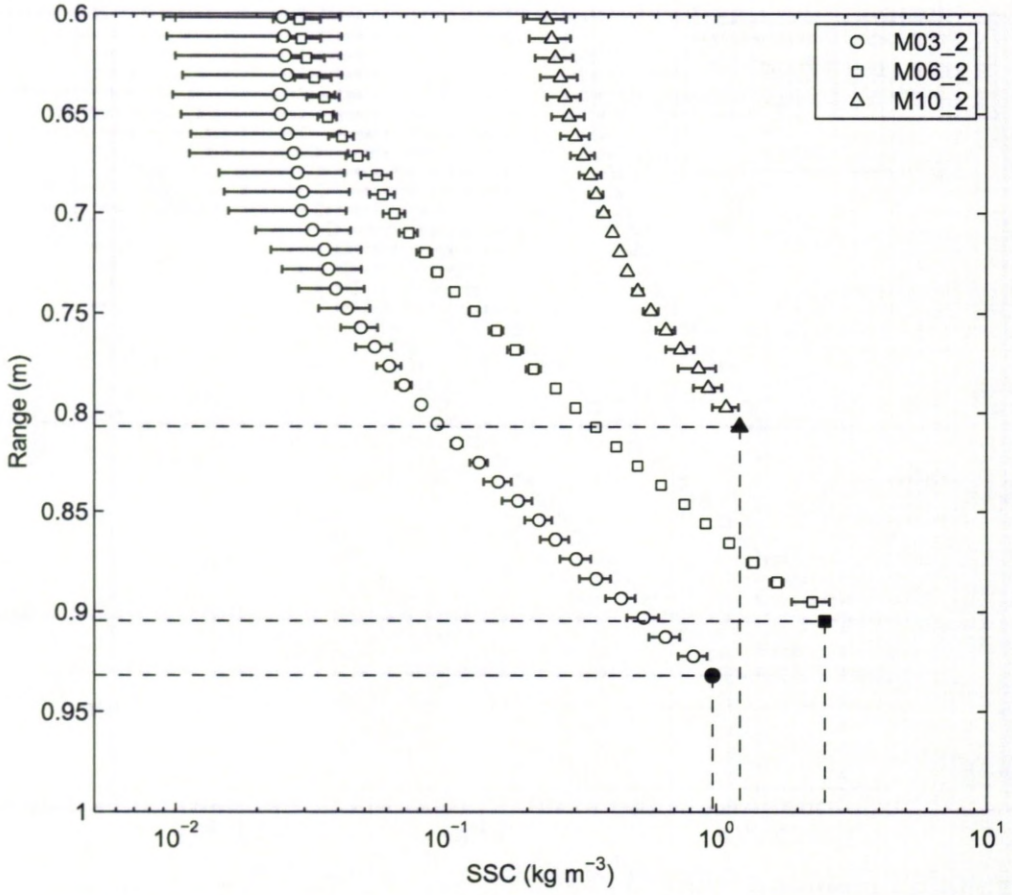

Figure 4.10: Three examples of the distribution of time average suspended sediment concentration, SSC, mean-averaged over the three ABS frequencies, with range from the ABS transceivers. The nominal bed levels and reference concentrations (solid shapes) extrapolated down to bed level are indicated.

the burst with the exception of between $\sim 400 - 700$ seconds. During this period the ABS was translated along a cross-shore line to a position directly above a ripple crest, and the 0.92m range bin is contaminated by the bed. Thus, between $\sim 400 - 700$ seconds the nominal bed level was 0.92m from the ABS transceivers. Above the remainder of the time-series, the nominal bed-level was 0.94m from the transceivers, as the 0.94m signal is contaminated by the bed.

Figure 4.10 shows three examples of the time average explicit inversion results. Between each of the results from the three experiments shown, the bed level changed due to the continual evolution of the bed in response to the changing wave forcing (see Chapter 7). The ABS backscatter is only inverted down to the last range bin that was not contaminated by the bed. Figure 4.10 shows the nominal bed levels determined by examining the ABS backscatter from each channel and the concentrations extrapolated to these levels (reference concentrations) using exponential functions fitted to the SSC profiles in the range $0.01\text{m} < z < 0.06\text{m}$.

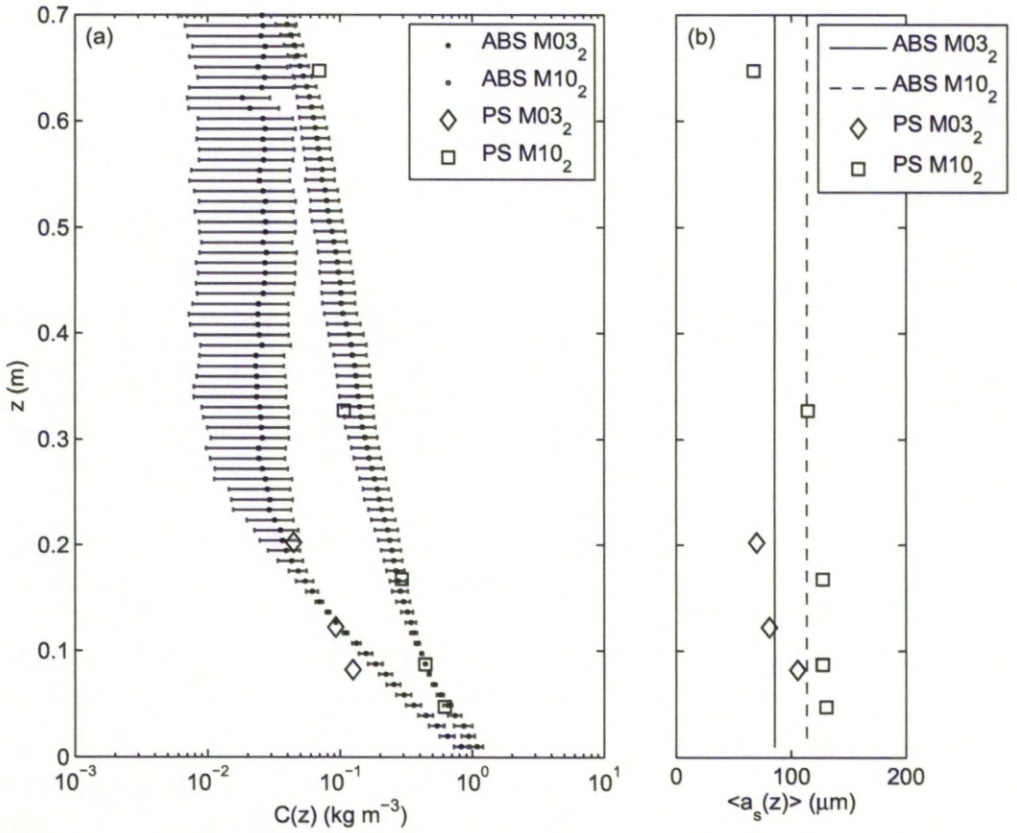

Figure 4.11: (a) Two examples of the distribution of time average suspended sediment concentration, $C(z)$, with distance from the bed, z, and (b) the height constant particle size profiles, $< a_s(z) >$, (−, −−) used. In (a) the mean of the results from the three ABS frequencies are shown and the error bars are the corresponding standard error. The results from the pumped samples, PS, are also shown by the diamonds and squares for M03_2 and M10_2 respectively.

Comparison of inversion results with pumped samples

Figure 4.11(a) shows the results from the explicit acoustic inversion for sediment concentration performed on the RMS backscattered voltage during experiments M03_2 and M10_2, along with the results from the pumped samples. Figure 4.11(b) shows the height constant grain size profiles, $< a_s >= 86\mu$m ($D_{s50} = 316\mu$m) and $< a_s >= 114\mu$m ($D_{s50} = 327\mu$m) for experiments M03_2 and M10_2 respectively, used in the inversions, and the sizes determined from the pumped samples. The reference range for the explicit inversions in each case was approximately 0.1m above the bed, and around this range the error on the ABS concentration is accordingly small. Far away from the bed, $z > 0.3$m, the error in the ABS concentrations is relatively large, especially for M03_2. This is most likely due to the scattering and attenuation properties of the sediments being poorly characterised higher up in the water column, i.e. the assumed homogeneity in terms of particle size distribution was inappropriate in the case of M03_2. In general however, the agreement with the pumped sampled sediment concentration (Figure 4.11(a)) is good, especially for M10_2.

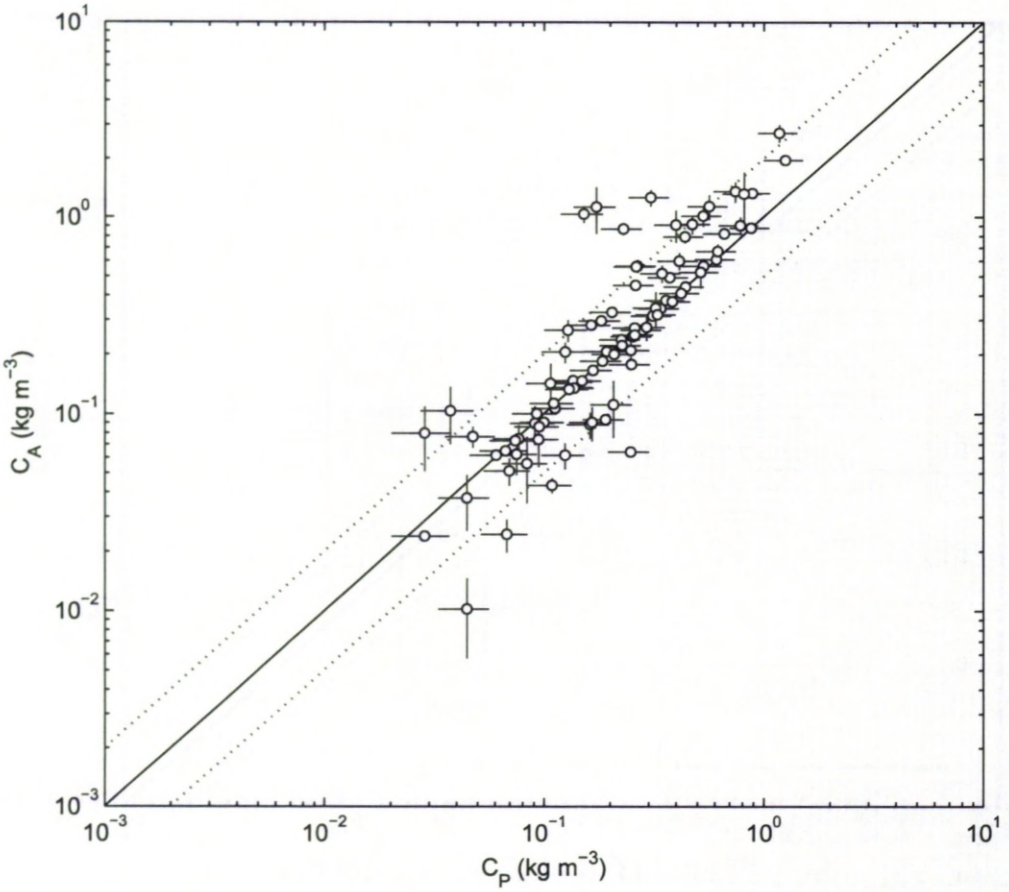

Figure 4.12: Comparison of the time average suspended sediment concentrations obtained from the ABS, C_A, and the pumped samples, C_P, for all the available pumped sample data. The lines corresponding to $C_A = C_P$ $(-)$ and $C_A = 2C_P$ and $C_A = 0.5C_P$ $(\cdots)$ are shown. The error bars show $\pm$ the standard error of the mean of the three ABS frequencies for C_A and $\pm$ 20% $\pm$ the error incurred whilst weighing for C_P.

Figure 4.12 shows a comparison of the suspended sediment concentration from the explicit ABS inversions, C_A, and the pumped samples, C_P. C_A are the mean of the results from the three ABS transceivers and the error bars are the associated standard errors. Results from both the fine and medium-grained bed experiments are included. The error bars for C_P are $\pm$20% and the error incurred during the weighing process of the dry sediment samples. The majority of data fall within the lines indicating a factor of two difference, which is consistent with the level of accuracy achievable with ABS suggested by Vincent (2007).

4.6.2 Investigating alternative particle size profiles

Figure 4.11 shows that in the case of M03_2 there is a large error on the SSC concentrations from the ABS for $z > 0.3$m, relative to the smaller errors close to the bed. In order to investigate whether these errors are due to the assumption of particle size homogeneity, a particle size profile decaying with distance from the bed was used in the acoustic inversions. Power law

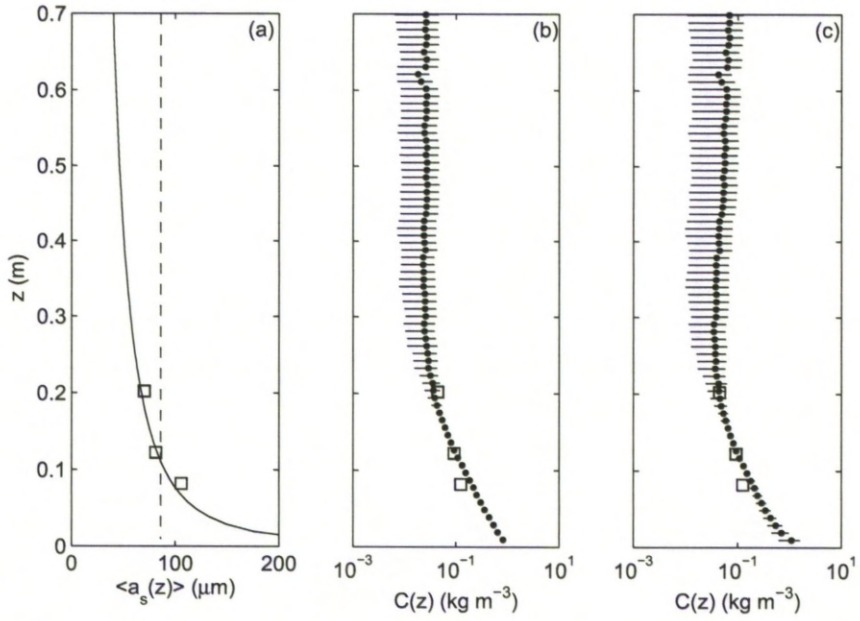

Figure 4.13: Comparison of the explicit inversion results from M03_2 using height constant (b) and power law (c) size profiles. The height constant (−−) and power law (−) size profiles are shown in (a) and the results from the pumped samples are shown with the squares.

profiles of the form $< a_s(z) >= a(z/z_r)^{-b}$, where a and b are constants and $z_r = 0.1$m, were fitted to the available pumped sample data by performing linear regressions on log a_s and log z. These profiles were then used to compute $< f >$, $< \chi >$, K_s and ξ profiles for use in the explicit inversions.

The results from the time average SSC inversions for SSC using height constant and power law size profiles are shown in Figures 4.13 – 4.16 for experiments M03_2, M06_2, M08_1 and M10_2 respectively. During each of these experiments three or more pumped samples were successful, enabling the accurate calculation of particle size profiles. In all these cases the power law particle size profile fits the pumped sample results reasonably accurately but in the case of M08_1, Figure 4.15(a), $< a_s >$ increases to large sizes close to the bed. In general, there is little or no improvement on the accuracy of SSC over the explicit inversions relying on height constant $< a_s >$ profiles. On the contrary, in the case of M03_2, shown in Figure 4.13, the error on the SSC for $z > 0.3$m and $z < 0.1$m increases with the use of the power law profile. In the case of M06_2, shown in Figure 4.14, the fitted $< a_s >$ profile highly agrees with the four pumped samples but there is no discernable difference between the two inversion results in Figures 4.13(b) and 4.13(c). For M08_1, the SSC close to the bed in Figure 4.15(c) is larger than that in Figure 4.15(b) despite the large increase in $< a_s >$ close to the bed, and the uncertainly on the SSC is also larger. Finally, there is little difference in the SSC profiles resulting from the two inversions during M10_2 shown in Figure 4.16.

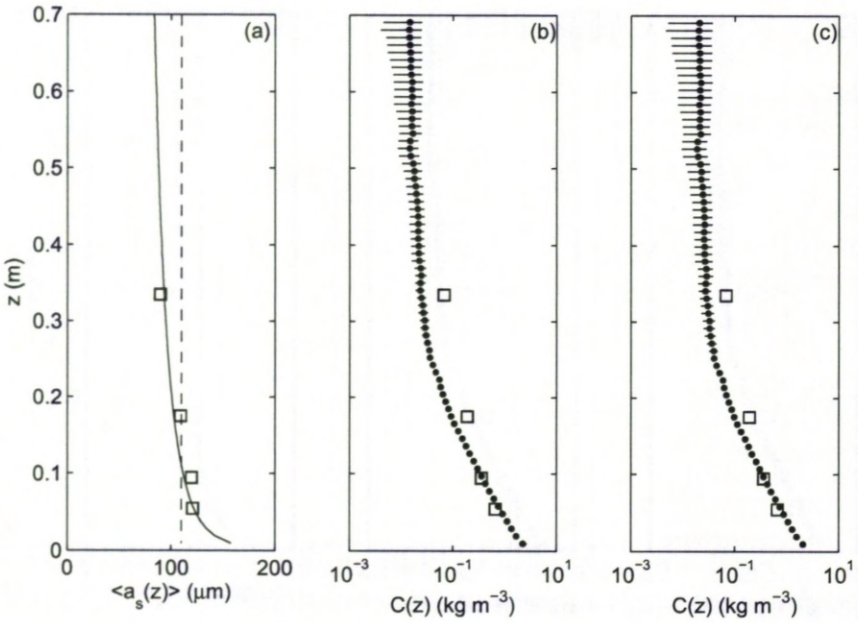

Figure 4.14: Comparison of the explicit inversion results from M06_2 using height constant (b) and power law (c) size profiles. The height constant (– –) and power law (–) size profiles are shown in (a) and the results from the pumped samples are shown with the squares.

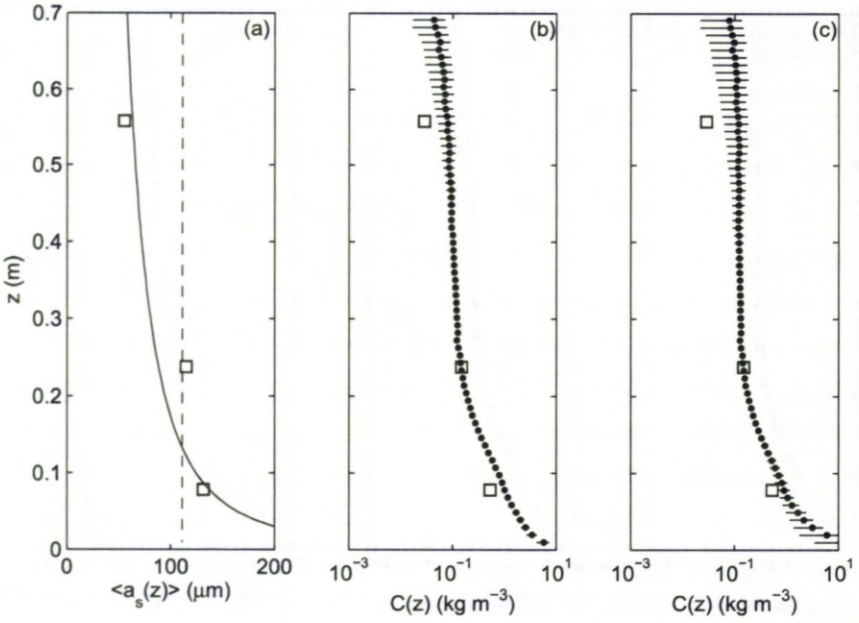

Figure 4.15: Comparison of the explicit inversion results from M08_1 using height constant (b) and power law (c) size profiles. The height constant (– –) and power law (–) size profiles are shown in (a) and the results from the pumped samples are shown with the squares.

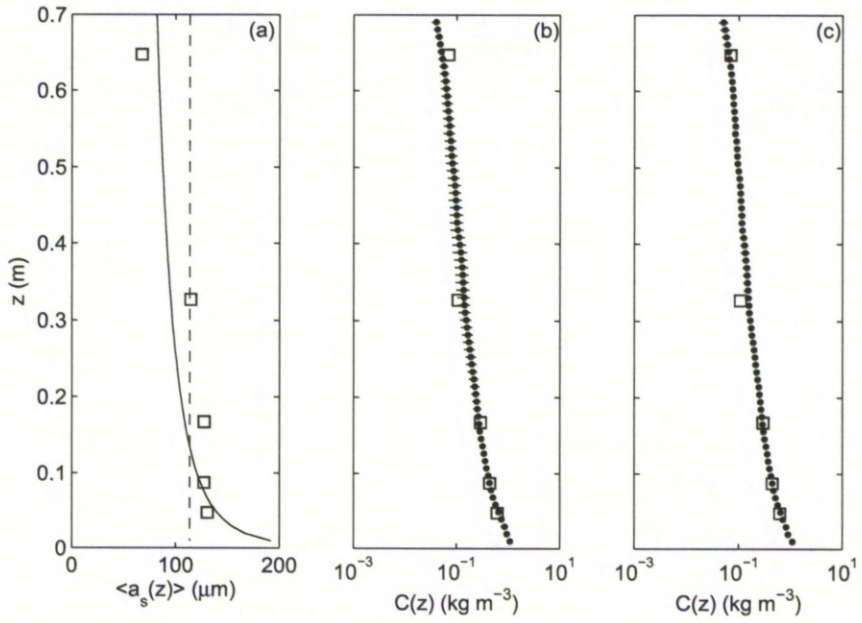

Figure 4.16: Comparison of the explicit inversion results from M10_2 using height constant (b) and power law (c) size profiles. The height constant (−−) and power law (−) size profiles are shown in (a) and the results from the pumped samples are shown with the squares.

4.7 Implicit inversions for sediment concentration of the ABS backscatter time-series

The explicit ABS inversion methods described in Section 4.6 are convenient methods for inverting to sediment concentration when independent measurements of the concentration are available, such as the pumped samples. The pumped samples were, however, not always successful and were not taken during all the Deltaflume experiments. The explicit inversion method also only yields time average suspended sediment concentration. For the experiments where no pumped samples were taken and for the inversion of the full ABS time-series, yielding instantaneous suspended sediment concentrations at 4Hz, an alternative inversion method must, therefore, be applied. This section outlines the implicit inversion method used to invert the full ABS time-series from each experimental burst to instantaneous sediment concentration. The veracity of this method is then tested by taking time averages of the inverted concentrations over the length of each measurement burst and comparing these results with the pumped sampled sediment concentrations.

4.7.1 Assessment of uncertainties in the ABS system constants

Section 4.2.2 highlights that the implicit inversion requires knowledge of the ABS system constant, K_t, for each frequency channel. The results from the explicit inversions described in Section 4.6 were used to determine K_t for each channel. Equation (4.4) can be rearranged to

	1 MHz	2 MHz	4 MHz
Fine-grained experiments	0.0021 ± 0.0004	0.0037 ± 0.0006	0.0010 ± 0.0002
Medium-grained experiments	0.0074 ± 0.0005	0.0090 ± 0.0006	0.0027 ± 0.0002

Table 4.2: The mean K_t values obtained for use during the fine and medium-grained experiments. The uncertainties indicated are the standard errors of the means.

give (Thorne and Hanes, 2002; Thorne et al., 2007)

$$K_t = \beta \, M^{-1/2} \, e^{2r\alpha_s}. \tag{4.18}$$

K_t was then calculated by evaluating equation (4.18) from the results for each explicit inversion in Section 4.6 for each channel. There was approximately 10% uncertainty on the K_t values due to the 20% uncertainty on the pumped sampled sediment concentrations. There was however some scatter in K_t between experiments outside this 10% uncertainty. There was also a clear difference between the K_t values obtained above the fine and medium-grained beds. The K_t values can drift with time, especially during transport of the ABS and when there are large variations in temperature. The majority of the ABS electronics was positioned on the side of the Deltfalume, with only the transceivers deployed in the water, and would have received a large temperature variation during the course of each day. During the emptying of the Deltaflume between the fine and medium-grained experiments the frame and all the instruments were removed. This could explain the difference in the K_t values obtained during the fine and medium-grained experiments. Another likely reason for the difference in K_t obtained above the fine and medium-grained beds is that the intrinsic sound scattering characteristics of the two sediment types differed. If this was the case, then the expressions used for χ and f (Thorne and Meral, 2008) would have described the intrinsic sound scattering characteristics of the fine and medium-grained suspensions to differing levels of accuracy. Taking these considerations into account two K_t values were calculated for each ABS channel - for the fine and medium-grained experiments - and are listed in Table 4.2.

4.7.2 Implicit ABS inversions for sediment concentration

In Section 4.6.2, there was found to be little advantage in considering a height varying size profile in the ABS inversions. Thus, as in Section 4.6.1, the sediment suspensions were considered to be homogenous in terms of their size distributions. The particle size profiles were calculated using equations (4.12a) and (4.12b) and were used together with the relative standard deviations, given by equation (4.13), to calculate the ensemble scattering and attenuation characteristics of the sediments, $< f >$ and $< \chi >$. Defining the size profiles in this manner enabled only the sediment mass concentration, at each height above the bed, to be sought. The iterative implicit inversion method outlined in Section 4.2.4 was used to invert for a time-series of SSC profiles for each experiment and for each ABS channel. Figure 4.17 shows a one minute time-series

of inverted SSC from the M04 experiment, where the significant wave height was 0.64m and the crest of a steep sided two-dimensional ripple was below the ABS (Chapter 5). The results from each of the three ABS channels are shown in Figure 4.17. Through the time-series shown there are a number of peaks in the SSC associated with the advection of a sediment laden vortex over the ripple crest (see Chapters 5 and 6). The three ABS transceivers were aligned perpendicular to the flow (along-shore) and were each 0.05m apart. The results from the three ABS channels agree in terms of the timing of the peaks in the SSC, indicating a high level of along-shore coherence. There are, however, small variations across the three results due to the spatial separation of the three transceivers. In terms of the SSC magnitude, there are also discrepancies across the three results shown in Figure 4.17. Whilst this too is due to the spatial separation of the transceivers it is also likely associated with the uncertainty surrounding the K_t values.

In order to assess the accuracy of the SSC magnitudes resulting from the implicit inversions of the ABS time-series, a comparison was made with the pumped samples. The inverted SSC time-series were time averaged over the burst length of each experiment. Figure 4.18 shows these results, C_I, plotted against the pumped sampled SSC, C_P, with error bars indicating $\pm 20\%$ of the C_P values and the standard error of the mean taken across the three ABS channels. The majority of data lie within the lines indicating a factor of two difference typical of the ABS (Vincent, 2007), although there are a number of outliers.

4.8 Summary

This chapter first introduced the ABS and outlined the different methodologies for the inversion of backscattered intensity to sediment concentration and mean particle size. These inversion methods were then validated using data from a homogenous sand suspension of known concentration and size distribution. All the inversions performed well in this idealised and carefully controlled environment. In the Deltaflume, measurements of the suspended sediments were made by pumped sampling and using the ABS. These two independent measurements thus offered a means by which to validate the two sets of measurements.

Section 4.6 presented the results from a number of explicit inversions using both height constant and power law decaying mean size profiles. On the whole there was very little difference between the two sets of results. One major drawback of the power law decaying size profiles was the under-representation of the mean size at high elevations above the bed. This forced the inverted concentrations to be relatively high at these elevations (e.g. Figure 4.13(c)). It is important to represent the mean size correctly close to the bed, where the highest concentrations are found, so to prevent positive feedbacks occurring due to the inaccurate calculation of the sediment attenuation (see Section 4.2.5). The near bed SSC is also of primary interest in this study and can contribute highly towards the net flux of sediment (Van der Werf et al., 2006). For these reasons the inversion methods adopted here use height constant size distribution

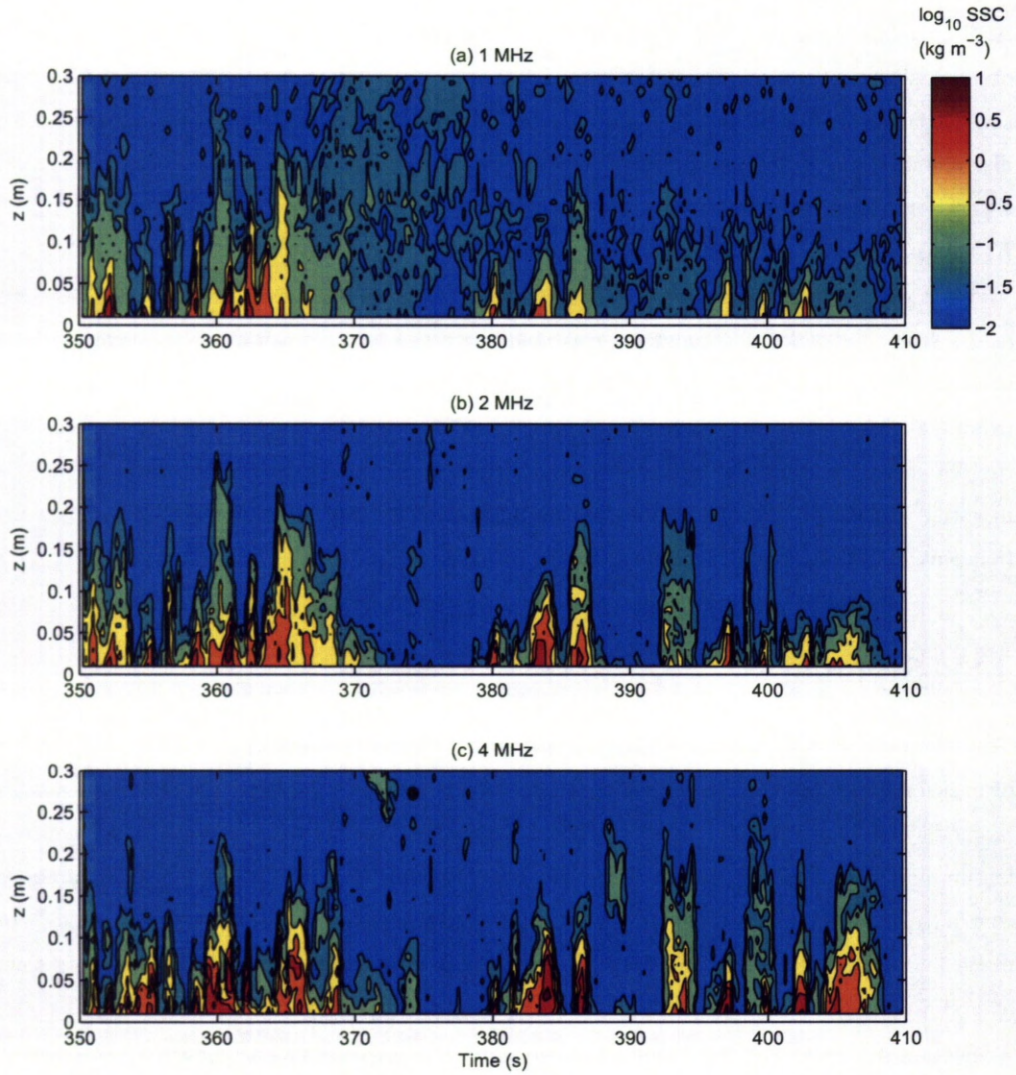

Figure 4.17: One minute time-series of suspended sediment concentration from the ABS inverted using an implicit iterative approach. Results from the three ABS channels operating at (a) 1MHz, (b) 2MHz and (c) 4MHz are shown.

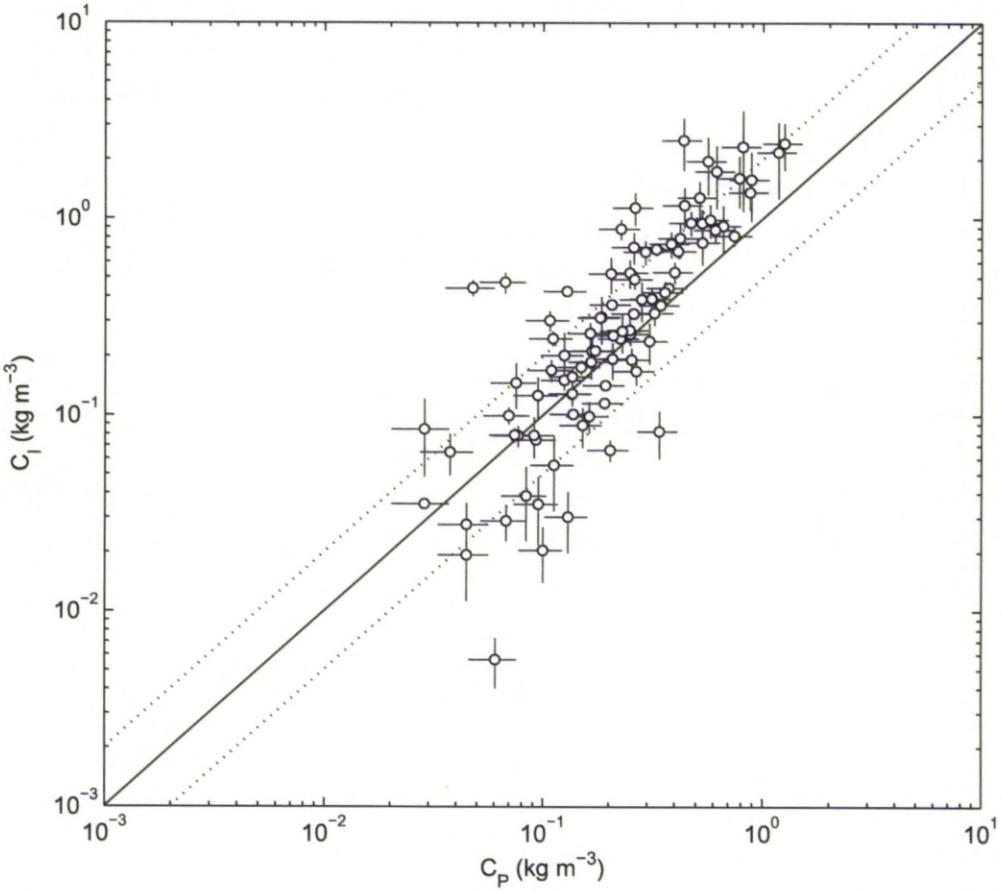

Figure 4.18: Comparisons of the time-mean suspended sediment concentrations obtained from implicit inversions of the ABS time-series, C_I, and the pumped samples, C_P, for all the available pumped sample data. The lines corresponding to $C_I = C_P$ $(-)$ and $C_I = 2C_P$ and $C_I = 0.5C_P$ $(\cdots)$ are shown. The error bars show $\pm$ the standard error of the mean of the three ABS frequencies for C_I and $\pm$ 20% $\pm$ the error incurred whilst weighing for C_P.

profiles that are good representations of the near bed sediment suspensions.

A comparison of the time average explicit inversions for SSC with the pumped samples (Figure 4.12) showed a good agreement in the majority of cases. This is unsurprising considering the fact that a number of the pumped samples were used to constrain the inversions. There were, however, a number of outliers due to (i) inherent uncertainties associated with the ABS (Vincent, 2007), (ii) an inaccurate description of the size distribution at these points, (iii) uncertainties associated with the pumped samples (Section 4.4.4), (iv) the spatial separation of the pumped sampling nozzles and the ABS of 0.8m and (v) the lack of knowledge regarding the exact timing of the pumped sampling. This last point regarding the timing of the pumped sampling is most likely one of the greatest courses of discrepancy between the pumped samples and the ABS. This is because the waves were irregular and because of the occurrence of wave groups during the Deltfalume experiments. Chapter 6 shows that under the largest waves the SSC was correspondingly high, whereas under the smaller waves very little suspended material was in suspension. Chapter 6 also shows there to be time lags between the onset of large waves and the propagation of sediment through the water column. Whether the pumped samples were taken, before, during or after such wave packets must, therefore, have contributed to differences between their results and that of the ABS averaged over the whole burst.

Section 4.7 outlines the implicit inversion of the ABS time-series. The mean averages through the burst length of each experiment compared reasonably well with the pumped samples (Figure 4.18). There are, however, significantly more outliers than the comparison with the explicit inversion results (Figure 4.12). Whilst being subject to the same uncertainties as the explicit inversions, these results contained additional errors because they were reliant on the K_t values obtained in Section 4.7.1 and were not this time constrained by the pumped samples.

4.9 Conclusions

The ABS offers non-intrusive measurements of suspended sediments at turbulent and intra-wave timescales (Thorne and Hanes, 2002) and at centimetre vertical resolution. The explicit inversions performed here gave time average SSC profiles within the factor of two typical of ABS devices (Vincent, 2007). Explicit inversions are used in Chapter 7 to study how the burst-average SSC profiles responded during the Deltaflume storm sequence in terms of both magnitude and shape.

The implicit inversions performed here gave time-series of instantaneous SSC profiles at 4Hz. The absolute magnitude of SSC resulting from these inversions agreed to a lesser degree, than the explicit results, with the pumped samples. It does not necessarily follow that the instantaneous SSC magnitudes have large errors, as the pumped samples are not necessarily error free. However, the pumped samples offered the only independent measurements of sediment concentration and the explicit results must therefore be viewed with more certainty than the implicit results, in terms of magnitude. The results from the sediment tower presented

in Section 4.3 also suggest that the explicit inversion methodology yields more accurate SSC magnitudes.

The main advantage of the implicit inversion results, over the explicit results, is one of temporal resolution. In Chapters 5 and 6 the results from the implicit inversion are used to study the SSC profiles at intra-wave and wave period time scales respectively. The fact that the time averages of the absolute magnitudes of these implicit results did not highly agree with the pumped samples is not considered to be vitally important in Chapters 5 and 6 where the relative magnitudes from wave-to-wave and through the wave cycle are principally investigated.

Chapter 5

Intra-wave observations of sediment entrainment processes above sand ripples under irregular waves

Abstract

Measurements of intra-wave sediment entrainment processes are reported above ripples under irregular waves generated in a large scale flume facility. The data consists of substantive observations of small scale processes collected at high spatial and temporal resolution under irregular wave forcing, typical of coastal environments. Acoustic measurements were made of water velocities, bedforms and suspended sediment concentration over plane and rippled beds. During each rippled bed experiment, measurements were taken over the crests of steep sided ripples, above which flow separation was considered likely to occur. Above the ripple crests, a strong intra-wave variation in the near bed suspended sediment, indicative of vortex formation and shedding, was observed to dominate wave half cycles where the orbital diameter was greater than 1.2 times the ripple wavelength, λ. The irregular waves were parameterised with a significant wave height, H_s, and a significant orbital diameter, d_s. Thus, during irregular wave conditions and over steep ripples where $d_s/\lambda > 1.2$, vortex shedding was deemed as the dominant sediment entrainment process. Furthermore, the percentage of wave half cycles where vortex shedding was observed, was found to scale as $26d_s/\lambda$. These results demonstrate, for under irregular waves, the existence of a clear suspended sediment structure consistent with vortex shedding, previously observed under regular waves.

Citation: O'Hara Murray, R. B., P.D. Thorne and D. M. Hodgson (2011), Intrawave observations of sediment entrainment processes above sand ripples under irregular waves, J. Geophys. Res., 116, C01001, doi: 10.1029/2010JC006216.

5.1 Introduction

In oscillatory flow, and above steep 2D ripples, the boundary layer between the flow and the bed can separate in the lee of the ripple, thus forming a vortex which at flow reversal is ejected into higher parts of the flow. The near bed hydrodynamics and momentum transfer is dominated by vortex formation and shedding and the effect that this process has on near bed sediment suspensions is profound. Sediment can be trapped in the shed vortex, which is advected both horizontally and vertically (Bijker et al., 1976; Hansen et al., 1994), and is released as the vortex propagates above the bed and dissipates as turbulence becomes dominant. Under vortex shedding conditions maximum sediment pickup occurs as the vortex is advected over the ripple crest around the instants of flow reversal (Nakato et al., 1977; Sleath and Wallbridge, 2002). In contrast, over a flat bed where vortex shedding does not occur, maximum sediment pickup occurs at times of peak shear stress at the bed, closely preceding peak free-stream velocity (Davies and Thorne, 2008). Davies and Villaret (1999) interpreted the vortex shedding process above ripples in terms of a convective stress close to the bed, described by a strongly time varying convective eddy viscosity with peaks at flow reversal. The time dependence of such a convective eddy viscosity has also been examined with a cloud-in-cell discrete vortex model, above a ripple bed, and peaks were observed to occur at flow reversal (Malarkey and Davies, 2004). Thus, these different entrainment processes impact upon the respective mixing mechanisms above flat and rippled beds: coherent convective processes dominate close to rippled beds under vortex shedding conditions, whereas turbulent diffusion dominates above flat beds (Nielsen, 1992; Thorne et al., 2009a). More recently, these convective and diffusive mixing processes have been related to the form of the sediment diffusivity profile (Thorne et al., 2009a).

It is becoming increasingly well established that the coherent and repeatable phenomenon of vortex shedding above ripples can entrain sediment to considerably greater heights than above a flat bed. This is true both in a time averaged sense (e.g. Thorne et al., 2002) and at certain phases during the wave cycle (e.g. Bijker et al., 1976; Nakato et al., 1977; Block et al., 1994; Davies and Thorne, 2005; Van der Werf et al., 2007). Under symmetrical waves the vortex shedding process occurs twice every wave cycle: on the onshore and offshore sides of the ripple crest during the onshore and offshore phases of the wave cycle respectively. The ejection of sediment laden vortices above the ripple crest occurs at flow reversal and this leads, for example, to the vortex generated during the onshore wave half cycle being advected in the offshore direction. Thus, under asymmetric waves where the onshore orbital velocities are largest, an offshore pumping of sediment can occur (Bijker et al., 1976; Davies and Thorne, 2008).

The process of vortex formation and shedding is inherently linked to the bedforms present under such conditions, namely vortex ripples, over which flow separation can occur. Under quiescent wave forcing conditions the bedforms present are often those of relicts remaining from times of stronger wave activity (Nielsen, 1992), otherwise the bed is nominally plane.

During these conditions, which can be described as lower-stage plane bed, there is little in the way of suspended sediment pickup as the bed shear stress is low and the relict bedforms are non-active. Under surface waves of low steepness, long crested 2D ripples start to emerge on the bed. As the surface wave steepness increases, the ripple steepness increases and boundary layer separation is initiated. During these conditions vortex ripples become active and begin to shed vortices. Thus, vortex ripples spread over the bed and the process of vortex formation and shedding can dominate the suspended sediment dynamics. As the steepness of the surface waves increase further the bedforms reduce in steepness and tend towards a (transitional) 3D morphology where the crests first become sinuous and broken in form before becoming washed out. Eventually, as the surface wave steepness continues to increase towards storm conditions, the bed becomes an upper-stage plane bed with sheet flow dominant.

Ripples with wavelengths that scale with the wave orbital diameter are termed orbital ripples (Clifton, 1976; Clifton and Dingler, 1984), are predominant in laboratory experiments and are steep sided with ripple height to wavelength ratios (steepness) greater than 0.1. Whilst orbital ripples can be found in the field, anorbital ripples, with wavelengths roughly proportional to the bed sediment grain size, are much more common (Wiberg and Harris, 1994). Anorbital ripples occur when the orbital diameter is larger than the ripples wavelength. Thus, anorbital ripples can be referred to as decaying ripples, present at times of transition between orbital ripples and upper-stage plane bed (Allen, 1997). Suborbital ripples are a transitional type and occur when the orbital diameter is between that of orbital and anorbital ripples.

Some of the earliest observations of vortex entrainment of sediment above ripples were made by Bagnold (1946) in an oscillating water tank. Bijker et al. (1976) inferred the process of vortex shedding from observations of suspended sand transport opposite to the direction of wave propagation as well as making photographic observations of the vortex shedding and sediment entrainment process. Some of the earliest intra-wave measurements of suspended sediment concentration (SSC) were made by Nakato et al. (1977) in regular oscillatory flow generated in a water tunnel. Nakato et al. (1977) observed two dominant peaks in the SSC during the wave cycle and contributed these to vortex ejection during each wave half cycle. Vortex shedding has also been directly observed in the laboratory under regular (Tunstall and Inman, 1975) and irregular (Villard and Osborne, 2002) free surface waves and its existence inferred in the field (Ardhuin et al., 2002). Observations of SSC have been made under waves and over ripples on a macro-tidal beach where a weak current was present using an Acoustic Backscatter System, ABS, (Osborne and Vincent, 1996), although evidence of vortex generation was only found during the onshore phase of the wave cycles. More recently, the SSC profile on an intra-wave time scale under regular oscillatory flow has been measured using ABS (Thorne et al., 2003; Davies and Thorne, 2005; Van der Werf et al., 2007). A coherent phenomenon consistent with the entrainment of sediment in a lee-wake vortex shed at flow reversal was identified, thus confirming the existence of vortex entrainment processes at large scale under regular oscillatory flow. One recent development was that of Nichols and Foster (2007) who

made observations of the near-bed velocity field, above an asymmetrical ripple under irregular waves in a large wave flume, using a Particle Image Velocimetry, PIV, system and found that the ejection of a vortex was a function of the flow acceleration.

In laboratory experiments, regular waves are often used for simplicity, however irregular waves simulate nature more closely (Soulsby, 1997), containing a broad spectrum of wave heights and periods. The near bed velocity field under regular waves provide a repeatable orbital excursion that is conducive to both the formation of wave ripples and the subsequent formation of lee-wake vortices in each wave half cycle. In contrast to regular waves, the horizontal velocity field under irregular waves has a distribution of velocity amplitudes, oscillation periods and thus orbital excursion diameters, which govern the formation of ripples and the suspension of sediment. Thus, vortex formation and shedding will not necessarily occur during each wave half cycle under irregular waves. It is questionable therefore, whether the intra-wave signatures present in the suspended sediment dynamics of vortex formation and shedding, are dominant under irregular waves, as is the case under regular oscillatory flow (e.g. Davies and Thorne, 2005; Van der Werf et al., 2007). Furthermore, it is at present unknown in an irregular wave sequence, under which wave half cycles vortex formation occurs. Refining our understanding of this has significant implications as many models simply characterise the flow with average parameters such as the significant wave height, H_s. It is therefore useful to quantify the fraction of waves where vortex shedding is expected to occur under different hydrodynamic regimes, described by H_s for example.

The Deltaflume of Deltares, Delft Hydraulics, the Netherlands, is a large flume facility ideal for the study of sediment transport processes at near field-scales. In 2001, a comprehensive dataset of measurements covering the sediment transport triad of wave forcing, bedforms and suspended sediment (Thorne and Hanes, 2002) was collected, under irregular waves. These data have been reported previously in studies focusing on the bedforms (Williams et al., 2004; Williams and Bell, 2006). In the present study, the bedforms are re-examined and the intra-wave structure of the suspended sediments is studied for the first time. The underlying questions this present study addresses are (i) whether vortex formation and shedding is a dominant mechanism of sediment entrainment under irregular waves, (ii) under what proportion of wave half cycles this mechanism occurs and (iii) whether these occurrences can be parameterised by the ratio of orbital diameter to ripple wavelength as suggested by Malarkey and Davies (2002). Finally, irregular wave forcing is often parameterised by the significant wave height which is in turn commonly used within models. Hence, in the present study the relationship between the significant wave height, the ripple dimensions, and the occurrence of vortex shedding is investigated because of the direct relevance this has with existing numerical modelling frameworks.

5.2 Models and prediction of vortex shedding

Davies and Thorne (2008) presented a simple modelling framework for oscillatory flow above

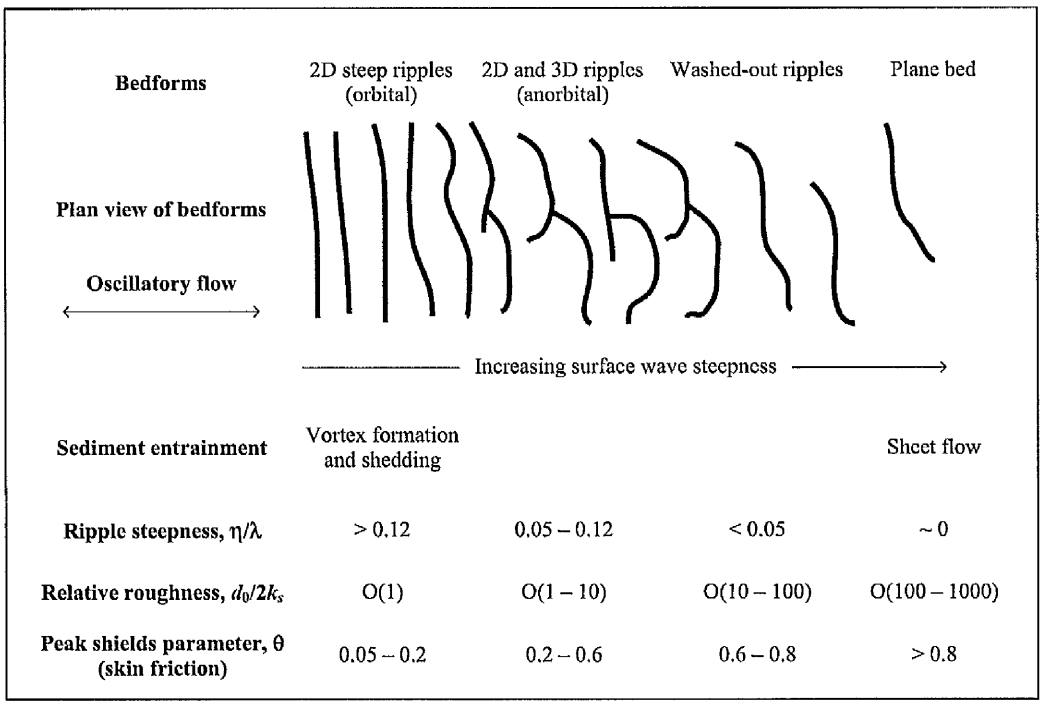

Sediment entrainment	Vortex formation and shedding			Sheet flow
Ripple steepness, η/λ	> 0.12	0.05 – 0.12	< 0.05	~ 0
Relative roughness, $d_0/2k_s$	O(1)	O(1 – 10)	O(10 – 100)	O(100 – 1000)
Peak shields parameter, θ (skin friction)	0.05 – 0.2	0.2 – 0.6	0.6 – 0.8	> 0.8

Figure 5.1: Schematic of bedform characteristics related to hydrodynamic and bedform parameterisations (based on Davies and Thorne, 2008; and Thorne et al., 2009a).

erodible sandy beds. Figure 5.1 shows a schematic of common bedform regimes under regular oscillatory flow, from the vortex shedding regime to the upper-stage plane bed, under increasing surface wave steepness. Beneath (regular) waves, the orbital excursion diameter of each wave half cycle, d_0, scales with the surface wave steepness. Key to parameterising bedform regimes is the Shields parameter, a dimensionless measure of the balance between disturbing (shear stress) and stabilising forces on individual surface sediment particles. Figure 5.1 shows the skin friction Shields parameter, θ, increasing with the surface wave steepness. Another parameterisation is the relative roughness, $d_0/2k_s$, where k_s is the equivalent roughness which describes the influence the bed has on the flow. Above lower-stage plane beds, the dominate contribution to the roughness is the Nikuradse grain roughness due to skin friction typically given by (Soulsby, 1997)

$$k_s = 2.5D_{50}. \tag{5.1}$$

Based on this equivalent grain roughness, the grain roughness Shields parameter, $\theta_{2.5}$, can be defined as (e.g. Nielsen, 1992)

$$\theta_{2.5} = \frac{f_{2.5}U_0^2}{2(s-1)gD_{50}} \tag{5.2}$$

where s is the ratio of sediment density to water density ($s = 2.65$ for quartz sand), D_{50} is the median grain diameter of the bed sediment, g is the acceleration due to gravity, U_0 is the wave orbital amplitude and $f_{2.5}$ is the grain roughness wave friction factor (skin friction) based on equation (5.1). One expression for $f_{2.5}$ is that developed by Soulsby (1997) for rough turbulent

flow which with equation (5.1) substituted in is given by

$$f_{2.5} = 0.237(d_0/5D_{50})^{-0.52}. \tag{5.3}$$

When bedforms are present, the dominant contribution to the roughness is due to form drag (Van Rijn, 2007) and k_s is often expressed in terms of the ripple dimensions. One commonly used form for k_s above a rippled bed is (Grant and Madsen, 1982; Nielsen, 1992; Styles and Glenn, 2002; Davies and Thorne, 2008)

$$k_s = \alpha\, \eta\ \ (\eta/\lambda) \tag{5.4}$$

where η and λ are respectively the height and wavelength of the ripples present on the bed. There are conflicting reports as to the precise value of α. For example, Grant and Madsen (1982) proposed α=27.7 whereas Nielsen (1992) proposed α=8. There can also be roughness associated with a moving sand layer, e.g. during sheet flow conditions (Grant and Madsen, 1982; Nielsen, 1992), such as (Nielsen, 1992)

$$k_s = 170 D_{50}\sqrt{\theta_{2.5} - 0.05}. \tag{5.5}$$

Nielsen (1992) proposed that above ripples both the form drag due to the ripples and the moving sand layer contribute towards the total equivalent roughness, such that

$$k_s = 8\eta\frac{\eta}{\lambda} + 170 D_{50}\sqrt{\theta_{2.5} - 0.05}. \tag{5.6}$$

5.2.1 Vortex shedding criteria

The ripples above which vortex formation and shedding occurs are termed vortex ripples and are typical during the '2D steep ripple' regime defined in Figure 5.1. Vortex shedding occurs only when the ripples are sufficiently steep for the boundary layer to separate on the lee of the ripple crests (Sleath, 1984). Hence, the steepness of the ripple is one control over whether vortex formation and shedding occurs and is used in the expression for k_s above rippled beds, equation (5.4). It is widely assumed that vortex shedding only starts when $\eta/\lambda > 0.1$ (Davies and Thorne, 2005). Allen (1979) suggested that $\eta/\lambda \approx 0.13$ marks the transition from rolling-grain to vortex ripples and Malarkey and Davies (2004) considered $0.13 \leq \eta/\lambda \leq 0.2$ to define an approximate vortex shedding regime. Likewise, Davies and Villaret (2002) considered the bed to be 'dynamically plane', where no vortex shedding processes occur, when $\eta/\lambda < 0.12$. Thus, the η/λ values in Figure 5.1 indicate whether flow separation is likely to occur in each regime.

As indicated in Figure 5.1, $d_0/2k_s$ increases with the evolving bed under progressively increasing wave steepness. In the vortex ripple regime, where $d_0/2k_s$ ~O(1), k_s is related to the ripple dimensions by equation (5.4). Taking the ripple steepness as $\eta/\lambda = 0.12$ and $\alpha = 8$

(Nielsen, 1992), k_s can be related the ripple height, $k_s = 0.96\eta$, or the ripple wavelength, $k_s = 0.1252\lambda$, and in the vortex shedding regime the relative roughness is given by

$$d_0/2k_s \approx 4.34 d_0/\lambda. \tag{5.7}$$

Malarkey and Davies (2002) used the parameter d_0/λ to define a secondary vortex shedding criterion, $1 \leq d_0/\lambda \leq 4$, which roughly equates to $4.3 \leq d_0/2k_s \leq 17.4$ using equation (5.7). This criteria, $1 \leq d_0/\lambda \leq 4$, has significant implications for sediment entrainment and transport. Beneath regular waves, where d_0/λ is relatively constant, this is not such an issue, but beneath irregular waves it implies that vortex shedding will occur intermittently due to the distribution of orbital diameters. When d_0/λ is between $1 - 4$, vortex shedding is expected to dominate the entrainment of sediment. The non-separating flow limit, $d_0/\lambda = 1$, is where it is unlikely for the flow to be strong enough for boundary layer separation to occur. The upper limit, $d_0/\lambda > 4$, defines the point where the organised flow structure of vortex formation and shedding starts to give way to more homogenous turbulence where peaks in the sediment pickup occur at phases that are more in line with flat bed (sheet flow) behaviour (Malarkey and Davies, 2002). The observations of Nichols and Foster (2007) using PIV confirmed both intermittent vortex shedding under irregular waves and also its dependence on the flow velocity (related to the orbital excursion). The dependence of the parameter d_0/λ on the ripple wavelength has strong implications in the natural environment where there is likely to be a distribution of ripple wavelengths present on the bed. The dependence of vortex shedding on d_0/λ has been examined theoretically with cloud-in-cell and discrete vortex models and compared with laboratory measurements of the water particles in two-dimensions (Malarkey and Davies, 2002) but not to our knowledge under field scale irregular waves, or through observations of the suspended sediments and fluid flow.

5.2.2 Suspended sediment concentrations

One method of predicting the sediment concentration under oscillatory flow is to separate the magnitude and distribution of SSC above the bed. For example, the time average profile of SSC above ripples and under waves, $C(z)$, is often expressed in the form

$$C(z) = C_0 \exp(-z/L) \tag{5.8}$$

where z is the height above the bed and L is the vertical decay length scale. The reference concentration, typically taken at the bed level, is a measure of the concentration magnitude and is commonly expressed theoretically in terms of the grain roughness Shields parameter ($\theta_{2.5}$) given by equation (5.2). Above ripples, Nielsen (1986) modified $\theta_{2.5}$ to account for flow

enhancement near the ripple crest:

$$\theta_r = \frac{\theta_{2.5}}{(1 - \pi\eta/\lambda)^2}, \tag{5.9}$$

where λ and η are the wavelength and height of the ripples respectively. Nielsen (1986) found a cubic dependence of the mass reference concentration, C_0, taken over the ripple crest (at crest level) on θ_r:

$$C_0 = 0.005\rho_s\theta_r^3, \tag{5.10}$$

where ρ_s is the sediment density. Equation (5.10) was confirmed by Thorne et al. (2002) under large scale regular waves although the empirical coefficient, 0.005 in equation (5.10), was found to be 0.0022 ± 0.0005, close to a factor of two smaller.

Reference concentrations based on the Shields parameter, e.g. equation (5.10), are time averages, often over many wave cycles, i.e. $C_0 = \overline{c_0(t)}$ where $c_0(t)$ is the instantaneous reference concentration as a function of time, t, and the over bar indicates a time average. Similarly, the grain roughness Shields parameter defined here ($\theta_{2.5}$, equation (5.2)) is based on the orbital velocity amplitude, U_0. It follows that the instantaneous, time varying, reference concentration, $c_0(t)$, cannot be straightforwardly expressed in terms of $\theta_{2.5}$ and θ_r defined here. From a modelling point of view, Davies et al. (1997) discussed the difficulties associated with applying the reference concentration approach in time dependant sediment suspension problems. They commented that one way to overcome these difficulties is with the use of a time varying sediment pickup function based on the SSC gradient near the bed. Nevertheless, it is established that variations in sediment entrainment through the wave cycle lead to instantaneous variations in $c_0(t)$, and therefore that sediment pickup and $c_0(t)$ are intrinsically linked.

Nielsen (1992) suggested empirical equations for the decay length scale of the SSC profile given by equation (5.8):

$$L = \begin{cases} 0.075\frac{U_0}{w_s}\eta & \frac{U_0}{w_s} < 18 \\ 1.4\eta & \frac{U_0}{w_s} \geq 18. \end{cases} \tag{5.11}$$

The settling velocity of the suspended sediment, w_s, can be calculated from knowledge of the median grain size of the suspended sediment, D_{s50}, using the formula of Soulsby (1997)

$$w_s = \frac{\upsilon}{D_{s50}}[\sqrt{10.36^2 + 1.049D_*^3} - 10.36] \tag{5.12}$$

where υ is the kinematic viscosity of water and D_* is a dimensionless grain size given by

$$D_* = \left[\frac{g(s-1)}{\upsilon^2}\right]^{1/3} D_{s50}. \tag{5.13}$$

Under fixed wave forcing conditions (e.g. $U_0 = 1\text{m/s}$), U_0/w_s is < 18 typically when coarse sediments (i.e. $w_s > 18^{-1}\text{m/s}$, $D_{ss50} > 370\mu\text{m}$) are in suspension. In this case, L varies with U_0/w_s and the ripple height (η). When $U_0/w_s > 18$, i.e. for finer sediment (i.e. $w_s \leq 18^{-1}\text{m/s}$,

$D_{s50} < 370\mu$m), L is only dependant on η, and $C(z)$ decays at the same rate under different wave forcing conditions as long as the ripples have the same height. When $U_0/w_s < 18$, i.e. when coarse sediments are in suspension, equation (5.11) is dependant on the sediment settling velocity. This is likely to be a source of uncertainty in the prediction of L where a broad sediment size distribution is present. In these cases the settling velocity distribution should be considered. It is worth noting that there has been some work on the suspensions of graded sediment (e.g. Nielsen, 1983, 1992; Tomkins et al., 2003).

5.3 Experimental instrumentation and methodology

Irregular waves with a JONSWAP spectrum (Carter, 1982) were generated for a number of significant wave heights in the Deltaflume of Deltares Delft Hydraulics, the Netherlands. This large scale flume (230m long, 5m wide and 7m deep) enables a variety of sediment transport processes to be monitored at field scale.

Experiments were conducted first over a fine-medium-grained sand bed and then over an upper-medium-grained sand bed. Using laser granulometry, the two sediment beds were found to have grain size distributions lognormal in form, with the fine-medium-grained bed having $D_{10} = 161\mu$m, $D_{50} = 258\mu$m and $D_{90} = 408\mu$m and the upper-medium-grained bed having $D_{10} = 243\mu$m, $D_{50} = 375\mu$m and $D_{90} = 577\mu$m. In each case, a 0.7m deep sediment bed was laid down in the centre of the flume in a 30m long region spanning the width of the flume. A series of experiments were performed over each sand bed. For both the fine-medium-grained and upper-medium-grained experiment sets, the sand bed was initially a horizontal plane bed (Bell and Williams, 2002) and was not flattened between experiments such that each experiment inherited the bed morphology formed during the previous experiment. Each experiment differed only by the significant wave height, H_s, of the surface wave forcing, such that over the course of the experiments H_s varied between $0.2 - 1.9$m. In total, 16 experiments were conducted over the fine-medium-grained sand bed which are referred to here as F01, F02, ..., F16, and 17 experiments were conducted over the upper-medium-grained sand bed which are referred to here as M01, M02, ..., M17. The peak spectral period was held at a constant 6.1s during all the experiments.

Figure 5.2 is a schematic of the instruments deployed on a frame aligned to one side of the flume on the sandy bed. In this study, acoustic data from two Nortek Acoustic Doppler Velocimeters, ADV-1 and ADV-2, an Acoustic Ripple Profiler, ARP, a Sector Scanning Sonar, SSS, and an Acoustic Backscatter System, ABS, were examined to respectively study the water velocities, bedform cross-sections, plan-form bedform features and suspended sediments. A pumped sampling system (Bosman et al., 1987) was mounted on the instrument frame and samples of the suspended sediment laden water were taken during a number of experiments and were used here to provide time average suspended particle size and concentration. The horizontal (along-shore) and vertical positioning of the instruments relative to the side of the

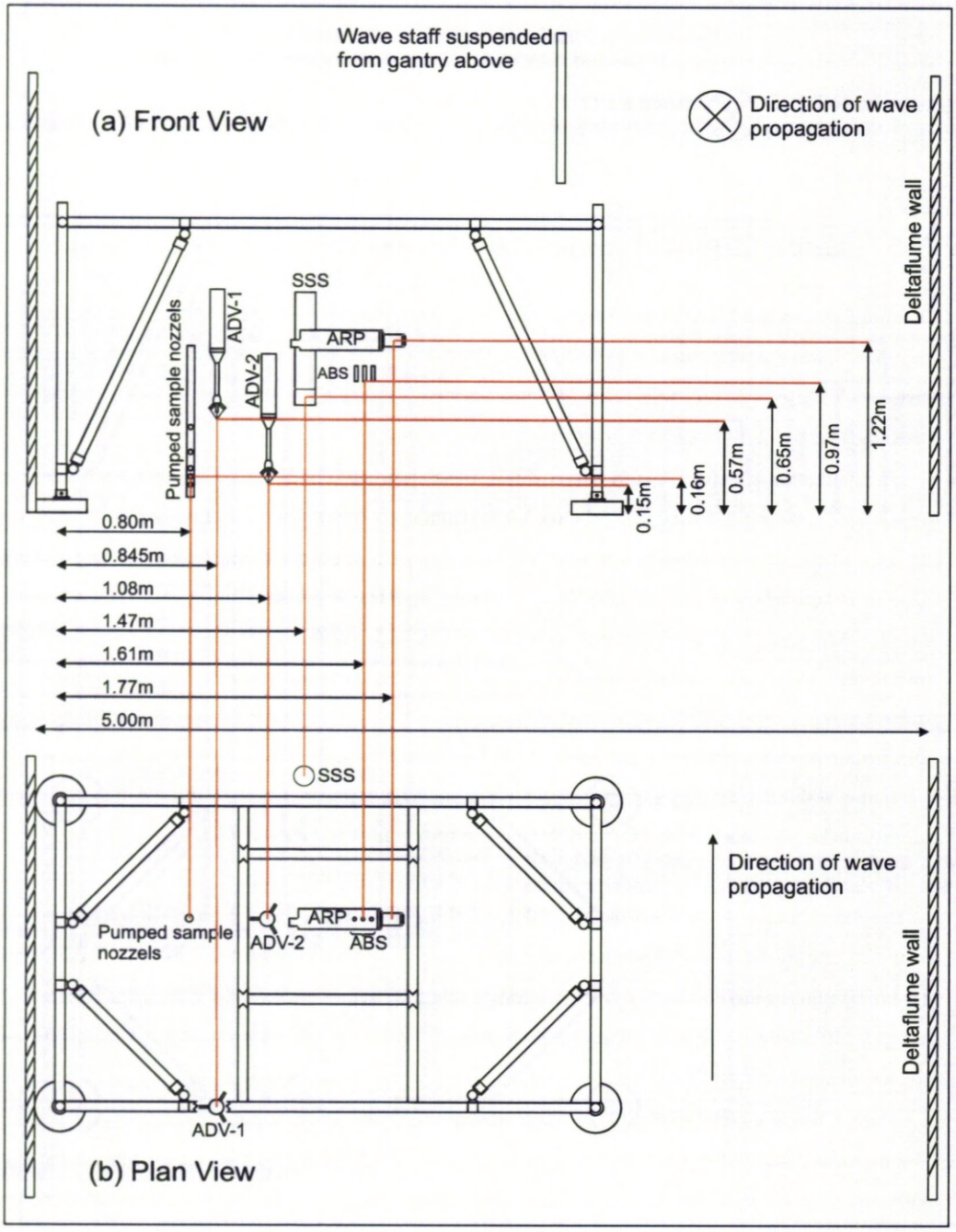

Figure 5.2: Schematic of the instrument frame deployed in the Deltaflume with the locations of the Acoustic Ripple Profiler (ARP), Acoustic Backscatter System (ABS), Acoustic Doppler Velocimeters (ADV-1 and ADV-2), Sector Scanning Sonar (SSS) and Pumped sampling nozzles indicated.

instrument frame closest to the wall of the Deltaflume and the surface of the undisturbed sandy bed are respectively indicated in Figure 5.2. During the course of the experiments the local level of the sand bed varied due to ripple formation and the feet of the instrument frame settling into the sand. Thus, the vertical distances between the instruments and the sandy bed varied over the experimental period. The SSS operated at 1.2MHz mechanically scanning through 400 angular steps during each revolution taking approximately 60s (Williams et al., 2004) and was positioned at the onshore end of the instrument frame. The ARP operated at 2MHz scanning a 4m transect of the bed approximately every 63 seconds, at centimetre horizontal resolution and sub-centimetre vertical resolution providing a 2D profile of the bed, and how it changed with time. The 16Hz time-series obtained from the ADVs consisted of 3 orthogonal components of flow: horizontal along-flume (cross-shore), horizontal across-flume (along-shore) and vertical. ADV-1 and ADV-2 were mounted on the frame such that their measuring volumes were respectively 0.57m and 0.145m above the base of the instrument frame, measuring respectively the free-stream and near bed water velocities. The ABS comprised 3 transducers aligned perpendicular to the flow (along-shore), operating at 1, 2 and 4MHz, and these monitored the SSC above the bed at 1cm vertical resolution. The ABS collected backscatter profiles at 128Hz at each frequency, which were each subsequently block averaged in order to improve the statistical reliability of the results to produce backscatter profiles at 4Hz. The pumped samples were dry-weighed yielding time average concentration measurements at five heights above the bed. A correction factor of 1.4 was applied to the pumped sampled sediment concentrations on the basis of the findings of Bosman et al. (1987). Subsequently, these dried pumped samples were analysed using laser diffraction to obtain the distribution of grain sizes. The ARP, ABS and ADV-2 were collocated on an along-shore line (perpendicular to the flow) ensuring that they were approximately at the same location on a 2D ripple cross-section. Finally, the elevation of the water surface was monitored by a wave staff mounted on a gantry above the flume. Further details of the Deltaflume, the 2001 experimental setup and the instruments deployed can be found in Williams et al. (2003, 2004, 2005) and Williams and Bell (2006).

In the present study, data from four Deltaflume experiments are examined. The first, F08, was selected on the grounds that vortex ripples were not present and the bed approximated to an upper-stage plane bed above which no rippled bed sediment dynamics occurred. During experiments M04, M05 and M06, steep sided ripples, the dimensions of which conform to descriptions of vortex ripples, were present. During these three experiments the ABS was above a ripple crest, and these measurement periods are referred to in the present study as 'the measurement bursts'. To summarise, data from F08 and M04 – M06 enabled flat bed and rippled bed sediment dynamics to be studied respectively under irregular waves. The profiles of SSC were phase locked to the ADV velocities. Thus, working in the phase domain, ensemble averages over many wave cycles were computed, enabling the underlying intra-wave structure of the SSC above plane and rippled beds under irregular waves to be studied. Whether this

Exp.	H_s (m)	T_p (s)	h (m)	k (m^{-1})	U_s (m/s)	d_s (m)	$f_{2.5}$	$\theta_{2.5}$	d_s/D_{50}
F08	1.45	6.11	3.99	0.18	0.98	1.91	0.0053	0.61	7388
M04	0.64	6.11	4.01	0.18	0.43	0.84	0.0099	0.15	2230
M05	0.83	6.11	4.01	0.18	0.56	1.09	0.0087	0.22	2904
M06	1.05	6.11	3.97	0.18	0.71	1.38	0.0077	0.32	3682

Table 5.1: Temporally averaged experimental parameters for the Deltaflume experiments.

intra-wave structure, beneath irregular waves, displays the same features in the rippled bed cases to that below regular waves (e.g. Davies and Thorne, 2005) is investigated in the present study.

5.4 Data analysis and results

5.4.1 Irregular wave forcing

The irregular surface waves were generated conforming to JONSWAP spectra (Bell and Williams, 2002) and the elevation was measured at 25Hz by wave staffs suspended above the flume. The significant wave height, H_s, was calculated for each experiment as (e.g. Soulsby, 1997; Wiberg and Sherwood, 2008)

$$H_s = 4\sqrt{m_0} \tag{5.14}$$

where m_0 is the variance of the water surface elevation. The peak spectral period, T_p, for each experiment was taken as the inverse of the frequency at which the power spectral density of the water surface elevations peaked. Table 5.1 lists these calculated values of H_s and T_p for each experiment. The dispersion equation was solved using average water depths, h, obtained from a pressure sensor present in the Deltaflume and T_p. Table 5.1 lists the water depths and resulting wave numbers, k, together with predictions of the significant velocity amplitude, U_s, and orbital excursion diameter, d_s, based on linear wave theory:

$$U_s = \frac{\pi\, H_s}{T_p \sinh(kh)} \tag{5.15}$$

$$d_s = U_s T_p / \pi. \tag{5.16}$$

These U_s and d_s values were used in place of U_0 and d_0 in equations (5.2) and (5.3) to calculate $\theta_{2.5}$ and $f_{2.5}$ for each experiment, and the results are included in Table 5.1. The spectra of the water surface elevation were examined and compared with theoretical JONSWAP spectra (Carter, 1982; Podgorski et al., 2000) based on the observed values of H_s and T_p. Figure 5.3 presents the theoretical and observed wave spectra for each experiment, and shows that the theoretical spectral compare well with the data in both amplitude and width.

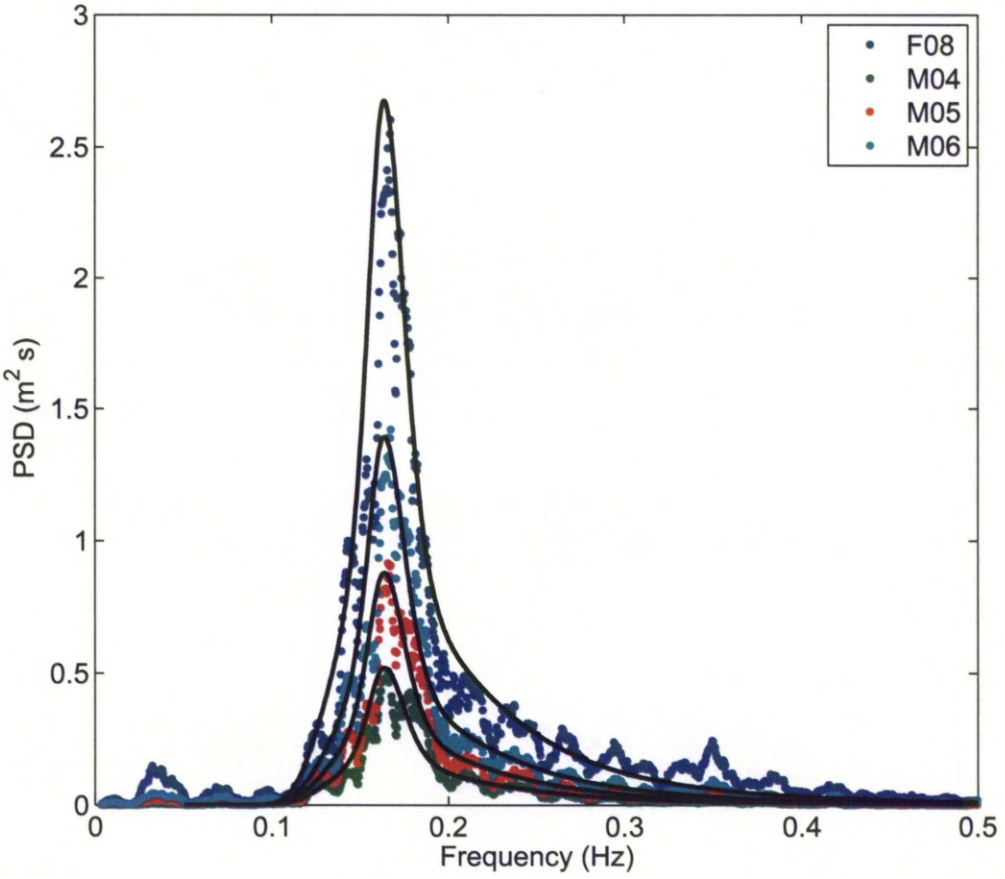

Figure 5.3: The power spectral density (PSD) of the surface elevation recoded by the wave staff during the four Deltaflume experiments with a 21 point running average applied and the theoretical JONSWAP spectra (black lines) with measured H_s and T_p as inputs and a peak enhancement factor of $\gamma = 3.3$.

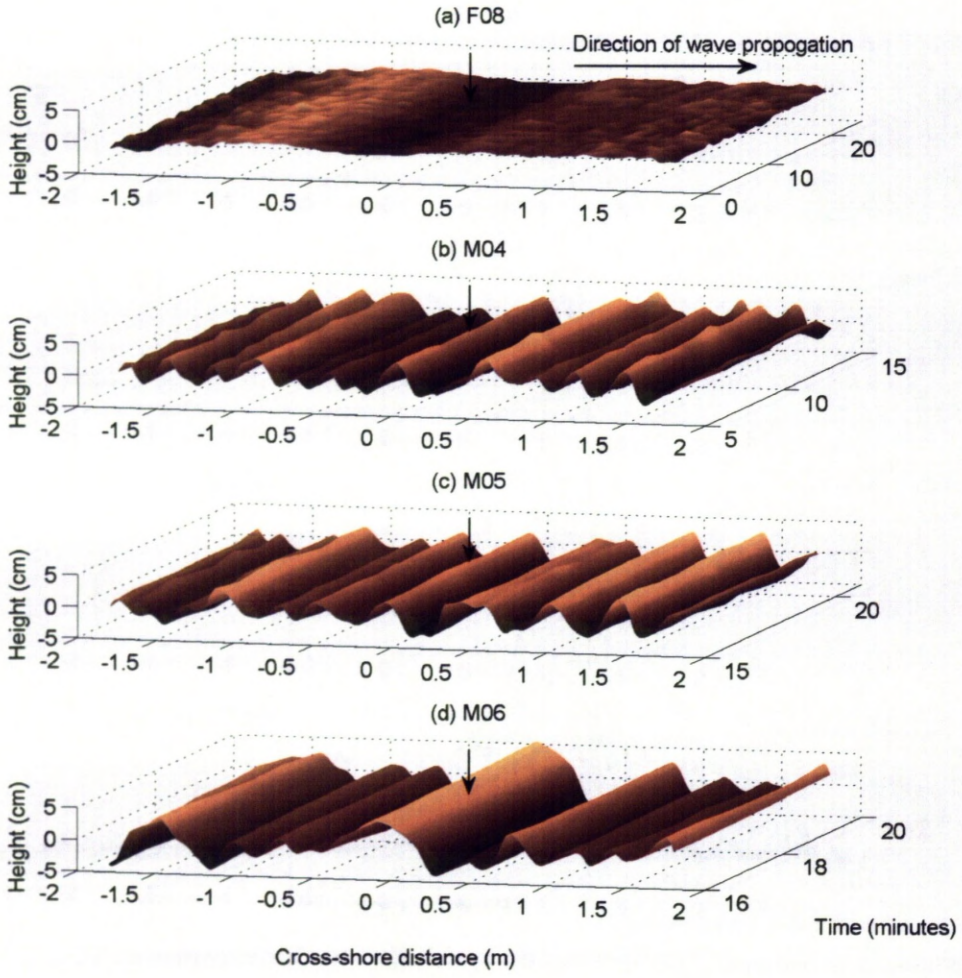

Figure 5.4: Bed profiles obtained from the acoustic ripple profiler (ARP) during (a) plane bed and (b – d) rippled bed Deltaflume experiments. The measurement bursts considered during the rippled bed experiments were chosen on the grounds that a crest of a ripple was below the acoustic backscatter systems (ABS) situated above the origin of the horizontal (cross-shore) axis, indicated by the arrows in the figures.

Spatially and temporally averaged ripple dimensions						
Exp.	λ (m)	$\sigma(\lambda)$ (m)	η (m)	$\sigma(\eta)$ (m)	η/λ	$\sigma(\eta/\lambda)$
M04	0.25	0.02	0.0254	0.0018	0.09	0.01
M05	0.23	0.01	0.0256	0.0015	0.10	0.00
M06	0.33	0.02	0.0331	0.0029	0.09	0.01
Temporally averaged dimensions of ripple below ABS						
Exp.	λ_0 (m)	$\sigma(\lambda_0)$ (m)	η_0 (m)	$\sigma(\eta_0)$ (m)	η_0/λ_0	$\sigma(\eta_0/\lambda_0)$
M04	0.33	0.01	0.0468	0.0032	0.14	0.01
M05	0.34	0.01	0.0462	0.0025	0.13	0.01
M06	0.73	0.01	0.0770	0.0080	0.11	0.01

Table 5.2: Mean-average cross-sectional dimensions of the ripples along the whole ARP transect (λ, η and η/λ) and those individual ripples in line with the ABS (λ_0, η_0 and λ_0/η_0) and their standard deviations (σ) for each of the rippled bed bursts considered.

5.4.2 Bedforms

The bedforms were observed using an Acoustic Ripple Profiler (ARP) and a Sector Scanning Sonar (SSS). The ARP time-series were examined and, in the case of the rippled bed experiment, temporal regions where the ripples were in a steady state and the ARP was consistently over a ripple crest were identified. These temporal regions defined the burst for each rippled bed experiment during which the data were examined. Similarly, for the plane bed experiment (F08) a burst was chosen on the grounds that the bed was in a steady state throughout. Figure 5.4 shows the temporal variation in these 2D bed profiles during the bursts, which were low-pass filtered with a Gaussian filtering window to remove high frequency spatial fluctuations. Figure 5.4(a), F08, for the fine-medium-grained bed shows the remnants of a rippled bed which was washed out to form a long wavelength bedform, similar to those observed by Hanes et al. (2001). This washed out bed approximates, for the purposes here, to an upper-stage plane bed above which no rippled bed sediment dynamics were expected to occur. Equation (5.5) was used to calculate the equivalent roughness due to a moving sand layer, and this yielded a relative roughness of $d_s/2k_s = 28.97$. This $d_s/2k_s$ value and the Shields parameter for F08 listed in Table 5.1 place F08 within the washed-out ripples regime in Figure 5.1. Figures 5.4(b-d) show that during the upper-medium-grained experiments rippled beds were formed. A turning point analysis was performed to extract the spatial distribution of ripple wavelengths, heights and steepness for each profile. The wavelength of a ripple was taken as the distance between two troughs surrounding a crest, the height of this ripple was taken as the mean average crest to trough height difference either side of the ripple crest and the steepness was taken as the height to wavelength ratio. Table 5.2 lists the spatial and temporal mean average ripple wavelengths, λ, heights, η, and steepness, η/λ and their associated standard deviations, σ, for the rippled bed experiments. The temporal mean average dimensions of the ripple directly below the ARP transducer during each experiment, λ_0, η_0 and $\eta_0\lambda_0$, were also calculated and the results are shown in Table 5.2.

Figure 5.5 shows the temporal mean cross-section 0.6m either side (on a cross-shore line)

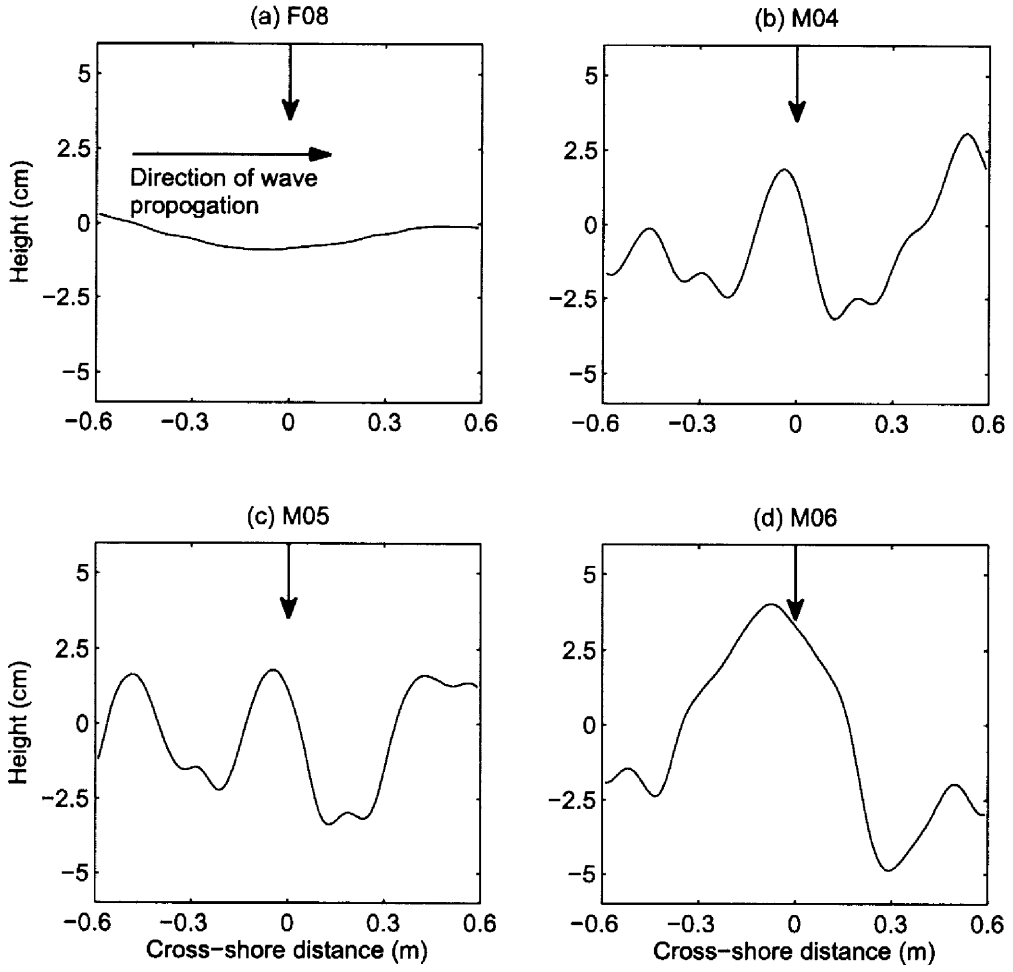

Figure 5.5: Time-mean average of the ARP bed profiles under the ABS during (a) plane bed and (b – d) rippled bed experiments when the ABS was approximately above a ripple crest. The ARP, ABS and ADV-2 were nominally positioned above the origin of the horizontal cross-shore axis, indicated by the arrows in the figures.

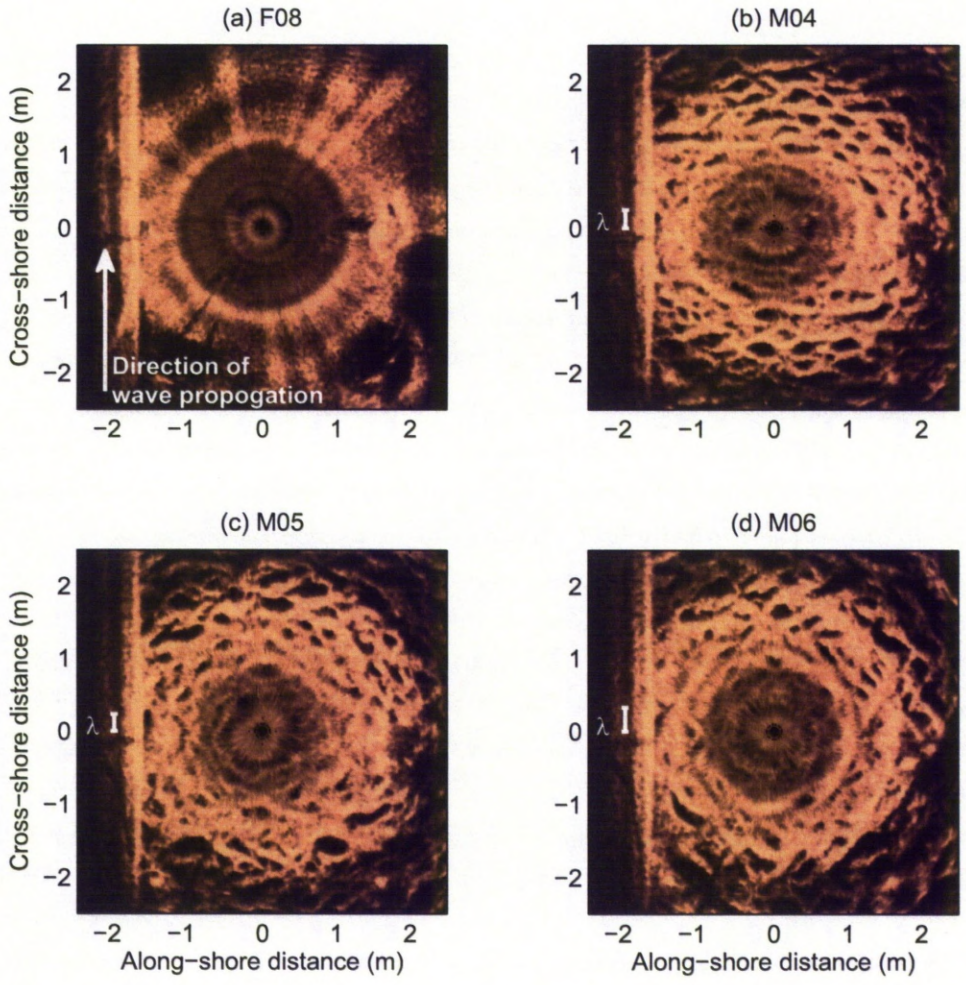

Figure 5.6: Sector Scanning Sonar (SSS) results from (a) plane bed and (b – d) rippled bed Deltaflume experiments. In the case of the rippled bed experiments (b – d) the typical ripple wavelengths, λ, determined by analysis of the ARP data are indicated.

of the ARP, ABS and ADV-2 for each of the four experiments. Figure 5.5 clearly shows that during the rippled bed bursts the acoustic devices were approximately above a ripple crest. The spatial and temporal average ripple steepness in the rippled bed cases (η/λ, Table 5.2) are close to 0.1, above which vortex shedding starts to occur (Davies and Thorne, 2005). The steepness of the ripples directly below the acoustic instrumentation (η_0/λ_0, Table 5.2) were above this threshold, suggesting that it was likely for vortex shedding to have occurred below the ABS transducers.

In addition to the ARP cross-sections, the SSS data were examined in order to reveal the plan-form geometry of the rippled beds. The SSS data were rectified from polar coordinates to square grid and a slant range correction was applied (Bell and Williams, 2002). Figure 5.6 shows the SSS results in the form of two-dimensional 5x5m images of the bed produced just prior to the measurement bursts considered here. The temporally and spatially average ripple wave-

lengths obtained from the ARP (Table 5.2) during M04 – M06 are indicated in Figures 5.6(b-d) showing the ripple crest lengths to be typically longer than their wavelengths. However, the ripple crests are sinuous, especially during M05 and M06. The grain roughness Shields parameters ($\theta_{2.5}$) for M04, M05 and M06 listed in Table 5.1 suggest (using the parameterisations in Figure 5.1) the bedforms present were 2D during M04 and M05 and dominantly 2D with 3D ripples emerging during M06. Such a classification is in agreement with the results from the ARP (Figures 5.4 and 5.5) and SSS (Figure 5.6). Using the dimensions of the ripples below the ABS (η_0 and η_0/λ_0, Table 5.2) and equation (5.6), $d_s/2k_s$ was calculated to be 5.75, 7.30 and 6.85 during experiments M04, M05 and M06 respectively. These values are broadly in agreement with the dominantly 2D classification using the $\theta_{2.5}$ values, although suggestive that both M05 and M06 should have 3D ripples emerging, which broadly agrees with the SSS images (Figure 5.6). Using instead the dimensions of the spatially averaged ripples (η and η/λ, Table 5.2), $d_s/2k_s$ was found to be 10.84, 11.58 and 12.15 during experiments M04, M05 and M06 respectively, which moves the classification more into the 3D realm (according to the parameterisations in Figure 5.1). It is concluded here therefore, that during M04 the rippled bed was dominantly 2D in form. During M05 however, 3D ripples started to emerge and the plan-form geometry of the bed is thus classified as quasi-2D (Pedocchi and Garcia, 2009). During M06 the 3D ripples continued to emerge and became more dominant features on the bed, although there remained some remnants of the quasi-2D ripples. From these classifications of the plan-form geometry, it was concluded that the ripples beneath the ARP were sufficiently long-crested for them to be classified as locally two dimensional for the present analysis.

5.4.3 Suspended sediments

The root mean square, RMS, average voltage backscattered from the suspended sediments measured by the ABS transceivers can be expressed as (Thorne and Hanes, 2002)

$$V_{rms} = \frac{< f >}{\sqrt{< a_s > \rho_s}} \frac{K_t}{\psi r} M^{1/2} \mathrm{e}^{-2r(\alpha_w + \alpha_s)} \tag{5.17a}$$

where

$$\alpha_s = \frac{1}{r} \int_0^r \frac{3 < \chi >}{4 < a_s > \rho_s} M(r) dr \tag{5.17b}$$

is the attenuation due to sediment. In equations (5.17a) and (5.17b) ψ accounts for the departure from spherical spreading in the near field of the transducers (Downing et al., 1995), r is the range from the transducers, M is the mass concentration of the sediment, K_t is the ABS system constant, $< a_s >$ is the mean radius of the suspended sediments and α_w is the attenuation coefficient due to the water absorption. The brackets, $< >$, indicate an average taken over the particle number size distribution of the suspended sediment. The functions f and χ describe the intrinsic backscattering and attenuation characteristics for narrowly sieved sediments (Moate and Thorne, 2009), expressions for which were chosen on the grounds that they represent natural sands (Thorne and Meral, 2008). Solving equation (5.17) for the sediment

concentration (M) at each range bin from the transceivers is non-trivial, as α_s is a function of M. Thus an inversion methodology is required.

Grain size distributions

The type and width of the suspended sediment grain size distribution affects the backscattering and attenuation characteristics of the sediments, and can therefore strongly influence the acoustic ABS inversion (Moate and Thorne, 2009). It is therefore important to represent the ensemble scattering characterises of the suspension by averaging f and χ over the particle number size distribution present in suspension, to obtain $< f >$ and $< \chi >$. In this study, the near bed SSC is of primary importance and within the bottom 0.25m of the bed the suspended median grain diameter, D_{s50}, of the pumped samples collected was nominally uniform with height above the bed. Hence the mass size distributions from the lower three pumped sampling nozzles (typically within 0.25m of the bed) were combined for each experiment. These mass size distributions of the pumped samples were found to be lognormal in form. Figure 5.7 shows the cumulative size distribution of the mass concentration (open circles) of the combined pumped sampled results for each experiment. Fitted to these data are lognormal cumulative distribution functions with their D_{s50} values indicated. To obtain $< f >$ and $< \chi >$ for the acoustic inversion, the mass size distributions were converted to particle number size distributions, the cumulative distribution functions of which are also shown in Figure 5.7 with their arithmetic means, $< a_s >$, indicated. These lognormal size distributions (Figure 5.7) were characterised by their standard deviation to mean ratios, $\sigma(a_s)/ < a_s >$, of 0.42, 0.64, 0.39 and 0.35 for experiments F08, M04, M05 and M06 respectively. Thus, the ensemble backscattering and attenuation characteristics of the suspended sediment, $< f >$ and $< \chi >$, were calculated by averaging f and χ over the lognormal size distributions of the suspended sediment described by the $\sigma(a_s)/ < a_s >$ values.

Acoustic inversion

Initial explicit inversions (Lee and Hanes, 1995; Thorne and Hanes, 2002) for sediment mass concentration were performed on the RMS time average backscattered voltage from each transceiver. The RMS time averages were calculated over the time periods during which the pumped samples were taken and the pumped sampled (time average) sediment concentrations were used to constrain the explicit inversions. To further aid the inversions, the height constant grain size profiles from the pumped samples were used. The grain sizes for each experiment were those indicated in Figure 5.7. In order to gain instantaneous concentration profiles, implicit inversions (Thorne and Hanes, 2002), for sediment mass concentration, were performed on the 4Hz ABS backscatter time-series. The ABS system constant, K_t, required in the implicit inversions, for each of the three ABS transceivers was determined from the explicit inversion results. Thus, the implicit ABS inversions were linked to the pumped sampled concentrations from the four experiments.

The implicit inversions resulted in time-series of SSC profiles at 4Hz for each frequency.

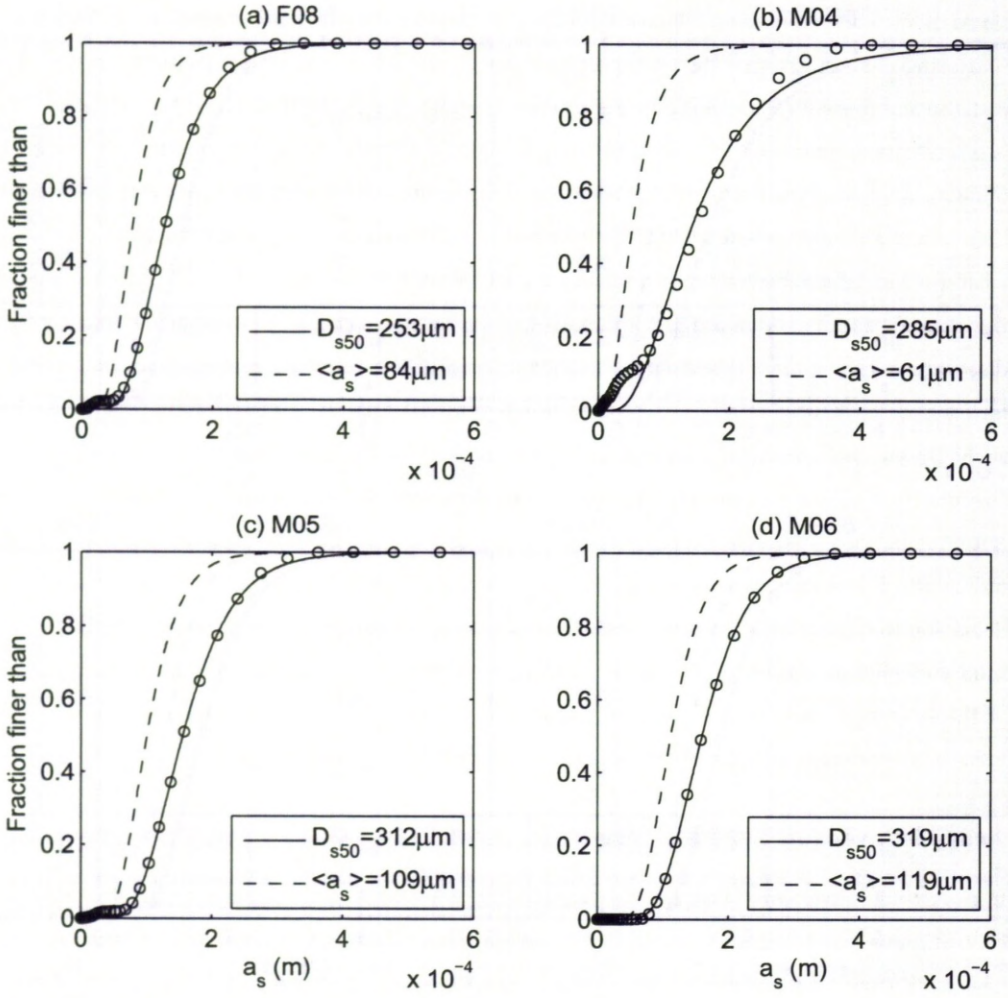

Figure 5.7: Lognormal mass concentration (−) and number of particles (− − −) grain size cumulative distributions fitted to the results from the grain size analysis of the pumped samples taken during the (a) plane bed and (b–d) rippled bed Deltaflume experiments. The median grain diameter, D_{s50}, of the mass distributions and the mean grain radius, $< a_s >$, of the number of particles distributions are indicated in each case.

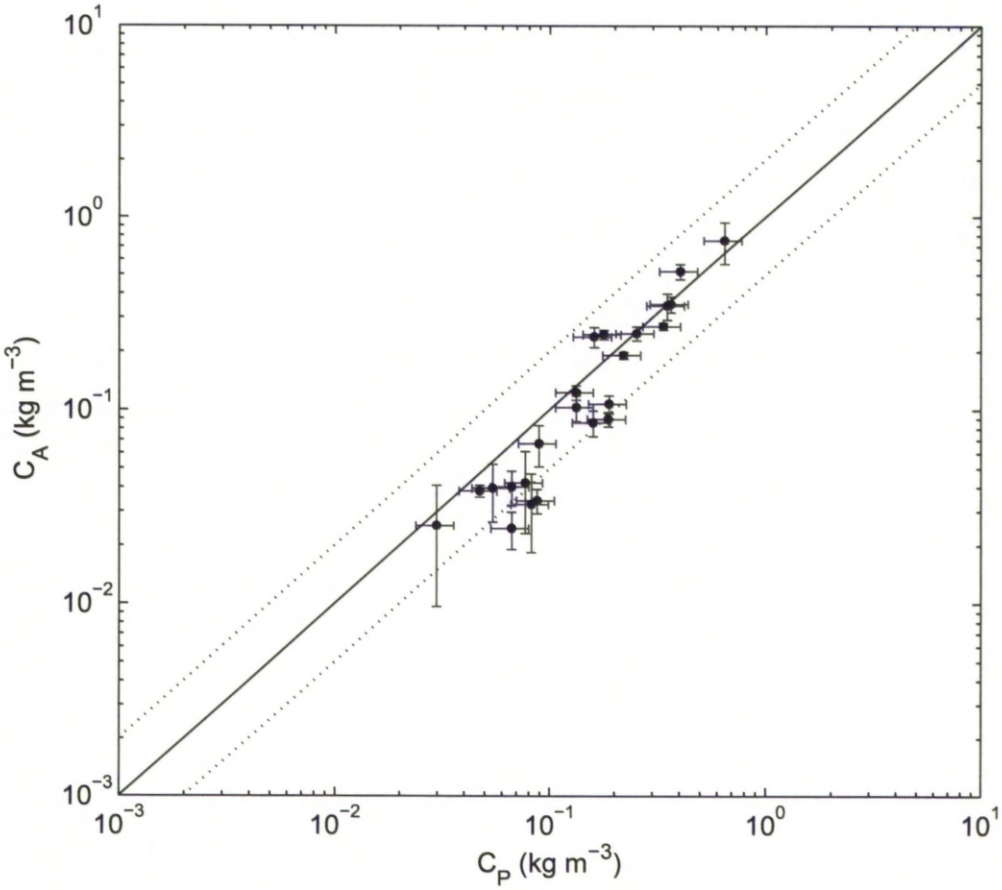

Figure 5.8: Regression plot of the mean time average ABS, C_A, and pumped sampled, C_P, suspended sediment concentration with the lines corresponding to $C_A = C_P$ $(-)$ and $C_A = 2C_P$ and $C_A = 0.5C_P$ $(\cdots)$ shown. The error bars show $\pm$ the standard error of the mean of the three ABS frequencies for C_A and $\pm 20\%$ for C_P.

Mean time averages of these results were calculated for each experiment, and at each frequency, in order to test their validity against the independent pumped sampled measurements. Figure 5.8 shows the time average sediment concentrations from the implicit inversions, C_A, compared with the concentrations obtained from the pumped samples, C_P. There are errors associated with both C_A and C_P. C_A is the mean of the inversion results from the three ABS frequencies and the error bars indicate the associated standard error. The error on C_P indicated is $\pm 20\%$, which is the typical error found by Moate and Thorne (2009). Sediment concentration estimates from the ABS are typically accurate to within a factor of two (Vincent, 2007) and the majority of data in Figure 5.8 falls within this range. A regression on the data in Figure 5.8 gave $C_A = (1.18 \pm 0.14)C_P - (0.05 \pm 0.03)$ with $R^2 = 0.93$. This regression and Figure 5.8 both confirm the veracity of the ABS measurements of suspended sediment concentration.

Time average SSC profiles

Figure 5.9 shows the time average SSC profiles, $C(z)$, obtained from the calibrated implicit inversions. The three profiles obtained above the rippled beds (M04 – M06) are similar in form and generally increase in magnitude with the significant wave height. All three rippled bed SSC profiles in Figure 5.9 exhibit a near exponential decay, of similar gradient, within the bottom 15cm. An exponential function, of the form given by equation (5.8), was fitted to the concentration measurements within 0.02 – 0.12m above the bed level. In the rippled bed cases, the resulting exponential decay length scales, L, were between 0.06 – 0.07m and the reference concentrations, C_0, obtained by extrapolating to the bed level, were between 1.5 – 2.2 kg m^{-3}. These observations of C_0 are somewhat below predictions made using the equation (5.10) of Nielsen (1986), but are broadly within the scatter of data used by Nielsen (1986).

Predictions were made of the SSC profiles using equation (5.8) with L predicted by the formula of Nielsen (1992) (equation (5.11)) and C_0 values from the data. In evaluating equation (5.11) the hydrodynamic (U_s) and bed (η_0) conditions in Tables 1 and 2 were used along with the formula of Soulsby (1997) (equation (5.12)) for the sediment settling velocities. In order to include the effect that the grain size distribution had on the SSC profiles, the settling velocity distribution was taken into account using the method outlined by Davies and Thorne (2002). The size distributions of the suspended sediment (Figure 5.7) were divided into five volumetrically equal fractions and the SSC profile for each of these fractions calculated. For all but the finest fraction in each case $U_s/w_s < 18$ and in equation (5.11) L was a function of U_s. The predictions of the SSC profiles above the rippled beds included in Figure 5.9 are the mean averages of the profiles calculated for each of the five size fractions. There is a slight departure from the exponential decay of equation (5.8) due to the inclusion of the settling velocity distribution. The characteristic decay length scale of these predicted profiles differed to those observed by up to 40%. One reason for the disagreement between the prediction and observation of C_0 and L is the variation in velocity amplitudes from wave-to-wave, i.e. U_s may not be a good representative velocity for the irregular wave field. This variation in U_0 from

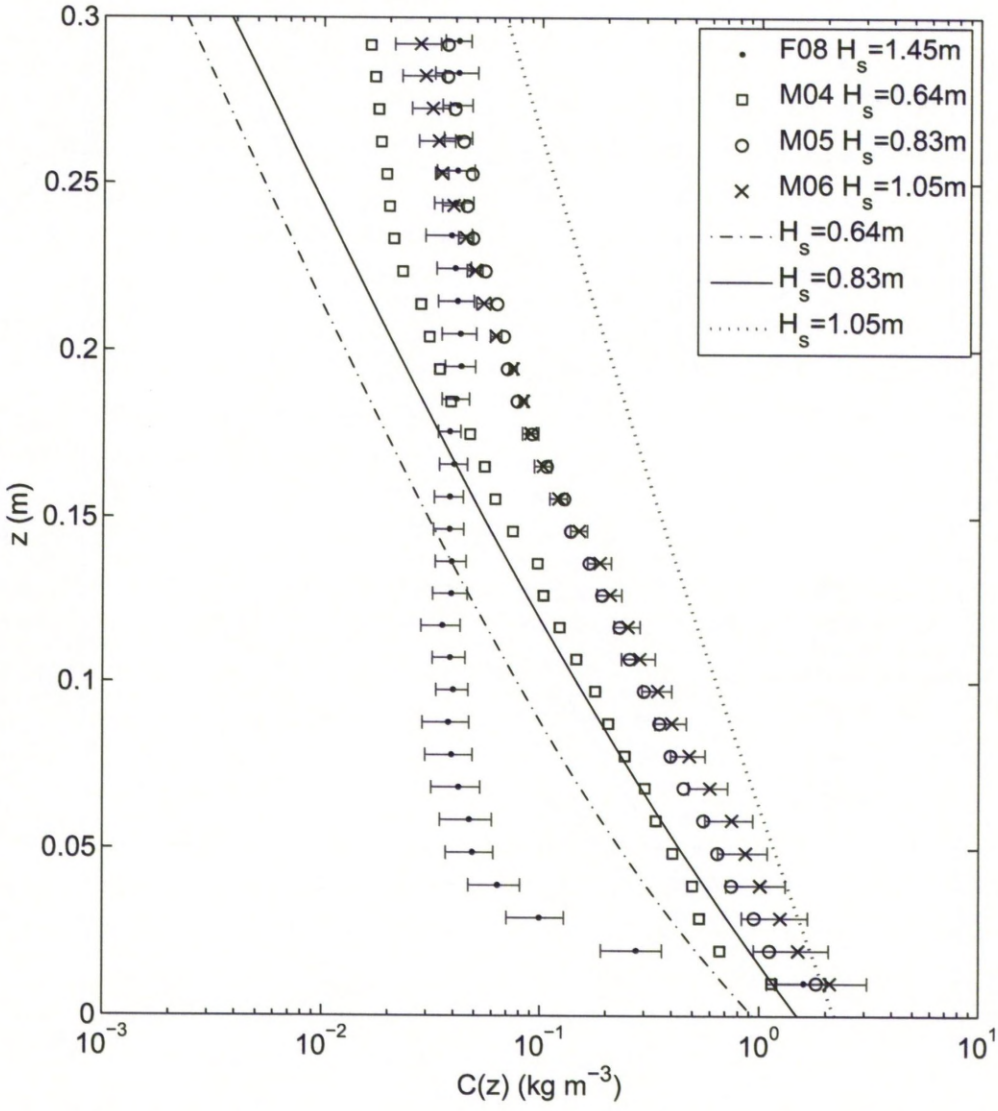

Figure 5.9: Suspended sediment concentration profiles, $C(z)$, for each experiment, mean time averaged over 17 minutes during which the pumped samples were collected, and mean averaged over the three ABS frequencies. The standard error of the mean of the three ABS frequencies is shown as error bars for the measurements taken during F08 and M06 in order to indicate typical measurement uncertainty through the profile. The empirical SSC profile of Nielsen (1986) is shown for each rippled bed experiment, M04 ($-\cdot-$), M05 ($-$) and M06 ($\cdots$).

wave-to-wave influences the sediment entrainment process, which is the investigative focus of this paper. Whether the entrainment of sediment was dominated by the same process during the whole time period that the SSC profiles in Figure 5.9 were averaged over is an important consideration.

5.4.4 Intra-wave water velocities

The bed level during each experiment obtained from the ARP and ABS records were in agreement and indicated that the sampling volumes of ADV-1 and ADV-2 were approximately 0.5 and 0.1m respectively above the bed during the course of the rippled bed experiments (M04 – M06). During the fine-medium-grained plane bed experiment, F08, the instrument frame settled into the bed such that the sampling volume of ADV-1 was 0.35m above the bed and that of ADV-2 was below the bed level. Hence no data from ADV-2 gathered during F08 was used. For the rippled bed experiments, the near bed velocities from ADV-2 were used to identify the wave cycles in the phase-locking analysis of the SSC time-series (Section 5.4.5). In the case of F08, where the sampling volume of ADV-2 was below bed level, velocity data from ADV-1 were used.

Each time-series component (obtained from the ADVs at 16Hz) was despiked using a Phase-Space Thresholding Method (Goring and Nikora, 2002) with detected spikes replaced by linear interpolations using the surrounding data points and run for 10 iterations. The velocity components were rotated to correct for any misalignment of the instruments with the main flow directions. This was done by considering each combination of two velocity components in turn and aligning one of the components with the principle axis of variation (Emery and Thompson, 1997). The result was a fully rotated system of 3 orthogonal velocity components. Here, positive water particle velocities corresponding to the direction of wave propagation are referred to as onshore velocities and negative water particle velocities towards the wave generator as offshore velocities. Following this convention the horizontal along-flume velocity component is referred to here as the cross-shore component.

In order to determine the timing of each wave half cycle accurately, turbulent fluctuations were removed from the cross-shore ADV velocity time-series' by applying a rectangular low-pass filter and a zero-crossing analysis was used to identify the times of flow reversal. These filtered time-series were compared with the non-filtered time-series confirming that no significant changes in amplitude and phase of the velocities occurred during the analysis. The zero-up crossings were defined as the start of each wave cycle, and the orbital velocity amplitudes and orbital diameters corresponding to each wave half cycle were sought. The velocity amplitudes were taken as the maximum velocity magnitude between successive zero-crossings, and the onshore and offshore velocity amplitudes, U_{on} and U_{off} respectively, were distinguished from one another. Figure 5.10(a) shows approximately 30 seconds of the filtered ADV-2 velocity time-series from M04 with the U_{on} and U_{off} values for the second wave cycle indicated. The orbital diameters were calculated by integrating the velocity time-series between successive zero-

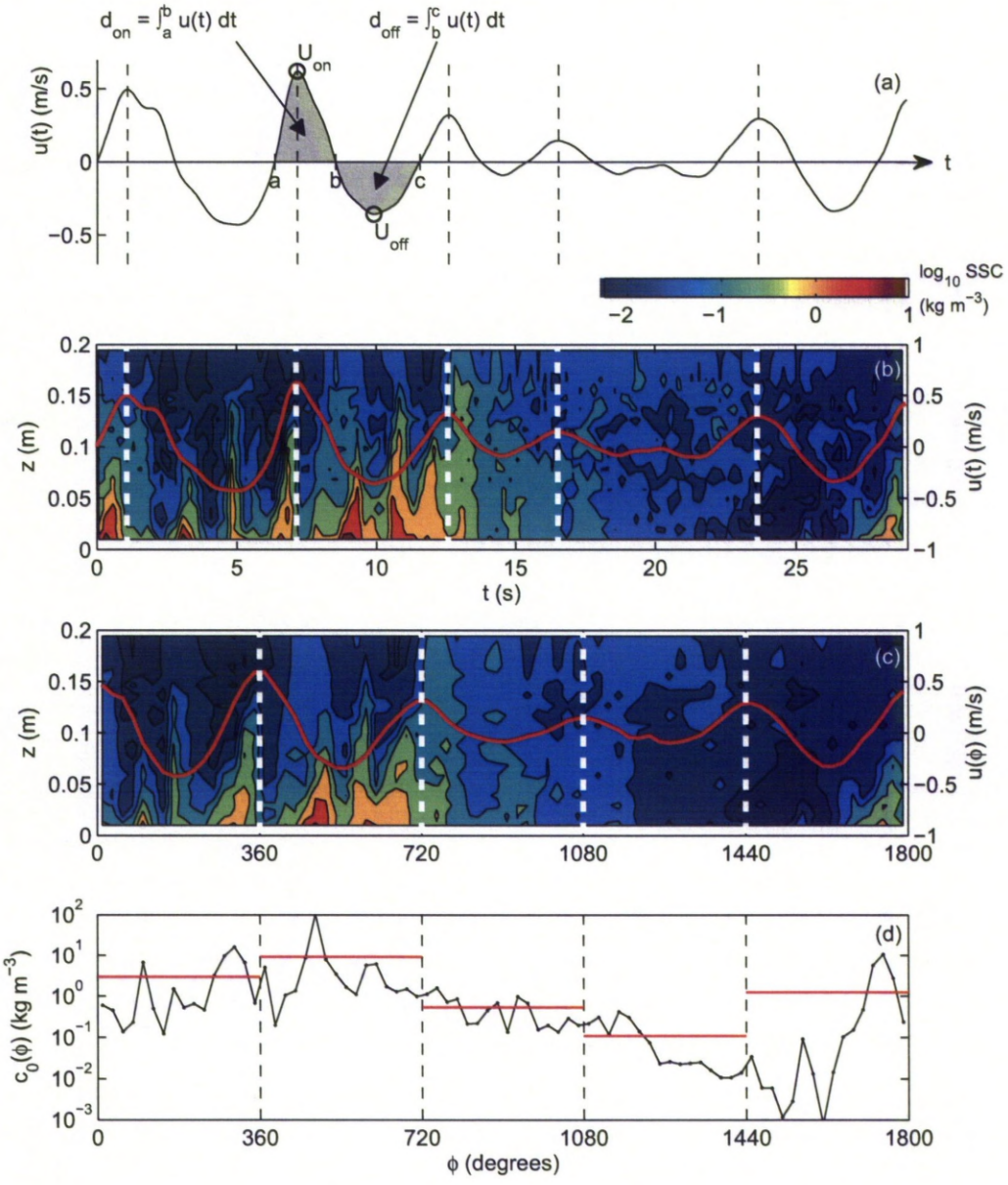

Figure 5.10: Five wave cycles ($\sim$ 30 s) from M04 of (a) filtered ADV-2 velocity time-series, (b) suspended sediment concentration (SSC) in the time, t, domain, (c) SSC in the phase, ϕ, domain and (d) instantaneous reference concentration, $c_0(\phi)$, as a function of ϕ. Each wave cycle is indicated by the vertical dashed lines. In (a) the onshore and offshore orbital amplitudes, U_{on} and U_{off} respectively, and onshore and offshore orbital diameters, d_{on} and d_{off} respectively, are defined for the second wave cycle. In (b) and (c) the orbital ADV velocity, u, from (a) is overlain. In (d) the cycle mean reference concentration, $\overline{c_0(\phi)}$, for each wave cycle is shown in red.

crossings, and the onshore and offshore values, d_{on} and d_{off} respectively, were distinguished from one another. For example, in Figure 5.10(a) a zero-up crossing occurs at time a, the subsequent zero-down crossing occurs at time b and the orbital diameter corresponding to this onshore wave half cycle can be calculated by

$$d_{on} = \int_a^b u(t)dt \tag{5.18}$$

where $u(t)$ is the time-series of velocity, with $u(t) > 0$ in the onshore direction. The orbital diameter corresponding to the subsequent offshore wave half cycle is calculated in a similar manner, as indicated in Figure 5.10(a). This approach was taken because the flow was irregular. If the flow was sinusoidal with period T and a velocity amplitude of U_0, i.e. if $u(t)$ was replaced with $U_0 \sin(2\pi t/T)$, then equation (5.18) would be equivalent to the more familiar equation of linear wave theory, $U_0 T/\pi$. Following this zero-crossing analysis, a distribution of onshore and offshore velocity amplitudes (U_{on} and U_{off}) and orbital diameters (d_{on} and d_{off}) were constructed for each experiment.

5.4.5 Phase ensemble averaging the SSC

There is inherent variability in the ABS signal due to the random, Rayleigh distributed, phasing of the acoustic returns (Thorne et al., 1993). This variability in the backscatter signal was reduced significantly by averaging over 32 independent measurements of the acoustic backscatter, thus reducing the backscatter signal from 128Hz to 4Hz. The standard error on such an average is a factor of $\sqrt{32}$ smaller than if no averaging were performed (Thorne and Hanes, 2002).

Small scale sediment transport processes are highly influenced by the turbulent nature of the boundary layer flow over rough beds, hence there is an intrinsic stochastic variability in the SSC field. This is the case under both regular and irregular waves, but in the case of irregular waves there is considerable variance in the near bed turbulence from wave-to-wave (Vincent and Hanes, 2002). In order to observe consistent features in the intra-wave SSC field, ensemble averaging over a number of wave cycle was therefore necessary.

Figure 5.10(b) shows a series of SSC profiles, with the height above the bed, z, ranging from $0 - 20$cm, during five wave cycles (approximately 30 seconds) of M04 in the time domain, with the filtered ADV velocity from Figure 5.10(a) superimposed. Each wave cycle was identified from the zero-crossing and turning point time-series analysis of the filtered ADV velocity, and the wave cycles are distinguished in Figures 5.10(a and b). Each wave cycle was defined to start at the point of maximum velocity in the onshore (positive) direction. Using this definition allowed the sediment dynamics occurring around flow reversal to be clearly observable within the wave cycle. The wave irregularity can be observed in Figures 5.10(a and b), both in terms of the wave amplitude and the wave period. Because the wave period varied from wave-to-wave, it was not possible to simply ensemble average over recurrent time steps equal to the wave period, as has been carried out under regular oscillatory flow (Davies and Thorne, 2005; Van der Werf

et al., 2007). Instead a procedure phase-locking the ABS concentration profiles with the ADV orbital velocities was performed, so that the ensemble averaging could be carried out in the phase domain rather than the time domain. Figure 5.10(c) shows the same series of SSC profiles and ADV velocities as Figure 5.10(b), but in the phase domain, and again the wave cycles – now equally spaced – are indicated. The resolution of the phase domain is 22.5° (16 SSC profiles per wave cycle). Figure 5.10(c) shows five wave cycles of SSC profiles in the phase domain for illustration only. The SSC profile series considered for each experiment were the bursts identified in Section 5.4.2 during which the ABS was over a ripple crest. There were between 50 – 100 wave cycles in the SSC profile series for each rippled bed experiment, depending on the length of measurement burst. Figure 5.10(d) shows the instantaneous reference concentration, $c_0(\phi)$, for five wave cycles and will be discussed later in Section 5.4.6.

Figure 5.11(a) and Figures 5.11(b-d) present the SSC results above the flat bed and the three rippled beds respectively, phase ensemble averaged over the measurement bursts. Figures 5.11(a-d) show the underlying intra-wave variation of the SSC with height above the bed and Figure 5.11(e) shows the corresponding phase ensemble averaged orbital velocity, $< u >$, for each experiment. There is seen to be a clear difference between the structure of the SSC field during the flat bed (Figure 5.11(a)) and rippled bed experiments (Figures 5.11(b-d)). Above the flat bed, the sediment concentration is high in the bottom 2 cm and decays abruptly above this. There is also no significant intra-wave variation in the SSC. Conversely, above the rippled beds the concentration decay rate is more gradational with distance from the bed and there is a clear intra-wave structure present with peaks in the sediment concentration occurring around flow reversal (90° and 270°). The intra-wave structure of the SSC is most similar during experiments M04 (Figure 5.11(b)) and M05 (Figure 5.11(c)) with the peaks in the concentration occurring at the same phase angles and the concentrations throughout the wave cycle being comparable. During M06 (Figure 5.11(d)), the sediment concentration peaks earlier in the wave cycle than during the previous two experiments. In terms of SSC magnitude, at the height of one ripple height above the rippled beds, the concentration peaks are between 1.01 – 1.85 kg m^{-3} around the instances of flow reversal and consistently drop to below 0.34 kg m^{-3} around the instances of maximum velocity.

5.4.6 Bed levels and reference concentrations

The ABS system allows for the accurate identification of the bed level directly below the transducers, knowledge of which is crucial for studying the dynamics of near bed sediment suspensions. Measurement bursts were considered where a ripple crest was below the ABS and the bed levels were constant in time, i.e. when there was no ripple migration or bed evolution. These ABS backscatter time-series were compared across all three frequencies and were found to increase exponentially towards the bed. The bed level was taken at the level of the first measurement significantly larger than the exponential trend. The instantaneous reference concentration as a function of phase, $c_0(\phi)$, where ϕ is the phase angle, was taken at the bed level,

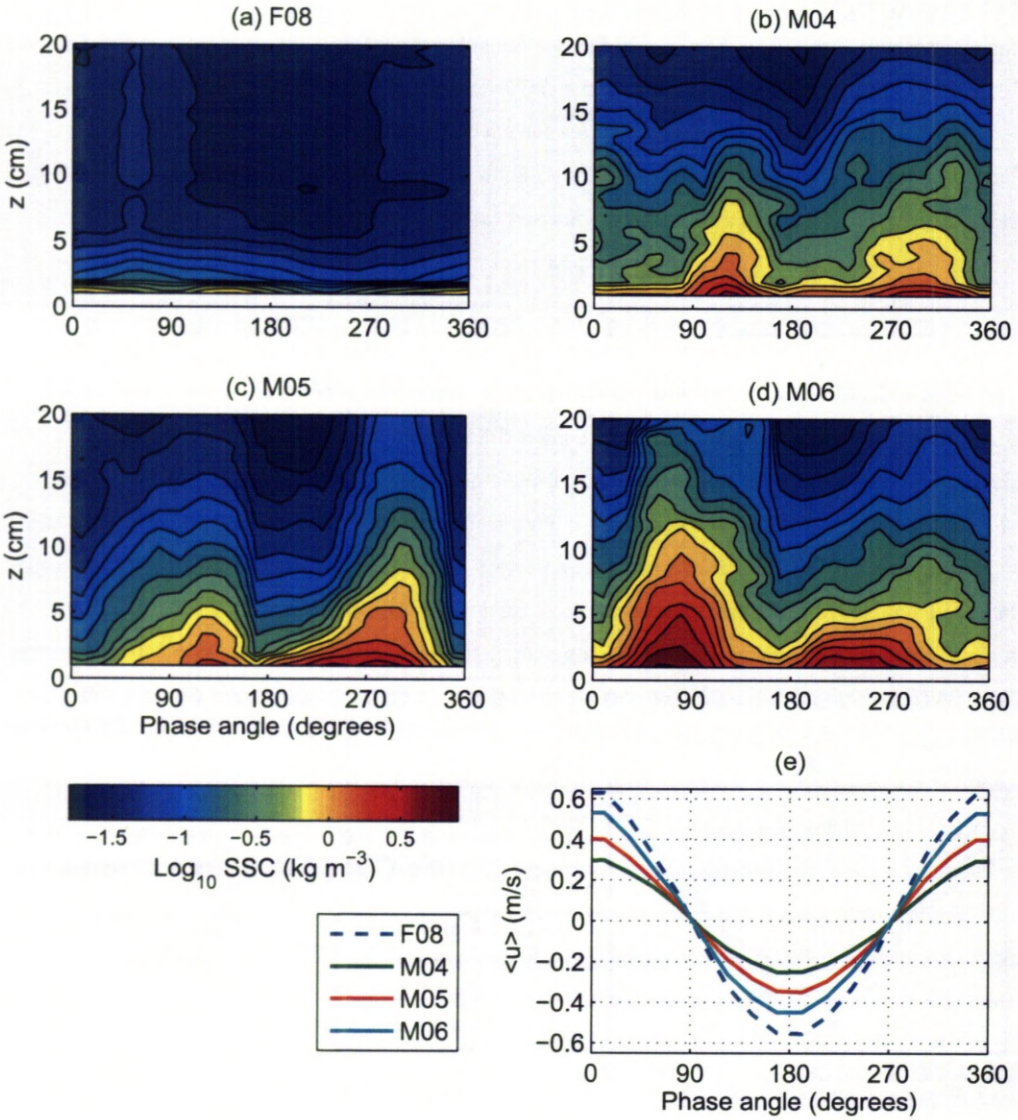

Figure 5.11: Intra-wave variation in the suspended sediment concentration, SSC, with height above the bed, z, phase-locked to the near bed velocities and phase ensemble averaged over the bursts during (a) plane and (b – d) rippled bed conditions. In (e) the ensemble averaged intra-wave near bed velocity, $< u >$, for each experiment is shown. The results shown are the mean concentrations from the 1 and 2 MHz ABS frequencies.

which in the cases of the rippled beds was approximately the ripple crest level. An exponential function, of the form given in equation (5.8), was fitted to the measurements of the SSC within 0.02 – 0.05 m above the bed level, and $c_0(\phi)$ was obtained by extrapolation to the crest. This was done for each concentration profile within the 16 profiles per wave cycle phase-series described in Section 5.4.5. Figure 5.10(d) shows the calculated instantaneous reference concentration as a function of phase ($c_0(\phi)$) for five wave cycles. For each wave cycle, the cycle mean reference concentration, $\overline{c_0(\phi)}$ where the over bar indicates an average over the wave cycle, is indicated. The $\overline{c_0(\phi)}$ values were used to normalise the instantaneous intra-wave $c_0(\phi)$ values within each wave cycle. This normalisation from wave-to-wave within the irregular wave sequence enabled the underlying structure of the intra-wave reference concentration to be studied.

Figure 5.12 shows the phase ensemble averaged normalised intra-wave reference concentrations, $< c_0(\phi)/\overline{c_0(\phi)} >$, for each experiment, where the brackets, $< >$, indicate phase ensemble averaging over 50 – 100 wave cycles and the error bars show the standard error of the ensemble averages. Considering the relative size of peaks in $< c_0(\phi)/\overline{c_0(\phi)} >$ and the associated standard error, during an average wave cycle, the rippled bed cases (Figures 5.12(b-d)) show two distinct peaks occurring around flow reversal (90° and 270°). Conversely, the flat bed case has smaller peaks occurring around peak flow when the shear stress is highest over the plane bed (Figure 5.12(a)). The relative amplitude of the peaks in the rippled bed experiments compare well and the timing of the peaks in experiments M04 and M05 compare well (with peaks occurring 24° (onshore) and 11° (offshore) after flow reversal). The peaks in $< c_0(\phi)/\overline{c_0(\phi)} >$ during M06, on the other hand, preceded flow reversal by 34°.

Reference concentration magnitudes

Net suspended sediment flux calculations crucially depend on the magnitude of the SSC in suspension which in turn depends on the reference concentration (i.e. equation (5.8)). Under irregular waves the instantaneous reference concentration, $c_0(\phi)$, and hence the cycle mean, $\overline{c_0(\phi)}$, varies from wave-to-wave. Thus, the prediction of $\overline{c_0(\phi)}$ under irregular waves is important in the modelling of SSC profiles within wave resolving process models such as the 'research' models studied by Davies et al. (2002).

Here, for irregular waves, an approach similar to the time average analysis used by Nielsen (1986) is adopted for a wave-by-wave analysis. For each wave cycle, the cycle mean ripple modified Shields parameter, $\bar{\theta}_r$, was calculated using equation (5.9) and by taking the wave orbital amplitude and diameter for each wave cycle, U_0 and d_0 respectively, as the mean of the two half cycles, i.e. $U_0 = 0.5(U_{on} + U_{off})$ and $d_0 = 0.5(d_{on} + d_{off})$. Figure 5.13 shows the cycle mean reference concentration, $\overline{c_0(\phi)}$, from each of the three rippled bed experiments (M04 – M06) plotted against $\bar{\theta}_r$ along with the empirical equation of Nielsen (1986), equation (5.10). The $\overline{c_0(\phi)}$ values shown are the mean of the values obtained from the results of the 1 and 2 MHz ABS frequencies and the error bars show the standard error of the mean. The error bars of the $\bar{\theta}_r$ values are the result of propagating the standard error of each quantity though equation

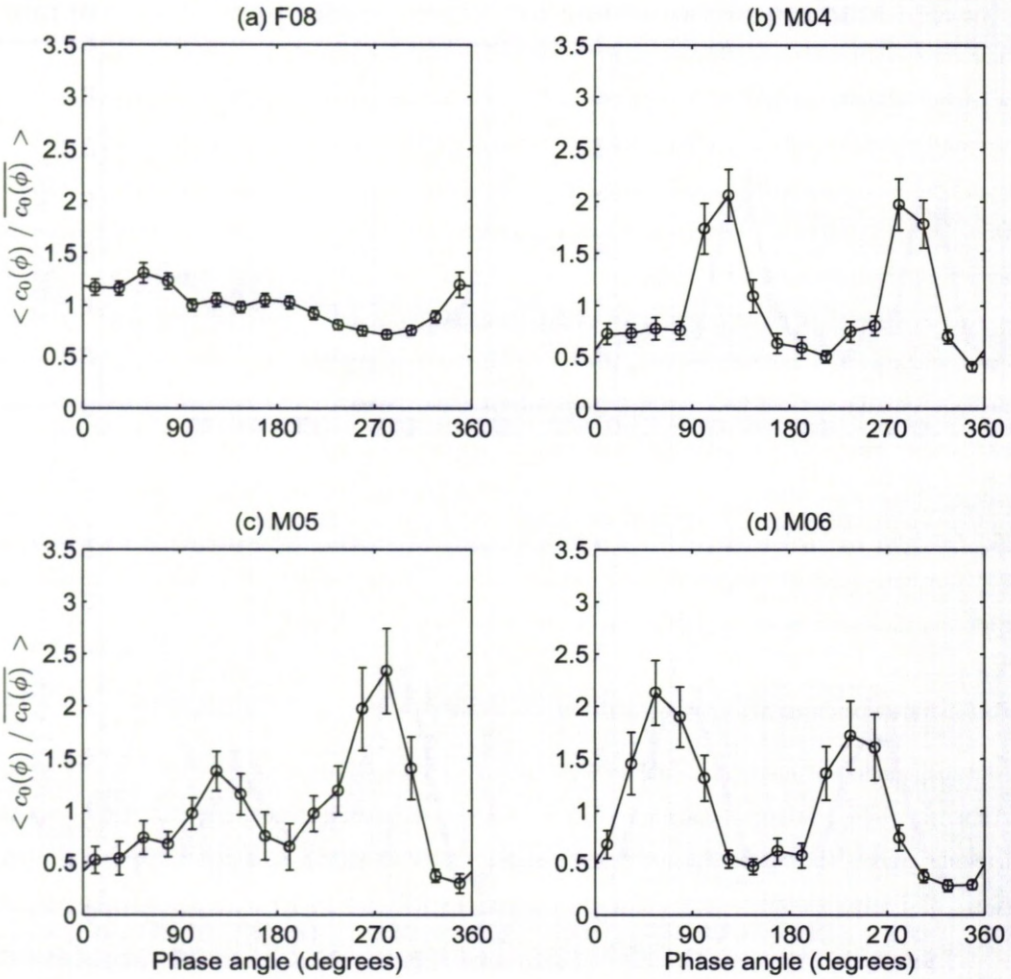

Figure 5.12: Phase ensemble averaged normalised intra-wave reference concentrations, $< c_0(\phi)/\overline{c_0(\phi)} >$. The ensemble averaging, $< >$, is over all the wave cycles during (a) plane and (b – d) rippled bed conditions, and the error bars show the standard error of the ensemble averaging. Both $c_0(\phi)$ and $\overline{c_0(\phi)}$ were calculated from mean concentration values from the 1 and 2 MHz ABS frequencies.

(5.9). The majority of the data compares reasonably well with the equation of Nielsen, though with a few outliers. These outliers tend to correspond to wave half cycles where $d_0/\lambda_0 < 1$, below which flow separation is not expected to occur (Malarkey and Davies, 2002), and are indicated in Figure 5.13 with open circles. A linear regression has been made in log-log space on $\overline{c_0(\phi)}$ and $\bar{\theta}_r$, where $d_0/\lambda_0 \geq 1$, yielding

$$\overline{c_0(\phi)} = (0.0116 \pm 0.0034)\rho_s \bar{\theta}_r^{3.50\pm0.32} \tag{5.19}$$

with a correlation coefficient of $R^2 = 0.78$. Equation (5.19) broadly agrees with the equation of Nielsen (1986), equation (5.10), in terms of the approximate cubic relation between $\overline{c_0(\phi)}$ and θ_r. The coefficient is somewhat larger than that of Nielsen. The difference between equation (5.19) and that of Nielsen may be due to the fact that cycle mean, rather than time average, reference concentrations are presented here and that the regression was on data where $d_0/\lambda_0 \geq 1$.

5.5 Investigating the vortex shedding regime

Equation (5.7) relates the relative roughness of the bed, $d_0/2k_s$, to the parameter d_0/λ which Malarkey and Davies (2002) used as a parameterisation of the sediment suspension process, namely vortex shedding. The $d_0/2k_s$ values of the rippled bed found in Section 5.4.2 fall within the secondary vortex shedding criteria of Malarkey and Davies (2002) suggesting that vortex shedding should have occurred during these experiments.

The peaks in the ensemble averaged intra-wave SSC in Figure 5.11 and the reference concentration in Figure 5.12 coincide. Over the rippled beds, these peaks occur around flow reversal and can be interpreted as a signature of flow separation and the process of vortex shedding. Figures 5.11 and 5.12 are phase ensemble averages over full wave cycles and indicate the average response of the suspended sediments to the irregular wave forcing. Under regular waves, ensemble averaging helps to reveal the underlying sediment transport phenomena, due to the sediment entrainment process being repeated every wave cycle. However, under the irregular waves used in the present study, the situation was more complicated since each wave was different and therefore less consistency was expected in the suspended sediment field from wave-to-wave. The reason for this variability between wave cycles was because the d_0/λ parameter varied from wave-to-wave and was not sufficient under every wave for the vortex shedding process to occur, i.e. the vortex shedding criteria of Malarkey and Davies (2002), $4 \leq d_0/\lambda \leq 4$, was not fulfilled under every wave. This can alternatively be thought of as a disequilibrium between the flow and bedforms during some wave cycles. Despite this, the ensemble averaged results in Figures 5.11 and 5.12 show an intra-wave variation of the suspended sediment field consistent with that which occurs above ripples and under regular oscillatory flow on average (Davies and Thorne, 2005; Van der Werf et al., 2007). However, one must be aware that the ensemble average results (Figures 5.11 and 5.12) have been phase ensemble averaged over both

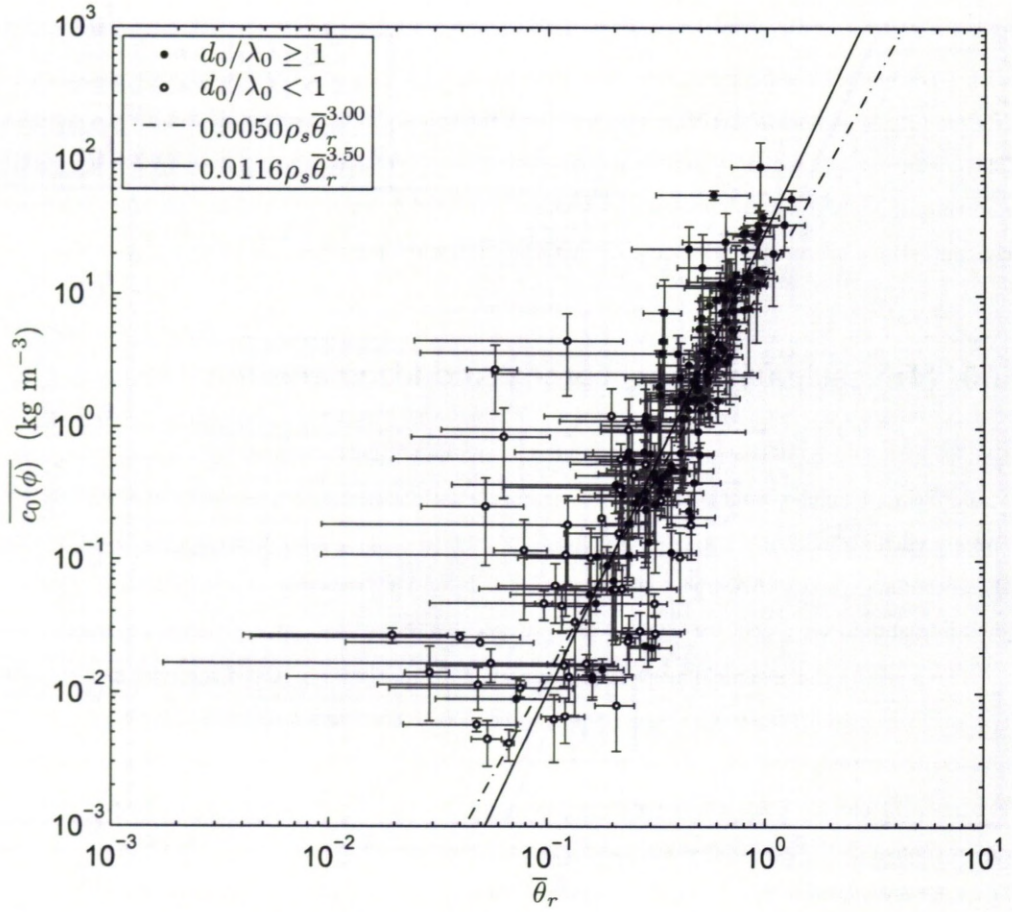

Figure 5.13: Wave cycle mean reference concentrations, $\overline{c_0(\phi)}$, during the rippled bed experiments against the wave cycle averaged ripple modified skin friction Shields parameter, $\overline{\theta}_r$. $\overline{c_0(\phi)}$ is the mean of the results from the 1 and 2 MHz ABS frequencies and the error bars are the associated standard error. The error bars for θ_r shows the standard error due to the wave asymmetry and the uncertainty in the ripple steepness. Those points corresponding to wave half cycles where $d_0/\lambda_0 < 1$, where $d_0 = 0.5(d_{on} + d_{off})$ and λ_0 is the wavelength of the ripple below the ABS, are indicated with open circles. The predictor of Nielsen (1986) is shown $(-\cdot-)$ together with the results of a regression analysis $(-)$ performed on those values corresponding to wave half cycles where $d_0/\lambda_0 \geq 1$.

vortex shedding and non-vortex shedding events, but that the vortex shedding events dominate and are thus revealed through ensemble averaging.

In this section, the dependence of vortex shedding on the parameter d_0/λ, inherently linked to the relative roughness of the bed (equation (5.7)), is investigated by examining the phase ensemble averaged intra-wave variations in the reference concentration during a number of intervals of d_0/λ_0, where d_0 refers to either d_{on} or d_{off} and λ_0 is the measured wavelength of the ripple below the ABS (Table 5.2).

For each of the three rippled bed experiments the distributions of d_0/λ_0 were divided into classes of width $d_0/\lambda_0 = 0.2$. Phase ensemble averages of $c_0(\phi)/\overline{c_0(\phi)}$ were taken over the wave half cycles within each class to yield phase ensemble averages over half wave cycles within a discrete class of d_0/λ_0. This was carried out for both for onshore (d_{on}/λ) and offshore (d_{off}/λ) distributions and for each of the three ripple bed experiments in turn. By examining $< c_0(\phi)/\overline{c_0(\phi)} >$ in each discrete class of d_0/λ, it was identified that the vortex shedding signature, identified as a distinct peak in $< c_0(\phi)/\overline{c_0(\phi)} >$ around flow reversal, was consistently only present in those classes where $d_0/\lambda_0 \geq 1.2$. This was true for both onshore and offshore wave half cycles. Figures 5.14(a – d) show phase ensemble averages of the normalised reference concentration for onshore and offshore wave half cycles where $d_{on/off}/\lambda_0 < 1.2$ and $d_{on/off}/\lambda_0 \geq 1.2$. The upper limit, at which vortex shedding ceases to occur, has not been examined because there were insufficient wave half cycles where $d_0 > 4\lambda$ for any meaningful conclusions to be drawn. When $d_0/\lambda_0 < 1.2$ (Figures 5.14(a and b)), $< c_0(\phi)/\overline{c_0(\phi)} >$ shows no coherent structure through the wave half cycle, whereas when $d_0/\lambda_0 \geq 1.2$ (Figures 5.14(c and d)), $< c_0(\phi)/\overline{c_0(\phi)} >$ exhibits distinct peaks around flow reversal. Therefore, $d_0/\lambda = 1.2$ is interpreted here as a threshold below which flow separation does not occur and above which it does and the process of vortex formation and shedding dominates the suspension of sediment. The combined distributions of d_{on}/λ_0 and d_{off}/λ_0 from each rippled bed experiment are shown in Figure 5.14(e) and Figure 5.14(f) respectively. Also indicated is the threshold value of $d_0/\lambda_0 = 1.2$ above which vortex shedding has been assessed to occur. Approximately 70% of the onshore wave half cycles and 58% of the offshore wave half cycles fall above this threshold.

Table 5.3 shows the results presented in Figure 5.14 (e) and (f) for the three individual rippled bed experiments. These results suggest vortex shedding occurred approximately 12% more often around flow reversal after the onshore wave half cycles than after the offshore wave half cycles. This is most likely due to the asymmetry of the velocity amplitude, evident in Figure 5.11(e). To investigate this, the mean average of the onshore and offshore velocity amplitudes were calculated ($\overline{U_{on}}$ and $\overline{U_{off}}$, Table 5.3). These results demonstrate the onshore velocity amplitude was on average 1.2 times larger across all three experiments. Such asymmetry in the velocity field, and the associated dominant sediment pickup after the onshore wave half cycles, has strong implications in terms of the net cross-shore sediment transport over vortex ripples. This is because the suspended sediment picked up after the onshore wave half cycle is

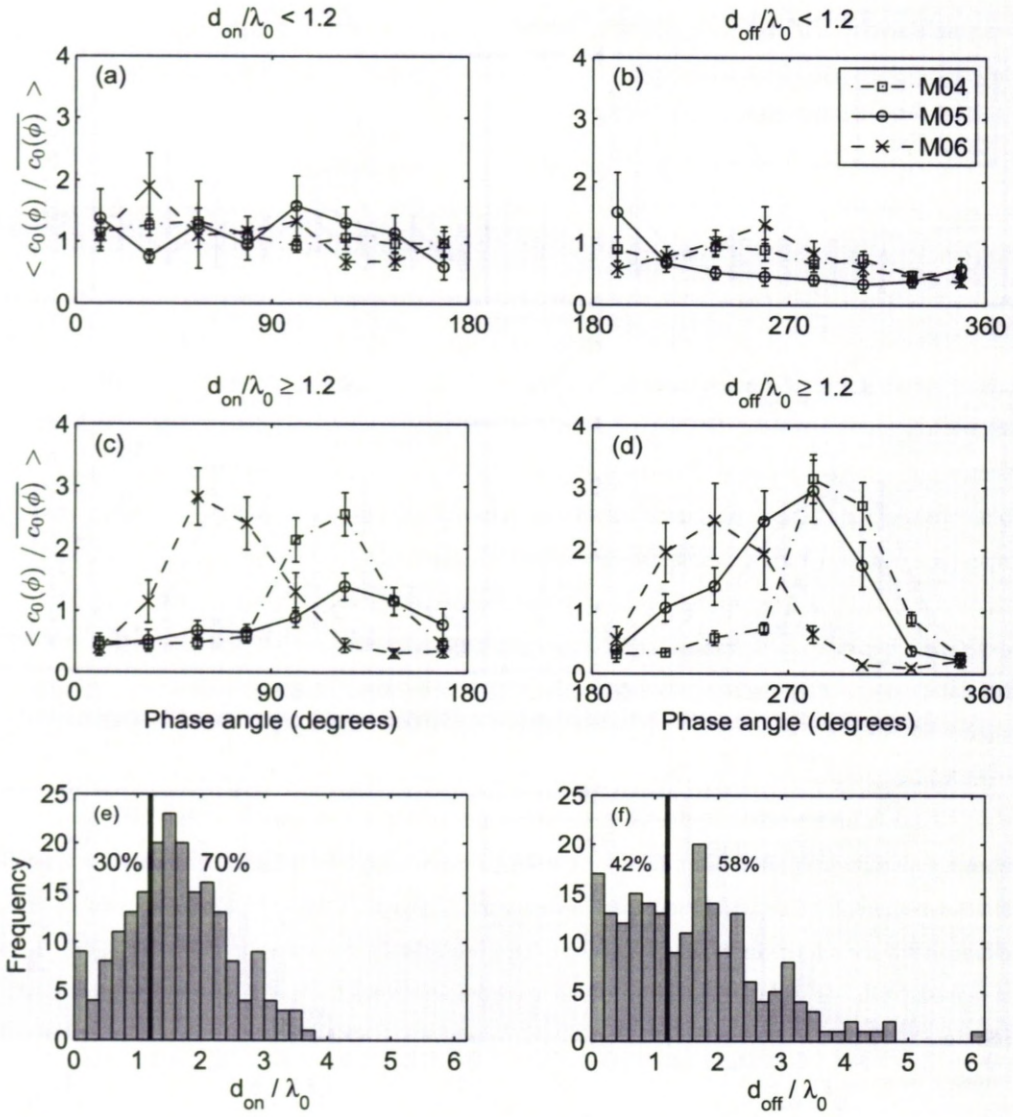

Figure 5.14: Phase ensemble averaged normalised intra-wave reference concentrations, $< c_0(\phi)/\overline{c_0(\phi)} >$. The ensemble averaging, $< >$, is over wave half cycles where (a) $d_{on}/\lambda_0 < 1.2$, (b) $d_{off}/\lambda_0 < 1.2$, (c) $d_{on}/\lambda_0 \geq 1.2$ and (d) $d_{off}/\lambda_0 \geq 1.2$ for the three rippled bed experiments (M04 – M06). The ensemble averaging was performed separately over the onshore (a, c) and offshore (b, d) wave half cycles and the error bars show the standard error of the ensemble averages. The distributions of onshore (e) and offshore (f) orbital diameter to ripple wavelength ratios, combined from the three rippled bed experiments are shown with the d_{on}/λ_0 and $d_{off}/\lambda_0 = 1.2$ threshold and percentage of waves either side of it indicated.

				Wave half cycles assessed as vortex shedding		
Exp.	d_s/λ_0	$\overline{U_{on}}$	$\overline{U_{off}}$	Onshore %	Offshore %	Combined %
M04	2.55	0.31	0.26	66	53	60
M05	3.21	0.42	0.36	88	76	82
M06	1.89	0.55	0.47	60	49	54

Table 5.3: The percentage of wave half cycles assessed as vortex shedding. As well as the onshore and offshore results for each experiment, the combined onshore and offshore results are shown for each experiment in the right hand column. The mean onshore and offshore velocity amplitudes, $\overline{U_{on}}$ and $\overline{U_{off}}$ respectively, are shown along with the significant orbital diameter to ripple wave length ratio, d_s/λ_0, for each experiment.

transported offshore during the offshore wave half cycle (Bijker et al., 1976).

Whether the occurrence of vortex shedding can be related to statistical representations of the wave forcing, such as H_s or d_s obtained by spectral analysis of the velocity or surface wave fields, is an important issue as it has direct modelling implications. Table 5.3 shows d_s/λ_0, where d_s is the significant orbital diameter from Table 5.1, for each experiment. The fraction of wave half cycles where $d_{on}/\lambda_0 \geq 1.2$ or $d_{off}/\lambda_0 \geq 1.2$ were a consistent fraction of d_s/λ_0. Taking the average of these fractions gives the percentage of wave half cycles where vortex shedding occurs as $(26 \pm 1)d_s/\lambda_0$.

Finally, in order to further examine the threshold value of $d_0/\lambda = 1.2$ obtained through examination of the intra-wave reference concentrations, phase ensemble averages of the SSC field were taken over wave cycles where $d_0/\lambda_0 < 1.2$ and $d_0/\lambda_0 \geq 1.2$ respectively, where $d_0 = 0.5(d_{on} + d_{off})$. Figures 5.15(a, c, e) present the phase ensemble averages taken over wave cycles where $d_0/\lambda_0 < 1.2$ for experiments M04, M05 and M06 respectively, and show low values of SSC throughout the wave cycle and little intra-wave variability. Figures 5.15(b, d, f) present the phase ensemble averages taken over wave cycles where $d_0/\lambda_0 \geq 1.2$ for experiments M04, M05 and M06 respectively. When $d_0/\lambda_0 \geq 1.2$, a familiar intra-wave structure similar to those shown in Figures 5.11(b-d) is present with strong peaks in the SSC occurring around flow reversal, indicating vortex formation and shedding is occurring. Figures 5.15(g, h) present the phase ensemble average intra-wave variation in the orbital velocities, $< u >$, when $d_0/\lambda_0 < 1.2$ and $d_0/\lambda_0 \geq 1.2$ respectively, from which it can be seen that $d_0/\lambda_0 < 1.2$ represents the more quiescent wave cycles in the measurement bursts. The important feature present in Figure 5.15 is the clear difference in the phase ensemble averaged SSC fields, both in terms of magnitude and intra-wave structure, between wave cycles where $d_0/\lambda_0 < 1.2$ and where $d_0/\lambda_0 \geq 1.2$. These results are consistent with the intra-wave structure of the reference concentrations in Figure 5.14 and confirms that below irregular waves, $d_0/\lambda = 1.2$ is a suitable threshold above which vortex formation and shedding become the dominant mechanism of sediment suspension above ripples.

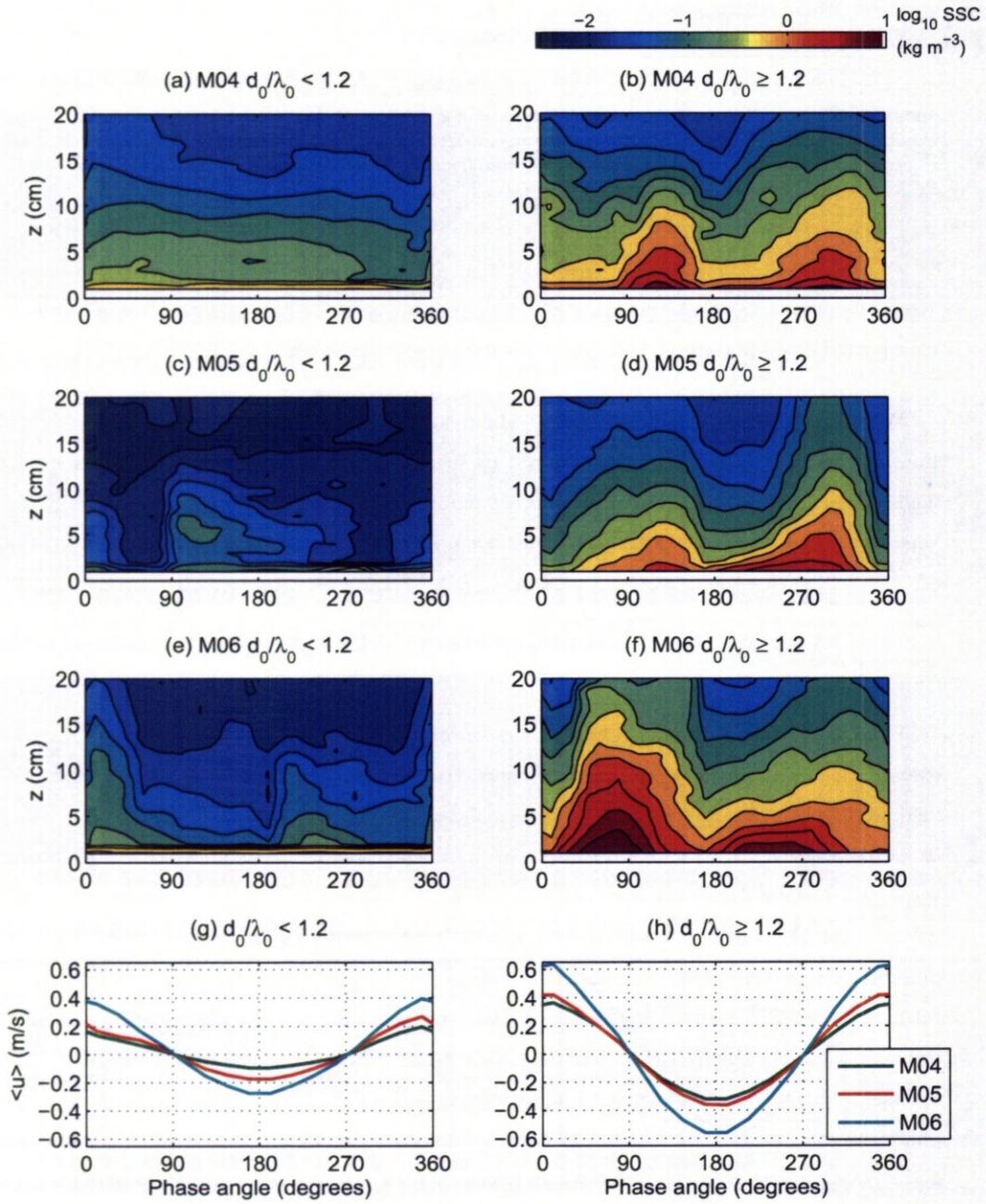

Figure 5.15: Intra-wave variation in the suspended sediment concentration, SSC, with height above the bed, z, phase locked to the near bed velocities and phase ensemble averaged over wave cycles where $d_0/\lambda_0 < 1.2$ (a, c, d) and $d_0/\lambda_0 \geq 1.2$ (b, d, e) for the rippled bed experiments, M04 (a, b), M05 (c, d) and M06 (e, f). In (g) and (h) the intra-wave near bed velocity ensemble averaged over wave cycles where $d_0/\lambda_0 < 1.2$ and $d_0/\lambda_0 \geq 1.2$ respectively, for each experiment are shown.

5.6 Discussion

Four experiments conducted in the Deltaflume under irregular wave forcing have been presented. Particular attention has been paid to the wave forcing, bedforms, fluid velocities, suspended sediment concentrations and reference concentrations. In particular, the variation of the suspended sediment fields and fluid velocities on an intra-wave timescale were studied here. During the first experiment, where $D_{50} = 258\mu$m, the significant wave height, H_s, was 1.45m and the shallow (non-vortex shedding) ripples present during previous wave forcing regimes (with smaller H_s) were washed out. The sediment dynamics above this bed thus approached that of a dynamically (upper-stage) plane bed. During the latter three experiments, where $D_{50} = 375\mu$m and $H_s = 0.64 - 1.05$m, a (steep sided, vortex shedding) rippled bed formed. These four experiments were chosen primarily so that two contrasting bed and sediment dynamics regimes, from those portrayed in Figure 5.1, could be presented. The sediment dynamics under different dynamic, but not strongly contrasting, flow conditions were studied, under which substantial sediment transport was expected. F08 enabled the sediment dynamics above a plane upper-stage bed to be observed and contrasted with that occurring above the rippled beds of M04 – M06.

5.6.1 Bedforms

During the measurement bursts considered there was little or no change in the bed morphology. For example, during the rippled bed bursts there was no significant ripple migration or evolution in terms of ripple amplitude or height changes. Why there was no ripple migration observed during these bursts is an obvious question especially as ripples were observed to migrate as much as one ripple wavelength in 17 minutes in the Deltaflume under regular waves (Davies and Thorne, 2005). This is interpreted to be related to the irregular wave forcing. Faraci and Foti (2002) showed that the ripple migration rate is influenced by the irregularity of the flow and that higher migration rates occur under regular waves. Traykovski et al. (1999) found the average onshore migration rate of ripples in a field environment to be 24 cm/day. Such migration rates would be unobserved over the length of the bursts considered in these experiments, hence the non-migration of the ripples over these timescales is not unexpected. The irregularity of the waves also explains why there was little evolution of the ripple geometry during the measurement bursts here: under irregular waves, where there is less of a dominant orbital length scale than under regular waves, ripples tend to remain in an initial configuration or evolve more slowly than under regular waves (Marsh et al., 1999).

Orbital ripples scale with the diameter of orbital motion, d_0, close to the bed (Clifton, 1976). Whilst the ripples observed here lie in the suborbital regime (Wiberg and Harris, 1994), it is still useful to compare their wavelength to d_0, as d_0 has a strong influence on their geometry. Miller and Komar (1980) proposed that the wavelength of orbital ripples was $\lambda = 0.65 d_0$ and Wiberg and Harris (1994) later reported $\lambda = 0.62 d_0$. These two results give $d_0/\lambda = 1.5$ and 1.6 which is larger than the value of $d_0/\lambda = 1.2$ for the initiation of vortex shedding found

Exp.	λ_M (m)	η_M (m)	η_M/λ_M	λ_W (m)	η_W (m)	η_W/λ_W	λ_S (m)	η_S (m)	η_S/λ_S
F08	0.35	0.015	0.04	0.12	0.008	0.07	0.12	0.003	0.02
M04	0.43	0.088	0.21	0.40	0.067	0.17	0.35	0.053	0.15
M05	0.45	0.087	0.19	0.36	0.060	0.17	0.32	0.047	0.15
M06	0.45	0.073	0.16	0.31	0.049	0.16	0.29	0.039	0.14

Table 5.4: Predicted ripple dimensions using the formulae of Mogridge et al. (1994), λ_M, η_M and η_M/λ_M, Wiberg and Harris (1994), λ_W, η_W and η_W/λ_W, and Soulsby and Whitehouse (2005), λ_S, η_S and η_S/λ_S.

here, but is well within the range of values where vortex shedding is expected, according to the criteria of Malarkey and Davies (2002). The fact that the parameter d_0/λ can be used both for the prediction of bed morphology (Miller and Komar, 1980; Wiberg and Harris, 1994) and the process of sediment entrainment illustrates the inherent link between bed morphology and the sediment entrainment process. Furthermore, d_0/λ is inherently linked to the equivalent roughness of vortex ripples by equation (5.7).

Comparison with ripple predictions

The bed roughness, which is heavily dependant on the ripple dimensions, is an important consideration when modelling boundary layer flows (Davies and Thorne, 2008) and in many cases must be predicted from knowledge of the predominant flow conditions and bed sediments. Thus, ripple geometry prediction under waves is an active research area and a number of prediction schemes and formulae exist, based on parameters such as the orbital diameter characterising the flow (e.g. Mogridge et al., 1994; Wiberg and Harris, 1994; Soulsby and Whitehouse, 2005). It was interesting therefore to compare the results of such prediction schemes with the direct measurements of ripples here, to provide insight into the expected bedform, and sediment suspension, conditions under the Deltaflume oscillatory flow.

The suborbital regime defined by Wiberg and Harris (1994) can be expressed as $1800 < d_0/D_{50} < 5500$. Ripples with d_0/D_{50} smaller than 1800 or larger than 5500 are therefore within the orbital and anorbital regimes respectively. The d_s/D_{50} values for the Deltaflume experiments are listed in Table 5.1 and show that the flat bed (F08) and rippled beds (M04 – M06) are respectively within the anorbital and suborbital regimes of Wiberg and Harris (1994). Using the significant orbital diameters and peak spectral periods from Table 5.1, the prediction formulae of Mogridge et al. (1994), Wiberg and Harris (1994) and Soulsby and Whitehouse (2005) were applied to the flow conditions during the Deltaflume bursts to find expected values for the ripple dimensions, the ripple wavelength, height and steepness. The results are listed in Table 5.4. In Table 5.4 λ_M, η_M and η_M/λ_M are the dimensions of the ripples according to the predictor of Mogridge et al. (1994), λ_W, η_W and η_W/λ_W are the dimensions of the ripples according to the predictor of Wiberg and Harris (1994) and λ_S, η_S and η_S/λ_S are the dimensions of the ripples according to the predictor of Soulsby and Whitehouse (2005). All these predictors are based on large amounts of data, and should therefore be most comparable with the spatial and temporal averages of the ripple dimensions measured using the ARP, λ,

η, and η/λ in Table 5.2. However, all the predictions of the ripple height were 1.2 – 3.5 times larger than the measured spatial and temporal averages (η, Table 5.2) and all the predictions of the ripple steepness were 1.5 – 2.3 times larger than η/λ (Table 5.2). Similarly, for the flow conditions during M04 and M05, the predictions of the ripple wavelengths were 1.4 – 2.0 λ. The predictions of the ripple wavelength during the M06 flow conditions were generally more accurate with values ranging from 0.9 – 1.4 λ. Finally, Table 5.4 shows the results using the flow conditions during F08, where a reasonably plane bed was known to exist. The results all predict shallow ripples with heights in the range 0.3 – 1.5 cm, an order of magnitude smaller than the ripples known to be present during the rippled bed experiments (M04 – M06). However, the wavelengths of 0.12 – 0.35 m were significantly shorter than the long wavelength bedform observed in Figure 5.4(a). Overall, the predictor of Soulsby and Whitehouse (2005) predicted ripple dimensions most in line with those observed here. The predicted ripple wavelengths were 0.9 – 1.4 λ, the predicted ripple heights were 1.2 – 2.1 η and the predicted ripple steepness were 1.5 – 1.7 η/λ. The discrepancy between the predicted and observed ripple dimensions is here contributed to the fact that only three rippled beds were examined here and that the significant wave orbital diameters and peak spectral wave periods from Table 5.1 are not necessarily the best parameterisation of the irregular wave fields. Furthermore, Hanes et al. (2001) found that ripple measurements from three field campaigns were approximately within a factor of two of those given by ripple prediction schemes.

5.6.2 Timings of peak sediment entrainment

The most striking similarity between the three rippled bed experiments is the ensemble averaged intra-wave SSC fields (Figures 5.11(b-d)) and reference concentrations (Figures 5.12(b-d)), in terms of timing and magnitude. It is well established that under regular waves and over a bed with steep ripples, sediment laden vortices are ejected over the ripple crest around the instances of flow reversal and that peaks in the SSC occur at these times above the ripple crest (e.g. Davies and Thorne, 2005; Van der Werf et al., 2007). Therefore, the clear peaks observed here, under irregular waves, in the ensemble averaged intra-wave SSC (Figure 5.11) and reference concentrations (Figure 5.12) around the instants of flow reversal support the concept of the process of vortex shedding taking place under irregular waves.

Whilst peaks in the SSC occurred around flow reversal during each of the rippled bed experiments, there are differences in the precise timing of the SSC peaks. The phase at which $< c_0(\phi)/\overline{c_0(\phi)} >$ peaks in M04 and M05 compare well and occur between 11 – 24° after flow reversal, broadly agreeing with the results of Van der Werf et al. (2007), whereas the $< c_0(\phi)/\overline{c_0(\phi)} >$ peaks in M06 precede flow reversal by 34°. A similar phenomenon was observed above the crests of vortex ripples by Block et al. (1994) beneath regular waves in a large flume tank (97m long). Block et al. (1994) observed the SSC to peak (i) 10 – 20° after flow reversal when η/λ=0.16 and d_0/λ = 1.62 and (ii) 20° before flow reversal when η/λ = 0.11 and d_0/λ = 2.63. This phase shift was attributed to the difference in the d_0/λ parameterisa-

tion (Block et al., 1994). The phase shift observed here between M04 and M06 is of a similar magnitude to that observed by Block et al. (1994), but the d_s/λ_0 value during M06 is smaller than that during M04. The ripple measured below the ABS during M06 was larger than the majority of ripples present on the bed at the time. The bed morphology was also dominantly three-dimensional during M06 and the bedforms may not have been truly in equilibrium with the flow. Perhaps, therefore, the λ_0 length scale was an inappropriate choice for the case of the M06 experiment. Using instead the spatially averaged ripple wavelength, λ in Table 5.2, produces $d_s/\lambda = 4.18$ which is larger than that during M04 and therefore more consistent with the result of Block et al. (1994).

5.6.3 Implications

The occurrence of the process of vortex shedding is well established under regular oscillatory flow (e.g. Davies and Thorne, 2005; Van der Werf et al., 2007) but is not well verified under irregular waves at field scale. This work verifies that, under field scale irregular waves, the process of vortex shedding not only occurs, but can be a dominant mechanism of sediment suspension during both onshore and offshore wave half cycles. When modelling sediment fluxes, the prediction of the sediment suspension under waves can have a profound effect, i.e. wave asymmetry can lead to the process of vortex shedding encouraging an offshore pumping of sediment (Bijker et al., 1976; Davies and Thorne, 2008). Such an asymmetry in the intra-wave velocity was observed here contributing to 12% more vortices being generated during the onshore wave half cycles beneath irregular waves. Therefore it is important for the process of vortex shedding to be considered within models of larger scale sediment transport. Commonly, the only readily available information about the hydrodynamic and sediment transport regime at a field location is the wave climate which, for simplicity, is often expressed in terms of the significant wave height, H_s, and peak spectral period, T_p. Such a modelling approach is simplistic, but often necessary in otherwise computationally demanding wide area models. It is therefore useful for the relation between H_s and the process of sediment entrainment due to vortex shedding to be discussed. H_s can readily be used to estimate an equivalent significant velocity amplitude, U_s, (Wiberg and Sherwood, 2008) or significant orbital diameter, d_s, close to the bed, which in turn can be related to vortex shedding with the parameter d_s/λ, where λ is the characteristic ripple wavelength. The dependency of the occurrence of vortex shedding on d_s/λ has been examined here under irregular waves. It has been found that the percentage of waves assessed as vortex shedding approximately scales as $26d_s/\lambda$ over steep vortex ripples. Furthermore, d_s, can be directly related to the significant wave height and peak spectral period using a relation based on linear wave theory, equation (5.16). Thus, these observations on the frequency of vortex shedding events under irregular waves could serve as a practical assessment of vortex shedding within sediment transport models reliant on parameters such as H_s.

5.7 Conclusions

The results presented here were achieved by making acoustic measurements, on an intra-wave timescale, of the sediment suspensions under JONSWAP irregular waves over both plane and rippled beds, under different significant wave heights. A striking difference between the intra-wave structure of the suspended sediments over a plane bed and rippled beds was observed. Over the rippled beds, the results demonstrate a clear suspended sediment structure consistent with lee wake vortex shedding previously observed under regular waves (Davies and Thorne, 2005). Even though the significant wave height was different in each rippled bed experiment, the intra-wave structure and magnitudes of the SSC were remarkably similar. This consistency is ascribed to the similarity in the bedforms present – namely ripples with $\eta/\lambda > 0.1$ where boundary layer separation and vortex shedding can occur – rather than simply the wave forcing. This study establishes that vortex shedding occurs under field scale irregular free surface waves, with vortex shedding occurring under a percentage of the waves that appears to scale with the ratio of significant orbital diameter to ripple wavelength, d_s/λ, by a factor of ~ 26. Furthermore, it was consistently observed that around 12% more vortex shedding events occurred after onshore wave half cycles than after offshore wave half cycles. This was due to wave asymmetry, and could lead to substantial offshore suspended sediment transport over longer timescales than the duration of the experiment. Malarkey and Davies (2002) suggest $1 \leq d_0/\lambda \leq 4$, equivalently expressed as $4.3 \leq d_0/2k_s \leq 17.4$ using equation (5.4) with $\eta/\lambda = 0.12$ and $\alpha = 8$, as a vortex shedding regime. The lower limit was tested here under irregular waves and a threshold value $d_0/\lambda = 1.2$, above which vortex shedding was a dominant entrainment process, was found. These results could serve as a practical assessment of vortex shedding within sediment transport models reliant on parameters such as the significant wave height, which can be related to d_s.

The use of acoustics is proving to be a powerful tool in the study of near bed sediment dynamics. These conclusions are based on results from one-dimensional, vertical, measurements, over ripple crests, of SSC and point measurements of the near bed flow. In recent years, acoustic technology has advanced and it is now possible to make detailed, collocated, one-dimensional measurements of the bed, the flow and the suspended sediments at high temporal and spatial resolutions (e.g. Thorne et al., 2009b). In the future, these techniques will be applied in increasingly more natural environments, such as large scale flumes, as well as the field. Further insight will be gained into the complex sediment transport processes occurring at small spatial and temporal scales within rough boundary layers predominant in the coastal marine environment.

Acknowledgments

This work was supported by the European Union, through its access to large-scale facilities, and by the Natural Environment Research Council and the University of Liverpool for PhD funding. The authors thank Prof. J. J. Williams at Associated British Ports, who coordinated

the Deltaflume experiments and Dr. Paul S. Bell and Dr. Benjamin D. Moate at the National Oceanography Centre for help with analysing the flow and ripple data. We thank Prof. Stephen S. Flint at the School of Environmental Sciences, University of Liverpool, for his support. The constructive reviews from Prof. Peter Nielsen at the University of Queensland, Australia, and an anonymous reviewer are also much appreciated. We especially thank Prof. Alan G. Davies at the School of Ocean Science, Bangor University, Wales, for his many useful conversations and suggestions.

Chapter 6

Wave groups and the character of sediment resuspension over an evolving sandy bed

Abstract

High resolution measurements of the suspended sediment concentration and water velocity were made using an Acoustic Backscatter System and Acoustic Doppler Velocitmeter under irregular free-surface waves. The waves were generated in a large scale flume facility and above a number of bedform types. These data are analysed in (i) the frequency domain in order to examine the frequency at which sediment suspensions occur within the oscillatory bottom boundary layer and the free stream, and (ii) the time domain in order to examine the instantaneous entrainment and vertical transport of sediment at intra-wave, wave average and wave group timescales. During the course of the experiments the significant wave height was systematically stepped up enabling the character of sediment suspensions under a number of flow and bedform regimes to be studied. Sediment suspensions within the near bed boundary layer were dominated by intra-wave entrainment. In contrast, the free stream sediment suspensions were dominated by the vertical advection of sediment at wave group timescales. During wave groups the sediment suspension field was characterised by the upward advection of sediment due to the continual injection of turbulence under a series of waves (wave pumping). The character of a wave group is considered to be an important control over sediment suspensions within the free stream. Four distinct types of wave groups were identified and the instantaneous sediment suspension field below each type examined. It was found that wave groups characterised by an abrupt termination of the group strongly influenced the sediment concentration within the free stream. Wave groups are a feature of irregular wave forcing, typical in the field, and efforts must therefore be made to further understand their influence on sediment suspensions.

6.1 Introduction

Under irregular waves, the suspended sediment concentration (SSC) changes over a range of time scales (Hanes, 1991; Osborne and Greenwood, 1993). These fluctuations occur at high, intra-wave, frequencies associated with individual waves (Osborne and Vincent, 1996; Villard and Osborne, 2002; O'Hara Murray et al., 2011, and Chapter 5) and also at low, infra-gravity, frequencies (Hanes, 1991; Osborne and Greenwood, 1993) associated with wave groups (Larsen, 1982; Shi and Larsen, 1984). The suspension of sediment is strongly dependant on the hydrodynamics and the type of bedforms present (Ribberink and Al-Salem, 1994; Vincent et al., 1999; Grasmeijer and Kleinhans, 2004). Above steep sided two-dimensional ripples flow separation can occur during each wave half-cycle, forming a sediment laden vortex, which at flow reversal is ejected into higher parts of the flow (Nakato et al., 1977; Hansen et al., 1994; Sleath and Wallbridge, 2002). In these conditions, the intra-wave suspension of sediment is a convective entrainment process occurring twice in a wave cycle (Davies and Thorne, 2005; Van der Werf et al., 2007; Thorne et al., 2009a). When the bed is plane the entrainment of sediment occurs when the peaks in the bed shear stress generate turbulence, which occurs just ahead of peak free stream velocity (Davies and Thorne, 2008). These intra-wave entrainment processes are strongly dependant on the properties of each incident wave: its height, period and asymmetry. During a group of waves, however, the SSC also depends on the properties of antecedent waves. For example, at a given height above the bed the SSC is often higher under waves late in a group than under similar waves early in a wave group (Hanes, 1991; Villard et al., 2000; Vincent and Hanes, 2002). This can be due to wave-pumping, where within each wave cycle sediment is entrained to higher elevations before it can settle. If there is a continual injection of turbulence under consecutive waves in a wave group, then more sediment will be supported, and there will be more vertical advection of turbulence during the passage of a wave group than an individual wave (Osborne and Greenwood, 1993). A consequence of the wave-pumping process is a time lag between the initial entrainment of sediment at the bed and higher than average concentrations at higher elevations (Vincent and Hanes, 2002).

This work examines time-series of SSC up to 0.8m above a number of different bedform types that developed in a large scale wave flume as the significant wave height was systematically stepped up. Over a variety of bedforms the fluctuations in SSC close to the bed are associated with intra-wave entrainment processes. Further away from the bed the SSC variation is solely a function of the wave group and is dependant on antecedent waves. This is because the vertical extent to which the intra-wave processes dominate is limited by the ripple height (Van Rijn, 1993; Van der Werf et al., 2006; Thorne et al., 2009a). This work supports the importance of considering wave groups when trying to understand sediment entrainment and transport processes, and raises the question of how important the character of the wave group is, such as the number of waves and distribution of wave heights in a group.

6.2 Experiments, instrumentation and data analysis

The Deltaflume of Deltares Delft Hydraulics, the Netherlands, is a large scale flume (230m long, 5m wide and 7m deep) that enables sediment transport processes to be monitored at field scale. Irregular waves with a JONSWAP spectrum (Carter, 1982) were generated for a series of significant wave heights during which the bed adopted a number of different morphological forms. A series of experiments was conducted over a fine-medium-grained sand bed, referred to here as the fine-grained bed, and an upper-medium-grained bed, referred to as the medium-grained bed. Using laser granulometry, the fine and medium-grained sediment beds were found to have lognormal grain size distributions with median grain diameters, D_{50}, of 258μm and 375μm respectively. In each case, the bed was 0.7m deep and was laid down in the centre of the flume in a 30m long region spanning the width of the flume. Prior to the 25 minute measurement burst of each experiment, the irregular waves were run for one hour to allow the bedforms to reach equilibrium (Marsh et al., 1999). Figure 6.1 is a schematic of the instruments deployed on a frame in the centre of the sandy bed and at one side of the Deltaflume. The Nortek Vector Acoustic Doppler Velocimeter (ADV) measured the water velocities at one point $\sim$ 0.5m above the bed and recorded three components of flow at 16Hz. The cross-sectional and plan-form geometry of the bedforms were respectively monitored by the 2.0MHz Acoustic Ripple Profiler (ARP) and 1.2MHz Sector Scanning Sonar (SSS). Vertical profiles of the suspended sediment concentration, at intra-wave (4Hz) time scales, were measured by the Acoustic Backscatter System (ABS). The ABS comprised three transceivers operating at 1.0, 2.0 and 4.0 MHz, aligned perpendicular to the flow (along-shore). Finally, a number of pumped samples of the suspended sediments (Bosman et al., 1987) were taken from up to five heights above the bed during a number of experiments. These samples were analysed using laser granulometry to obtain grain size distributions of the suspended sediment.

In this study, measurements of the wave forcing, bedforms and suspended sediment concentration (SSC) made above the medium-grained bed are primarily examined. Wave generated bedforms quickly emerged on the medium-grained bed and, as the significant wave height was stepped up, exhibited a number of different plan-form and cross-sectional configurations. Thus, measurements of the SSC were made above an evolving sandy bed and the response of the SSC during the passage of wave groups, and over different bedforms, is examined. In addition, the effect of grain size on the SSC during wave groups is discussed by comparing the results from the medium-grained bed with those from the fine-grained bed under comparable wave forcing conditions but different bed morphology.

6.2.1 Irregular wave forcing and wave groups

For each experiment, the ADV velocity components were despiked using a Phase-Space Thresholding Method (Goring and Nikora, 2002) and rotated to correct for any misalignment of the instruments with the main flow direction by calculating the principle axis of variation (Emery

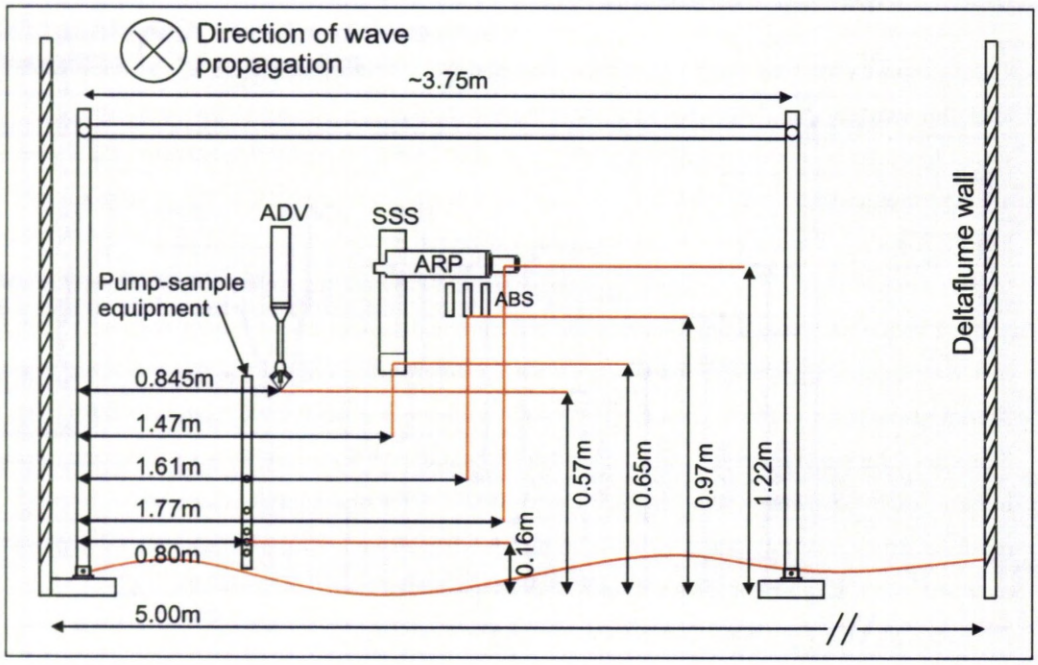

Figure 6.1: A schematic of the instruments deployed on a frame in the Deltaflume showing the locations of the Acoustic Doppler Velocimeter (ADV), Acoustic Ripple Profiler (ARP), Sector Scanning Sonar (SSS) and Acoustic Backscatter System (ABS).

Exp.	D_{50} (μm)	w_s (μm)	H_s (m)	U_s (m/s)	d_s (m)	$\theta_{2.5}$	λ (m)	η (m)	η/λ	Plan-form bedform geometry
M01	375	0.045	0.336	0.217	0.421	0.055	0.227	0.004	0.017	2D
M02	375	0.045	0.435	0.279	0.541	0.080	0.145	0.01	0.0670	2D
M03	375	0.045	0.535	0.344	0.669	0.109	0.211	0.024	0.105	2D
M04	375	0.045	0.638	0.410	0.795	0.141	0.224	0.026	0.109	2D
M05	375	0.046	0.847	0.545	1.059	0.215	0.289	0.029	0.099	q-2D
M06	375	0.046	1.050	0.678	1.316	0.297	0.350	0.032	0.093	q-2D
M07	375	0.047	1.293	0.818	1.589	0.392	0.536	0.045	0.086	3D
M08	375	0.048	1.507	0.960	1.863	0.497	0.609	0.056	0.088	3D
M09	375	0.048	1.635	1.044	2.026	0.562	0.747	0.074	0.107	Hummocks
M10	375	0.048	1.711	1.071	2.079	0.584	0.975	0.084	0.076	Hummocks
M11	375	0.048	1.634	1.023	1.987	0.546	0.960	0.070	0.075	Hummocks
F01	258	0.032	0.278	0.179	0.347	0.049	-	-	-	Plane
F02	258	0.032	0.371	0.238	0.462	0.075	0.148	0.008	0.053	2D
F03	258	0.033	0.495	0.318	0.617	0.116	0.176	0.012	0.070	2D
F04	258	0.033	0.635	0.410	0.795	0.169	0.193	0.010	0.052	q-2D
F05	258	0.034	0.838	0.538	1.044	0.252	0.644	0.018	0.027	q-2D
F06	258	0.035	1.060	0.669	1.300	0.349	0.950	0.016	0.016	2D
F07	258	0.036	1.276	0.799	1.550	0.453	0.866	0.012	0.014	2D
F08	258	0.037	1.453	0.908	1.762	0.547	-	-	-	Plane
F09	258	0.036	1.353	0.839	1.630	0.488	-	-	-	Plane

Table 6.1: Temporally averaged experimental parameters and bedform conditions for the irregular wave Deltaflume experiments.

and Thompson, 1997). During the series of experiments the significant wave height was systematically stepped up and down, whereas the peak spectral wave period, T_p, was kept constant at 6.1s. Therefore, the surface wave steepness increases with the significant wave height. The significant wave height was calculated for each experiment from the power spectral density (PSD) of the horizontal cross-shore velocity component from the ADV using (Wiberg and Sherwood, 2008)

$$H_s = 4\sqrt{\sum_i^N \frac{S_i \Delta f_i}{[2\pi f_i \cosh(k_i z_A)/\sinh(k_i h)]^2}}, \tag{6.1}$$

where S_i and k_i are the power spectral density and wavenumber respectively at the frequency f_i, z_A is the height of the ADV above the bed, h is the mean water depth, $\Delta f_i = f_{i+1} - f_i$ and N is the number of frequency intervals within the range $0.06 \leq f \leq 0.4$. This frequency interval was chosen in order to exclude high frequency contributions due to turbulence and those frequencies associated with attenuated wave motions. In a similar manner, the significant orbital velocity was calculated using (Wiberg and Sherwood, 2008)

$$U_s = \sqrt{4\sum_i^N S_{v,i} \Delta f_i}. \tag{6.2}$$

The H_s and U_s results from the Deltaflume experiments are listed in Table 6.1 along with the significant orbital diameter given by $d_s = U_s T_p/\pi$, with T_p=6.1s, and the grain roughness Shields parameter given by

$$\theta_{2.5} = \frac{f_{2.5} U_s^2}{2(s-1) g D_{50}}. \tag{6.3}$$

In equation (6.3), s is the ratio of sediment density to water density (s=2.65 for quartz sand was used), g is the acceleration due to gravity and $f_{2.5}$ is the grain roughness wave friction factor (skin friction) based on the equivalent Nikuradse grain roughness, $k_s = 2.5 D_{50}$, calculated using the formula of Soulsby (1997).

Figure 6.2(a) shows extracts of the horizontal cross-shore velocity time-series from the ADV for M03, M06 and M09 during which H_s was 0.54m, 1.05m and 1.63m respectively. The systematic increase in velocity amplitudes with H_s is clearly observed in Figure 6.2(a). One feature in Figure 6.2(a) is the presence of wave groups during each experiment, with two or more wave cycles, typically 6-10, growing then shrinking in velocity amplitude. Figure 6.2(a) also shows that the timing of the wave groups is consistent across the experiments. This is because the JONSWAP algorithm used by the wave paddle differed only by the significant wave height for each experiment. Figure 6.2(b) shows the power spectral density (PSD) of the 25 minute bursts of ADV cross-shore velocity time-series from the same three experiments as in Figure 6.2(a). The major peak around 0.2Hz in Figure 6.2(b) corresponds to oscillations at the wave frequency and is broad because the waves were irregular. The second, lower frequency, peak corresponds to the wave groups and is broad because of the variation in wave group timings during each measurement burst.

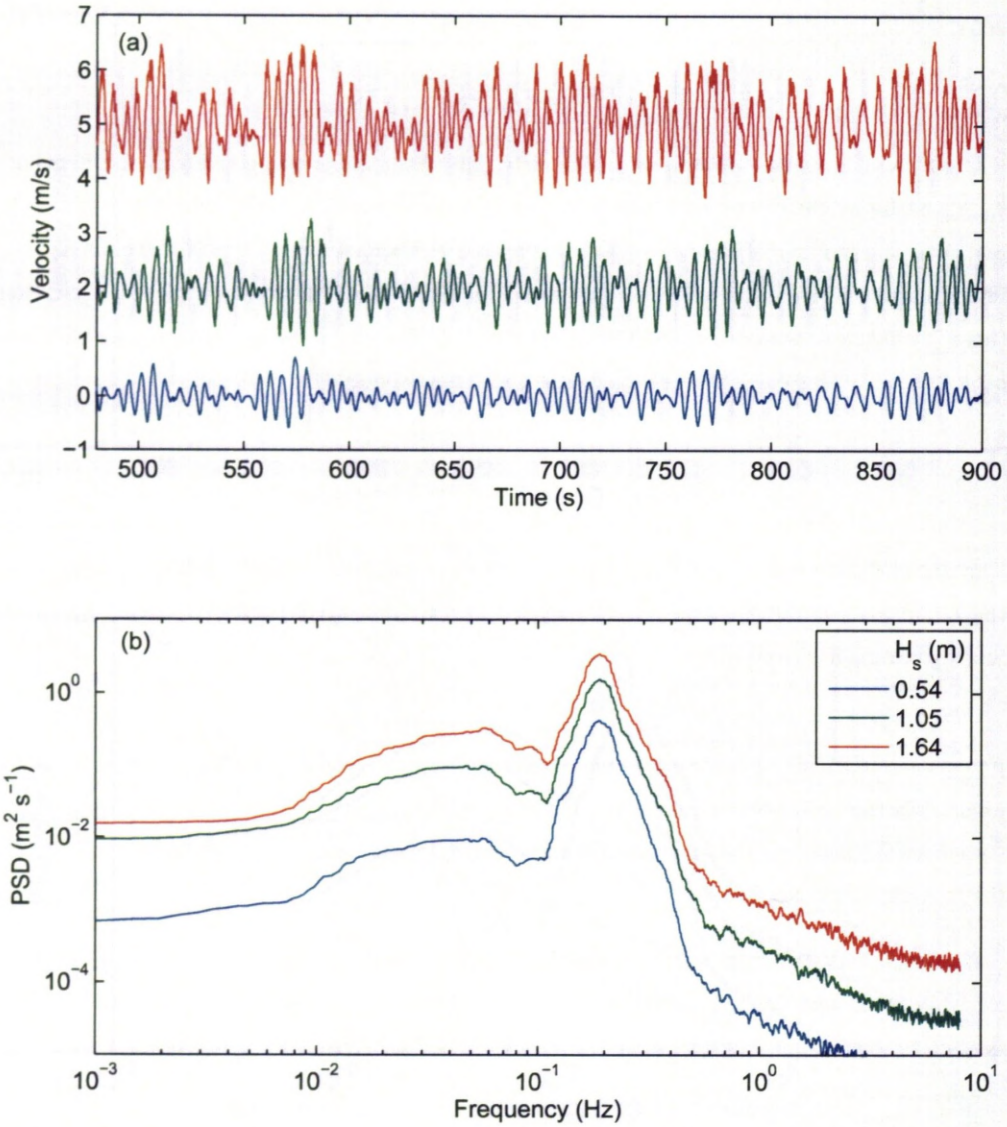

Figure 6.2: Example results from the cross-shore velocity recorded by the ADV. (a) Time-series extracts from three experiments (M03, M06, M09) where the significant wave height, H_s, was 0.54, 1.05 and 1.63m. The results in each case are offset in order to distinguish the three results. (b) The power spectral density, PSD, from the same three experiments as in (a).

6.2.2 Bedforms

The ARP scanned a 4m cross-shore transect of the bed approximately once a minute at centimetre horizontal resolution and sub-centimetre vertical resolution providing cross-sectional profiles of the bed. Figure 6.3(a) shows the ARP results from the Deltaflume experiments considered in this paper conducted above the medium-grained bed, during which H_s was stepped up, in the form of surfaces. Each surface is composed of $\sim$ 10 minutes worth of data. The SSS results were rectified from polar to square grid coordinates (Bell and Williams, 2002) to give 5x5m images of the bed, enabling the plan-form geometry of the bedforms to be studied. Figures 6.3(b - f) show a selection of these results depicting the different ripple plan-form configurations that emerged as H_s was increased. The plan-form geometries of the ripples during each experiment were classified using the terminology of Pedocchi and Garcia (2009) who described ripples as either two-dimensional (2D), quasi-two-dimensional (q-2D) or three-dimensional (3D). These plan-form ripple geometries were observed during the Deltaflume experiments and their occurrence is indicated in Figure 6.3(a). Whilst $H_s = 0.34 - 0.64$m (M01 - M04) the ripples were 2D. As H_s increased through 0.85m and 1.05m (M05, M06) the ripples became quasi-2D, and then 3D when $H_s = 1.29$m and 1.51m (M07, M08). When H_s was stepped up further to 1.63 – 1.71m (M09 – M11) the 3D ripples became much larger and resembled lunate mega-ripples (Vincent and Osborne, 1993; Vincent et al., 1999) or hummocks (Green and Black, 1999). The plan-form geometry classifications for each experiment are listed in Table 6.1.

A turning point analysis was used to extract the nominal dimensions of the ripples during each experiment from the ARP cross-sections. A low pass Gaussian filter removed high frequency spatial fluctuations and a running average smoothed through spikes due to sediment resuspension under large waves. Ripple wavelengths were taken as the horizontal distances between adjacent troughs either side of a crest, ripple heights were taken as the mean average crest to trough difference either side of the crests and the ripple steepness were taken as the height to length ratios. The average ripple wavelengths, λ, heights, η, and steepness, η/λ, are listed in Table 6.1 for each experiment.

6.2.3 Suspended sediments

The ABS recorded vertical profiles of root mean square backscatter amplitude at a temporal resolution of 4Hz. These 4Hz, 25 minute long, time-series were converted to instantaneous SSC profiles at 4Hz using a semi-analytical acoustic inversion, commonly referred to as an implicit inversion (Thorne and Hanes, 2002). These acoustic inversions were aided by measurements of the suspended sediment size distributions obtained from pumped samples of the sediment laden water as described by O'Hara Murray et al. (2011, and Chapter 5), who confirm the veracity of this inversion methodology. The bed level directly below the ABS was tracked during each ABS time-series through an examination of the near bed backscattered intensity received by each transceiver. There were small variations in the nominal bed level due to large entrainment

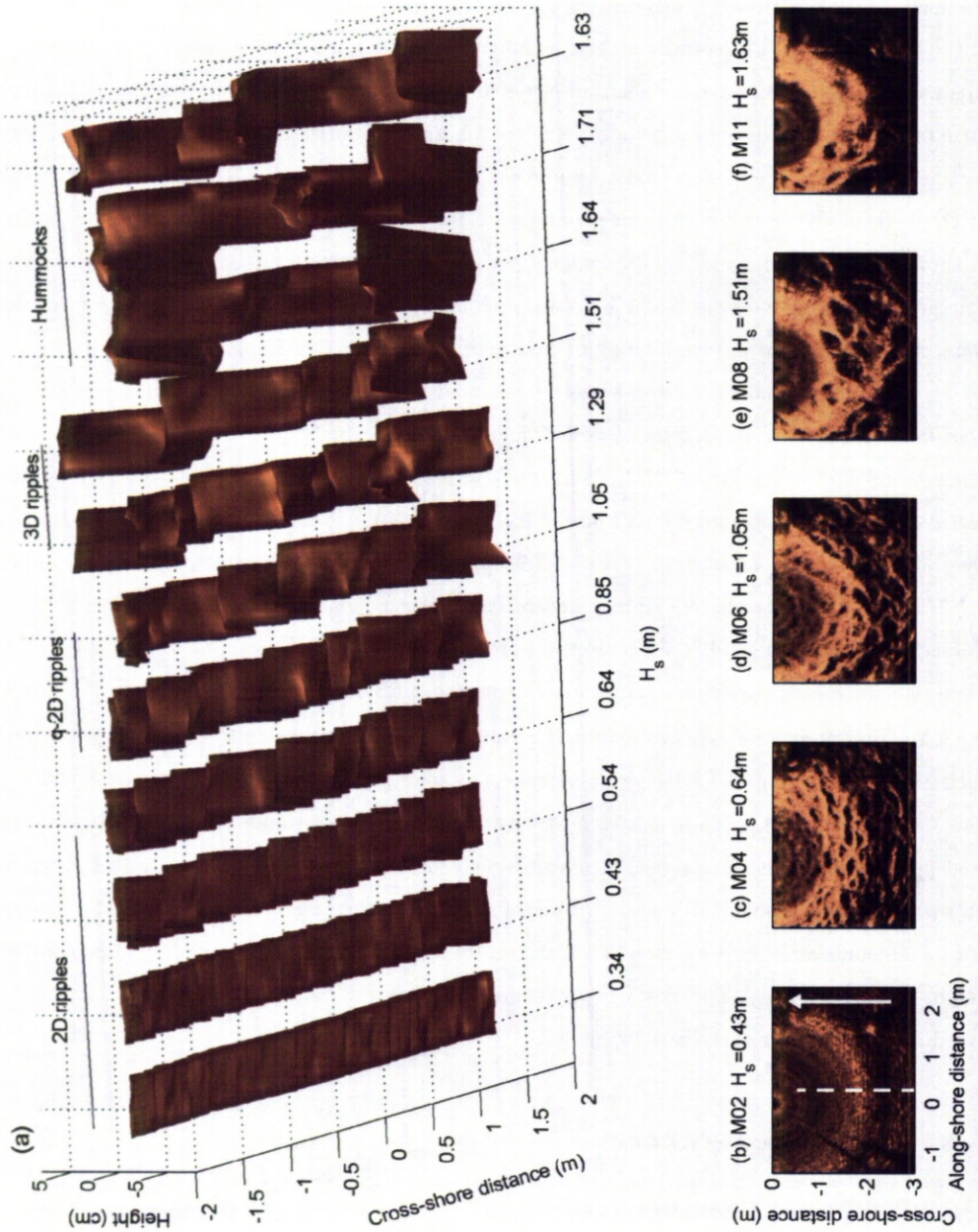

Figure 6.3: (a) Acoustic ripple profiler cross-sections and (b – f) sector scanning sonar plan-form images, depicting the response of the medium-grained sandy bed to step changes in the significant wave height, H_s. In (a) the plan-form geometry classifications given are indicated as either 2D, quasi-2D, 3D or hummocky. In (b) the direction of wave propagation ($\longrightarrow$) and the ARP transect line ($- - -$) are indicated.

events under the more energetic waves and changes in the ripple heights over time (Doucette and O'Donoghue, 2006).

The median sediment sizes of the pumped samples taken and mean averaged over the approximate 0.5m vertical range above the bed were found to vary linearly with the grain roughness Shields parameter. Thus, a linear function was fitted to the available data and was used to calculate the median grain size in suspension for each experiment. Table 6.1 lists the resulting average settling velocities, w_s, for each experiment calculated using the formula of Soulsby (1997). The settling velocities did not vary considerably between experiments and the mean average settling velocity of the fine and medium-grained suspended sediments were 0.034m/s and 0.046m/s respectively.

Figure 6.4 shows five time-mean SSC profiles obtained from experiments (a) M02, (b) M04, (c) M06, (d) M08 and (e) M11 where H_s ranged from 0.43 - 1.63 m. As H_s was stepped up the plan-form bed morphology evolved from having (a) 2D ripples of low steepness, (b) steep sided 2D ripples, (c) quasi-2D ripples, (d) 3D ripples to (e) lunate mega-ripples or hummocks. For $H_s < 1$m, there is a clear increase in the magnitude of the SSC profiles with H_s. For $H_s > 1$m, the near bed SSC remains at approximately 2 kg m^{-3} close to the bed, $z < 0.05$m. For $z > 0.05$m, however, the SSC continues to increase with H_s. This change in near bed SSC magnitude is most likely connected with the transition from 2D to 3D plan-form bedform morphology at the higher wave forcing conditions of $H_s > 1$m.

6.2.4 Wave-averaging the suspended sediment concentration profiles

The timing of each individual wave cycle within a measurement burst was identified from the cross-shore ADV velocity time-series. The start of each wave cycle was defined as the time of flow reversal from offshore flow to onshore flow. This was done by applying a rectangular low-pass filter, in order to remove turbulent fluctuations, and using a zero-crossing analysis to identify the times of flow reversal. These filtered time-series were compared with the non-filtered time-series confirming that the velocities incurred no significant changes in amplitude and phase during the analysis. Having determined the timing of each individual wave cycle in a 25 minute measurement burst, cycle-mean profiles of SSC were obtained from the ABS time-series of instantaneous SSC.

Figure 6.5 shows a 5 minute time-series from M04 of (a) cross-shore velocity, (b) instantaneous SSC at 2Hz up to 0.5m above the bed and (c) wave cycle-mean SSC at 5 heights above the bed. The first 10 wave cycles, identified by the zero-crossing analysis of the velocity time-series, are indicated by the vertical dashed lines in Figure 6.5. During M04, $H_s = 0.64$m and the ripples were 2D with average steepness of $\eta/\lambda = 0.11$ (Table 6.1). During the time-series shown in Figure 6.5, however, the ABS was above a ripple crest with a wavelength of 0.33m, height of 0.047m and steepness of 0.14 (O'Hara Murray et al., 2011, and Chapter 5). The individual peaks in the SSC close to the bed, $z < 0.2$m, in Figure 6.5(b) occur consistently just after flow reversal and can be contributed to the ejection of sediment laden vortices over the ripple

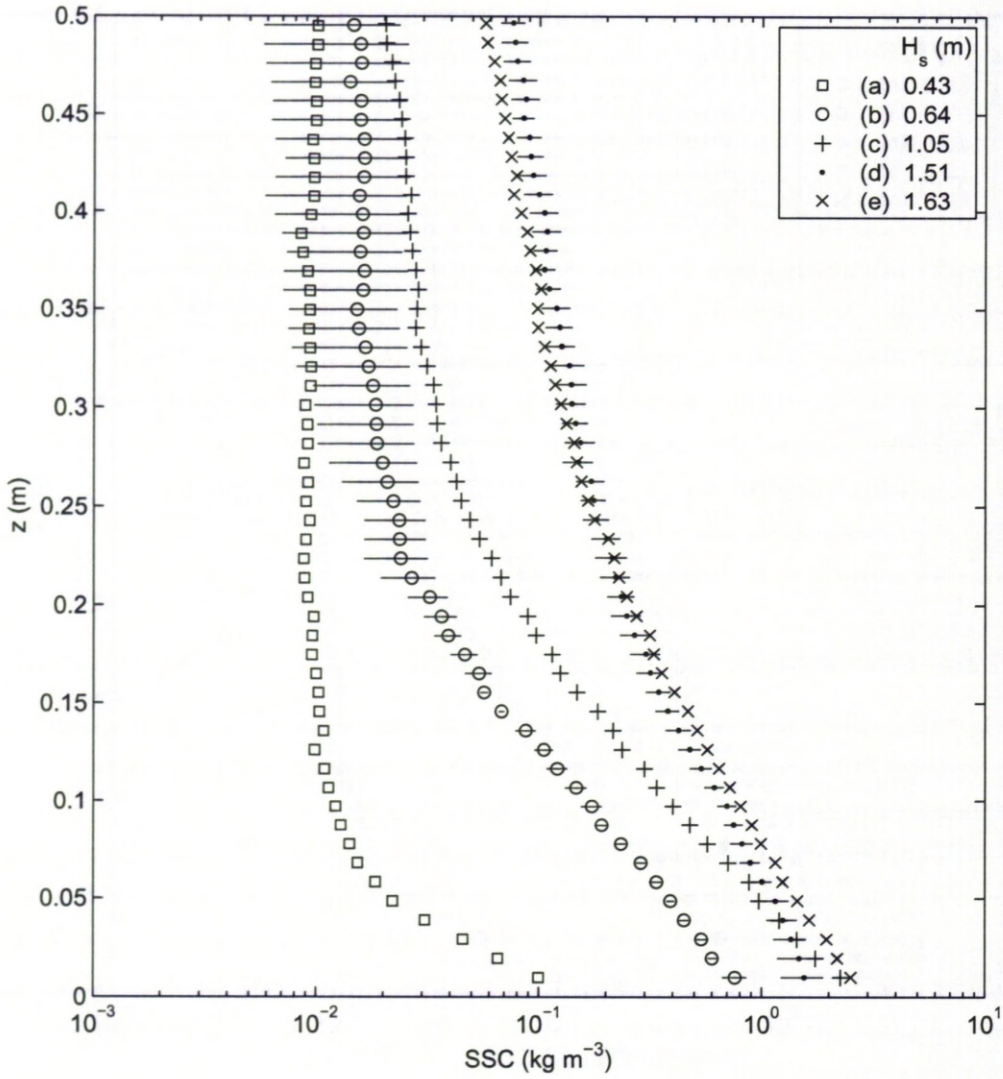

Figure 6.4: Time-mean suspended sediment concentration, SSC, profiles from (a) M02, (b) M04, (c) M06, (d) M08 and (e) M11 during which the significant wave height, H_s, varied from 0.43 – 1.63m and different bedforms were present. The results show the mean taken across the results from the three ABS transceivers and the standard error in shown in the cases of (b) M04 and (d) M08 indicating the typical uncertainty in the measurements.

crest (O'Hara Murray et al., 2011, and Chapter 5). This process does not occur after every wave half cycle in Figure 6.5, but only when the orbital diameter is greater than the ripple wavelength (Malarkey and Davies, 2002; O'Hara Murray et al., 2011, and Chapter 5), and are hence intermittent through the time-series.

6.3 Results

Figure 6.5 shows intermittent sediment suspension events occurring close to the bed, $z < 0.10$m, at a frequency of one or two times the wave frequency, most likely associated with entrainment by vortices. In addition to these high frequency events close to the bed, there are three, lower frequency, suspension events in Figure 6.5 that are associated with the passage of wave groups. For example, around 175s in Figure 6.5, the orbital velocities were small, with velocity amplitudes of $\sim$ 0.07m/s, but increased to velocity amplitudes of $\sim$ 0.75m/s by 200s. For z<0.10m, SSC responded quickly to this increase in velocity amplitude, as can be seen in Figures 6.5(b) and 6.5(c), and started to increase at around 190s. For z>0.1m, the SSC was slower to respond and only started to increase around 200s. Figure 6.5(c) shows that the peak in near bed, $z \leq 0.1$m, SSC occurred at $\sim 200 - 210$s, whereas further away from the bed, z>0.2m, the SSC peaked at $\sim 210 - 215$s, 2 - 3 wave cycles later. This response of the SSC to the passage of a wave group is due to the wave-pumping effect (Villard et al., 2000; Vincent and Hanes, 2002), previously observed in the Deltaflume experiments by Williams and Bell (2006). During the third wave group in Figure 6.5, around 200s, the sediment was pumped up to approximately 0.8m in approximately 10 seconds. Taking the settling velocity as 0.046m/s gives an opposing upwards velocity due to pumping of approximately 0.126m/s.

6.3.1 Time scales of sediment entrainment above an evolving bed

The PSD of the instantaneous SSC was calculated for each experiment, to further examine the frequencies at which sediment entrainment occurred through the 25 minute bursts. Figure 6.6 presents the PSD of the instantaneous SSC 0.01m above the bed for experiments M01 - M11 and the PSD of the horizontal cross-shore velocity from M04, $H_s = 0.64$m. The grouping in Figure 6.6 is in accordance with the emergence of different plan-form bedform geometries during the experimental sequence, and enables the differences in the frequency of sediment entrainment above two distinct bedform types to be examined. During M01 - M06 the ripples had 2D or quasi-2D plan-form geometries and the PSDs of the SSCs from these experiments are shown in Figure 6.6(a). Figure 6.6(b) shows results from M07 - M11 during which the bed was dominated by 3D ripples or large hummocks. The velocity PSD in Figure 6.6(c) is shown for comparison with the concentration PSD in Figure 6.6(a and b). For each experiment, the concentration PSD has a broad peak around 0.05Hz coinciding with the broad peak in the velocity PSD due to the wave groups. This peak dominates the near bed concentration PSD in most experiments and suggests that the majority of sediment entrainment occurred over the wave group time

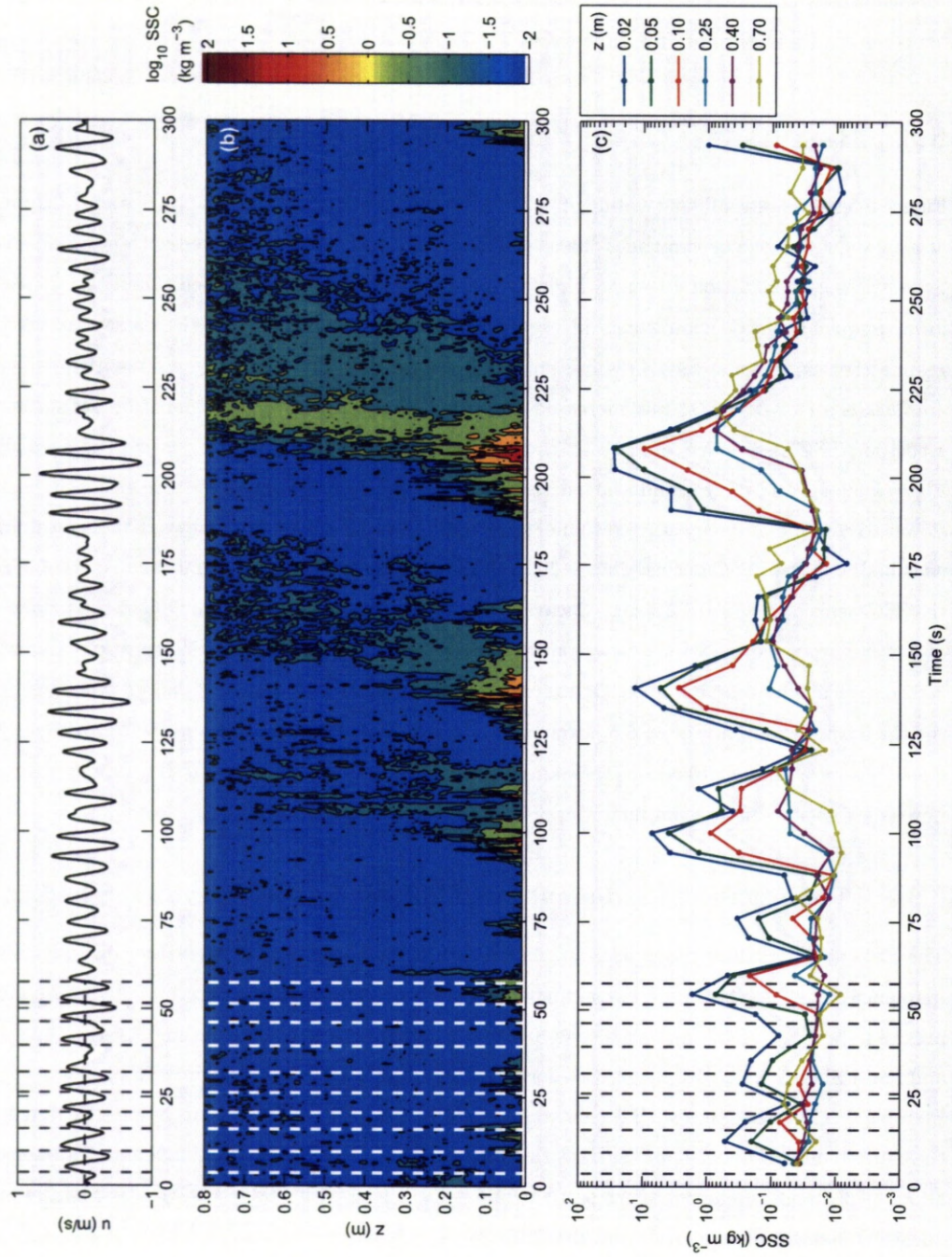

Figure 6.5: A 5 minute time-series from M04 of (a) cross-shore velocity, u, (b) SSC at 2Hz for $0 < z < 0.5$m from the 1MHz ABS and (c) wave cycle-mean suspended sediment concentration, SSC, at 5 heights, z, above the bed from the 1MHz ABS. The first 10 wave cycles are indicated with the dotted lines in each figure.

scale. At higher frequencies, there are a number of peaks in the concentration PSDs, the amplitude of which are close to an order of magnitude smaller than the broad low frequency peaks. In Figure 6.6(a), these secondary peaks are around 0.35Hz, approximately twice the wave frequency, and are consistent through M01 - M06. In Figure 6.6(b), the secondary peaks in the PSDs are at approximately the wave frequency.

6.3.2 Variations in SSC time scales with height above a rippled bed

Figure 6.7 shows the PSD of the SSC at 7 heights above the bed between 0.01 - 0.30m from M04 where $H_s = 0.64$m and the bed was dominated by steep sided 2D ripples (Figure 6.3(a, c)). At all these heights there are dominant, primary, peaks at wave group frequencies, and a number of smaller, secondary, peaks at higher frequencies. Close to the bed, $z \leq 0.10$m, these secondary peaks are at twice the wave frequency, and are most likely associated with the entrainment of sediment-laden vortices. At $z = 0.01$m, the magnitude of the secondary peak is of the same order of magnitude as the primary peak, indicating that there was a strong vortex shedding influence close to the bed. At higher elevations, the magnitude of the secondary peaks relative to the primary peaks diminishes somewhat and for $0.1\text{m} < z < 0.2\text{m}$ the secondary peaks are at the frequency of once in a wave cycle. The sediment in this region was likely to be a combination of sediment entrained locally and advected after down stream entrainment. For $z > 0.2$m there was comparatively little intra-wave variation in the SSC, and it was only during the passage of wave groups that the sediment was pumped to these higher elevations, as shown in Figure 6.5.

6.3.3 Instantaneous SSC above an evolving bed

Figure 6.8 shows 5 minute time-series' of instantaneous SSC at 1Hz up to 0.5m above the bed for five experiments with differing wave forcing and bedform conditions. The experiments shown are (a) M02, (b) M04, (c) M06, (d) M08 and (e) M11 where H_s ranged from 0.43 - 1.63 m and the bedforms were (a) 2D ripples of low steepness, (b) steep sided 2D ripples, (c) quasi-2D ripples, (d) 3D ripples and (e) hummocks, as shown in Figure 6.3. The horizontal velocity times-series from the ADV are also shown in Figure 6.8. The timings of the waves and wave groups were closely matched though these five experiments. In terms of orbital velocities, the only major difference between each experiment was the orbital velocity amplitude of each wave, as the sequence of wave periods remained quasi-constant through the experiments. Figure 6.8(a) shows results from M02 when $H_s = 0.43$m and small 2D ripples of low steepness were present on the bed. In this case there was little sediment entrainment in the majority of wave cycles, with only the orbital velocity amplitudes of the larger waves being sufficient to entrain sediment. On two occasions the SSC was > 1 kg m^{-3} ($\log_{10}$ SSC > 0) close to the bed, and this was after the largest wave in two wave groups, at approximately 130 and 200 seconds. During these wave groups the suspended sediment was pumped upwards, such that after the passage of each wave group the SSC was > 0.1 kg m^{-3} at z=0.5m and < 0.01 kg m^{-3} at z=0.05m. When $H_s = 0.64$m

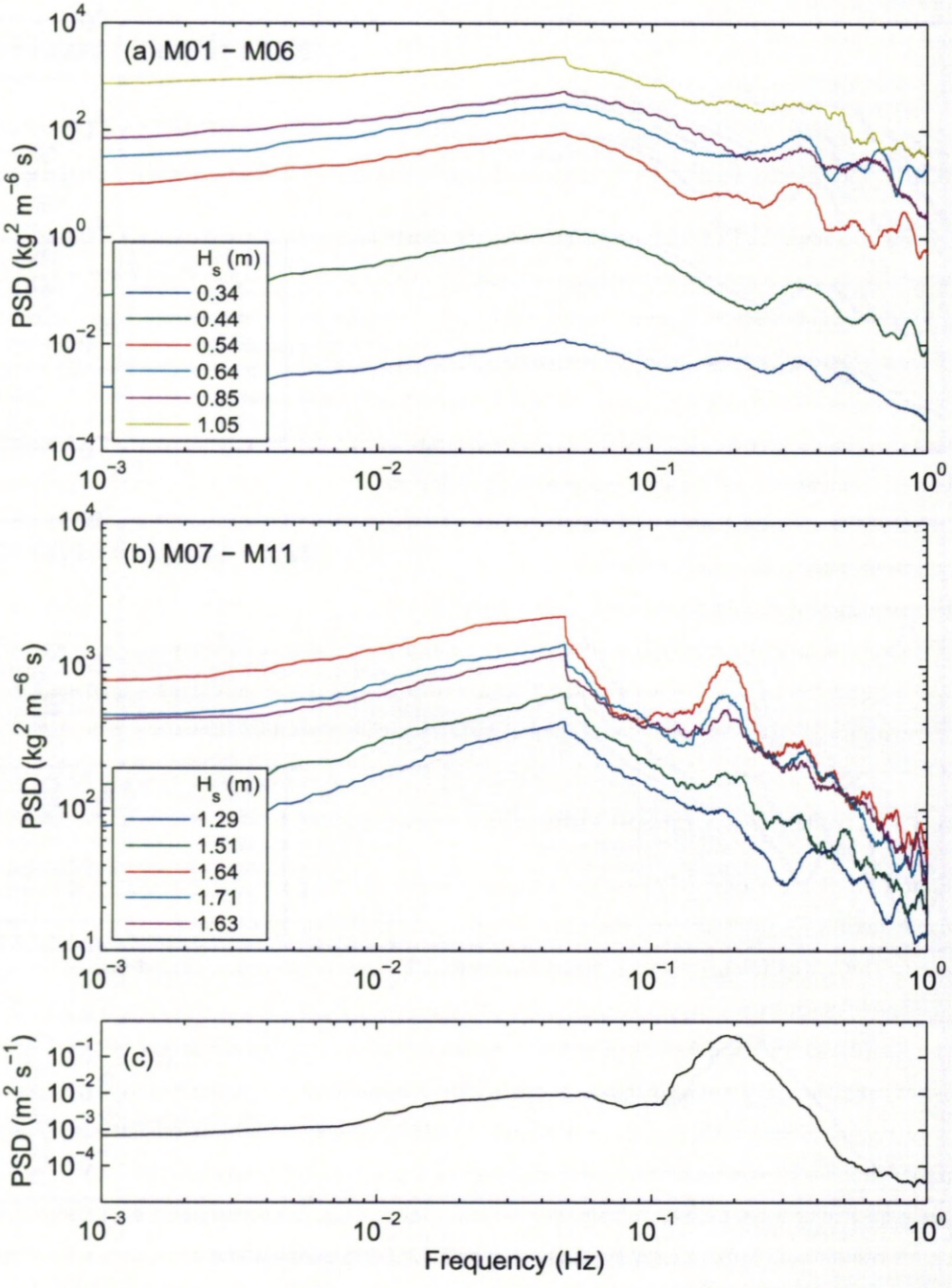

Figure 6.6: The power spectral density, PSD, of (a, b) instantaneous suspended sediment concentration, SSC, from the ABS and (c) horizontal cross-shore velocity from the ADV. (a) shows SSC results from M01 – M06 when 2D or quasi-2D ripples populated the bed, (b) shows results from M07 – M11 when the bed was 3D rippled or hummocky and (c) shows the velocity results from M04.

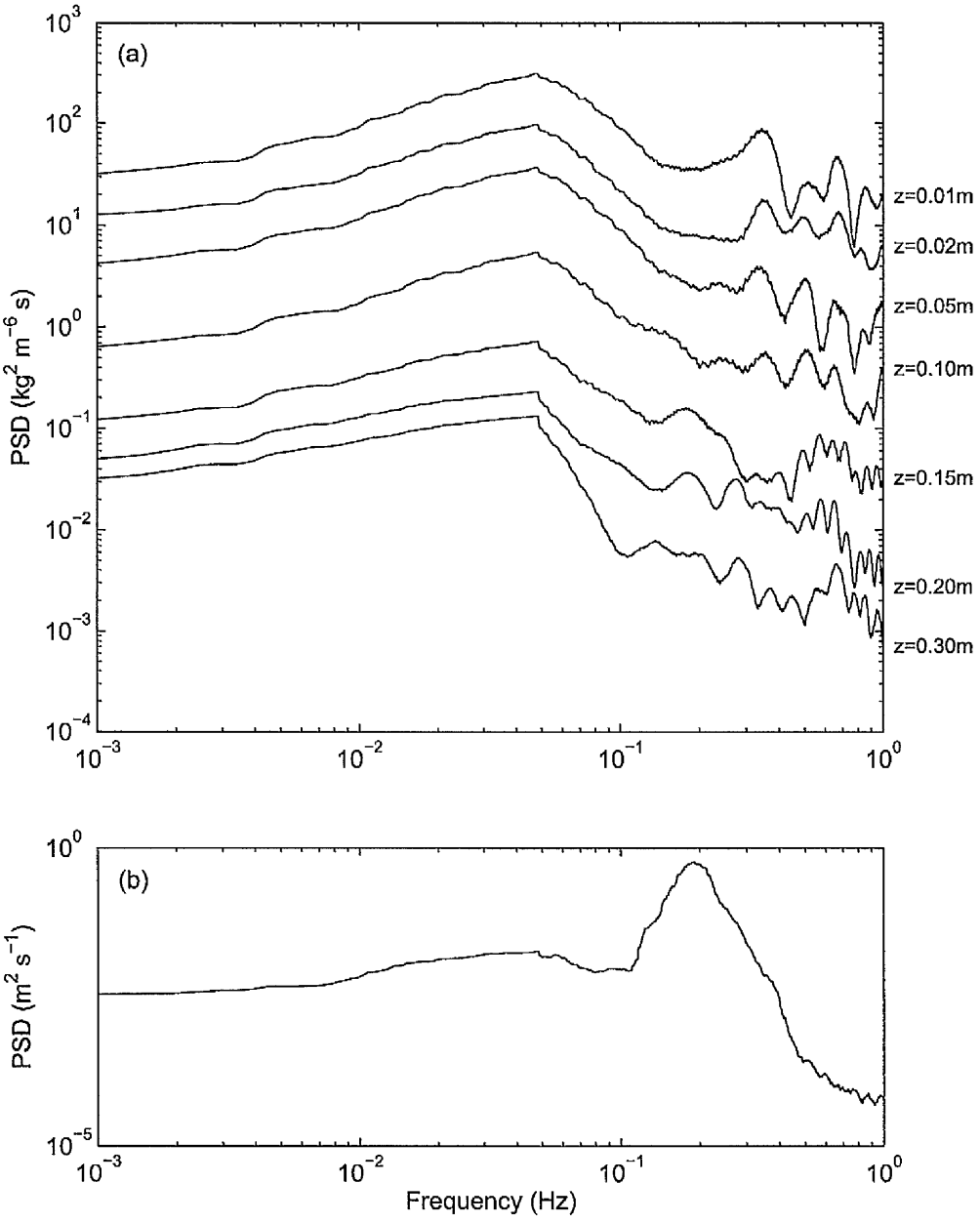

Figure 6.7: The power spectral density, PSD, of (a) instantaneous suspended sediment concentration, SSC, at different heights, z, above the bed, and (b) horizontal cross-shore velocity from M04.

and steep sided ripples were present on the bed there was a similar underlying structure to the SSC field (Figure 6.8(b)) with sediment pumping starting at approximately 130 and 200 seconds. There was also some sediment pumping due to a shorter duration wave group starting at approximately 90 seconds. There were however increased amounts of intermittent entrainment under the smaller orbital velocities associated with vortex entrainment (O'Hara Murray et al., 2011, and Chapter 5). The results in Figure 6.8(c) are from M06 when $H_s = 1.05$m and steep sided quasi-2D ripples dominated the bed, and shows enhanced sediment entrainment during the three dominate wave groups. The sediment entrainment occurring at wave frequencies occurred during most of the wave cycles, however, and successfully entrained sediment to $z \sim 0.2$m. This is because the orbital diameter was greater than the ripple wavelength for most wave cycles in this experiment (O'Hara Murray et al., 2011, and Chapter 5). In Figure 6.8(d), showing results from when $H_s = 1.51$m and 3D ripples dominated the bed, the SSC at $z > 0.3$m was > 0.1 kg m^{-3} during most of the 5 minute time-series. The SSC at z=0.05m was lower under the larger waves than when $H_s = 1.05$m (Figure 6.8(c)). The faces of the quasi-2D ripples in M06 were steeper than the 3D ripples in M08 and encouraged flow separation and enhanced turbulence production close to the bed. Finally, Figure 6.8(e) shows the SSC field when $H_s = 1.63$m and large hummocks populated the bed. When $H_s = 1.63$m the SSC was generally lower, throughout the water column, than when $H_s = 1.51$m. This was most likely associated with the transition from 3D ripples to hummocks, reducing turbulence production and coherent vortex formation and shedding.

6.4 Discussion

Time-series of SSC up to 0.8m above the bed have been examined above an evolving medium-grained sandy bed. The order of bedform development as the significant wave height stepped up was: 2D ripples, quasi-2D ripples, 3D ripples and hummocks. Whilst the suspension of sediment occurred at a variety of different time scales, a common feature across all the experiments was increased sediment suspension during the passage of wave groups. This observation is in accordance with previous studies both in wave flumes (Villard et al., 2000; Vincent and Hanes, 2002; Williams and Bell, 2006) and in the field (Hanes, 1991; Osborne and Greenwood, 1993). The existence of high SSC at low wave-group frequencies is evident from both Figure 6.6 showing the SSC 0.01m above the bed in the frequency domain, and Figure 6.8 showing the SSC up to 0.8m above the bed in the time domain. Nevertheless, processes acting at higher, intra-wave, frequencies play an important role in the initial resuspension of sediment close to the bed. Furthermore, the influence of different bedforms and sediment grain-sizes on SSC is discussed by analysing SSC from the fine and medium-grained experiments under the same hydrodynamic conditions. Finally, the character of the wave groups and the implications of considering groups rather than individual waves in the modelling of coastal sediment transport is considered.

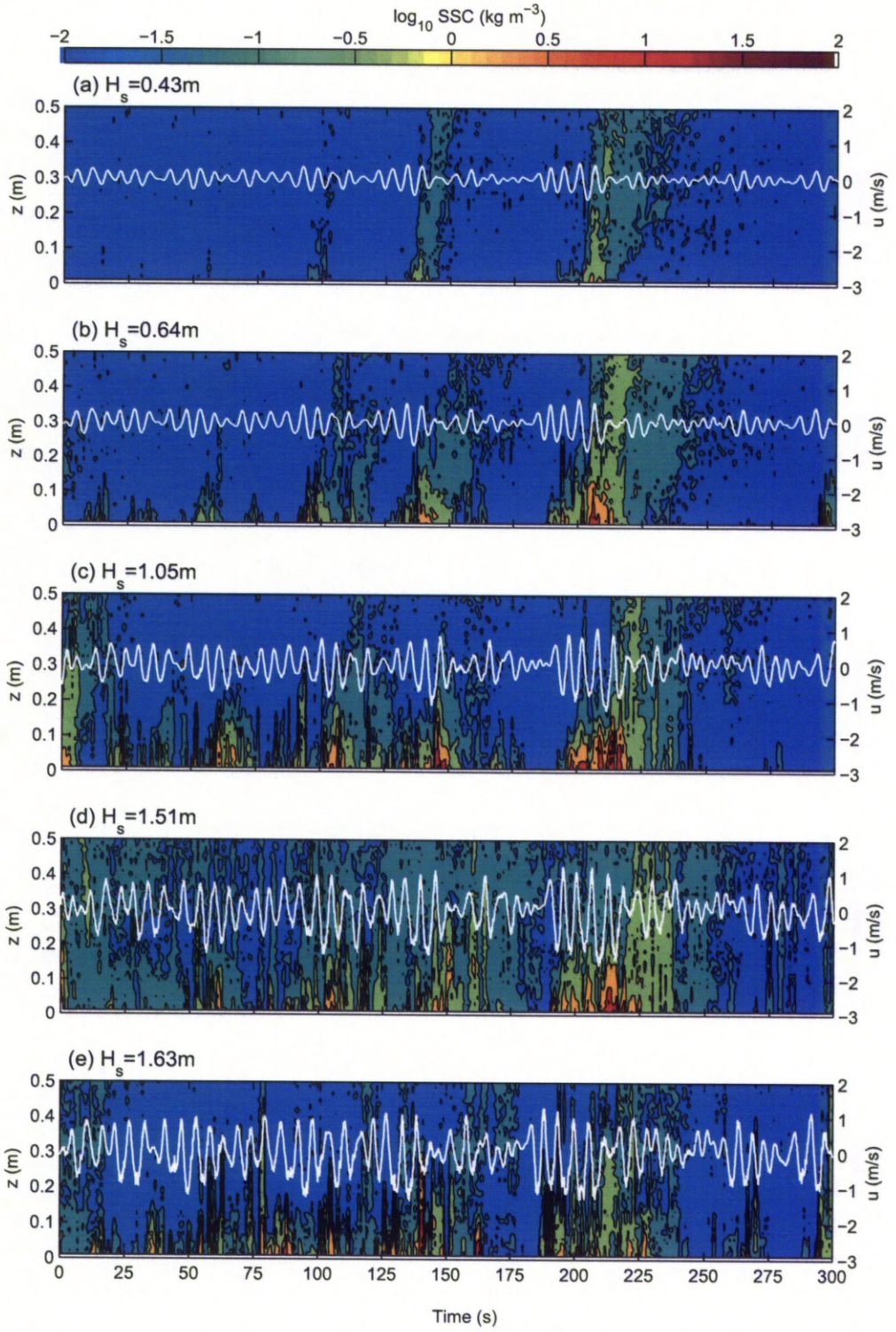

Figure 6.8: Time-series of instantaneous suspended sediment concentration (SSC) at 1Hz up to 0.5m above the bed from (a) M02, (b) M04, (c) M06, (d) M08 and (e) M11 during which the significant wave height, H_s, and bedform conditions differed. The height above the bed, z, is indicated on the left. The horizontal velocity time-series are shown in white with the velocity, u, scale on the right.

6.4.1 Near bed intra-wave sediment suspension processes over an evolving bed

The largest orbital velocities occurred during the passage of wave groups, and it is these high near bed velocities that are mainly associated with intra-wave sediment entrainment. For example vortex entrainment occurs above ripples when the orbital diameter is between one and four times the ripple wavelength (Malarkey and Davies, 2002). Hence, at 0.01m above the bed there are dominant peaks in the PSD of SSC at wave group frequencies. There are, however, peaks in the PSD of near bed SSC at higher, intra-wave, frequencies. There is a striking difference in the frequency of these intermittent intra-wave suspensions above (i) the 2D ripples and (ii) the 3D ripples and hummocks. Above the 2D ripples, the intra-wave suspension process occurred twice in the wave cycles and are associated with either the peak in shear stress occurring close to maximum velocity (Davies and Thorne, 2008) or with the advection of sediment-laden vortices over ripple crests around flow reversal (Nakato et al., 1977; Sleath and Wallbridge, 2002; Davies and Thorne, 2005; Van der Werf et al., 2007). Such intra-wave suspensions depend heavily on the orbital velocity and are intermittent under irregular waves (O'Hara Murray et al., 2011, and Chapter 5). Thus the peaks at intra-wave frequencies in Figure 6.6(a) have lower magnitudes than the broad peaks at wave group frequencies. Above the 3D ripples and hummocks the entrainment of sediment at intra-wave frequencies was again intermittent due to their dependence on the orbital velocity. Figure 6.6(b) shows these intra-wave processes to have occurred at the wave frequency. Vincent et al. (1999) observed a similar phenomena above mega-ripples: peak entrainment occurring above the mega-ripple crest at the instance of onshore-offshore flow reversal. The SSC remained high through the offshore half-cycle, due to the local advection of vortices at flow reversal and the advection of sand from other points on the mega-ripple profile (Vincent et al., 1999).

6.4.2 Comparison of wave group sediment resuspension above fine and medium-grained beds

Sediment resuspension patterns under wave groups above the medium-grained and fine-grained sand beds were compared. During M05, where $H_s = 0.85$m, the bed was dominated by quasi-2D ripples with an average steepness of 0.10. During F05, H_s was comparable (0.84m), but the quasi-2D ripples dominating the bed had a lower average steepness of 0.03. The other average ripple dimensions during these experiments are listed in Table 6.1. Figures 6.9(a and b) show 4 minute time-series of instantaneous SSC at 1Hz up to 0.5m above the medium-grained and fine-grained beds during M05 and F05 respectively, where $H_s \sim 0.85$m. Also shown in Figure 6.9 are the respective bedform cross-sections 1m either side of the ABS on a cross-shore line. Figures 6.9(c and d) are discussed later. During these time-series, presented in Figures 6.9(a and b), the orbital velocity amplitudes were <1m/s and two groups of higher than average orbital velocity amplitudes passed around 1250s and 1390s. During M05 there

was little sediment entrainment outside these wave groups. During F05, however, there was continual sediment entrainment during most wave cycles, due to the smaller grain size on the bed. Under the first wave group around 1250s, intra-wave sediment suspension occurred above both the medium and fine-grained beds in the near bed region of $z < 0.2$m. Wave pumping then entrained this sediment higher up. Whilst above the fine-grained bed the SSC was higher than that of the medium-grained bed for z<0.1m, in the region 0.1m<z<0.2m the SSC was generally higher above the medium-grained bed. One reason for this is the steeper ripples on the medium-grained bed, above which vortices helped to entrain sediment to these elevations at intra-wave time scales. For z>0.2m, the SSC was higher above the fine-grained bed: the fine grains were more efficiently pumped upwards whilst the medium grains settled downwards at a higher velocity. High concentrations of the fine-grained sand were maintained for considerably longer, $\sim$ 25s, than the medium-grained sand.

Figures 6.9(c and d) show the instantaneous SSC above the medium and fine-grained beds during M08 and F08 respectively, where $H_s \sim$ 1.5m. During M08 the medium-grained bed was dominated by large 3D ripples, the average dimensions of which are listed in Table 6.1. In contrast, during F08 the fine-grained bed was nominally planar. In Figures 6.9(c and d) the majority of orbital velocity amplitudes were <1m/s and only exceeded 1m/s during the two wave groups around 1250s and 1390s. During M08, the two wave groups marked periods of near bed sediment entrainment under consecutive waves and entrained sediment high above the bed, due to wave-pumping. During F08 the bed was planar and sheet flow processes were dominant. There was little intra-wave sediment entrainment and yet there were periods of SSC $\sim$1kg m^{-3} through the 0.5m shown in Figure 6.9(d). This generally occurred immediately after high orbital amplitudes associated with wave groups. During the wave groups themselves, the near bed SSC peaked. During the passage of wave groups the SSC confined to the sheet flow layer must, therefore, have been extremely high and eventually 'burst' from the near bed region and quickly pumped upwards by the relatively strong wave forcing. The high SSC through the water column in Figure 6.9(d) is the sediment settling out during the later passage of smaller waves. This bursting from the bed after the peak in the wave group is similar to the 'decay burst' phenomenon noted by Villard et al. (2000) and Vincent and Hanes (2002) where higher than average suspension events occurred toward the end of wave groups, under rapidly decreasing wave heights.

There were increased amounts of intra-wave sediment entrainment activity close to the bed under waves outside the wave groups during M08 (Figure 6.9(c)) compared with M05 (Figure 6.9(a)) due to the larger orbital velocities. Whilst the near bed intra-wave events in M08 occurred more frequently and typically had higher vertical coherence than in M05, the SSC further away from the bed was typically lower in M08 than in M05, even though H_s was larger. This is interpreted to be because of the interaction of the hydrodynamics and the steep sided ripples present during M05 where coherent vortices entrained significant concentrations of sediment (O'Hara Murray et al., 2011, and Chapter 5).

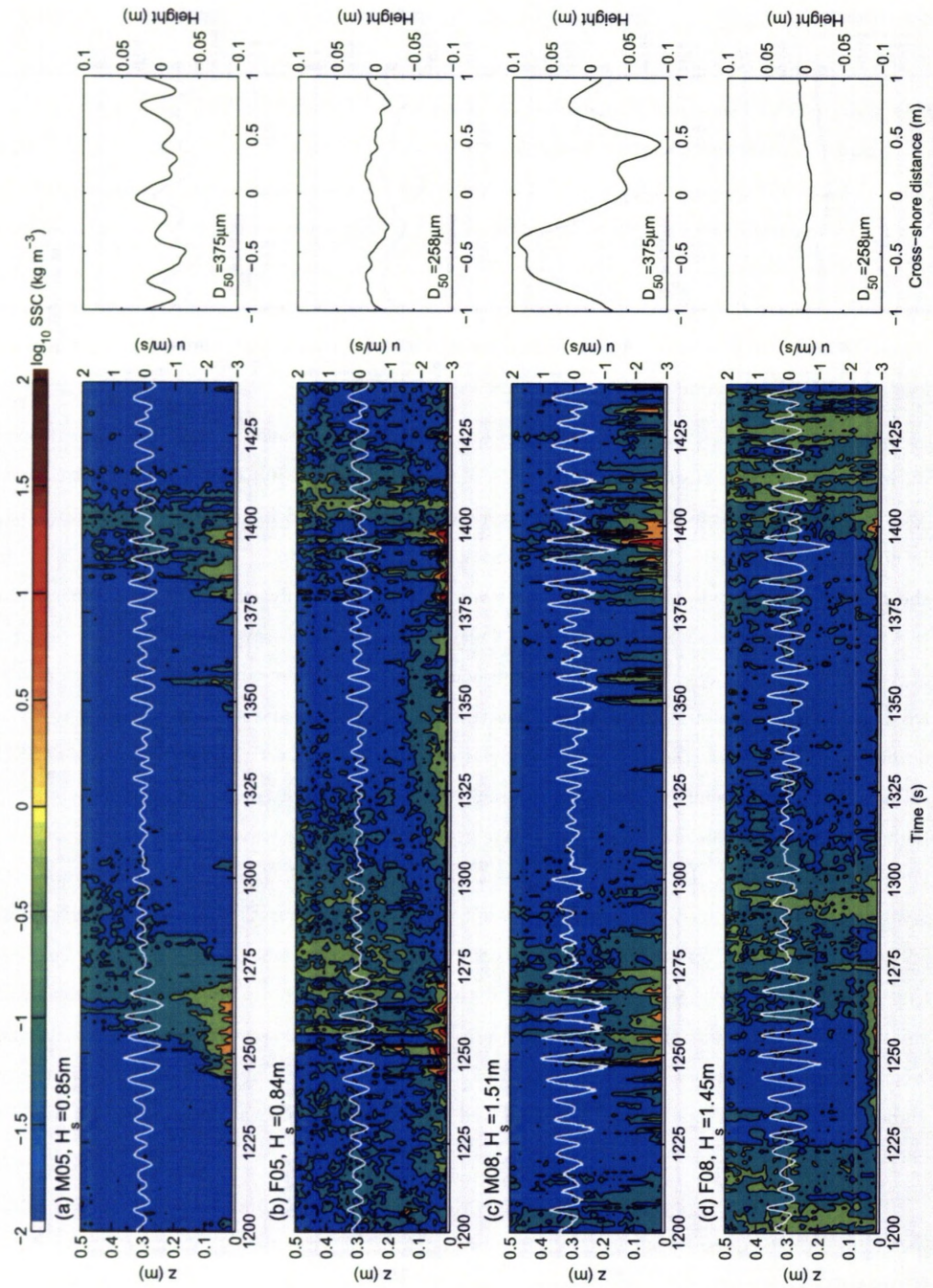

Figure 6.9: Time-series of instantaneous suspended sediment concentration (SSC) at 1Hz up to $z = 0.5$m above the bed from (a) M04, (b) F04, (c) M08 and (d) F08. The bedform cross-sections from the acoustic ripple profiler are shown on the right for each experiment and the median grain diameters of the bed sediment, D_{50}, are indicated.

The wave cycle-mean SSC profiles through a wave group above the medium-grained and fine-grained beds are now compared. Figure 6.10(a) shows the horizontal velocity time-series of the wave group identified around 1250s in Figure 6.9 with the wave cycles defined to start at the zero-up crossings (offshore-onshore flow reversal). Figure 6.10(b) shows the corresponding wave cycle-mean SSC profiles above the medium-grained (black solid lines) and fine-grained (red dashed lines) rippled beds, together with their wave group mean profiles (fainter lines). The cycle-mean SSC profiles changed shape during the passage of the wave group, broadly in accordance with changes observed by Villard et al. (2000). This was due to (i) enhanced intra-wave suspension during the larger waves and (ii) wave-pumping effects. The medium and fine-grained sands broadly follow a similar response, although there are clear differences due to the different grain size and ripple geometries, including ripple steepness. During the first two waves, the SSC was lower than the wave group mean at all heights above the bed. It is under the larger third and fourth waves that the SSC close to the bed approached and increased above the group-mean concentration. This near bed concentration remained high during the four largest waves and only reduced below the wave group mean concentration during the seventh, smaller, wave. Above 0.2m there was a delayed response with the SSC only approaching the wave group mean SSC during waves four and five above the fine and medium-grained beds respectively. The response of the medium-grained sand was slower due to the larger grain sizes. During the final two (fine) and three (medium) waves in the wave group the SSC was generally higher for $z > 0.2$m than for $z < 0.2$m: the sediment pumped up during the passage of the wave group remained in suspension while there was little intra-wave sediment entrainment under the final small waves. Under the four largest waves, waves 3 - 6, the decay of sediment concentration with height was approximately exponential up to $\sim$ 0.13m and $\sim$ 0.08m above the medium and fine-grained rippled beds respectively, approximately 4.5 times the respective ripple heights. The height to which time average SSC profiles are exponential is typically three to four times the ripple height (Van Rijn, 1993; Van der Werf et al., 2006; Thorne et al., 2009a), as was found to be the case in Chapter 5. This region of exponential decay is closely related to the vertical extent of turbulence, or boundary layer thickness, due to flow separation and the upward propagation of vortices (Villard et al., 2000). The vertical extent of turbulence is larger, $\sim$ 4.5 times the ripple height, during the largest waves in the group than during the measurement burst on average, $\sim$ 3 times the ripple height. The exponential decay length scales, L, of the cycle-mean SSC profiles were roughly constant during waves 3 - 6, with $L =$ 0.03 - 0.06m above the medium-grained bed and $L = 0.01$m above the fine-grained bed. These differences in L above the two bed types are associated with the corresponding differences in ripple steepness and the extent to which flow separation occurred (see Chapter 5).

During M03 - M06, $H_s = 0.54 - 1.05$m, the bed was populated by steep sided 2D or quasi-2D ripples. The time average SSC profiles from M04 and M06 presented in Figure 6.4 - lines (b) and (c) - are similar in form because of the common bedform conditions. In Figure 6.10(b) the only cycle-mean profiles that resemble the time average profiles presented in Figure 6.4

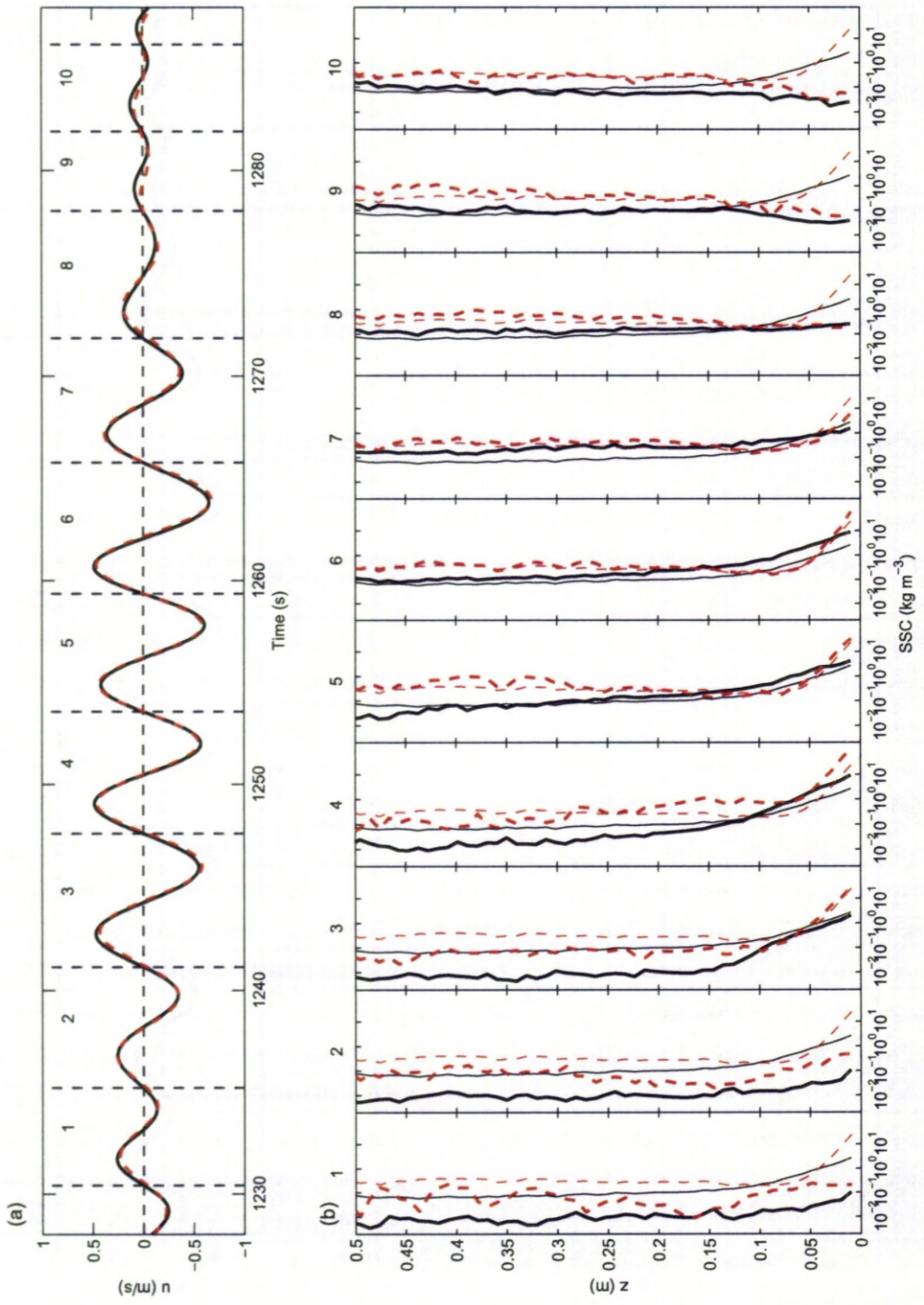

Figure 6.10: Wave cycle mean suspended sediment concentration, SSC, profiles from M05 (black) and F05 (red) through a wave group. (a) shows the horizontal velocity time-series from the ADV with each wave cycle identified, and (b) shows the cycle mean SSC profiles for each wave. Also shown in (b) by the fainter lines are the wave group mean SSC profiles.

are those from the largest four waves, waves 3 - 6. This is because during these waves there was substantial intra-wave sediment entrainment that contributed to the time average SSC profiles. The cycle-mean concentrations during the smaller waves also contribute to the total time average SSC, but mainly at elevations of $z > 0.2$m where SSC are maintained by wave pumping.

6.4.3 Importance of considering wave group character

The observation that wave groups entrain more sediment higher into the water column than individual waves indicates that the sediment is more susceptible to transport by near surface unidirectional currents beneath wave groups. The consideration of wave group character, may refine sediment transport models and the experimental design of field data collection. Here, a range of wave group types are identified. Wave groups are defined here as two or more waves that share similar velocity amplitudes (above and below the mean) that are separated by waves and/or wave groups of different, but not necessarily lower, velocities. Four broad types of wave groups are postulated and are depicted in Figure 6.11: (i) waxing (increasing velocity amplitudes), (ii) waning (decreasing velocity amplitudes), (iii) waxing then waning (increasing then decreasing velocity amplitudes) and (iv) constant (short-term regular velocity amplitudes). Another important variable in the character of wave groups is the number of waves in a group. The type of wave group, and the number of waves in a group, could have a significant impact on the height and amount of sediment suspension. One simple hypothesis is that a waxing wave group would pump more sediment higher above the bed than a waning wave group with the same number of waves. Another hypothesis considering two waxing wave groups with different numbers of waves, is that more sediment would be pumped higher under the group with more waves.

To start to test these hypotheses of wave group character, wave groups that conform to the four types, outlined in Figure 6.11, were identified in the ADV velocity time-series. Figure 6.12 shows the instantaneous SSC time-series during these four wave groups from M05 where $H_s = 0.85$m and the bed was populated by quasi-2D vortex shedding ripples. The wave groups identified all occurred during a 5 minute period of time, while the ABS was above the mid point between the crest and trough of a ripple. There are a number of factors that make this comparison difficult including (i) the difference in wave characteristics, including velocity amplitudes, across each type of group and (ii) the difference in length of each group. The wave groups were chosen in order to minimise such complications. For example, in Figures 6.12(a – c) the length of the time-series' shown are 34 seconds. Unfortunately, the group of approximately constant wave heights shown in Figure 6.12(d) is 63 seconds in duration. Despite these differences there are some general observations that can be made. The largest 'burst' of sediment to $z > 0.2$m occurred at the end of the waxing wave group shown in Figure 6.12(a). This is an example of a 'decay burst' occurring when a wave group is terminated by a sudden reduction in the orbital velocity amplitude (Villard et al., 2000; Vincent and Hanes, 2002). There are two

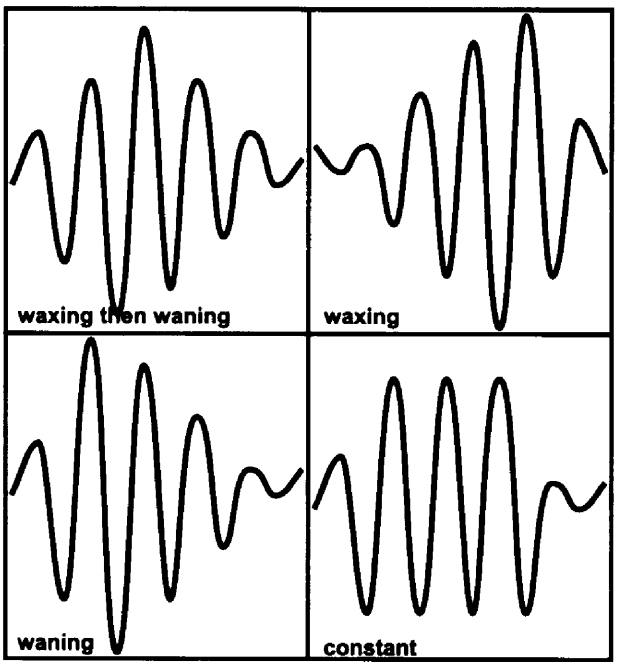

Figure 6.11: Cartoon of four wave group types.

vertical advection events shown in Figure 6.12(d): at the end of the group under the smaller velocity amplitudes and under the fifth oscillation, which is marginally smaller in amplitude than the other oscillations. This first vertical 'burst', at $\sim$ 340s, was relatively short lived and is likely to be associated with the high SSC entrained during the previous cycle. At the end of the wave group in Figure 6.12(d), there was a time lag of 2 cycles between entrainment at the bed and relatively high SSC at $z \sim 0.4$m, typical of the wave-pumping effect. During the wave groups shown in Figures 6.12(b and c) there were no upward 'bursts' because the wave groups were not terminated by a sudden reduction in the velocity amplitude, as was the case in Figure 6.12(a).

6.5 Conclusions

Over the large range of bedform and irregular wave forcing conditions observed entrainment events occurred throughout the water column at frequencies an order of magnitude smaller than the wave frequency. These infra-gravity events were due to the passage of wave groups, where higher than average orbital velocities led to repeated intra-wave sediment entrainment. The sediment entrained by intra-wave processes was then pumped to higher elevations with each subsequent wave cycle within the group at rates higher than the grain settling velocity. Time lags of 2 - 3 wave cycles were observed between initial sediment entrainment and peak SSC at $z > 0.5$m above the bed.

Intra-wave sediment suspension processes dominate the lower part of the flow, especially

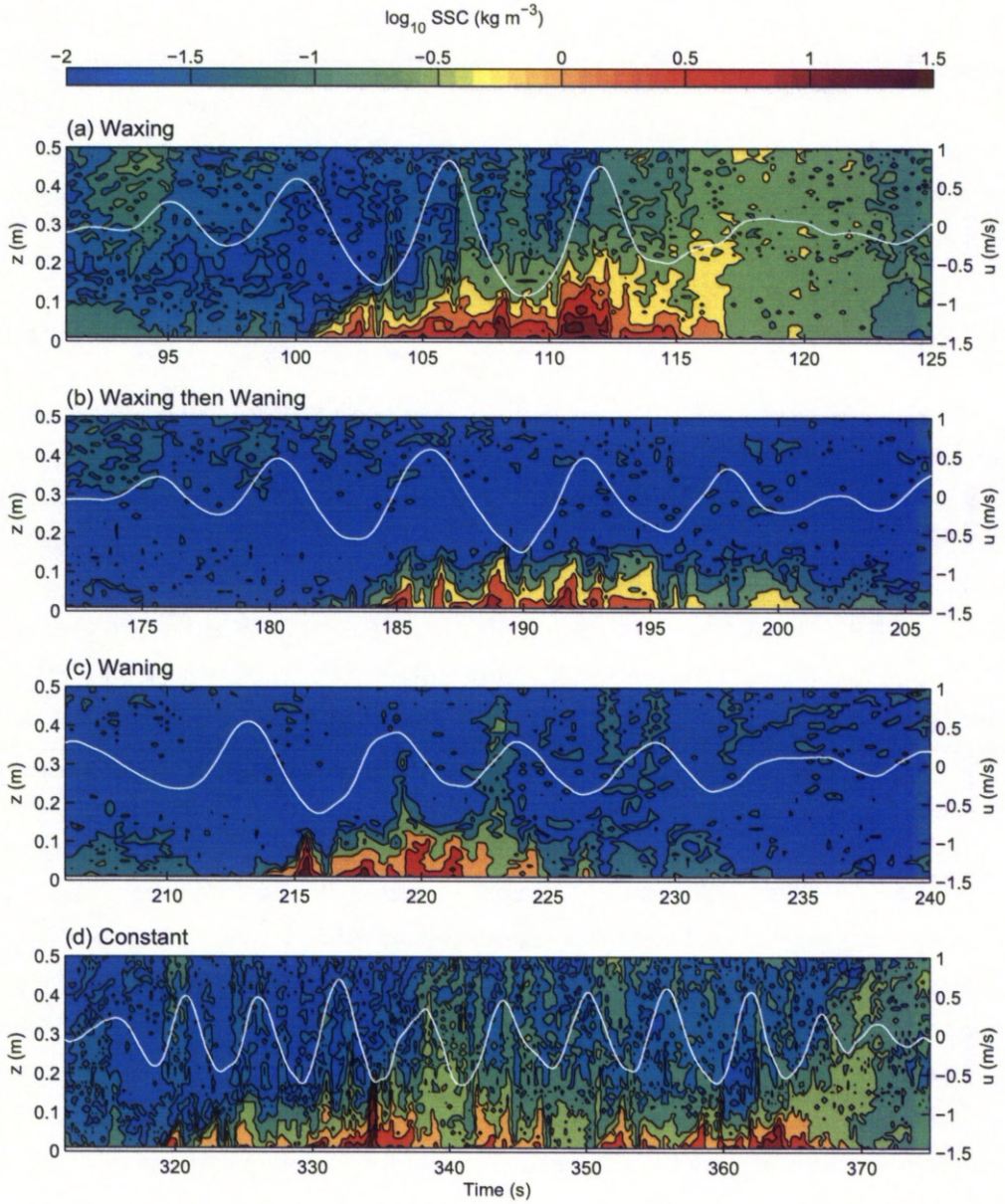

Figure 6.12: Examples of suspended sediment concentration, SSC, times-series under wave groups that broadly conform to four different types illustrated in Figure 6.11: (a) waxing, (b) waxing then waning, (c) waning and (d) constant. The height above the bed, z, is indicated on the left and the horizontal velocity time-series are shown in white with the velocity, u, scale on the right.

when coherent vortices are entrained, as is the case above ripples. This can result in high SSC in this near bed region that is arguably the most important to consider when calculating net suspended sediment transport (Van der Werf et al., 2006). It is however, important to also consider the entrainment of sediment to higher elevations under wave groups. The wave pumping effect examined here is a mechanism by which sediment can be entrained to elevations that would otherwise be unobtainable under randomly distributed waves with similar characteristics. Once at these high elevations the suspended sediments can remain in suspension for a number of wave periods, depending on its settling velocity. This substantially increased suspension time can lead to increased cross-shore or long-shore transport, especially in the presence of time average currents.

The comparison made of fine and medium-grained sediment suspensions under equivalent wave forcing confirmed that once entrained to high elevations via wave pumping, the fine-grained sand was more concentrated and remained in suspension for longer than the medium-grained sand. This is because of the difference in settling velocity between the two sand grain-sizes. The initial intra-wave entrainment of the medium-grained sand reached higher elevations than that of fine-grained sand however. This was due to the substantially steeper medium-grained ripples which encouraged enhanced turbulence production and vortex formation and shedding in some cases. Above both fine and medium-grained sands the wave boundary layer was larger under the more energetic waves in a group. It was during these waves that the vertical extent of mixing was at a maximum during which substantial sediment was entrained. The vertical decay length scales of the largest waves in the group were ~ 4.5 times the ripple height.

It is proposed that the characteristics of the wave group can strongly influence the suspension of sediment at elevations of $z > 0.2$m. Both waxing and constant wave group types are terminated by a sudden reduction in the velocity amplitude. Such sudden terminations encourage the 'decay burst' phenomenon (Villard et al., 2000; Vincent and Hanes, 2002) where substantial sediment concentrations can be advected high above the bed. The waning, and waxing then waning, wave group types have a more gradual termination. During the wave groups studied with these characteristics, there was no substantial vertical advection of sediment observed for $z > 0.2$m.

Wave groups are characteristic of irregular wave forcing, which is typical in the field. The simultaneous measurements of velocity and SSC presented here were made in a large scale flume facility, offering some reduction in the complexity of the natural world. However, much more refined experiments in smaller scale facilities are recommended to further examine the importance of irregular waves, and wave group character, on the SSC. Specifically, experiments with a strong control over the character of wave groups are recommended in order to reduce the uncertainties considered in Section 6.4.3. It is also advised to design experiments where wave groups are repeated (such as Villard et al., 2000), enabling stochastic uncertainties in the suspension field to be further reduced. The outcome of such detailed studies is important to inform numerical modeling workflow, and to refine the design of large scale and field experiments.

Acknowledgments

This work was supported by the European Union, through its access to large-scale facilities, and by the Natural Environment Research Council and the University of Liverpool for PhD funding. The authors thank Prof. J. J. Williams at Associated British Ports, who coordinated the Deltaflume experiments and Dr. Paul S. Bell and Dr. Benjamin D. Moate at the National Oceanography Centre for many usefully discussions regarding the analysis of the acoustic data. We would also like to thank Prof. Stephen S. Flint at the School of Environmental Sciences, University of Liverpool, for his support.

Chapter 7

A stormy inheritance: the interaction of irregular wave forcing, bedforms and suspended sediment concentrations in an experimental waxing and waning hydrodynamic regime

Abstract

The passage of a storm event was simulated in a series of field scale flume experiments by systematically stepping up and down the significant wave height of weakly asymmetrical irregular waves. This enabled the interaction of hydrodynamic forcing, bedforms, and suspended sediments to be analysed over a variety of sediment transport regimes. At each stage of the storm sequence, acoustic measurements were made of the water velocities, plan-form and cross-sectional bedform geometries and suspended sediment concentration profiles over a fine-grained sand bed and then over a medium-grained sand bed. At weak and intermediate wave forcing, suborbital ripples with a variety of different plan-form geometries dominated both the fine and medium-grained beds. At the peak in the storm sequence, the fine-grained bed flattened out, whereas on the medium-grained bed large hummocks, with dimensions comparable to mega-ripples, formed. During the waning stages of the storm sequence the fine-grained bed exhibited a delayed response to the drop in the wave forcing and inherited remnants remained from the peak in the storm. In contrast, the medium-grained bed responded relatively quickly to the drop in wave forcing and suborbital ripples reformed. The time-mean suspended sediment concentration profiles were examined in relation to both the wave forcing and bedform conditions during the storm sequence. Above ripples, the sediment concentration profiles decayed exponentially within a near bed layer that was at least equal in thickness to two times the exponential decay length scale. This is because the sediment diffusivity was height-constant close to the bed which is indicative of coherent sediment entrainment mechanisms. Within the near bed region above all of the rippled beds observed, the exponential decay length scale was found to vary with the Shields parameter, the ripple height and equivalent bed roughness that included both contributions due to sheet flow and form drag processes above steep sided ripples. Thus the bedform dimensions and suspended sediment concentration profiles were united during a waxing and waning storm sequence.

7.1 Introduction

The hydrodynamic forcing, the seabed, and the suspension of sediment together form a dynamic and interacting sediment transport triad (Thorne and Hanes, 2002). Therefore in a changing environment, typical of most near-shore zones, it is important to consider the interaction of all three components. There has been much work done on the response of sand ripples to changes in the hydrodynamics (Marsh et al., 1999; Traykovski et al., 1999; Doucette and O'Donoghue, 2006; O'Donoghue et al., 2006; Austin et al., 2007) and the differences in sediment resuspension above different bedforms have also received much attention (Ribberink and Al-Salem, 1994; Dolphin and Vincent, 2009). Studies have also been made in the field of all three components of the triad (e.g. Grasmeijer and Kleinhans, 2004). Such studies, however, involve highly complex hydrodynamic forcing due to the interaction of waves and currents as well as numerous other complications such as along-shore drift and bioturbation. Large scale facilities bridge the gap between the complex natural environment and overly simplified small scale laboratory setting and include oscillatory flow tunnels (Ribberink and Al-Salem, 1994; O'Donoghue and Clubb, 2001; O'Donoghue et al., 2006; Van der Werf et al., 2006, 2007) and wave flumes (Thorne et al., 2002, 2003; Williams et al., 2004; Davies and Thorne, 2005; Dohmen-Janssen and Hanes, 2005; Thorne et al., 2009a). An emerging common goal has been to study all three components of the sediment transport triad in such facilities, and to examine the interactions and feedbacks in detail. However, detailed measurements made under irregular free surface waves, representing a variety of hydrodynamic, bedform and sediment suspension regimes are still uncommon.

This paper presents measurements of the sediment transport triad, including wave forcing, bedforms and suspended sediments, taken during an experimental storm sequence generated in a large scale flume facility, the Deltaflume of Deltares, Delft Hydraulics, the Netherlands. The comprehensive dataset was collected under irregular free surface waves of varying height and steepness. Some of this data was used in previous studies focusing on the bedforms (Williams et al., 2004; Williams and Bell, 2006) and intra-wave structure of the suspended sediments (O'Hara Murray et al., 2011, and Chapter 5). Here, data from all the experiments are used and each component of the triad is studied in an integrated manner in order to address (i) how the sand bed responds to changes in the wave forcing; (ii) how the suspend sediment concentration, SSC, changes in response to the changing flow and bed conditions; (iii) whether relict bedforms persist after the peak in the storm sequence; and (iv) whether these relict features strongly influence the SSC.

Section 7.2 outlines some background and terminology and Section 7.3 introduces the experiments that were performed in the Deltaflume. In Section 7.4 the irregular wave forcing is parameterised and measurements of the water elevation and water velocities are compared. The response of the bed and SSC to the changing wave forcing is detailed in Sections 7.5 and 7.6 respectively. Finally, in Section 7.7, the three components of the sediment transport triad are brought together with a discussion of (i) inherited bed morphology and the influence it has on

the suspended sediments during the storm sequence; (ii) the influence of the wave irregularity on the bedforms and SSC; and (iii) the connection between the decay of SSC with height above the bed and the equivalent bed roughness.

7.2 Theory and terminology

7.2.1 Irregular wave parameterisations

Whether modelling suspend sediment concentration or the dimensions of the ripples on the bed it is important to accurately describe the hydrodynamics. The wave height and period of regular (monochromatic) waves can be used in conjunction with linear wave theory to calculate the regular near bed excursion influencing bedform development and sediment re-suspension. However, when the waves are irregular an equivalent regular wave is often used. This equivalent regular wave contains no information about the often broad distribution of wave heights and periods that induce a broad response from the near bed sediments. It is important, therefore, for the equivalent regular wave to describe the waves that are strongly influencing the near bed sediments. Many use the peak spectral period and significant wave height to describe this equivalent wave (e.g. Green, 1999) and others suggest that the root mean square wave height should be used (Fredsoe and Deigaard, 1992; Soulsby, 1997). It has also been suggested that the mean of the highest one tenth orbital velocity amplitudes captures the relevant hydrodynamics forcing bedform development (O'Donoghue et al., 2006; Amos et al., 1996).

7.2.2 Wave generated bedform classification

Wave generated bedforms are usually referred to as ripples. However, there are numerous types with different plan-form and cross-sectional geometries. Clifton (1976), and more recently Wiberg and Harris (1994), defined three kinds of ripples based on their cross-sectional geometric characteristics relative to the size of the wave orbital excursion diameter, d_0, defined beneath regular waves as

$$d_0 = U_0 T/\pi, \tag{7.1}$$

where U_0 and T are the wave orbital velocity amplitude and period respectively. The first kind of ripples are *orbital ripples* which have wavelengths, λ, that scale with d_0, for example $\lambda = 0.65 d_0$ (Miller and Komar, 1980), and sharp well defined trochoidal shaped crests. The second are *anorbital ripples* which are less steep than orbital ripples and have wavelengths that do not scale with d_0, but that depend on the median diameter of the bed sediment, D_{50}. An intermediate type, *suborbital ripples*, have wavelengths shorter than those of orbital ripples but still show some dependence on d_0. Clifton and Dingler (1984) proposed the approximate boundaries for the transition from orbital to suborbital and suborbital to anorbital as $d_0/D_{50} = 2000$ and 5000 respectively, with suborbital ripples occurring within this range. This terminology was adopted by Pedocchi and Garcia (2009) who also defined round-crested orbital ripples as being

steep sided ripples with wavelengths that scale with d_0 but, unlike orbital ripples, their crests were rounded. Hanes et al. (2001) introduced the terminology of short wave ripples (SWR) with $\lambda = 0.04-0.25$m and long wave ripples (LWR) with $\lambda = 0.35-2$m. SWR tend to encompass the majority of ripples including orbital, suborbital and anorbital. In contrast, LWR tend to have very low steepness, wavelengths larger than d_0, often have irregular and multimodal wavelength distributions and can be superimposed with SWR (Hanes et al., 2001; Williams et al., 2005).

In addition to the cross-sectional geometry, it is important to consider the plan-form geometry of wave ripples. This is because many of the quantitative models (e.g. Nielsen, 1981; Mogridge et al., 1994; Wiberg and Harris, 1994; Soulsby and Whitehouse, 2005) imply that the ripple crest lines are continuous and aligned perpendicular to the flow. This is not necessarily the case in many field settings (Marsh et al., 1999). Boyd et al. (1988) observed a number of wave formed ripples with different plan-form geometries on an ocean shore face, and defined six bedform types ranging from straight crested to bifurcated ripples. Osborne and Vincent (1993) classified wave generated bedforms in terms of their size, the suspension process occurring above them, the number of crest dimensions (i.e. their plan-form geometry) and whether the cross-sectional profile was symmetric. The terminology followed here for plan-form ripple geometry is that adopted by Pedocchi and Garcia (2009) who defined ripples as either (i) two-dimensional (2D) with long straight crests perpendicular to the flow, (ii) three-dimensional (3D) with irregular and short crests or (iii) almost two-dimensional (quasi-2D) with crests perpendicular to the flow but with shorter and more sinuous crests than those of 2D ripples.

7.2.3 Bedform evolution and inheritance under waves

Many sediment transport models assume the bed to have adjusted to any recent change in the hydrodynamics and to be in equilibrium. Often however, the bed is in a continual state of change, especially in areas such as the surf zone that experience great change through a tidal cycle (Austin et al., 2007). Changes in the wave steepness can have a profound effect on the bed, and in turn on the suspended sediments above. Under waves of low steepness, 2D ripples of low steepness typically dominate. As the waves steepen these 2D ripples increase in steepness, becoming vortex ripples (Davies and Thorne, 2008). As the wave steepness increases further, the bedforms reduce in steepness and the bed tends towards a transitional state of large, and often 3D, washed out ripples and hummocks (Vincent and Osborne, 1993; Green and Black, 1999). Eventually, under storm conditions, the bed becomes plane and sheet flow dominates.

Smaller bedform features, such as ripples, that form under waves of low steepness can generally adapt to new forcing conditions relatively quickly, such as tens of minutes (Traykovski et al., 1999). On the other hand, larger bedforms, such as hummocks, that form under more energetic waves, take longer to respond to changes in wave forcing. This is especially true if there is a reduction in wave forcing, associated with, for example, a waning of a storm. Such bedforms could therefore be left as relict forms.

7.2.4 The vertical distribution of suspended sediment

The suspended sediment concentration, SSC, profile, $C(z)$, can be expressed as

$$C(z) = C_r \, \Phi(z) \tag{7.2}$$

where $C_r = C|_{z=r}$ is the concentration magnitude at a specific near-bed elevation ($z = r$) and is termed the reference concentration and $\Phi(z)$ is the distribution of suspended sediment with height, z, above the bed, often termed the shape function. The time average sediment diffusion equation

$$w_s C + \varepsilon_s \frac{dC}{dz} = 0, \tag{7.3}$$

where w_s and ε_s are the sediment settling velocity and sediment diffusivity respectively, represents a balance between the downward sediment flux due to settling, $w_s C$, and the upward sediment flux, $\varepsilon_s dC/dz$, due to turbulent diffusion. Assuming the sediment diffusivity to be height constant, a solution to equation (7.3) is

$$C(z) = C_0 \, \mathrm{e}^{-z/L}, \tag{7.4}$$

with $L = \varepsilon_s / w_s$ being the exponential decay length scale and C_0 the reference concentration taken at $z = 0$, typically the ripple crest level. Both Nielsen (1992) and Van Rijn (1993) suggested that above rippled beds the diffusivity has a constant value within a near bed region of approximately three times the height of the ripples, η. Nielsen (1992) gave

$$\varepsilon_s = 0.016 k_s U_0, \tag{7.5a}$$

where k_s is the equivalent bed roughness due to the ripples given by $k_s = 8\eta \, \eta/\lambda$, and λ is the ripple wavelength. Van Rijn (1993) gave

$$\varepsilon_s = 0.004 D_* U_0 \times 3\eta, \tag{7.5b}$$

where $D_* = D_{50}[(s-1)g/\upsilon^2]^{1/3}$ is a dimensionless grain size with g, s and υ being the acceleration due to gravity, the sediment to water density ratio and kinematic viscosity of the water respectively. Nielsen (1992) also developed empirical expressions for L, for use above ripples and under waves, L_N, given by

$$L_N = \begin{cases} 0.075 \frac{U_0}{w_s} \eta & \frac{U_0}{w_s} < 18 \\ 1.4\eta & \frac{U_0}{w_s} \geq 18. \end{cases} \tag{7.6}$$

The dependence of L_N on the ripple height illustrates the role that the ripples play in the suspension of sediment under waves. For example, when $U_0/w_s > 18$ the ripple height is the only control on the decay length scale and the form of the SSC profile remains the same

regardless of the orbital velocity.

7.2.5 Empirical reference concentration formulae

There are a number of different empirical formulations for the reference concentration, C_r, taken at different near-bed elevations and suitable above different bed conditions, such as rippled or plane beds. One common approach is to expresses C_r as a function of the grain roughness Shields parameter, $\theta_{2.5}$, given by

$$\theta_{2.5} = \frac{f_{2.5} U_0^2}{2(s-1) g D_{50}}, \tag{7.7}$$

where s is the ratio of sediment density to water density (s=2.65 for quartz sand), g is the acceleration due to gravity and $f_{2.5}$ is the grain roughness wave friction factor (skin friction) based on the equivalent Nikuradse grain roughness, $k_s = 2.5 D_{50}$, and can be calculated using, for example, the formula of Soulsby (1997):

$$f_{2.5} = 0.237 (d_0 / 5 D_{50})^{-0.52}. \tag{7.8}$$

Nielsen (1986) and Green and Black (1999) found that the reference concentration taken at bed level, C_0, can be calculated as

$$C_0 = \alpha \, \rho_s \theta_{2.5}^3 \tag{7.9}$$

where ρ_s is the sediment density and α is a constant. Green and Black (1999) found that the value of α depends on the type of bedforms present with $\alpha = 0.005$ for hummocky and transitional beds, where sheet flow processes may have occurred, and $\alpha = 0.1$ for rippled beds. Nielsen (1986) found $\alpha = 0.005$ for plane beds (sheet flow) and rippled beds providing that the flow enhancement over the ripple crests was accounted for. This was done by replacing $\theta_{2.5}$ in equation (7.9) with a ripple modified Shields parameter given by

$$\theta_r = \frac{\theta_{2.5}}{(1 - \pi \, \eta / \lambda)^2}. \tag{7.10}$$

Lee et al. (2004) developed a formulation for the reference concentration taken at 1cm above the bed, C_1, in terms of $\theta_{2.5}$, w_s and the skin friction shear velocity, $u_{*2.5}$,

$$C_1 = (2.58 \pm 1.17)(\theta_{2.5} \, u_{*2.5} / w_s)^{(1.45 \pm 0.04)}. \tag{7.11}$$

The calculation of suspended sediment fluxes depends upon the magnitude of SSC close to the bed. Hence the accurate prediction of the reference concentration is important. In Section 7.6.4 these simple empirical models are compared with the reference concentrations measured during a range of flow and bed conditions.

7.3 Instrumentation and experimental storm sequence

The Deltaflume of Deltares Delft Hydraulics, the Netherlands, is a large scale flume (230m long, 5m wide and 7m deep) that enables sediment transport processes to be monitored at field scale. Irregular waves were generated in a series of experiments during which the significant wave height, H_s, was systematically stepped up and down in order to simulate the waxing and waning of a storm sequence. During the course of the experiments the peak spectral wave period, T_p, was held constant at $T_p \sim 6$ seconds such that the surface wave steepness increased with H_s. In this paper the systematic stepping up and down of H_s, in approximate 0.2m step sizes, is termed the *experimental sequence*. Similarly, the experiments during which H_s was stepped up are termed the *waxing phase* of the storm sequence and the experiments during which H_s was stepped down are termed the *waning phase* of the storm sequence. The experimental sequence was conducted twice: first over a fine-medium-grained sand bed and then over an upper-medium-grained sand bed. These two sediment beds are here referred to as the *fine* and the *medium*-grained beds. Using laser granulometry, the two sediment beds were found to have grain size distributions lognormal in form, with the fine-grained bed having $D_{10} = 161\mu$m, $D_{50} = 258\mu$m and $D_{90} = 408\mu$m and the medium-grained bed having $D_{10} = 243\mu$m, $D_{50} = 375\mu$m and $D_{90} = 577\mu$m. In each case, a 0.7m deep sediment bed was laid down in the centre of the flume in a 30m long region spanning the width of the flume. The sand beds were initially flat and were not flattened between experiments such that each experiment inherited the bed morphology formed during the previous experiment (Bell and Williams, 2002). Over the fine-grained bed 16 experiments were conducted and are referred to here as F01, F02, ..., F16. Similarly, over the medium-grained bed 17 experiments were conducted, referred to here as M01, M02, ..., M17. After each step change in H_s the waves were left running for one hour in order for the bedforms to reach an equilibrium state (Marsh et al., 1999), and then measurements were made for 25 minutes.

Figure 7.1 is a schematic of the instruments deployed on a frame aligned to one side of the Deltaflume in the centre of the sandy bed. The instrumentation has previously been described by Williams et al. (2004, 2005) and O'Hara Murray et al. (2011, and Chapter 5). In this study, data from a Nortek Vector Acoustic Doppler Velocimeter (ADV) were used to measure the water velocities. The ADV was mounted at the offshore end of the frame and its measuring volume was $\sim$ 0.5m above the bed. The ADV recorded at 16Hz the three components of the flow: horizontal along-flume (cross-shore), horizontal across-flume (along-shore) and vertical. The ADV velocity components were despiked using a Phase-Space Thresholding Method (Goring and Nikora, 2002) and rotated to correct for any misalignment of the instruments with the main flow direction by calculating the principle axis of variation (Emery and Thompson, 1997). In this study, the horizontal cross-shore velocity component is used. The bedforms were studied using a Sector Scanning Sonar (SSS) and an Acoustic Ripple Profiler (ARP) which were respectively mounted at the onshore end of the frame $\sim$ 0.6m above the bed and in the centre of the

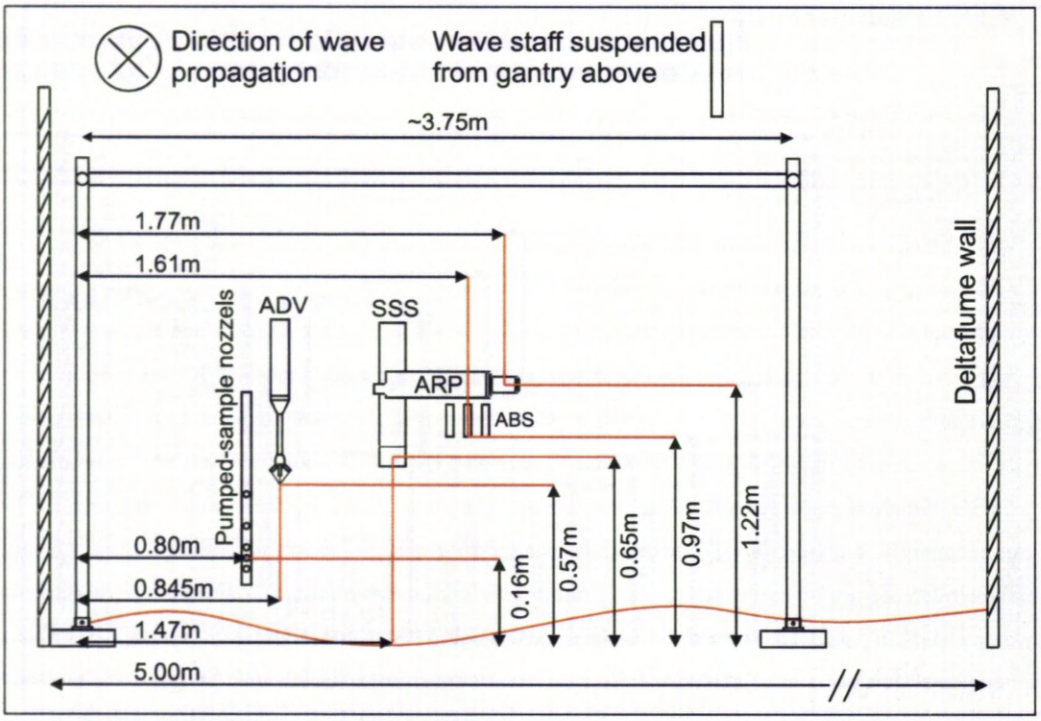

Figure 7.1: Schematic of the instrument frame deployed in the Deltaflume with the locations of the Acoustic Ripple Profiler (ARP), Acoustic Backscatter System (ABS), Acoustic Doppler Velocimeter (ADV), Sector Scanning Sonar (SSS) and pumped sampling nozzles indicated.

frame $\sim$ 1.2m above the bed. The 1.2MHz SSS results were rectified from polar to square grid coordinates (Bell and Williams, 2002) to give 5x5m images of the bed, enabling the planform geometry of the bedforms to be studied. The 2.0MHz ARP scanned a 4m across-shore transect of the bed approximately once a minute at centimetre horizontal resolution and sub-centimetre vertical resolution providing a cross-sectional profile of the bed, and how it changed with time. The suspended sediments were measured using an Acoustic Backscatter System (ABS) mounted in the centre of the frame $\sim$ 0.9m above the bed. The ABS comprised three transceivers, operating at 1.0, 2.0 and 4.0 MHz, aligned perpendicular to the flow (along-shore) and recorded backscatter profiles at 1cm vertical resolution. The ABS collected backscatter profiles at 128Hz at each frequency, which were each subsequently block averaged in order to improve the statistical reliability of the results to produce backscatter profiles at 4Hz. The ABS data, which have previously been studied at intra-wave time scales (O'Hara Murray et al., 2011, and Chapter 5), were used to measure the time average SSC. To aid the acoustic inversion of the ABS data, pumped samples (Bosman et al., 1987) were taken at up to five heights above the bed during each experiment. These samples of the suspended sediment were dry weighed to give the SSC and analysed using laser granulometry to obtain grain size distributions. Multiplication factors of 1.41 and 1.43 were applied to the fine and medium-grained pumped sampled SSC respectively, in order to account for the limited sediment trapping efficiency of the pumped sampling system Bosman et al. (1987).

7.4 Irregular wave forcing

The irregular surface waves generated conformed to JONSWAP spectra (Carter, 1982) with peak enhancement factors of $\gamma = 3.3$ (Bell and Williams, 2002). The water surface elevation, Γ, was measured at 25Hz by a wave staff suspended above the flume. The significant wave height was calculated from the standard deviation of the water surface elevation, $\sigma(\Gamma)$, for each experiment using

$$H_{s\Gamma} = 4\sigma(\Gamma). \tag{7.12}$$

The peak spectral wave period, T_p, was taken as the inverse of the frequency at which the power spectra of Γ peaked. $H_{s\Gamma}$ and T_p are listed in Table 7.1 for all the experiments apart from M10 and M11 when the wave staff failed to function correctly. In addition to these measurements from the water surface elevation, the significant wave heights were calculated from the horizontal cross-shore velocity recorded by the ADV. This enabled wave height measurements to be made for M10 and M11, and to provide independent wave height measurements for the other experiments. The method outlined by Wiberg and Sherwood (2008) was used to calculate the significant wave height from the power spectra of the horizontal cross-shore ADV time-series using linear wave theory:

$$H_s = 4\sqrt{\sum_{i}^{N} \frac{S_{v,i}\Delta f_i}{[2\pi f_i \cosh(k_i z_A)/\sinh(k_i h)]^2}} \tag{7.13}$$

where $S_{v,i}$ and k_i are the power spectral density and wavenumber respectively at the frequency f_i, z_A is the height of the ADV above the bed, h is the mean water depth, $\Delta f_i = f_i + 1 - f_i$ and N is the number of frequency intervals within the range $0.06 \leq f \leq 0.4$. This frequency interval was chosen in order to exclude high frequency contributions due to turbulence and those frequencies associated with attenuated wave motions. The H_s measurements are listed in Table 7.1. Typically, H_s was within $1 - 2\%$ of $H_{s\Gamma}$, confirming the veracity of the significant wave height measurements. Figure 7.2 shows the waxing and waning of the significant wave heights during the course of the experimental storm sequence conducted over the fine and medium-grained sand beds. During the course of the experiments the peak spectral wave period remained broadly constant with $T_p = 5.9 - 6.1$s, with the majority of the experiments having $T_p = 6.1$s.

7.4.1 Irregular wave orbital velocities and velocity asymmetry

One method for describing orbital velocities under irregular waves is to calculate the near bed orbital velocity amplitude of an equivalent regular wave. Thus, using linear wave theory and replacing the wave height and period by $H_{s\Gamma}$ and T_p the significant orbital velocity amplitude

Exp.	$H_{s\Gamma}$ (m)	H_s (m)	T_p (s)	$U_{s\Gamma}$ (m/s)	U_s (m/s)	d_s (m)	$f_{2.5}$	$\theta_{2.5}$	B
F01	0.289	0.278	6.082	0.192	0.179	0.347	0.013	0.049	-0.033
F02	0.379	0.371	6.068	0.252	0.238	0.462	0.011	0.075	0.020
F03	0.505	0.495	5.851	0.333	0.318	0.617	0.010	0.116	0.009
F04	0.644	0.635	5.851	0.425	0.410	0.795	0.008	0.169	0.000
F05	0.849	0.838	6.026	0.565	0.538	1.044	0.007	0.252	0.006
F06	1.060	1.060	6.111	0.701	0.669	1.300	0.007	0.349	0.037
F07	1.277	1.276	6.111	0.839	0.799	1.550	0.006	0.453	0.074
F08	1.474	1.453	6.111	0.967	0.908	1.762	0.006	0.547	0.067
F09	1.355	1.353	6.111	0.881	0.839	1.630	0.006	0.488	0.069
F10	1.268	1.270	6.111	0.827	0.791	1.535	0.006	0.446	0.061
F11	1.166	1.180	6.111	0.758	0.729	1.415	0.006	0.396	0.064
F12	1.065	1.077	6.111	0.694	0.667	1.295	0.007	0.347	0.060
F13	0.851	0.870	6.068	0.554	0.540	1.048	0.007	0.254	0.051
F14	0.649	0.658	6.068	0.421	0.408	0.793	0.008	0.168	0.040
F15	0.468	0.462	6.082	0.305	0.294	0.571	0.010	0.103	0.008
F16	0.354	0.352	6.068	0.231	0.220	0.428	0.012	0.067	-0.006
M01	0.350	0.336	6.068	0.234	0.217	0.421	0.014	0.055	0.047
M02	0.450	0.435	6.068	0.300	0.279	0.541	0.012	0.080	0.010
M03	0.548	0.535	6.068	0.367	0.344	0.669	0.011	0.109	0.019
M04	0.653	0.638	6.068	0.436	0.410	0.795	0.010	0.141	-0.009
M05	0.854	0.847	6.068	0.572	0.545	1.059	0.009	0.215	0.009
M06	1.061	1.050	6.111	0.713	0.678	1.316	0.008	0.297	0.011
M07	1.276	1.293	6.111	0.846	0.818	1.589	0.007	0.392	0.042
M08	1.472	1.507	6.111	0.976	0.960	1.863	0.007	0.497	0.034
M09	1.631	1.635	6.111	1.084	1.044	2.026	0.006	0.562	0.042
M10	-	1.711	-	-	1.071	2.079	0.006	0.584	0.056
M11	-	1.634	-	-	1.023	1.987	0.006	0.546	0.051
M12	1.473	1.498	6.111	0.967	0.940	1.825	0.007	0.482	0.047
M13	1.275	1.277	6.111	0.839	0.803	1.559	0.007	0.382	0.030
M14	1.065	1.098	6.111	0.702	0.692	1.344	0.008	0.306	0.013
M15	0.859	0.887	6.068	0.561	0.556	1.079	0.009	0.221	-0.016
M16	0.652	0.671	6.068	0.427	0.421	0.818	0.010	0.147	-0.040
M17	0.548	0.554	6.068	0.360	0.349	0.677	0.011	0.111	-0.054

Table 7.1: Temporally averaged experimental parameters for the irregular wave Deltaflume experiments.

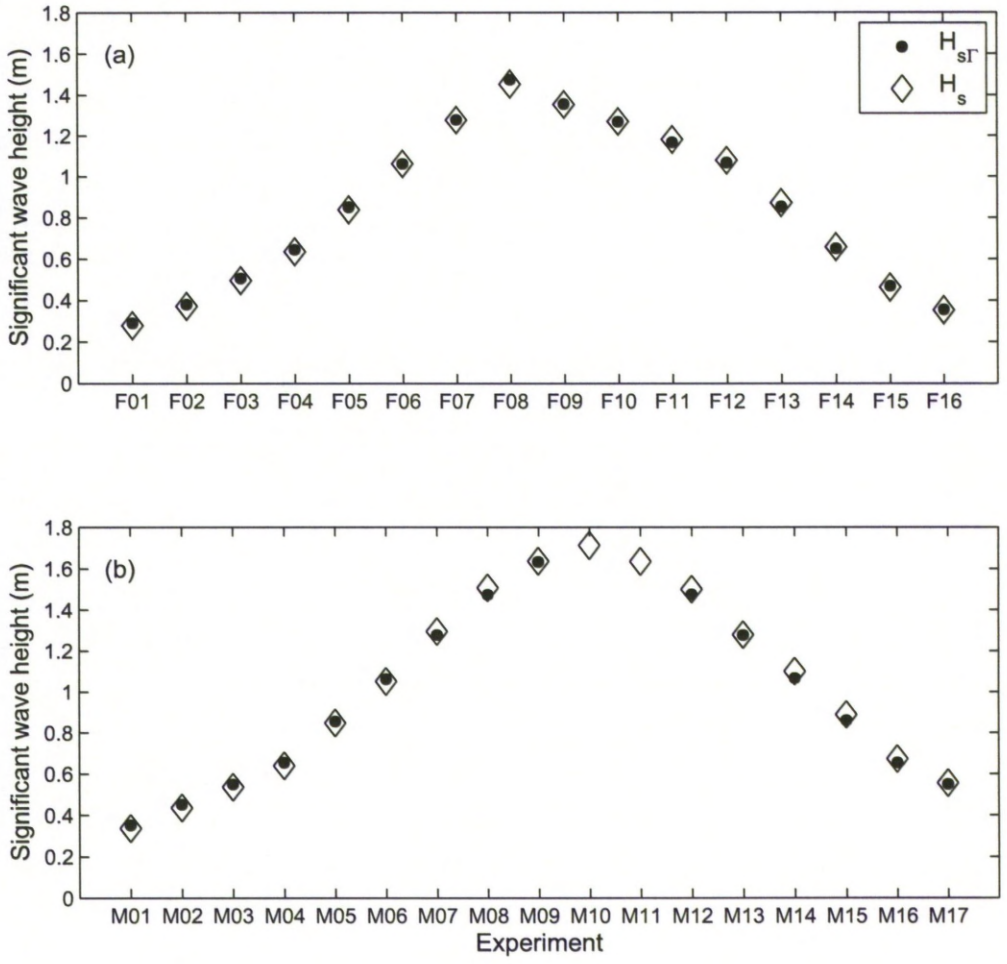

Figure 7.2: Significant wave height measurements from the water surface elevation, $H_{s\Gamma}$, and ADV velocities, H_s, for each the experiment during (a) the fine-grained and (b) the medium-grained experimental sequences.

at the top of the wave boundary layer was defined as

$$U_{s\Gamma} = \frac{\pi\, H_{s\Gamma}}{T_p \sinh(k_p h)} \tag{7.14}$$

where h is the water depth and k_p is the wavenumber obtained by solving the dispersion equation $(2\pi/T_p)^2 = g\, k_p \tanh(k_p h)$, where g is the acceleration due to gravity. An alternative method is to calculate the significant orbital velocity from the spectra of the ADV velocities, S_v, using

$$U_s = \sqrt{4 \sum_{i}^{N} S_{v,i} \Delta f_i}. \tag{7.15}$$

Equations (7.14) and (7.15) were used to calculate $U_{s\Gamma}$ and U_s respectively, and the results listed in Table 7.1. In general, it was found that $U_s/U_{s\Gamma} \sim 0.96$ suggesting a 4% reduction in $H_{s\Gamma}$ was necessary when using equation (7.14). This broadly agrees with the findings of Davies and Thorne (2005) who reduced the wave heights by 9% beneath regular waves.

The wave staffs failed to operate during M10 and M11 and the $H_{s\Gamma}$ and $U_{s\Gamma}$ values do not form a complete record through the experimental sequence. In this paper, therefore, H_s and U_s, from the ADV velocity time-series, are used to parameterise the irregular waves during the course of the experiments. For each experiment the significant wave orbital diameter was calculated using

$$d_s = U_s T/\pi \tag{7.16}$$

with the wave period taken as T=6.1s and the results are listed in Table 7.1. The U_s and ds values in Table 7.1 were used in place of U_0 and d_0 in equations (7.7) and (7.8) to calculate $\theta_{2.5}$ and $f_{2.5}$ for each experiment and the results are included in Table 7.1.

The estimates of orbital velocity in Table 7.1, $U_{s\Gamma}$ and U_s, are *average* parameterisations similar to the significant wave height, in that they represent velocity amplitudes associated with equivalent regular waves. They do not, however, provide insight into either the distribution of near bed orbital velocities present other than to say that they result from a JONSWAP irregular wave spectrum; or the asymmetry of the waves present. Therefore, a zero-crossing analysis was performed on the horizontal cross-shore ADV velocity time-series, in order to determine the onshore and offshore velocity amplitude distributions. First, a rectangular low-pass filter was applied in order to remove high frequency turbulent fluctuations. The filtered and unfiltered time-series were compared, confirming there were no significant changes in the amplitude and phase of the cross-shore velocities as a result of the filtering. In the zero-crossing analysis, the zero-up-crossings were taken as the start of each wave and the maximum (positive) and minimum (negative) velocities between consecutive zero-up-crossings were taken as the onshore and offshore velocity amplitudes respectively. The asymmetry of the orbital velocities were assessed by calculating an asymmetry parameter given by

$$B = (U_{on} - U_{off})/(U_{on} + U_{off}) = U_2/U_1, \tag{7.17}$$

where U_1 and U_2 are the first and second harmonic velocity amplitudes of the equivalent Stokes second order wave, associated with the irregular waves generated during each experiment. The results are listed in Table 7.1. The asymmetry parameters were generally positive and never exceeded 0.074 indicating there was on average a weak onshore dominant velocity asymmetry. The variation in B from experiment to experiment broadly followed the variation in significant wave heights: experiments with the highest wave forcing had the largest asymmetry parameters. Asymmetry in the wave can lead to substantial differences in both the pickup and transport of sediment within each wave half cycle, and has significant implications for net cross-shore suspended sediment transport (Bijker et al., 1976; Davies and Thorne, 2008). Wave asymmetry can also influence the development of bedforms (Vincent et al., 1999).

The calculations of the significant wave heights and orbital velocity amplitudes from the spectra of ADV velocities, in addition to the calculations based on the water elevations, enabled the parameterisation of M10 and M11 when the wave staff failed to operate. It is, however, important to note the high level of agreement between the measurements of the free surface and of the water velocities. This agreement confirms both the veracity of the data recorded and the calculations performed, but also serves to show that there was little interference by the flume or instrument frame on the water velocities close to the bed. Finally, it is important to accurately parameterise the flow as it underpins both the development of bedforms and pickup and transport of sediment.

7.5 Bedforms response to wave forcing

The SSS images and ARP data provided insight into the plan-form and cross-sectional geometry of the bedforms respectively. The terminology of Pedocchi and Garcia (2009) has been adopted for the description of the bedforms plan-form geometry: 2D, quasi-2D and 3D.

Williams et al. (2004) used a zero down-crossing analysis to extract bedform height and wavelength measurements from the ARP profiles, and obtained wavelength estimates from the SSS images. The bedform wavelength measurements from the ARP and SSS were found to be comparable, confirming that the ARP profiles were representative of the bed as a whole. Here, the ARP profiles were first de-trended by subtracting second or third order polynomials fitted to the profiles, and a zero-crossing-analysis was then performed. This procedure, however, failed to detect small ripples that did not cross the zero-line. For this reason a turning point analysis was used for this study. First, a low pass Gaussian filter was used to remove high frequency fluctuations from each profile in order to detect the underlying bedform profiles. There were occasional spikes in the ARP profiles most likely due to the resuspension of large concentrations of sediment under the more energetic waves. In order to smooth through these spikes, a temporal running average was performed on the ARP profiles collected during an experiment.

7.5.1 Fine-grained bedforms response to wave forcing

To observe how the plan-form and cross-sectional geometries of the bedforms responded to the changing wave forcing the SSS images and ARP profiles were studied together. Figure 7.3 presents the ARP and SSS results from eight fine-grained experiments: four during the waxing phase (F01, F02, F04 and F06), one at peak wave forcing (F08) and three during the waning phase (F12, F14 and F16). These show the different bedform types that developed as H_s was changed. Figure 7.3(a) presents the ARP results in the form of 4m long cross-sections of the bed as surfaces with three axes: cross-shore distance, vertical height and time. Each surface is composed of $\sim$ 10 minutes worth of data which show that there was little change in the bedform cross-sections during each experiment. An appreciation of the plan-from bedform geometry can be gained from the SSS images shown by Figures 7.3(b – i), and interpretative drawings obtained by tracing over the dominate crests lines are shown. The variable contrast and dark fringes, in Figures 7.3(b – i), are coursed by strong acoustic backscatter from sediment resuspension during the most energetic waves and to the SSS beam pattern (Williams et al., 2004).

During the first experiment over the fine-grained bed (F01) very low amplitude and short wavelength ripples, barely within the sensitivity of the ARP were present in the ARP scans shown in Figure 7.3(a) at H_s=0.28m. The SSS image, shown in Figure 7.3(b) does not readily resolve these very small ripples. During F02, straight crested 2D ripples, with crest lines aligned normal to the flow, were visible in both the ARP cross-sections (Figure 7.3(a) at H_s=0.37m) and SSS image (Figure 7.3(c)). As H_s increased the crests of the 2D ripples became more sinuous and curved such that by F04 quasi-2D ripples had formed. The ARP cross-sections, in Figure 7.3(a) at H_s=0.64m, from F04 show the ripples to be generally larger in amplitude and more spatially variable, in terms of both height and wavelength than during F02 (Figure 7.3(a) at H_s=0.37m). This variability was likely to have been because the profiles were taken over ripples the crests of which were curved and less continuous than true 2D ripples. Thus the ARP profiles and SSS image (Figure 7.3(d)) together support the inference of quasi-2D ripples during F04. Figure 7.3(e) shows that this quasi-2D plan-form bedform geometry was replaced by long and straight crested 2D ripples when H_s=1.06m. Figure 7.3(a) at H_s=1.06m shows the ARP cross-sections during M06 which confirm the existence of bedforms with $\sim$ 0.9m wavelengths. During F08, the wave forcing peaked at H_s=1.45m and the bed flattened out, as can be seen in Figure 7.3(f). The ARP cross-sections of the plane bed during F08 in Figure 7.3(a) at H_s=1.45m show a large scale, low amplitude, undulation in the bed with $\sim$ 2m wavelength broadly conforming to LWR (Hanes et al., 2001).

During the waning phase above the fine-grained bed, the SSS images resembled those from the waxing phase at similar H_s values. The SSS images from experiments F09 – F12 suggest that long crested 2D ripples with wavelengths similar to those in F06 formed. For example, Figure 7.3(e) and Figure 7.3(g), from experiments F06 and F12 respectively, where $H_s \sim$ 1m, show a similar plan-form view of the bed. The dominant feature, however, in the ARP cross-

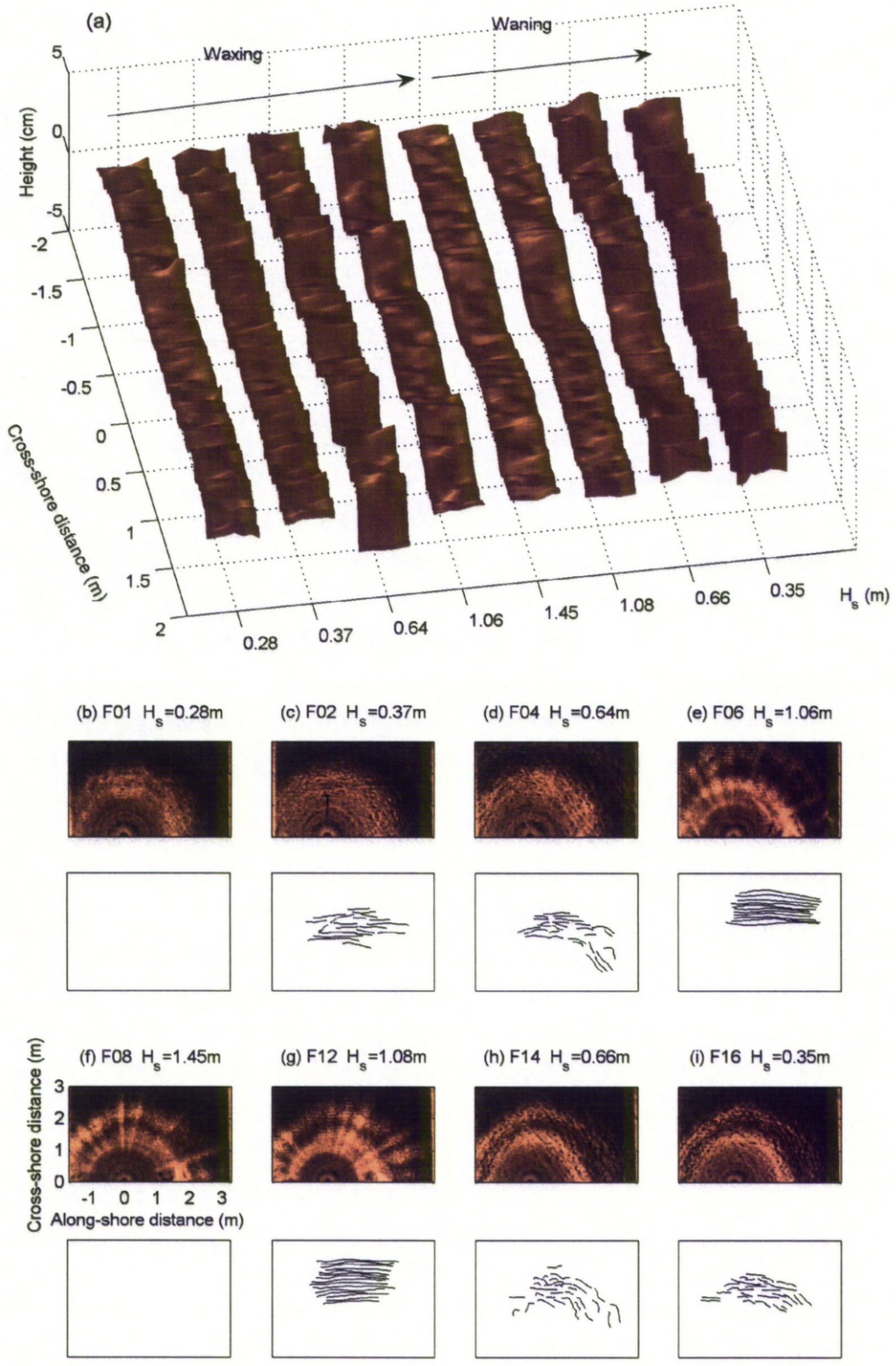

Figure 7.3: A selection of fine-grained bedform results highlighting the different bedform types that developed in response to step changes in the significant wave height, H_s. (a) The response of the ARP cross-sections during the waxing ($H_s = 0.28 - 1.45$m) and waning ($H_s = 1.45 - 0.35$m) phases of the experimental sequence. (b – i) The SSS images taken at the end of each respective experiment and interpretative drawings indicating the plan-form geometry.

sections during F12 shown in Figure 7.3(a) at H_s=1.08m, is a long wavelength $\sim$ 2m (LWR) feature. This difference between the ARP and SSS results indicate that ripples did not reform over the whole bed during the first few experiments of the waning phase (F09 – F12). By F14 the ripples were more 2D in plan-form, shown by Figure 7.3(h), and their cross-sections, shown by Figure 7.3(a) at H_s=0.66m, resembled those that formed under equivalent wave forcing during the waxing phase. There was, however, an underlying undulation reminiscent of the LWR present during F08 – F12. The response of the fine-grained bed to the waning wave forcing, with particular reference to the presence of relict structures, is further discussed in Section 7.7.

7.5.2 Medium-grained bedforms response to wave forcing

The response of the medium-grained bedforms to the waxing phase of the wave forcing was somewhat different to that of the fine-grained bedforms and this is shown in Figure 7.4. Note that the vertical scale in Figure 7.4(a) is twice that of Figure 7.3(a) in order to display the larger medium-grained bedforms. The initial medium-grained plane bed evolved into a bed of round crested ripples with 2D plan-form geometries and reasonably continuous crests by M02, as shown in Figure 7.4(b). The ARP cross-sections in Figure 7.4(a) at H_s=0.43m, show the ripple wavelengths to be reasonably uniform across the 4m transect. During M03 the ripple cross-sections, shown in Figure 7.4(a) at H_s=0.54m, suggest that the ripples increased in size and steepness. The ripples were clearly visible in the SSS image and Figure 7.4(c) shows the plan-form geometry to be 2D. Round crested quasi-2D ripples, with sinuous crest lines, formed during M05, shown by Figure 7.4(d), and the ARP cross-sections, in Figure 7.4(a) at H_s=0.85m, show that the ripple wavelengths and heights were more spatially variable across the 4m transect. During M07 large ripples with 3D plan-form geometries formed (Figure 7.4(e)) and the ARP cross sections, in Figure 7.4(a) at H_s=1.29m, indicate low amplitude structures between two larger amplitude structures. This spatial variability in the cross-sectional ripple geometry is due to the 3D plan-form geometry: the ripple crests were not necessarily parallel or perpendicular to the oscillatory flow direction and the ARP transects bisected ripple crests at both wide and narrow points. Figure 7.4(f) shows that at peak wave forcing (M10) there were bedform structures with 3D geometries similar to the hummocks described by Green and Black (1999), but their scale resembled that of lunate mega-ripples (Vincent and Osborne, 1993; Vincent et al., 1999). The cross-sections for these large structures during M10 are shown in Figure 7.4(a) at H_s=1.71m.

The order of the emergence of different plan-form geometries was broadly reversed during the waning of the surface wave forcing above the medium-grained bed. As H_s was stepped down from peak forcing, 3D ripples emerged during M12 and M13. The ARP and SSS results from M13 are shown in Figure 7.4(a) at H_s=1.28m and Figure 7.4(g) respectively. Quasi-2D ripples formed during M14 and M15 and the ARP and SSS results for M15 are shown in Figure 7.4(a) at H_s=0.89m and Figure 7.4(h) respectively. Finally, during M16 and M17, where H_s was

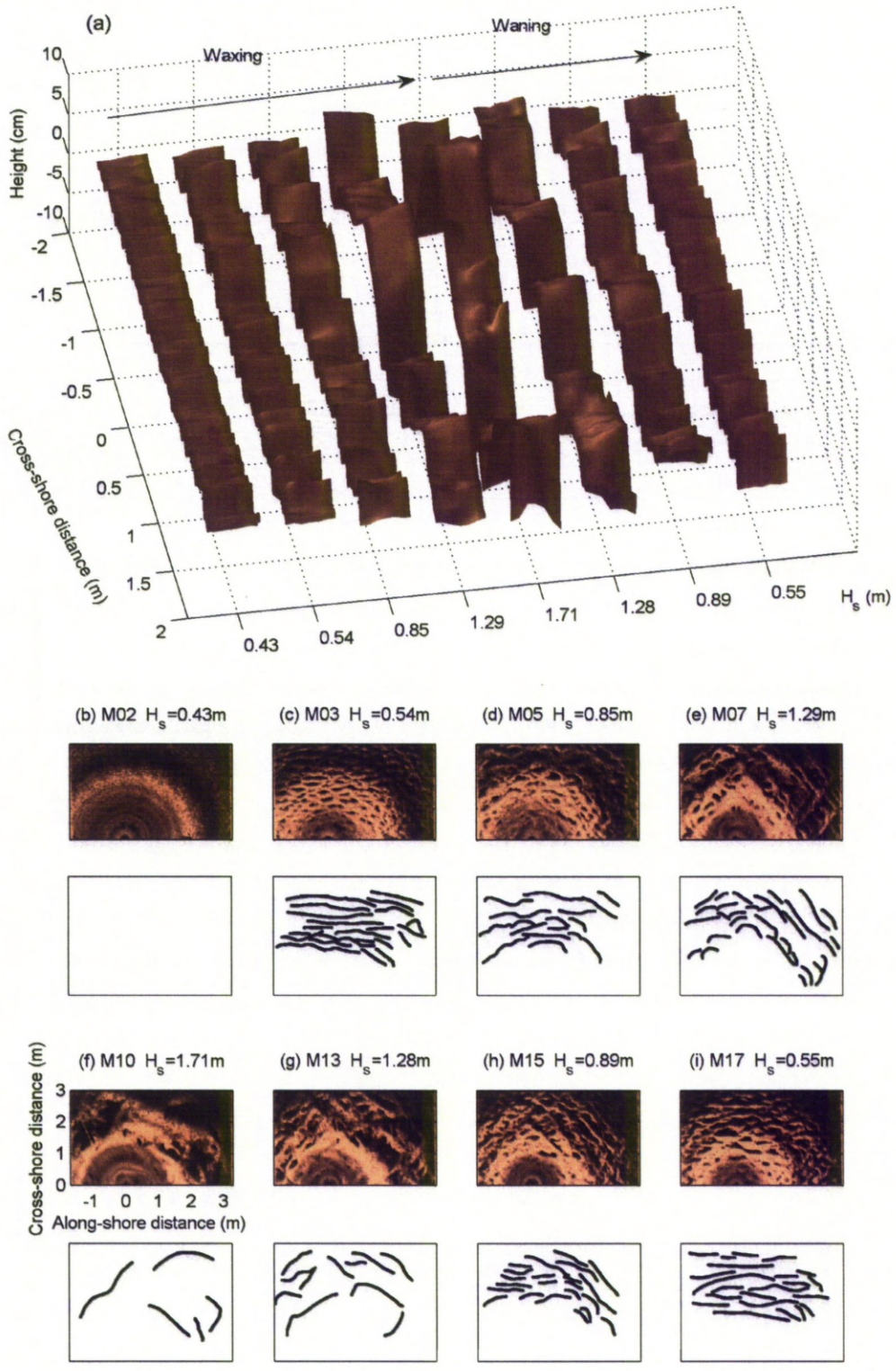

Figure 7.4: A selection of medium-grained bedform results highlighting the different bedform types that developed in response to step changes in the significant wave height, H_s. (a) The response of the ARP cross-sections during the waxing ($H_s = 0.43 - 1.71$m) and waning ($H_s = 1.71 - 0.55$m) phases of the experimental sequence. (b – i) The SSS images taken at the end of each respective experiment and interpretative drawings indicating the plan-form geometry.

reduced back down to 0.67m and 0.55m respectively, straight crested 2D ripples formed, as shown in Figure 7.4(a) at H_s=0.55m and Figure 7.4(i). The response of the medium-grained bed to the waning wave forcing and the presence of relict bedforms are discussed in Section 7.7.

7.5.3 Quantifying bedform dimensions

The ARP profiles were used to obtain detailed measurements of the wavelength and height of the bedforms during each experiment using a turning points analysis. The crests and troughs of each individual ripple were identified by the turning points in the ARP profiles. The ripple wavelengths were taken as the horizontal distance between two troughs either side of a crest. The associated ripple heights were taken as the mean of the crest to trough height difference on either side of a crest. The steepness of an individual ripple was taken as the height to length ratio. To avoid mistakenly detecting ripples where there were small undulations and spikes in the ARP profiles, the crest and trough associated with any ripple heights smaller than 1mm were excluded from the analysis.

It is important to consider the spatial distribution of ripple cross-sectional dimensions, as under irregular oscillatory flow these distributions are potentially broader then under regular oscillatory flow (Marsh et al., 1999). For each experiment distributions of measured bedform wavelengths, λ, heights, η and steepness, η/λ, were obtained from the ARP profiles. The mean values, $\bar{\lambda}$, $\bar{\eta}$ and $\overline{\eta/\lambda}$, and standard deviations are listed in Table 7.2. Table 7.2 also lists plan-form geometry classifications of plane bed (plane), 2D ripples (2D), quasi-2D ripples (q-2D), 3D ripples (3D) or mega-ripples/hummocks (MR) based on the findings in Sections 7.5.1 and 7.5.2. The responses of $\bar{\lambda}$, $\bar{\eta}$ and $\overline{\eta/\lambda}$ to the surface wave forcing was broadly in agreement with the trends previously observed by Williams et al. (2004). The width of the ripple wavelength and height distributions generally changed in response to changes in the plan-form bedform geometries. To illustrate this, Figure 7.5 shows a selection of the distributions of λ, η and η/λ from a number of experiments during which the plan-form bedform geometries differed, both during the waxing and waning phases. Figure 7.5(a – f) shows the fine-grained bedform dimensions and Figure 7.5(g – m) shows the medium-grained bedform dimensions. For each experiment shown in Figure 7.5 the plan-form geometry classification and significant wave height is indicated. The 2D rippled beds, shown by Figures 7.5(a, c, f, g, m), have relatively narrow λ and η distributions. As the crests lines became more sinuous and the plan-form geometries progressed through quasi-2D, in Figures 7.5(b, e, h, l), to 3D, in Figures 7.5(i, k), the λ and η distributions broadened. The narrow distributions of λ and η occurred when the cross-sectional geometry was spatially continuous across the 4m transect and this is consistent with the inference of 2D ripples. By comparison, the 3D rippled beds, shown by Figures 7.5(i, k), have broad and multi-modal distributions. This is because the ripple crest lines were not necessarily parallel or perpendicular to the oscillatory flow direction. Similarly, in Figure 7.5(j) the λ and η distributions are broader still and distinctly bi-modal corresponding to the presence of 3D mega-ripples. Above the fine-grained plane bed in Figure 7.5(d) the wavelength distribution

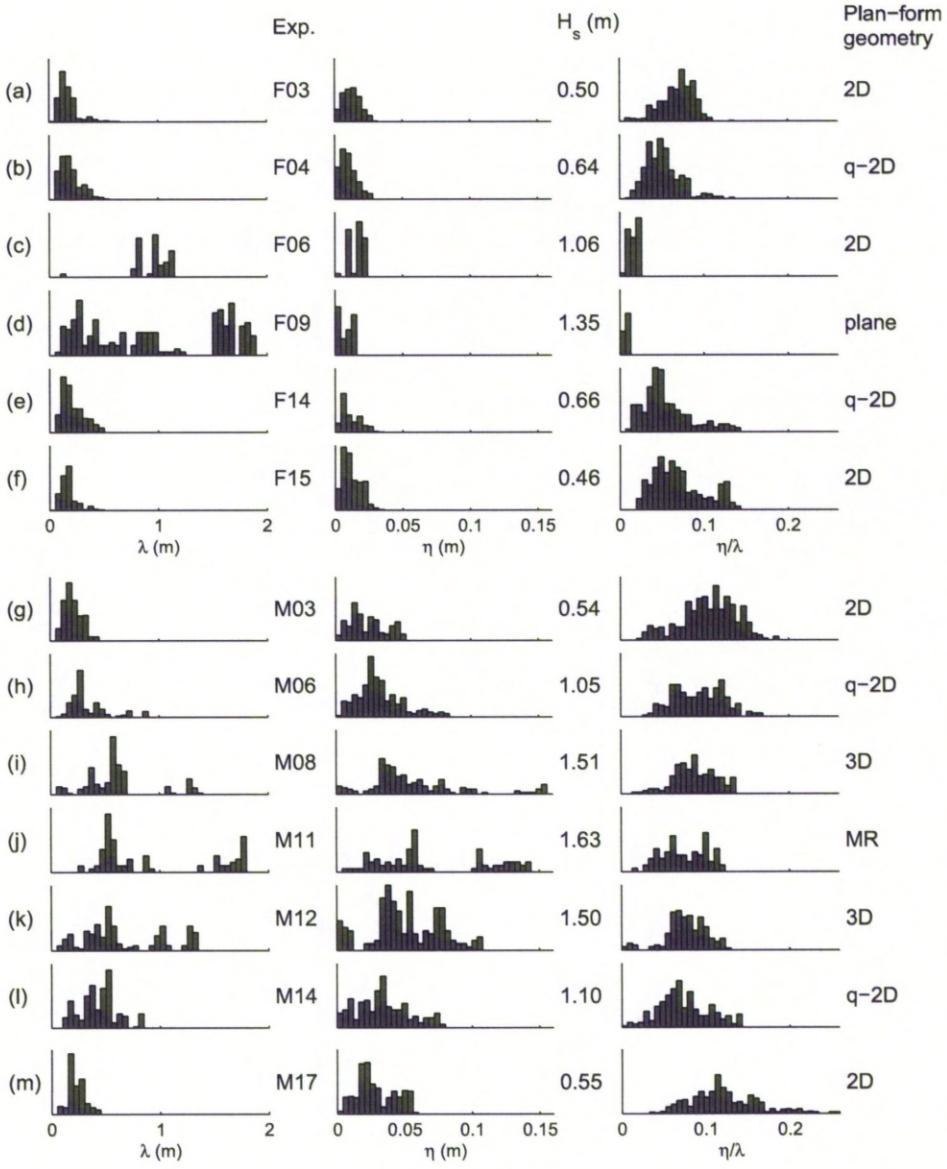

Figure 7.5: A selection of the distributions of λ, η and η/λ from a number of experiments during the experimental sequence during which different plan-form bedform geometries were observed. (a – f) show distributions of fine-grained ripples and (g – m) show distributions of medium-grained ripples.

Exp	$\bar{\lambda}$ (m)	$\sigma(\bar{\lambda})$ (m)	$\bar{\eta}$ (m)	$\sigma(\bar{\eta})$ (m)	$\overline{\eta/\lambda}$	$\sigma(\overline{\eta/\lambda})$	Plan-form geometry
F01	0.173	0.095	0.005	0.002	0.032	0.016	plane
F02	0.148	0.052	0.008	0.003	0.053	0.017	2D
F03	0.176	0.093	0.012	0.006	0.070	0.020	2D
F04	0.193	0.093	0.010	0.006	0.052	0.020	q-2D
F05	0.644	0.316	0.018	0.010	0.027	0.006	q-2D
F06	0.950	0.170	0.016	0.005	0.016	0.005	2D
F07	0.866	0.185	0.012	0.004	0.014	0.004	2D
F08	1.031	0.579	0.007	0.004	0.006	0.002	plane
F09	0.966	0.619	0.008	0.005	0.007	0.003	plane
F10	0.831	0.591	0.006	0.005	0.007	0.003	plane
F11	0.839	0.572	0.006	0.005	0.007	0.003	plane
F12	0.734	0.479	0.007	0.005	0.008	0.003	plane
F13	0.345	0.196	0.012	0.009	0.036	0.016	q-2D
F14	0.212	0.101	0.011	0.007	0.055	0.029	q-2D
F15	0.167	0.072	0.012	0.007	0.070	0.030	2D
F16	0.166	0.064	0.013	0.005	0.083	0.029	2D
M01	0.227	0.187	0.004	0.002	0.017	0.007	2D
M02	0.145	0.052	0.010	0.005	0.067	0.026	2D
M03	0.211	0.079	0.024	0.013	0.105	0.033	2D
M04	0.224	0.105	0.026	0.016	0.109	0.041	2D
M05	0.289	0.093	0.029	0.013	0.099	0.033	q-2D
M06	0.350	0.175	0.032	0.017	0.093	0.029	q-2D
M07	0.536	0.386	0.045	0.031	0.086	0.035	3D
M08	0.609	0.301	0.056	0.035	0.088	0.025	3D
M09	0.747	0.742	0.074	0.066	0.107	0.017	MR
M10	0.975	0.774	0.084	0.078	0.076	0.018	MR
M11	0.960	0.541	0.070	0.041	0.075	0.027	MR
M12	0.665	0.377	0.051	0.026	0.077	0.024	3D
M13	0.578	0.302	0.044	0.027	0.072	0.023	3D
M14	0.433	0.169	0.034	0.019	0.074	0.030	q-2D
M15	0.260	0.095	0.022	0.010	0.084	0.031	q-2D
M16	0.194	0.073	0.020	0.012	0.095	0.040	2D
M17	0.226	0.077	0.028	0.014	0.121	0.040	2D

Table 7.2: Mean ripple wavelength, $\bar{\lambda}$, height, $\bar{\eta}$, and steepness, $\overline{\eta/\lambda}$, measurements from the ARP results and classification of plan-form ripple geometry as either plane bed (plane), 2D ripples (2D), quasi-2D ripples (q-2D), 3D ripples (3D) or mega-ripples/hummocks (MR).

is very broad and multi-modal with λ ranging from 0 – 2m. The successfully extracted wavelength measurements are those modes in the distribution at $\lambda \sim 2$m, whereas the other modes correspond to higher frequency, and extremely low amplitude, undulations detected in error. The values for η and η/λ in Figure 7.5(d) are tightly distributed and do not exceed 0.02m and 0.02 respectively, supporting the inference that the bed was relatively planar.

7.5.4 Bedform dimensions response to wave forcing and comparison with ripple prediction formulae

There are a number of formulae employed in the prediction of ripple height, wavelength and steepness which require the input of different dynamic variables. For example, Nielsen (1981) argued that the mobility number was the most suitable dynamic variable that captured all the information regarding the flow and bed sediment necessary for the prediction of ripples. In order to compare the results of many ripple prediction schemes, it is necessary to present the results in terms of a suitable parameter. For the experiments conducted here, the peak spectral wave period was held constant throughout all the experiments, and the only two variables were the significant wave orbital diameter and the bed sediment. Thus the results presented here are in terms of the non-dimensional variable d_s/D_{50}, using the d_s values in Table 7.1.

Figure 7.6 shows the spatial and temporal mean ripple wavelength, $\bar{\lambda}$, height, $\bar{\eta}$, and steepness, $\overline{\eta/\lambda}$, measurements, with $\bar{\lambda}$ and $\bar{\eta}$ non-dimensionalised by D_{50}, from the ARP results plotted against d_s/D_{50}. The widths of the λ, η and η/λ distributions, a selection of which are shown in Figure 7.5, are indicated in Figure 7.6 by the vertical error bars showing two standard deviations about the mean of the respective parameters. The fine and medium-grained bedforms are indicated with squares and circles respectively. The bedforms classified as 2D are shown as solid symbols, the fine-grained plane bed conditions as open squares and the 3D medium-grained ripples as open circles. Finally in Figure 7.6, the ripple predictors of Wiberg and Harris (1994) and Soulsby and Whitehouse (2005) are shown for comparison.

Figure 7.6(a) shows $\bar{\lambda}/D_{50}$ broadly increasing proportionally with d_s/D_{50} and there is no separation of results associated with differences in ripple wavelength during the waxing and waning phases. The orbital, sub-orbital and anorbital regimes (Wiberg and Harris, 1994) are indicated in Figure 7.6(a). The ripple wavelength predictions of Wiberg and Harris (1994) and Soulsby and Whitehouse (2005) both increase with d_s/D_{50} within the orbital regime, reach a maximum and start to decrease within the sub-orbital regime and tend towards plane bed conditions in the anorbital regime. In contrast to these trends the observed wavelengths continue to broadly increase with d_s/D_{50} through all the regimes such that within the anorbital regime the wavelengths are much more in agreement with $\lambda = 0.62 d_s$, the orbital wavelength predictor of Wiberg and Harris (1994). This suggests that even within the anorbital ripple regime, $d_s/D_{50} > 5 \times 10^3$, the bedform wavelengths are still being influenced by orbital excursions near the bed. This was found to be the case by Vincent et al. (1999) who observed 3D mega-ripples with ~ 0.8m wavelengths under asymmetric waves.

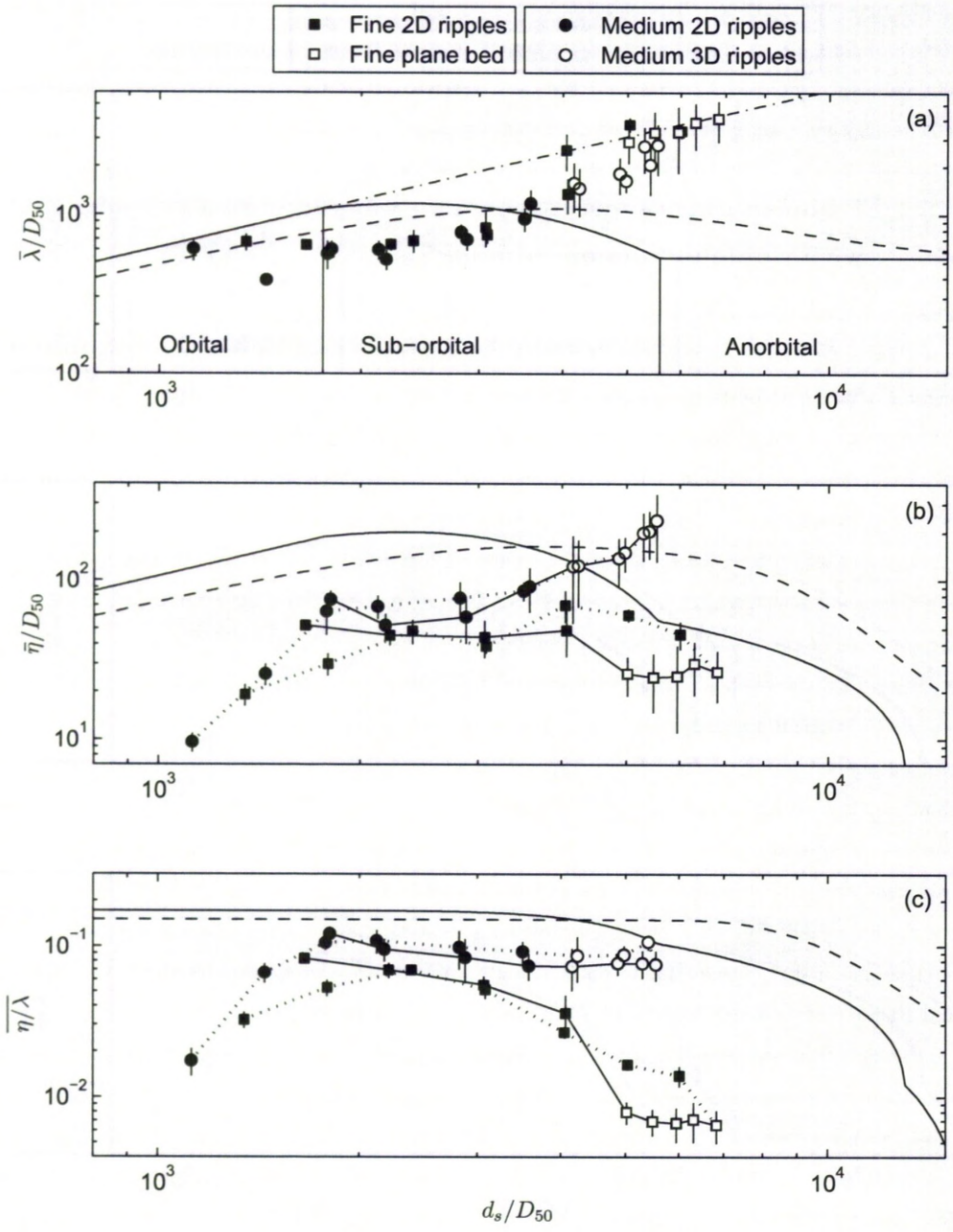

Figure 7.6: Average (a) ripple wavelength, $\bar{\lambda}$, and (b) ripple height, $\bar{\eta}$, non-dimensionalised by the median grain size of the bed sediment, D_{50}, and (c) average ripple steepness, $\overline{\eta/\lambda}$, plotted against the ratio of significant orbital diameter, d_s, and D_{50}. The results from the fine and medium-grained beds are distinguished by squares and circles respectively. The nominally plane bed (open squares) and 3D rippled (open circles) beds are indicated. The closed symbols indicate nominally 2D rippled bed conditions. The predictors of Wiberg and Harris (1994), $-$, and Soulsby and Whitehouse (2005), $- - -$, are shown and the orbital and anorbital boundaries of Wiberg and Harris (1994) are indicated in (a). Also shown in (a) is the line $\lambda = 0.62 d_s$, $- \cdot -$, defining the orbital wavelength of Wiberg and Harris (1994).

Figure 7.6(b) shows a difference in $\bar{\eta}$ during the waxing and waning phases. This is most evident in the results from the fine-grained bed (squares) at peak wave forcing within the anorobital regime of $d_s/d_{50} > 5 \times 10^3$. In order to show the response of the ripple height and steepness to step changes in d_s/D_{50}, the results in Figures 7.6(b and c) have been linked by dotted lines during the waxing phases and solid lines during the waning phases. In Figure 7.6(c), the fine-grained plane bed conditions (open squares), where $\overline{\eta/\lambda} < 0.01$, appeared first at the peak wave forcing conditions of $d_s/D_{50} \sim 7 \times 10^3$ but persisted well into the waning phase where ripples with steepness $\overline{\eta/\lambda} > 0.02$ were previously present. During the waning phase, suborbital ripples eventually reformed over the fine-grained bed, but not until $d_s/D_{50} < 4 \times 10^3$. The reformed ripples were marginally steeper than the those that formed during similar wave forcing conditions during the waxing phase. In contrast to this, the medium-grained ripples (circles) that formed during the waning phase (linked by solid lines) were marginally less steep than the medium-grained ripples of the waxing phase.

In Figures 7.6(b and c) $\bar{\eta}/D_{50}$ and $\overline{\eta/\lambda}$ diverge at $d_s/D_{50} \sim 4 \times 10^3$, with the results for the fine-grained sand bed (squares) being an order of magnitude smaller than the results for the medium-grained sand bed (circles). This divergence is associated with the fine-grained bed flattening out during peak flow conditions and the large 3D structures forming on the medium-grained bed. Within the orbital and sub-orbital regimes, $d_s/D_{50} < 5 \times 10^3$, the $\bar{\eta}/D_{50}$ and $\overline{\eta/\lambda}$ measurements are smaller than the predictions of Wiberg and Harris (1994) and Soulsby and Whitehouse (2005). The steepness measurements of the medium-grained ripples are typically around one half of the predicted values (Figure 7.6(c)). The fine-grained ripple steepnesses are between $4 - 10$ times smaller, mainly due to their large orbital scale wavelengths. Within the anorbital regime, the height of the medium-grained 3D structures shown in Figure 7.6(b) is reasonably well predicted by the formula of Soulsby and Whitehouse (2005) whereas their steepness in Figure 7.6(c) is still overestimated in comparison with the measurements. This is due to the occurrence of larger wavelengths than predicted.

7.6 Suspended sediment concentration measurements

The time-series of near bed mean backscatter signal from each ABS transceiver was examined in order to accurately identify the bed level for each burst. These signals were then root mean square (RMS) time averaged over each experimental measurement burst of 25 minutes. There is uncertainty as to the precise position of the ABS on the cross-sectional profile of the ripple below. The ABS and ARP were mounted on an along-shore line but were separated by $\sim 0.15m$. Thus, the precise position of the ABS relative to, say, the ripple crest, increased in uncertainty with the sinuosity of the ripple crests lines.

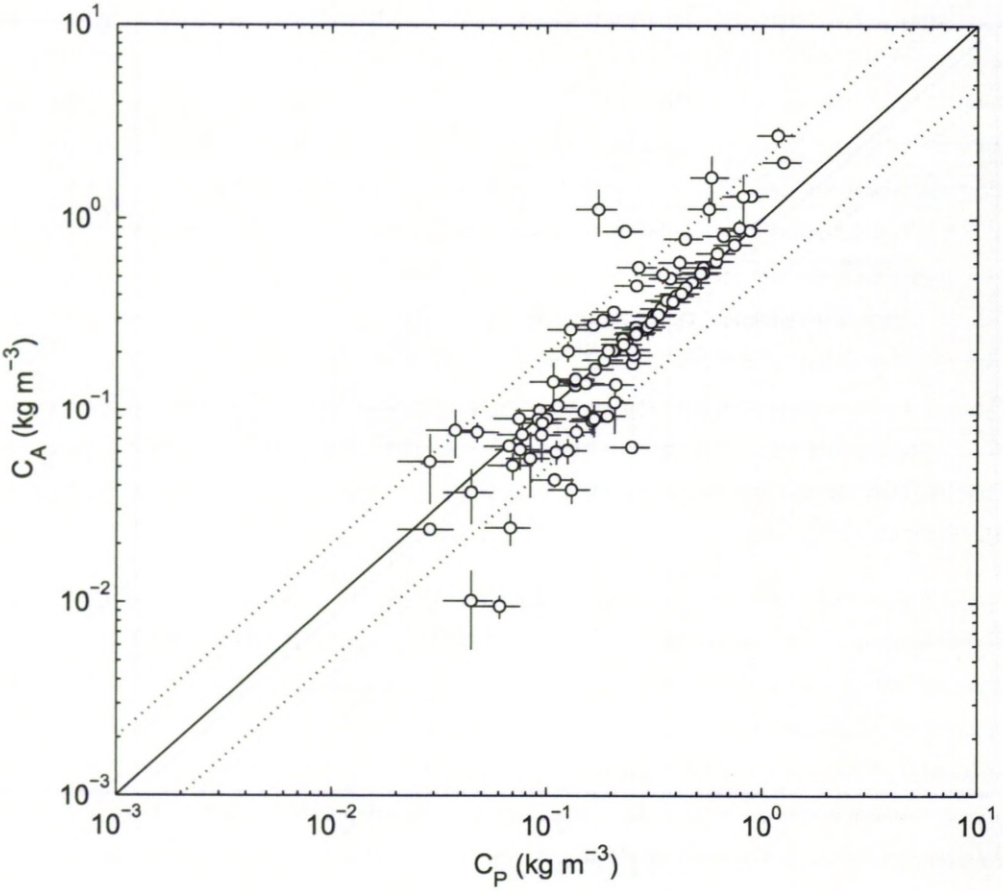

Figure 7.7: Comparison of the time average suspended sediment concentrations obtained from the ABS, C_A, and the pumped samples, C_P, for all the available pumped sampled data. The lines corresponding to $C_A = C_P$ $(-)$ and $C_A = 2C_P$ and $C_A = 0.5C_P$ $(\cdots)$ are shown. The error bars show $\pm$ the standard error of the mean of the three ABS frequencies for C_A and $\pm 20\%$ for C_P.

7.6.1 Acoustic inversion and validation

The RMS backscatter profiles were converted to time-mean SSC profiles using an explicit acoustic inversion (Lee and Hanes, 1995; Thorne and Hanes, 2002). This inversion relied on measurements of the SSC obtained from the pumped samples taken approximately 0.07 – 0.17m above the bed during each experiment. The suspended sediment size distributions were obtained from the pumped samples using laser grain size analysis, and these were used to aid the accuracy of the acoustic inversions. These height average size distributions were lognormal in form with mean sizes and widths that varied linearly as a function of $\theta_{2.5}$ for each experiment. Thus a linear function was fitted to the available data and this was used to calculate the size distribution for each experiment. The median suspended sediment diameter varied between $D_{s50} = 215 - 273\mu$m and $D_{s50} = 262 - 373\mu$m during the course of the experiments conducted above the fine and medium-grained beds, respectively.

The result of the inversion was an SSC profile from each of the three ABS transceivers, for

each of the experimental bursts. The mean of the SSC profiles across the three results was taken, yielding a single time-mean SSC profile, at 1cm vertical resolution, for each experiment. This increased the statistical reliability and provided uncertainty estimates on the SSC. Figure 7.7 shows a comparison between the time-mean sediment concentrations obtained from the ABS, C_A, and the pumped samples, C_P, for all of the available pumped sampled results from the five heights, z, above the bed. The error on C_P indicated is $\pm 20\%$, which is the typical error found by Moate and Thorne (2009). The majority of the results from the ABS and pumped samples are well within a factor of two, which is the typical accuracy of ABS (Vincent, 2007).

7.6.2 Suspended sediment concentration profiles response to wave forcing

Figure 7.8 shows the SSC profiles obtained from the ABS measurements above the fine-grained bed. Figures 7.8(a, b) show the SSC profiles obtained during the waxing phase of the experimental sequence, and Figures 7.8(c, d) show the SSC profiles obtained during the waning phase. The results shown are the mean of the results from the three ABS transceivers and the associated standard error is indicated for F03, F07, F12 and F15 to give an indication of the typical uncertainties. The four plots in Figure 7.8 show the SSC profiles obtained during different bed conditions. Figure 7.8(a) presents the first five profiles obtained during the experimental sequence, when the bed was plane or 2D/quasi-2D rippled. Figure 7.8(b) shows the SSC profiles obtained during experiments when the ripples had long and straight crests with $\sim$ 0.9m wavelengths. Figure 7.8(c) shows five SSC profiles measured after the bed had flattened out under the strong wave forcing of H_s=1.45m. Finally, Figure 7.8(d) presents the SSC profiles measured during the waning phase when 2D and quasi-2D ripples were present on the bed. The results in Figure 7.8 broadly show an increase or decrease in the concentration magnitude in accordance with the value of H_s.

From the groupings of the SSC profiles in Figure 7.8 it is apparent that there are distinct differences in the shapes of the SSC profiles above the different bedform types. During F01 the bed is plane and there is little in the way of suspended sediment due to the low wave forcing of H_s=0.28m. During F02 – F05, when the bed was rippled, there was a substantial increase in the near bed SSC. The SSC profile during F02 (Figure 7.8(a), H_s=0.37m) is upward concave in form on the log C, linear z axes. By comparison, the SSC profiles during F03 – F05 (Figure 7.8(a), $H_s = 0.50 - 0.84$m) are straight lines within the bottom 0.08 – 0.10m. On the log C, linear z axes, straight lines correspond to an exponential decay of the concentration profile with height above the bed. The distinct change in shape from upward concave to exponential between F02 and F03 is likely to be associated with the increase in ripple height from $\bar{\eta} = 0.008$m to $\bar{\eta} = 0.012$m that occurred between these experiments. The steeper ripples were likely to encourage flow separation, enhancing coherent vortex mixing, during each wave half cycle. Figure 7.8(b) shows the SSC profiles from F06 and F07, during which large ripples of low steepness and $\sim$ 0.9m wavelength were present on the bed, to be more upward concave in form,

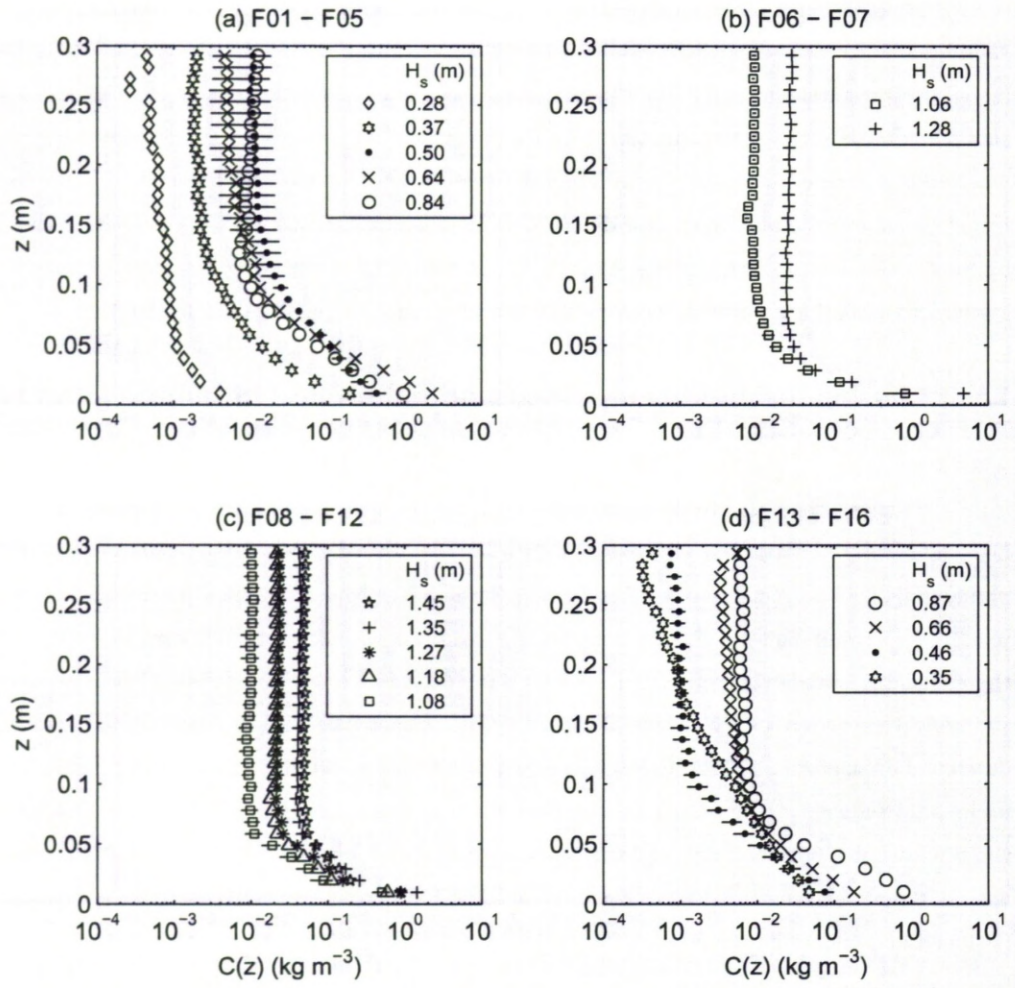

Figure 7.8: The suspended sediment concentration profiles, $C(z)$ where z is height above the bed, obtained above the fine-grained bed during (a, b) the waxing wave conditions and (c, d) the waning wave conditions. The results shown are the mean of the results from the three ABS transceivers and the associated standard errors are shown for F03, F07, F12 and F15.

at least within the bottom 0.10m. Figure 7.8(c) shows the SSC profiles from F08 – F12, when the bed was plane, to have approximate exponential forms within the range $0.01 < z < 0.05$m and to be nominally uniform for z > 0.05m. Finally, Figure 7.8(d) shows the SSC profiles from F13 – F16, where ripples were re-established on the bed, to have exponential forms within about the bottom 0.05 – 0.10m above the bed.

Figures 7.9(a, b) and 7.9(c, d) show the SSC profiles obtained from the ABS measurements above the medium-grained bed during the waxing and waning phases of the experimental sequence respectively. The organisation of results in Figure 7.9 broadly follows the occurrence of different medium-grained bed conditions. Figure 7.9(a) shows the SSC results from the start of the waxing phase during which 2D or quasi-2D ripples were present on the bed. Figure 7.9(b) shows results from the end of the waxing phase when the beds were dominated by 3D ripples

or large hummocks.

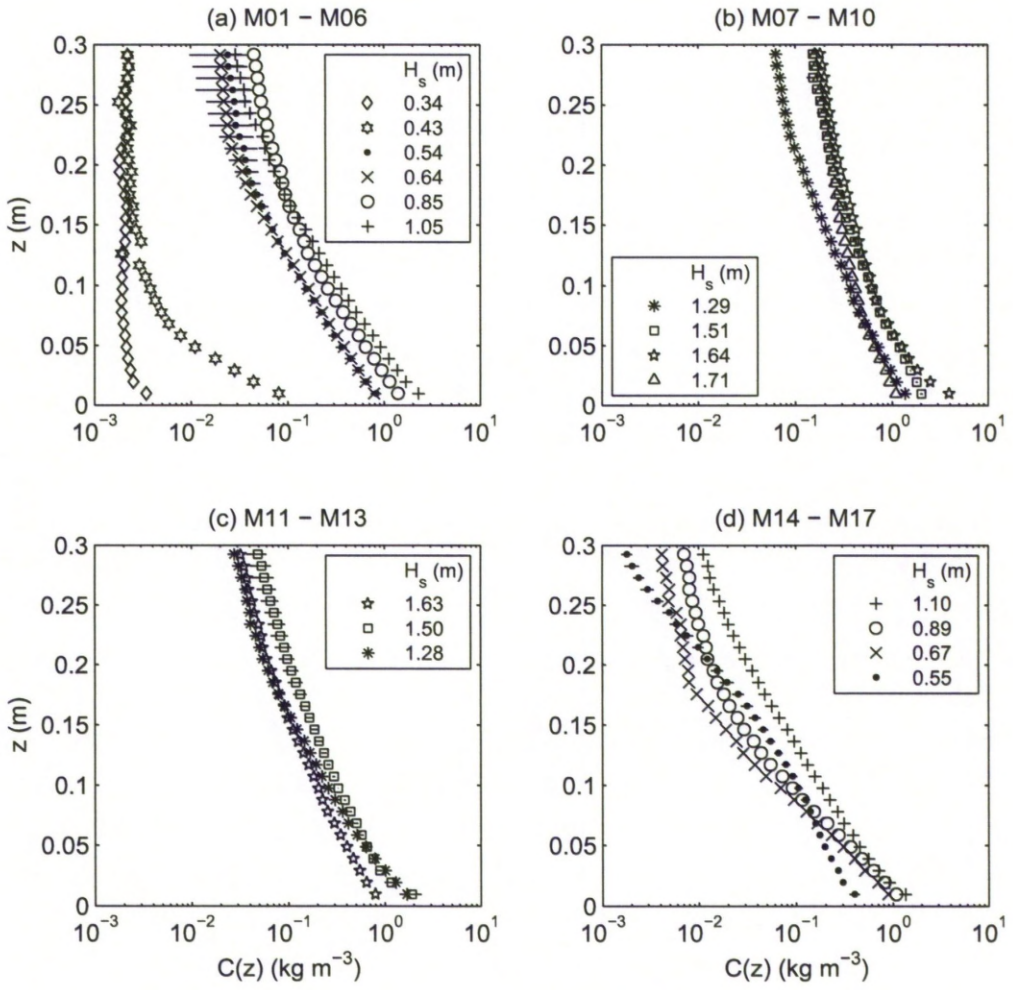

Figure 7.9: The suspended sediment concentration profiles, $C(z)$ where z is height above the bed, obtained above the medium-grained bed during (a, b) the waxing wave conditions and (c, d) the waning wave conditions. The results shown are the mean of the results from the three ABS transceivers and the associated standard errors are shown for M05, M09, M12 and M16.

Figure 7.9(c) shows results from the start of the waning phase and Figure 7.9(d) shows results from the end of the waning phase when 2D or quasi-2D ripples were present. When the bed was dominated by 2D or quasi-2D ripples (Figure 7.9(a, d)) there were changes in the SSC magnitudes associated with changes in H_s. Above the 3D ripples and mega-ripple features, the SSC profiles are of a similar magnitude (of the order 1 kg m^{-3} at $z \sim 0.01$m) even though H_s varied between $1.29 - 1.71$m. The majority of SSC profiles in Figure 7.9 exhibit exponential decays within the bottom $0.10 - 0.15$m, with some profiles continuing to decay exponentially beyond 0.15m. The exceptions are M01 and M02 in Figure 7.9(a) which are upward concave in form on the log C, linear z axes.

7.6.3 Near bed decay of suspended sediment concentration and reference concentrations

The majority of the SSC profiles presented in Figures 7.8 and 7.9 exhibit exponential decay close to the bed, indicative of a height constant diffusivity in this near bed region. Exponential functions of the form given by equation (7.4) were fitted to the SSC profiles from each experiment within 0.01m $< z <$ 0.05m by performing a linear regression on log C and z. This was done for the SSC profiles obtained from each ABS transceiver, and the mean and standard deviation for the three results were taken for each experiment in order to increase the statistical reliability and provide uncertainty estimates. The results from these regressions are listed in Table 7.3 along with the associated correlation coefficients, R_e^2. For the majority of SSC profiles, there was a high correlation between the regressions made and the data, with $R_e^2 > 0.98$ in the majority of cases. The exceptions include F01, F02 and M01 where $H_s < 0.37$m and the bed was either plane or the ripples present had very low amplitudes and steepness. During F06 and F07 ripples having low steepness and ~ 0.9m wavelengths were present, resulting in $R_e^2 = 0.95$ and 0.90 respectively. During M10 the wave forcing was at its peak above the medium-grained bed, large hummocks were present on the bed, resulting in $R_e^2 = 0.95$.

Above the fine-grained bed the exponential decay length scales of the fitted SSC profiles above the 2D and quasi-2D rippled beds (F02 – F07, F13 – F16) were between $L = 0.012 - 0.034$m, and are listed in Table 7.3. Above the medium-grained 2D and quasi-2D rippled beds, L was somewhat larger with $L = 0.034 - 0.068$m. The medium-grained ripples were both larger in amplitude and steepness than the fine-grained ripples, and thus were more likely to encourage the entrainment of sediment via vortices. This is most likely why the decay lengths above the medium-grained ripples were larger than those above the fine-grained ripples. At peak wave forcing above the fine-grained plane beds $L = 0.020 - 0.029$m and above the medium-grained hummocks and 3D ripples $L = 0.047 - 0.088$m.

The two equations of Nielsen (1992), equation (7.6), were calculated with $L_{N1} = 0.075 U_0 \eta / w_s$ and $L_{N2} = 1.4\eta$, with $U_0 = U_s$ and $\eta = \bar{\eta}$. The settling velocity, w_s, was calculated using the formula of Soulsby (1997) with D_{s50} obtained from the pumped samples. Figure 7.10 shows a comparison between the measured decay length scales, L, and (a) L_{N1}, (b) L_{N2} and (c) $L_N = L_{N1}$ or L_{N2} depending on whether U_s/w_s was < 18 or ≥ 18 (Nielsen, 1992). The predicted decay lengths that most agree with L are $L_{N2} = 1.4\bar{\eta}$ with many more of L_{N1} being less than L. For the majority of experiments $U_s/w_s < 18$ such that Figure 7.10(a) and Figure 7.10(c) differ little. Figure 7.10(d) shows a comparison between L and ε_s/w_s, where ε_s is the sediment diffusivity calculated using the formulae of Nielsen (1992), equation (7.5a) with black circles, and Van Rijn (1993), equation (7.5b) with white circles, with $U_0 = U_s$. The formula of Nielsen (1992) consistently under predicts L whereas that of Van Rijn (1993) performs somewhat better.

The fact that L agrees more closely with L_{N2} than L_{N1} in Figure 7.10(b) suggests that the

Exp	C_0 (kg m^{-3})	$\sigma(C_0)$ (kg m^{-3})	L (m)	$\sigma(L)$ (m)	R_e^2
F01	0.003	0.002	-0.012	-0.034	0.81
F02	0.162	0.133	-1.841	-1.855	0.71
F03	0.510	0.245	0.034	0.004	1.00
F04	5.571	3.178	0.014	0.002	1.00
F05	1.049	0.481	0.018	0.001	1.00
F06	0.420	0.304	0.017	0.004	0.95
F07	0.488	0.351	0.019	0.004	0.90
F08	0.414	0.230	0.029	0.002	1.00
F09	0.663	0.334	0.022	0.001	1.00
F10	0.425	0.235	0.022	0.001	1.00
F11	0.285	0.163	0.023	0.001	1.00
F12	0.273	0.167	0.020	0.001	1.00
F13	2.787	0.726	0.012	0.001	0.99
F14	0.311	0.227	0.019	0.002	0.98
F15	0.133	0.078	0.020	0.001	1.00
F16	0.063	0.028	0.033	0.003	0.99
M01	0.002	0.002	0.144	0.092	0.73
M02	0.105	0.041	0.034	0.018	1.00
M03	0.978	0.227	0.050	0.004	0.99
M04	0.908	0.129	0.057	0.004	1.00
M05	1.671	0.061	0.052	0.006	1.00
M06	2.525	0.405	0.049	0.006	1.00
M07	1.481	0.057	0.066	0.004	1.00
M08	2.354	0.133	0.071	0.007	1.00
M09	3.834	0.957	0.046	0.009	0.98
M10	1.243	0.373	0.088	0.025	0.95
M11	0.877	0.085	0.063	0.001	1.00
M12	1.682	0.544	0.057	0.015	0.98
M13	2.177	1.062	0.047	0.013	1.00
M14	1.481	0.414	0.044	0.008	1.00
M15	1.460	0.546	0.039	0.008	1.00
M16	1.199	0.192	0.036	0.005	0.99
M17	0.409	0.033	0.068	0.004	0.99

Table 7.3: Results from regressions made to the near bed, $z < 0.05$m, ABS measured SSC profiles including the reference concentration taken at bed level, C_0, the decay length scale, L, their associated standard deviations, σ, and mean correlation coefficients, R_e^2.

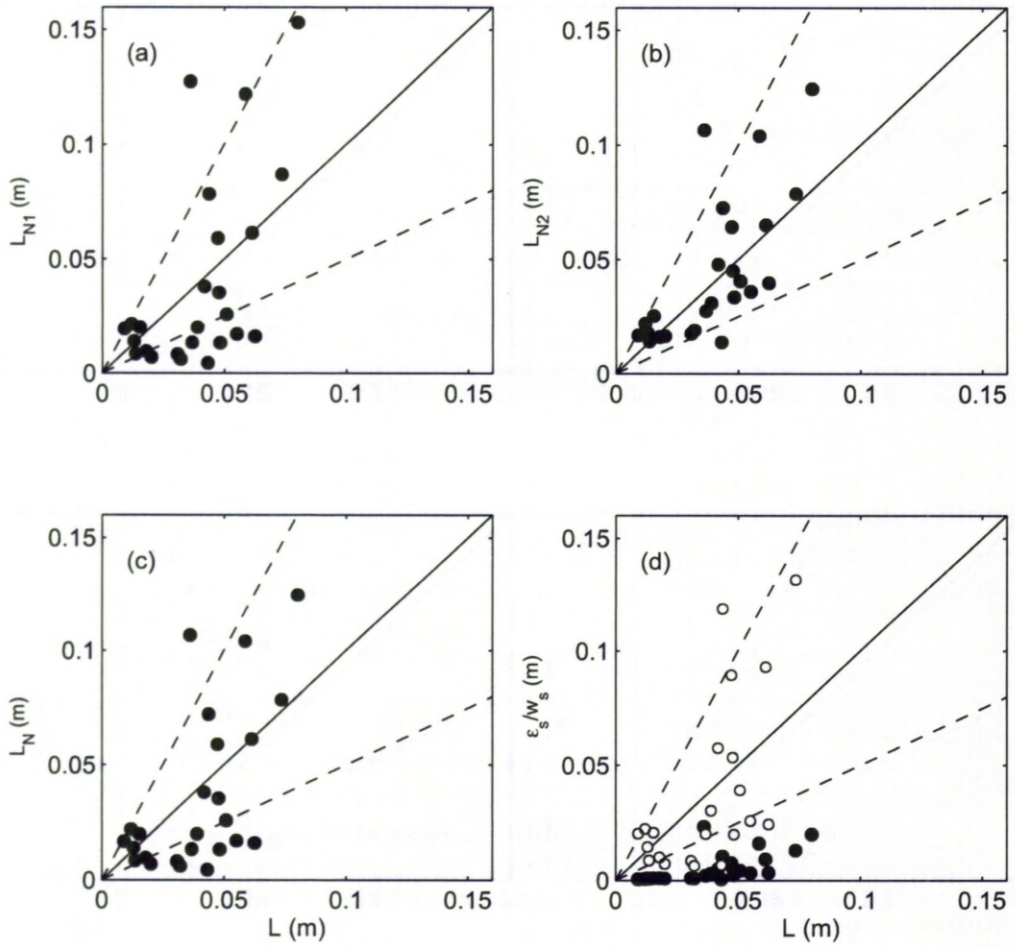

Figure 7.10: Comparison between the measured exponential decay length scales, L, and those predicted by the expressions of Nielsen (1992), (a) L_{N1} and (b) L_{N2}, and (c) $L_N = L_{N1}$ or L_{N2}. In (d) the decay length scale predicted using the expressions for the diffusivity of Nielsen (1992), equation (7.5a) closed circles, and van Rijn (1993) open circles, are compared with L. The lines depicting perfect agreement (−) and agreement within a factor of two are shown (− − −) in each plot.

dominant control over the exponential decay lengths are the ripple dimensions, in particular the ripple height. In Figure 7.10(d) the formula of van Rijn performed best, which included a dependence on the grain size, D_{50}. These relationships were examined more closely through dimensional analysis considering all the physical parameters at play. A strong correlation between $L/\bar{\eta}$ and $\theta_{2.5}^{-1}\,\overline{\eta/\lambda}$, the inverse grain roughness Shields parameter and average ripple steepness in Tables 7.1 and 7.2 respectively, was found for the experiments where 2D and quasi-2D ripples were present. However, $L/\bar{\eta}$ did not correlate well with $\theta_{2.5}^{-1}\,\overline{\eta/\lambda}$ during the times of peak wave forcing above the medium-grained hummocks. A stronger correlation was found by replacing $\overline{\eta/\lambda}$ with $k_s/\bar{\eta}$, where k_s is an enhanced bed roughness given by (Nielsen, 1992)

$$k_s = 8\bar{\eta}\,\overline{\eta/\lambda} + 170 D_{50}\sqrt{\theta_{2.5} - 0.05}. \tag{7.18}$$

This expression for k_s includes both contributions from the form drag above the ripples, first term, and the moving sand layer under the more energetic conditions, second term. Figure 7.11 shows $L/\bar{\eta}$ plotted against $k_s/(\theta_{2.5}\bar{\eta})$ for all the experiments, both fine and medium-grained, where either 2D, quasi-2D or 3D ripples or hummocks were present along with the result from a linear regression on the data,

$$L/\bar{\eta} = (0.12 \pm 0.03)k_s/(\theta_{2.5}\bar{\eta}) + (0.64 \pm 0.25) \tag{7.19}$$

with $R^2 = 0.78$. This result suggests that during the times of relatively strong wave forcing, where large 3D ripples and hummocks populated the medium-grained bed, the roughness contribution from the moving sand layer strongly contributed towards the exponential decay length scale, L. Conversely, when the waves were less steep and the bed was populated by 2D ripples, L was strongly controlled by the ripple steepness, $\overline{\eta/\lambda}$.

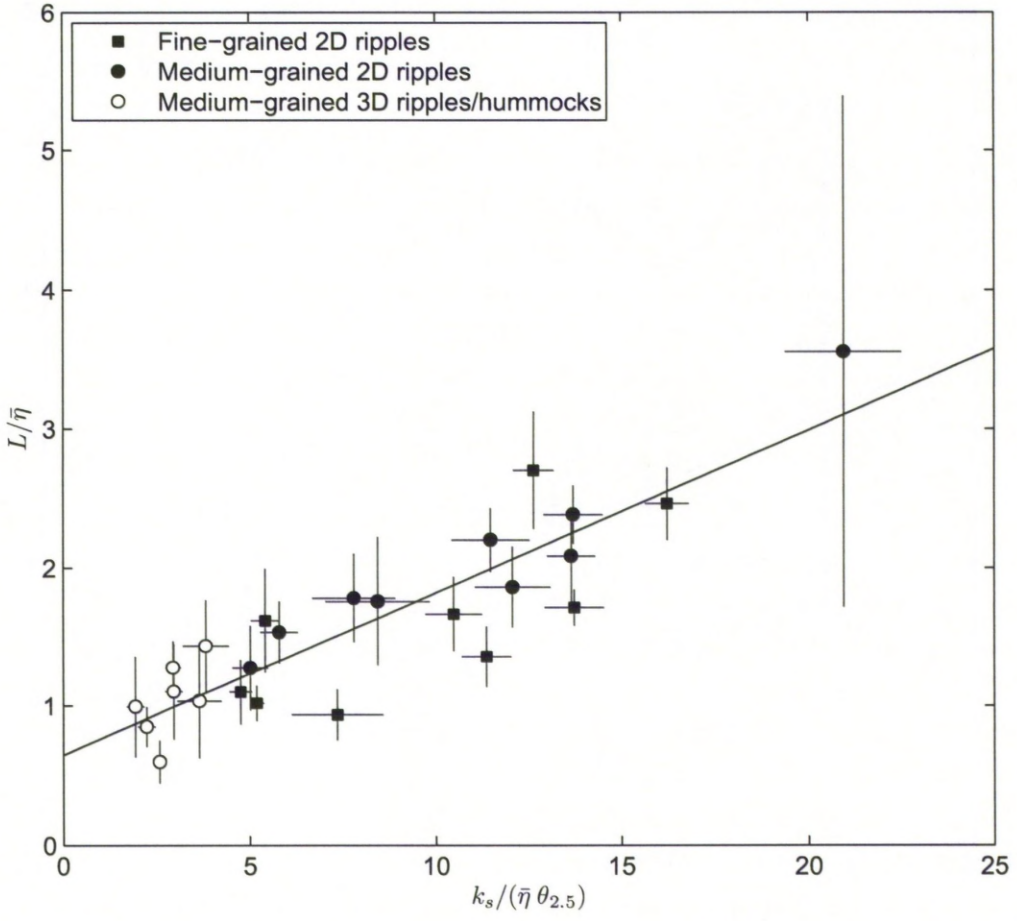

Figure 7.11: The measured exponential decay length scales, L, divided by the average ripple height, $\bar{\eta}$, plotted against $k_s/(\theta_{2.5}\bar{\eta})$, where k_s is an enhanced roughness including contributions from ripple form drag and a moving sand layer and $\theta_{2.5}$ is the grain roughness Shields parameter.

7.6.4 Comparison between reference concentrations and empirical models

The measured reference concentrations for the SSC profiles from each experiment were compared with the empirical models of Nielsen (1986), Green and Black (1999) and Lee et al. (2004). The Nielsen (1986) and Green and Black (1999) equations predict the reference concentration taken at bed level, C_0, and were compared with the measured values listed in Table 7.3. The equation of Lee et al. (2004) predicts the reference concentration at 0.01m above the bed, C_1, and was compared with the mean ABS result for each experiment at z=0.01m. Figure 7.12 shows the reference concentrations from all the experiments through the experimental sequence plotted against (a) the grain roughness Shields parameter (b) the ripple modified Shields parameter (c) the parameter of Lee et al. (2004), $\theta_{2.5}\, u_{*2.5}/w_s$, and (d) a ripple modified version of the parameter of Lee et al. (2004), $\theta_r\, u_{*2.5}/w_s$. The standard deviations of the means over the results from the three ABS transceivers are shown and are generally small indicating good agreement between the three ABS results. For these results, the skin friction shear velocity was calculated using

$$u_{*2.5} = \sqrt{\frac{f_{2.5} U_s^2}{2}} \tag{7.20}$$

and equation (7.7) with $U_0 = U_s$ was used for the Shields parameter. For the calculation of θ_r, the ripple steepness values presented in Figure 7.6(c) were used. The settling velocity, w_s, was calculated using the formula of Soulsby (1997) with D_{s50} obtained from the pumped samples. In Figure 7.12, the reference concentration values obtained above the 2D and quasi-2D rippled beds are shown by the black symbols. The measurements made above the fine-grained plane beds and medium-grained 3D rippled beds are shown by the white squares and white circles respectively.

Figure 7.12 shows that most of the reference concentration measurements were between 0.1 – 10 kg m^{-3}, with those values $<$ 0.1 kg m^{-3} occurring at small values of the abscissa. In Figure 7.12(a) there is a clear separation of the measurements made above (i) the 2D rippled beds (black symbols) and (ii) the fine-grained plane beds and medium-grained 3D bedforms shown by white squares and circles respectively. With the modification of the Shields parameter in Figure 7.12(b), this separation is reduced somewhat but the two groups are still distinct. There is no distinguishable separation in the results obtained above the fine (squares) and medium-grained (circles) 2D rippled beds in Figure 7.12. This suggests that the Shields parameter's dependence on D_{50} adequately accounts for any difference in suspended sediment concentrations above the two bed sediment sizes.

The reference concentration prediction schemes of Nielsen (1986) and Green and Black (1999), given by equation (7.9) with α=0.1 and α=0.005, are plotted in Figures 7.12(a and b) and that of Lee et al. (2004), equation (7.11), is plotted in Figures 7.12(c and d). In Figure 7.12(a) the predictor of Green and Black (1999) for rippled beds, $C_0 = 0.1\, \rho_s \theta_{2.5}^3$, compares well with the 2D rippled bed data. The data corresponding to plane bed conditions (open

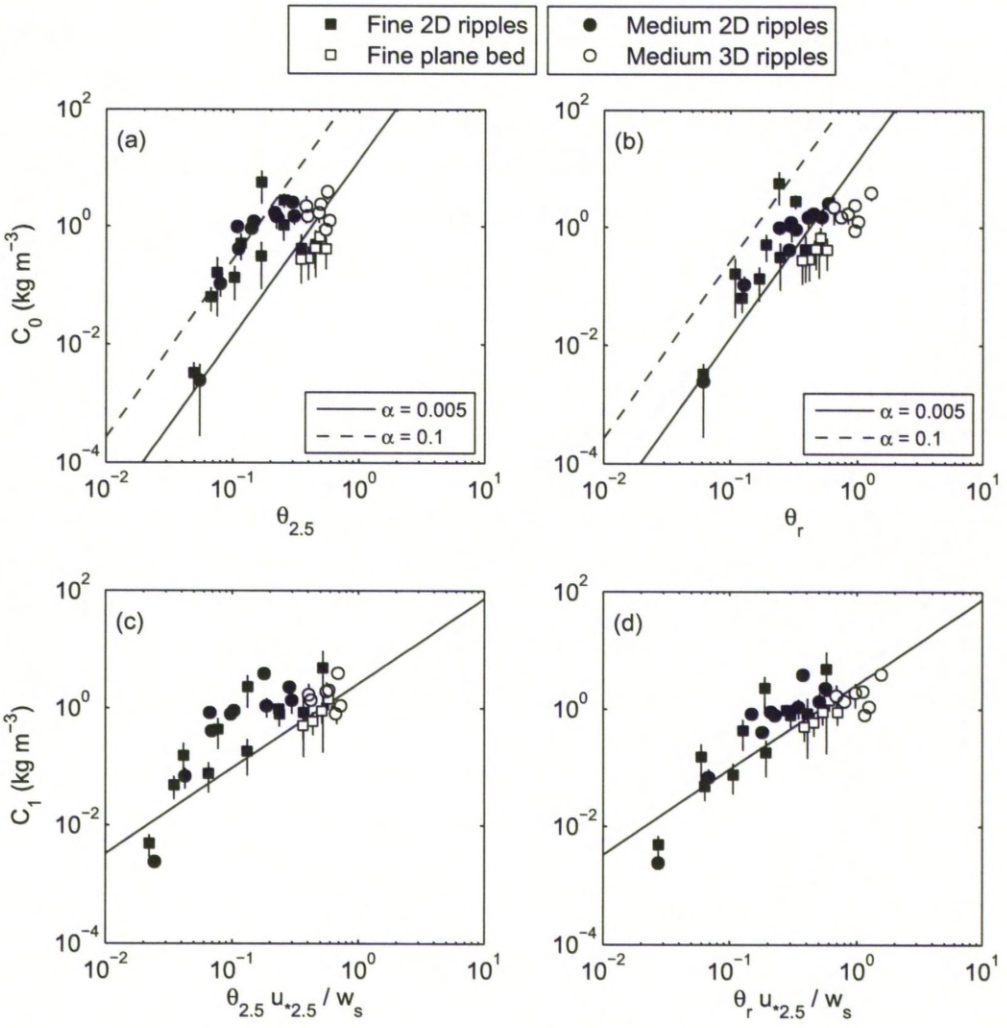

Figure 7.12: The reference concentration taken at either the bed level, C_0, or 1cm above the bed, C_1, mean averaged over the results from the three ABS transceivers plotted against (a) the grain roughness Shields parameter, $\theta_{2.5}$, (b) the ripple modified Shields parameter, θ_r, (c) the parameter of Lee et al. (2004), $\theta_{2.5}u_{*2.5}/w_s$ where $u_{*2.5}$ and w_s are the friction and settling velocities respectively and (d) the ripple modified parameter of Lee et al. (2004). The vertical error bars show the standard deviation of the mean values taken across the results from the three ABS transceivers. The results from the fine and medium-grained beds are distinguished by squares and circles respectively. The nominally plane bed (open squares) and 3D rippled (open circles) beds are indicated. The closed symbols indicate nominally 2D rippled bed conditions.

squares) and beds where the bedforms had 3D plan-form geometries (open circles) compare best with the predictor of Nielsen (1986), $C_0 = 0.005\,\rho_s\theta_{2.5}^3$. In Figure 7.12(b), where θ_r is used, the equation of Nielsen (1986) over predicts C_0 above plane (open squares) and 3D rippled (open circles) beds and generally under predicts C_0 above the 2D rippled beds. The equation of Lee et al. (2004) in Figure 7.12(c) generally performs poorly, although C_1 is predicted reasonably well above the 3D rippled beds. Modifying equation (7.11) by replacing $\theta_{2.5}$ with θ_r generally improves the prediction, as shown by Figure 7.12(d), and there is less scatter in the data. Overall, the equations most able to predict the reference concentration across all the different bed and wave forcing conditions are those of Nielsen (1986) and Lee et al. (2004) as long as the ripple modified Shields parameter is used.

7.7 Discussion

The analysis of the data collected in this experimental sequence permitted the interplay of the flow, bedforms, and sediment suspension processes under irregular waves during a simulated passing of a storm to be investigated. The response of the bedforms and the time average SSC profiles to the changing wave forcing were presented in Sections 7.5 and 7.6 respectively. The discussion begins here, in Section 7.7.1, by considering the difference in bedform morphology during experiments with comparable wave forcing but which were conducted before and after the peak forcing. Whether relict structures influence the time-mean SSC profiles is also considered. Section 7.7.2 discusses the connection between the irregular wave forcing and the observed three-dimensionality of the bedforms. Finally, in Section 7.7.3 a connection is made between (i) the exponential decay lengths of time-mean SSC profiles above 2D and 3D ripples; (ii) the bed roughness; and (iii) the height to which the SSC profiles are exponential.

7.7.1 Inherited bed and SSC

Figures 7.3 and 7.4 present the different bedform configurations that existed during the experimental sequence. The response of the fine-grained bed to the waning wave conditions was somewhat different to its response to the waxing wave phase at similar water velocities. Under comparable wave forcing conditions the ARP results show clear differences in the bed morphology before and after the peak in the wave forcing. The most notable difference is that the 2D bedforms that formed during F06 and F07, where $H_s = 1.06$ and 1.28m, were not as clearly observed in the ARP results from F10 – F12, where $H_s = 1.08 - 1.27$m. The results from the turning points analysis of the ARP profiles presented in Table 7.2 show that during F06 and F07, $\bar{\lambda} = 0.95$ and 0.87m, $\bar{\eta} = 0.016$ and 0.012m and $\overline{\eta/\lambda} = 0.016$ and 0.014. During F10 – F12, however, the average wavelength results were $\bar{\lambda} = 0.73 - 0.83$m suggesting that there were ripples present. The uncertainties on these measurements from F10 – F12 of $\sigma(\bar{\lambda}) = 0.48 - 0.60$m are, however, large and the corresponding ripple height measurements of $\bar{\eta} = 0.006 - 0.007$m are very small suggesting that the bed was in fact planar.

Figures 7.13(a and b) presents the ARP cross-sections from F06 and F12, when $H_s \sim 1$m, which show the bed during F12 to be nominally plane. There was however a large undulation present, shown in Figure 7.13(b), the wavelength of which was undetectable through the turning points analysis. The time-mean SSC profiles from F06 and F12 are presented in Figure 7.13(c) and are similar in terms of shape and magnitude, even though the bed morphology below the ABS was somewhat different. This suggests that the entrainment of sediment in these experiments is mainly associated with sheet flow processes starting to occur rather than processes associated with the ripples.

As the significant wave height was reduced further from $H_s = 1.08$m during F12, 2D ripples formed that were similar to those that formed during the waxing phase. Figures 7.13(d and e) show the ARP cross-sections from F04 and F14 where $H_s \sim 0.65$m. During F14 the ripples are a little more disorganised, compared with those during F04, and show some limited evidence of evolution processes, such as ripple splitting and merging (Hansen et al., 2001; Doucette and O'Donoghue, 2006). This suggests that during F14 the ripples were not fully developed and were not fully in equilibrium with the flow despite the fact that the $H_s = 0.66$m wave conditions had run for one hour prior to the F14 measurement burst. The primary difference between the F04 and F14 bed configurations is that the 2D ripples in F14 are superimposed on relict long wavelength features with $\lambda \sim 1.5$m comparable with LWR (Hanes et al., 2001). This LWR feature is most likely to be a relict of the long ~ 2m undulation present during the nominally plane bed conditions (F08 – F11). The time-mean SSC profiles from F04 and F14 are presented in Figure 7.13(f) and show a distinct difference in the magnitude of the near bed, $z < 0.1$m, SSC between the two experiments. The near bed exponential decay length scale, L, is also smaller during F04 than F14, as shown in Table 7.3. Further away from the bed, $z > 0.1$m, and considering the uncertainty in the measurements during F04 indicated in Figure 7.13(f), the SSC is similar during F04 and F14 and is of the order 0.01kg m^{-3}. The striking difference in time-mean near bed SSC is most likely associated with the difference in the position of the ABS relative to the cross-sectional profile of the ripple below. This is consistent with the notion that the entrainment of sediment in these experiments was mainly associated with rippled bed entrainment processes (vortex entrainment).

In the case of the medium-grained bed, there is less of a substantial difference between the bed states before and after the peak in wave forcing. Figures 7.13(g and h) show the ARP cross-sections from M04 and M16 during which $H_s \sim 0.65$m. Both rippled beds have reasonably steep sided ripples with $\overline{\eta/\lambda} = 0.109$ and 0.095 for M04 and M16 respectively. Figure 7.13(i) presents the time-mean SSC profiles from M04 and M16 and shows the SSC magnitudes to be similar close to the bed, $z < 0.05$m, but larger during M04 for $z > 0.05$m. The near bed exponential decay length scale, L, is a factor 1.6 larger during M04 than M16, as shown in Table 7.3. This is considered to be due to the difference between the ripples directly below the ABS, and hence their influence on this local sediment suspension field, during the two experiments. Figure 7.13(g) shows that the crest of a relatively large and steep sided ripple was above the

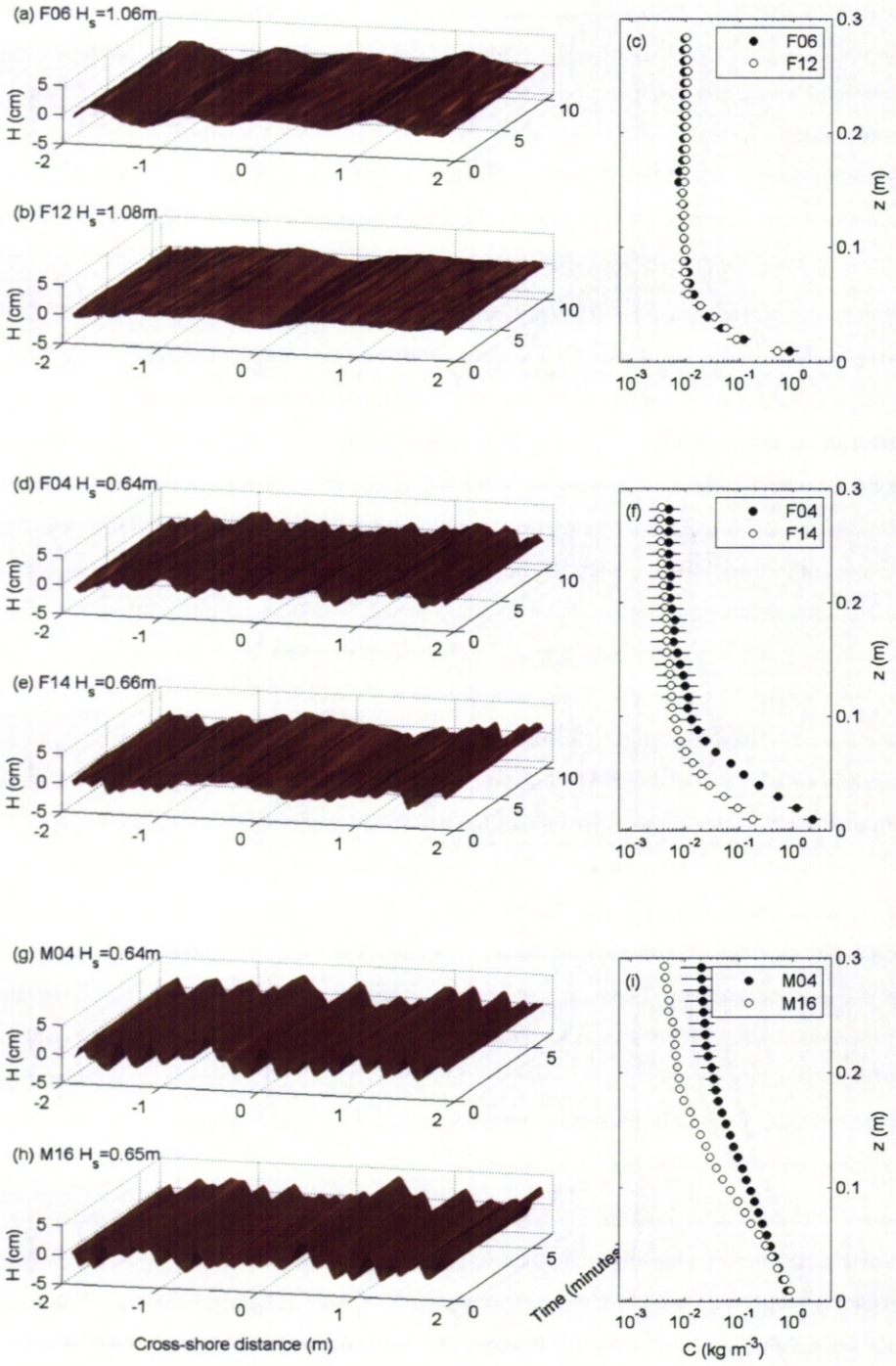

Figure 7.13: Examples of fine (a – d) and medium-grained (e – f) bedforms that emerged during similar wave forcing conditions but under waxing (a, c, e) and waning (b, d, f) phases of the experimental storm sequence. In (g – i) the time-mean SSC profiles above the bedforms presented in (a – f) are shown with those measurements taken during the waxing and waning phases shown by closed (•) and open (○) circles respectively.

origin of the cross-shore distance axis, where the ABS was positioned, during M04. Conversely, Figure 7.13(h) shows that a much smaller and shallower ripple was at this cross-shore location during M16.

7.7.2 Wave irregularity and bedform three-dimensionality

The examination of both cross-sectional and plan-form ripple geometry has shown many of the rippled beds to have a high degree of ripple three-dimensionality. Marsh et al. (1999) and O'Donoghue et al. (2006) compared the dimensions of ripples generated under regular and irregular oscillatory flow with a number of ripple prediction formulae, including that of Wiberg and Harris (1994) examined in Section 7.5.4 here. They generally found poor agreement between their measurements and the prediction formulae, especially in the case of irregular flow. Marsh et al. (1999) contributed this to the lack of a dominate near bed orbital length scale. O'Donoghue et al. (2006) found that the degree of ripple three-dimensionality was similar for regular and irregular flows, with the irregular flow characterised by the mean of the highest one tenth orbital velocity amplitudes. However, the degree of ripple three-dimensionality under irregular waves was larger than under regular waves, for large orbital velocity amplitudes. The irregular nature of the waves was therefore a likely cause of the ripple three-dimensionality and the failure of the ripple prediction formulae examined in Section 7.5.4.

7.7.3 SSC profiles above rippled beds

In Section 7.6.3 exponential profiles were fitted to the near bed SSC profiles measured by the ABS during each experiment. In general there were high correlations between the regressions made and the data, especially when ripples were present on the bed. In order to further examine the degree of agreement between the measurements and the theoretical profile given by equation (7.4), the SSC profiles were normalised by the regression coefficients, C_0 and L, listed in Table 7.3. The results are presented in Figure 7.14 showing all the SSC profiles obtained during experiments, both fine and medium-grained, where 2D or 3D ripples were present on the bed. The line $C/C_0 = \mathrm{e}^{-z/L}$ is shown in Figure 7.14 and indicates a perfect agreement between the data and the theoretical exponential profile (equation (7.4)). Figure 7.14 shows that the data are always exponential in form for $z < 2L$ and starts to deviate from the exponential decay for $z > 2L$. Van der Werf et al. (2006) observed this same phenomenon and contributed it to enhanced sand mixing above $z = 2L$.

An exponential SSC profile is a solution to the steady state sediment diffusion equation with a height constant diffusivity. The deviation of the SSC profiles in Figure 7.14 from the exponential profile, can be associated with the diffusivity starting to increase with z for $z > 2L$. Thorne et al. (2009a) made measurements of time average sediment diffusivity above ripples under weakly asymmetric regular waves in the Deltaflume. The results showed that above steep sided, vortex, ripples the sediment diffusivity was constant within the near bed region

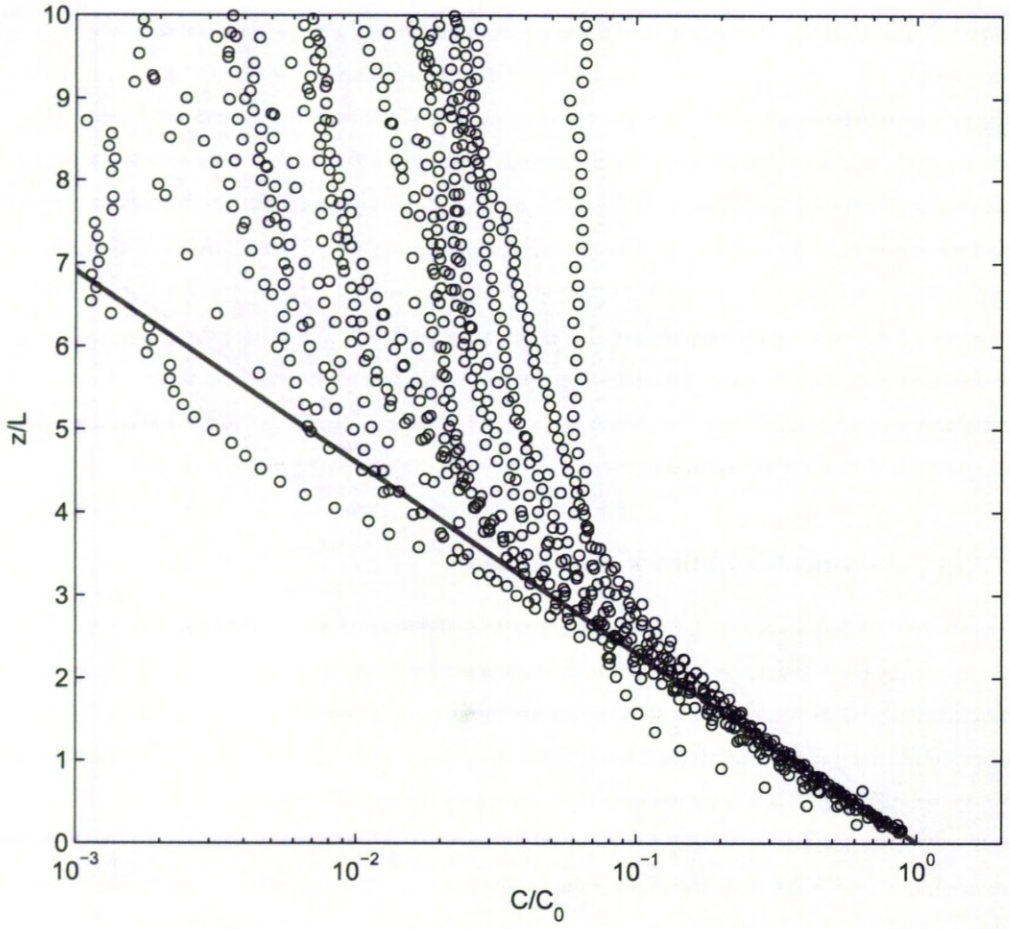

Figure 7.14: The SSC profiles, C, normalised by the reference concentration C_0, obtained during experiments where 2D or 3D ripples were present. The height above the bed, z, is normalised by the measured exponential decay length scales, L. The solid line shows $C/C_0 = e^{-z}$.

approximately equal in thickness to $1.3 \times 25\eta(\eta/\lambda)$, where η and η/λ are respectively the ripple height and steepness, or $3\eta - 4\eta$. Above this near bed region the sediment diffusivity increased linearly with height above the bed (Thorne et al., 2009a). Van Rijn (1993) proposed a three layer structure with a height constant diffusivity within a near bed region of thickness 3η given by equation (7.5b). Figure 7.14 implies that the thickness of the near bed layers observed here, in which the sediment diffusivity was height constant, L_z, are at least $L_z = 2L$. Using equation (7.19) to give L/η for each of the rippled bed experiments here gives $L_z = 2L = (3.3 \pm 1.2)\eta$ which broadly agrees with the findings of others (Nielsen, 1992; Van Rijn, 1993; Thorne et al., 2009a).

Above steep sided, vortex shedding, ripples, Nielsen (1992) related the exponential decay length scale, L, to the orbital velocity, settling velocity and ripple height, η, equation (7.6). Here, L/η was found to be strongly controlled by the parameter $k_s/(\theta_{2.5}\eta)$ over a broader range of bed conditions including 2D, quasi-2D and 3D ripples and hummocks. Crucially, the equivalent roughness, equation (7.18), comprises two terms. The first is the contribution from the form drag over the ripples and dominates when the ripples are steep sided and/or high. The second term is the contribution from the moving sand layer that only dominates under the more vigorous flow conditions when ripple steepness is small.

7.8 Conclusions

Acoustic measurements have been presented on the hydrodynamics, bedforms and suspended sediment concentration profiles, the interacting sediments triad, under weakly asymmetrical irregular waves during a simulated passing of a storm event. Measurements were made after step changes in the significant wave height, forming the experimental storm sequence, over both fine and medium-grained beds. Whilst the responses of the fine and medium-grained beds to the changes in the wave forcing were somewhat different, there were certain similarities. Over both bed types, 2D ripples emerged which at first increased in steepness with H_s and then decreased in steepness and became quasi-2D as H_s continued to increase. This is where the similarities during the waxing phases end. As H_s continued to increase, the fine-grained bed developed long-crested 2D ripples with long $\sim$ 0.9m wavelengths, whereas the plan-form geometry of the medium-grained ripples became increasingly 3D. At peak wave forcing the fine-grained bed became plane while large hummocks developed on the medium-grained bed. During the waning phases, the fine-grained bed remained plane and the long-crested 2D ripples observed during the waning phase failed to fully reform. Quasi-2D and 2D ripples eventually reformed on the fine-grained bed and were at first superimposed on LWRs (Hanes et al., 2001). In contrast, the response of the medium-grained bed to the waning wave forcing was broadly the reverse of that observed during the waxing phase. There is, however, evidence to suggest that the 2D rippled beds took longer to reform and were less steep than those during the waxing phase.

The SSC profiles and reference concentrations were examined in relation to both the wave

forcing and bedform conditions during the storm sequence. Whenever ripples were present on the bed, the time-mean SSC decayed exponentially within a near bed layer the thickness of which, L_z, is roughly equal to two times the exponential decay length scale, L (Figure 7.14). Furthermore, Figure 7.11 shows that L/η can be related to $k_s/(\theta_{2.5}\eta)$ by equation (7.19), where η is the ripple height, and this enables L_z to be predicted using $L_z = 2L$. The exponential decay of sediment is a solution to the sediment diffusivity equation with a height constant diffusivity. Thorne et al. (2009a) observed the sediment diffusivity to be height constant within a layer of thickness equal to three to four times the ripple height, beneath weakly asymmetric regular waves and above steep sided 2D ripples. The results obtained here, beneath irregular waves and over a greater range of ripple types, agree with these findings and suggest that the thickness of the near bed layer was on average 3.3 ± 1.2 times the ripple height during the course of the experimental sequence.

Acknowledgments

This work was supported by the European Union, through its access to large-scale facilities, and by the Natural Environment Research Council and the University of Liverpool for PhD funding. The authors especially thank Prof. J. J. Williams at Associated British Ports, who coordinated the Deltaflume experiments and Dr. Paul S. Bell and Dr. Benjamin D. Moate at the National Oceanography Centre for many usefully discussions regarding the analysis of the acoustic data. We would also like to thank Prof. Stephen S. Flint at the School of Environmental Sciences, University of Liverpool, for his support.

Chapter 8

Discussion and conclusions

Much of what is novel about this thesis is the examination of bedforms and suspended sediment concentrations in a large scale controlled environment beneath *irregular waves*, the more common mode of wave hydrodynamics in the field. The discussion starts, therefore, with a comparison of rippled beds and sediment suspensions beneath regular and irregular waves in the Deltaflume, in order to highlight some of the striking differences in sediment transport processes between these two distinct hydrodynamic regimes. The original research questions posed in Chapter 1 are then addressed, and recommendations of future work are presented.

8.1 A comparison with regular waves

Four years prior to the experiments studied here, a series of experiments were conducted in the Deltaflume using similar acoustic technology. Data from one regular wave experiment, previously examined by Thorne et al. (2003) was reanalysed for this discussion using the same techniques outlined in the previous chapters. These results are here compared with the irregular wave results from M04. In this analysis H is either the wave height or significant wave height for the regular and irregular wave experiments respectively. Similarly, in the case of irregular waves T refers to the peak spectral period, U_0 the significant orbital velocity amplitude and d_0 the significant orbital diameter. The Shields parameter, $\theta_{2.5}$, was calculated using equation (2.7) with the significant values of d_0 and U_0 used in the case of the irregular wave experiment. These parameters are listed in Table 8.1, along with the mean cross-sectional ripple dimensions, for the regular and irregular wave experiments examined. Whilst the height of the regular waves was 1.7 times larger than the significant height of the irregular waves, the orbital diameter values were similar. This was because the irregular waves had, on average, longer periods. The orbital diameter is arguably the dominate control over ripple formation and entrainment via vortices, and whilst d_0 was 1.18 times larger during the regular wave experiment, the d_0/λ values both fall within the criteria of Malarkey and Davies (2002) for vortex shedding. These two experiments are therefore examined, and compared, on the grounds that the dominant

Exp.	H (m)	T (s)	U_0 (m/s)	d_0 (m)	$\theta_{2.5}$	$\overline{\lambda}$ (m)	$\overline{\eta}$ (m)	$\overline{\eta/\lambda}$
Regular	1.06	5.00	0.59	0.94	0.29	0.39	0.054	0.14
Irregular	0.64	6.10	0.41	0.80	0.14	0.26	0.027	0.10

Table 8.1: Experimental parameters for the regular and irregular wave experiments considered.

sediment entrainment process was the same in both cases.

8.1.1 Bedforms

Figure 8.1 shows a comparison of the ripples present on the bed during (a) the regular wave and (b) the irregular wave experiments. There is a clear difference in terms of the amplitude and wavelength of the ripples present with the regular wave ripples being larger. This is in part due to the larger orbital diameters during the regular wave experiment with $d_0 = 0.94$m, whereas $d_0 = 0.80$m in the irregular wave experiment. What is striking though is the spatial variance in cross-sectional geometry in Figure 8.1(b) relative to that in Figure 8.1(a). This is emphasised by Figure 8.2 which shows histograms of the cross-sectional measurements obtained using a turning point analysis on both datasets. The mean wavelength, $\overline{\lambda}$, height, $\overline{\eta}$, and steepness, $\overline{\eta/\lambda}$, shown by the $\times$ in each figure, are listed in Table 8.1. In general the distributions of regular wave ripple dimensions (Figure 8.2(a – c)) have sharp well defined peaks. In the case of the regular wave experiment, the λ and η/λ distributions are normally distributed, whereas the η distribution is positively skewed, indicating that the mean size of 5.4cm is perhaps not the most appropriate choice. The median regular wave ripple height is 5.9cm. In comparison, the distributions of irregular wave ripple dimensions (Figure 8.2(d - f)) have less well defined peaks and are generally negatively skewed. This is especially evident in the case of the ripple height distribution (Figure 8.2(d)). These broader, less well defined, distributions are to some extent associated with the curvature of the ripple crest lines, as discussed in Chapter 7. The character of these irregular wave distributions of ripple dimensions is, however, also associated with the distribution of orbital forcing by the irregular oscillatory flow. The orbital length scale in the irregular wave experiment, is less well defined than in the regular wave experiment (Marsh et al., 1999). In summary, the ripple dimensions are smaller and more broadly distributed during the irregular wave experiment than the regular wave experiment. This is due to (i) the increased variation in orbital forcing and (ii) the curvature of the along-shore ripple crest lines.

Implications on paleoenvironmental reconstruction

These findings have some relevance in the interpretation of ancient wave forcing conditions, specifically the degree of wave irregularity, from preserved ripples. For example, the preservation of a number of adjacent trocoidal shaped ripples with the same (or closely matching) cross-sectional dimensions would have been more likely to occur during periods of prolonged forcing by a wave field with a narrow, rather than a broad, spectrum. In contrast to this, the inference

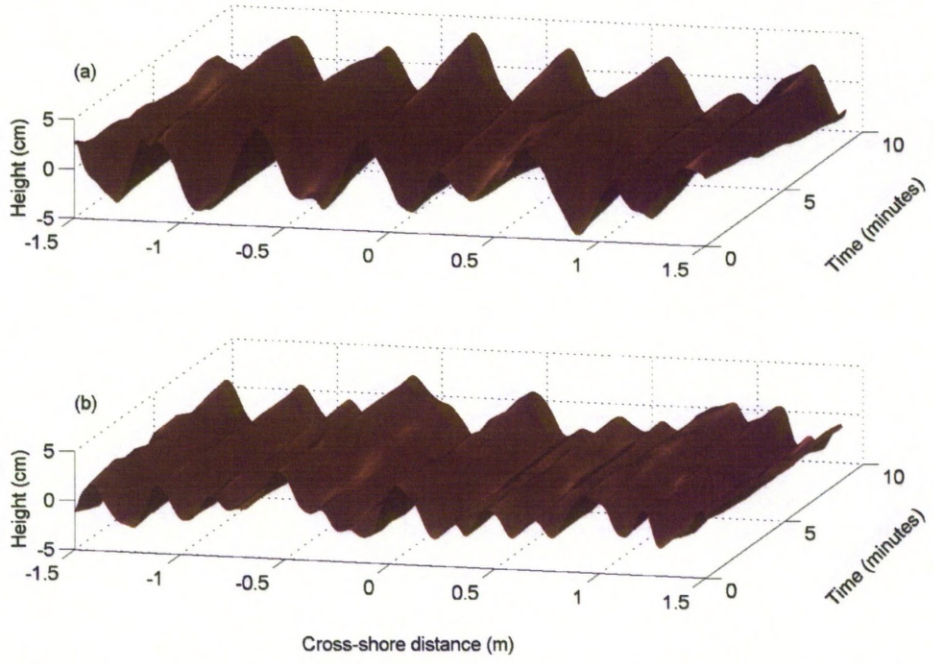

Figure 8.1: Results from the Acoustic Ripple Profiler for (a) regular wave and (b) irregular wave experiments.

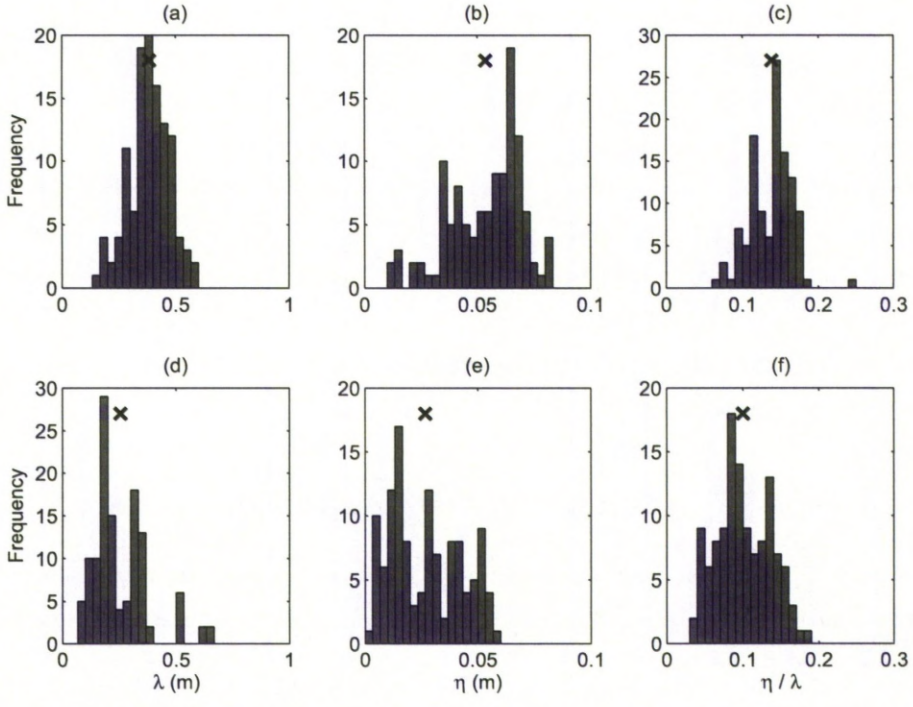

Figure 8.2: The spatial distribution of ripple wavelengths, λ, heights, η, and steepneess, η/λ, from (a – c) regular wave and (d – f) irregular wave experiments.

of a broad wave spectrum can be made from the preservation of ripples with a broad distribution of cross-sectional dimensions. On the coast, the wave spectrum is likely to be narrower on an open shore face than an enclosed shore face with substantial wave refections and interactions. It may therefore be possible, for example, to distinguish between these two paleoenvironments through an examination of the distribution of cross-sectional ripple dimensions.

8.1.2 Suspended sediment concentration time-series

Figure 8.3 shows time-series of suspended sediment concentration (SSC) above the rippled beds presented in Figure 8.1, under the (a) regular and (b) irregular wave experiments. The most striking feature of Figure 8.3(a) is the repeatability of the SSC field due to the regular wave forcing. There are differences from cycle-to-cycle, associated with the stochastic nature of sediment suspensions, but entrainment consistently occurs twice in every cycle. The whole water column is also in a state of equilibrium with a rhythmic variation in SSC at all heights above the bed. In contrast, Figure 8.3(b) shows the response of the SSC to the passing of a wave group during a sequence of irregular waves. Either side of the wave group the orbital velocities are relatively small and there is no intra-wave entrainment from the bed. The larger waves of the group induce vortices which entrain sediment over the ripple crest at flow reversal, as shown in Chapter 5. The water column beneath the irregular waves is out of equilibrium and the SSC at every height above the bed responds to the changing wave forcing. Close to the bed, the SSC responds to the increase in orbital velocity rapidly whereas further away from the bed there is a dependence on antecedent waves, as was show in Chapter 6. At a height of $z \sim 0.6$m the peak SSC occurs when the orbital velocity is relatively small. This is because of wave pumping of sediment and the decay burst phenomena (Villard et al., 2000) discussed in Chapter 6. Finally, it is of interest that because of the decay burst shown in Figure 8.3(b) the peak SSC at $z \sim 0.6$m is an order of magnitude larger than that at the same height in Figure 3.3(a). This is a striking difference which shows that despite the significant wave height of the irregular wave experiment being smaller than the wave height of the regular wave experiment, and the irregular ripple heights being smaller than the regular wave ripple heights, the SSC high above the bed can be larger. This has implications in terms of the net flux of suspended sediment under irregular waves.

8.2 Responses to initial research questions posed

Question 1. ***Can the sediment entrainment process of vortex formation and shedding be identified under irregular waves and how does it contribute to the intra-wave sediment suspension field?***

When ripples are steep sided, the oscillatory bottom boundary layer can separate in the lee of the ripple and form a vortex which can be ejected over the crest of the ripple at flow reversal. The ripple steepness is typically assessed by the ripple height to wavelength ratio,

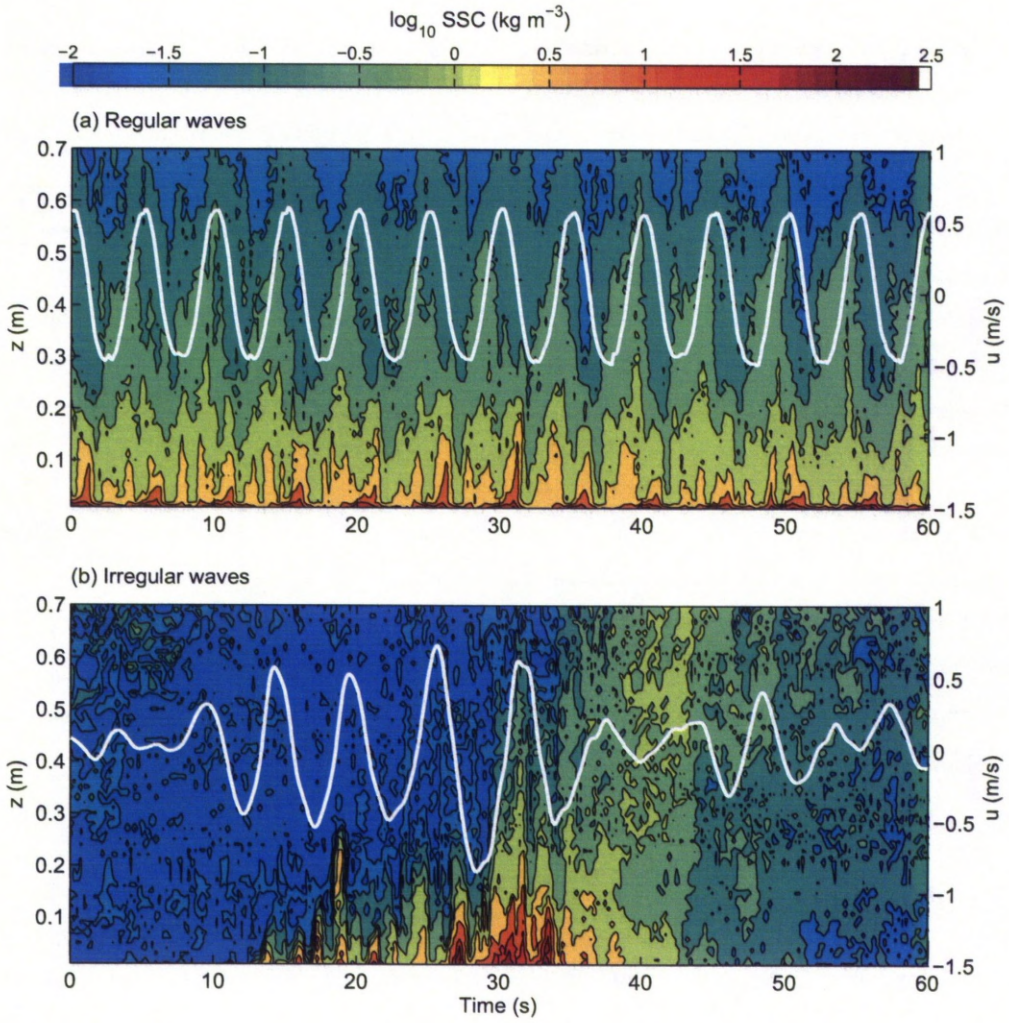

Figure 8.3: Time-series of suspended sediment concentration, SSC, from the Acoustic Backscatter System situated above a ripple crest for (a) regular wave and (b) irregular wave experiments. The orbital velocity time-series, u, from the ADV is also shown

η/λ. Malarkey and Davies (2004) considered $0.13 < \eta/\lambda < 0.2$ to define the vortex shedding regime, although it is commonly accepted that vortex shedding can start when $\eta/\lambda > 0.1$ (Davies and Thorne, 2005). In addition to this cross-sectional geometric requirement of the ripples, vortex coherency was considered to be highest when the ripples had two-dimensional (2D) plan-form geometries. Thus, in Chapter 5 the Deltaflume experiments where the ripples had 2D or quasi-2D plan-form geometries and $\eta/\lambda > 0.1$ were considered for an investigation into the intra-wave sediment suspension process of vortex formation and shedding. Under the irregular waves generated in the Deltaflume, there were typically broad spatial distributions of ripple cross-sectional measurements. Thus, it was important to consider both the spatially averaged ripple steepness and that of the ripple inducing local boundary layer flow separation.

Intra-wave sediment entrainment processes depend on the characteristics of each wave, which fluctuate from wave-to-wave under irregular waves. Intra-wave processes are also inherently stochastic in nature, due to the turbulent character of boundary layer flow. In Chapter 5, therefore, between 50 - 100 wave cycles were phase ensemble averaged over in order to examine the underlying sediment suspension field above the crest of steep 2D ripples. What emerged was consistent with the entrainment of sediment in vortices during each wave half cycle, previously observed in a large scale flume under regular waves (Davies and Thorne, 2005), with peak sediment pickup concentrations above the ripple crest occurring around flow reversal. This was shown by Figure 5.11 where the phase ensemble averaged SSC field above crests of 2D or quasi-2D ripples were contrasted with that above a plane bed. These results represented the SSC field on average. Whilst this effectively removed the effects of stochastic variability in the process, how the process differed from wave-to-wave was also effectively removed.

The intermittent nature of vortex formation and shedding beneath irregular waves was perhaps best illustrated in Chapter 6 where time-series of SSC were examined above ripples, e.g. Figure 6.5. This is because of the variability in the properties of each half cycle, namely their orbital velocity amplitude and half period. Figure 8.3 here compares time-series of SSC above ripples under regular and irregular waves. Whilst entrainment events occur consistently twice every wave cycle beneath regular waves, they only occur under the stronger waves beneath irregular waves. In order to examine in more detail the intra-wave entrainment processes it is important to remove some of the stochastic variability inherent in turbulent boundary layers. Therefore, in Chapter 5 discrete distributions of orbital diameters during sequences of irregular waves were examined. Each discrete class contained a number of half cycles and the instantaneous reference concentrations within each class were phase ensemble averaged to remove stochastic effects from the analysis. The orbital diameter, d_0, is a function of both the wave half period and velocity amplitude, and therefore captures a great deal of information regarding the wave half cycle. Physically, d_0 is the horizontal distance moved by the near bed fluid particles during each half cycle. The results, shown in Figure 5.14, demonstrate that the advection of sediment via vortex formation and shedding only occurred when $d_0 > 1.2\lambda$ where λ is the wavelength of the ripple inducing flow separation.

For the three rippled bed experiments considered in Chapter 5, d_0 was on average $> 1.2\lambda$ during 70% of onshore half cycles and 58% of offshore half cycles. This was due to a weak wave asymmetry where, on average, the orbital excursions of the onshore half cycle where greater than those during the offshore half cycle, mainly associated with a velocity asymmetry rather than an asymmetry in the half wave period.

Only two clear peaks during the wave cycle were observed in the SSC above the ripple crest in Chapter 5. This is consistent with the advection of a locally induced vortex at flow reversal. There was no evidence to suggest that the advection of vortices induced by upstream ripples were contributing to the local SSC field. This lack of horizontal vortex advection beneath irregular waves is due to (i) the vortices being incoherent over temporal scales longer than a wave cycle and (ii) the spatial rarity of steep sided ripples. If irregular waves are the more common mode of nearshore hydrodynamics then this spatial rarity of steep ripples has implications concerning the prediction of net sediment transport. For example, models that assume vortex shedding occurs at all points on a bed when $\overline{\eta/\lambda} > 0.1$ are likely to be inconsistent with the average sediment suspension and transport in the field.

In conclusion, the vortex entrainment of sediment has been identified beneath irregular waves. Under the irregular wave forcing the occurrence of this process was, however, limited by (i) the steepness of the ripples, (ii) the plan-form geometry of the ripples, (iii) the spatial distribution of ripple cross-sectional and plan-form geometries and (iv) the irregular occurrence of the process related to d_0/λ. Locally, above a steep sided ripple this process can contribute significantly to the SSC field and this contribution can differ between onshore and offshore half cycles, depending on the wave asymmetry. It was found in Chapter 5 that the percentage of waves where vortex formation and shedding dominate scales approximately with d_s/λ by a factor of 26, where d_s is the significant orbital diameter.

Question 2. ***What is the character of the sediment suspensions under wave groups?***

Figure 8.3 highlights a striking difference between a sediment suspension in equilibrium with the regular wave forcing and a sediment suspension beneath a wave group. How much of the suspension field in Figure 8.3(b) is due to (i) the presence of ripples and (ii) the character of the wave group? This question was addressed in Chapter 6 where time-series of instantaneous SSC were examined under a number of flow and bedform regimes. Whilst close to the bed the initial entrainment of sediment was an intra-wave process occurring intermittently, as discussed above, wave groups strongly influenced suspensions higher above the bed. The enhanced sediment suspensions during wave groups strongly characterised the whole time-series of SSC under irregular waves, at all heights above the bed.

Chapter 6 showed that the character of sediment suspensions under wave groups varied with the time average wave forcing and bedform conditions. This is because the availability of near bed suspended sediment to be pumped to high elevations beneath wave groups depends on the activity of intra-wave entrainment. Chapter 6 showed that the SSC above 0.3m from the bed

was higher and more sustained when $H_s = 1.51$m than when $H_s = 1.63$m. This was due to the enhanced intra-wave entrainment and turbulence production above the 3D ripples when $H_s = 1.51$m than above the hummocks when $H_s = 1.63$m.

The character of sediment suspensions beneath wave groups is also strongly dependent on the wave group characteristics. In Chapter 6, four different wave group types were identified and their associated sediment suspensions examined. Wave groups terminating with an abrupt decrease in orbital velocity amplitude, the waxing and constant types identified, strongly influenced the sediment suspensions high above the bed with decay bursts (Villard et al., 2000; Vincent and Hanes, 2002). A similar phenomenon was observed to occur above the fine-medium-grained plane bed where sheet flow processes were likely to be in operation. Wave pumping did not play a large role in this regime, as the suspended sediment was confined to a near bed sheet flow layer. After larger than average orbital velocities, however, the near bed confined sediment 'burst' upwards.

Question 3. ***How do sandy beds respond to changes in wave forcing and what is the influence of inherited bedforms?***

Chapter 7 studied the development of bedforms, on fine-medium-grained (fine-grained) and upper-medium-grained (medium-grained) sand beds, under step changes in the significant wave height. The changes in hydrodynamic forcing can be tracked on a bedform phase diagram for oscillatory flows, such as that of Allen (1979) (Figure 2.2), and are discussed in the context of this paradigm. The fact that the experiments were conducted twice, on beds with differing median grain diameters, enables two vertical lines to be examined on the bedform phase diagram of Allen (1979). The bedform phase diagram of Allen was compiled primarily using wave tank and oscillatory water tunnel data, but also field measurements taken on the continental shelf (west coast of North America). Figure 8.4 shows the bedform phase diagram with the results from the Deltaflume experiments shown as symbols. The separation on the abscissa, of $\sim 120\mu$m, in the results suggests there should be a small difference in the response of the two beds to the changing hydrodynamics. They should, however, broadly show the same response of lower-stage plane bed, low-steepness ripples, vortex ripples, low-steepness ripples and upper-stage plane bed. This was broadly the case, when considering the cross-section dimensions of the ripples, as shown by Figure 7.6. There was, however, a strong difference in the development of the two beds, when considering the plan-form ripple geometries. The plan-form ripple geometries, using the classification developed in Chapter 7, which broadly follows that of Pedocchi and Garcia (2009), are indicated in Figure 8.4. The 2D and quasi-2D ripples mainly populate the region of steep vortex ripples in Allen's diagram. The exceptions are the two long wavelength 2D results from the fine-grained bed. These are broadly within the low-steepness ripples regime. The fine-grained plane bed at $U_0 = 0.18$m/s is within the vortex shedding regime. This is likely to be because there had not been adequate orbital oscillations of 0.18m/s to form ripples during the experimental run time. The upper-stage plane bed results fall within the sheet flow regime,

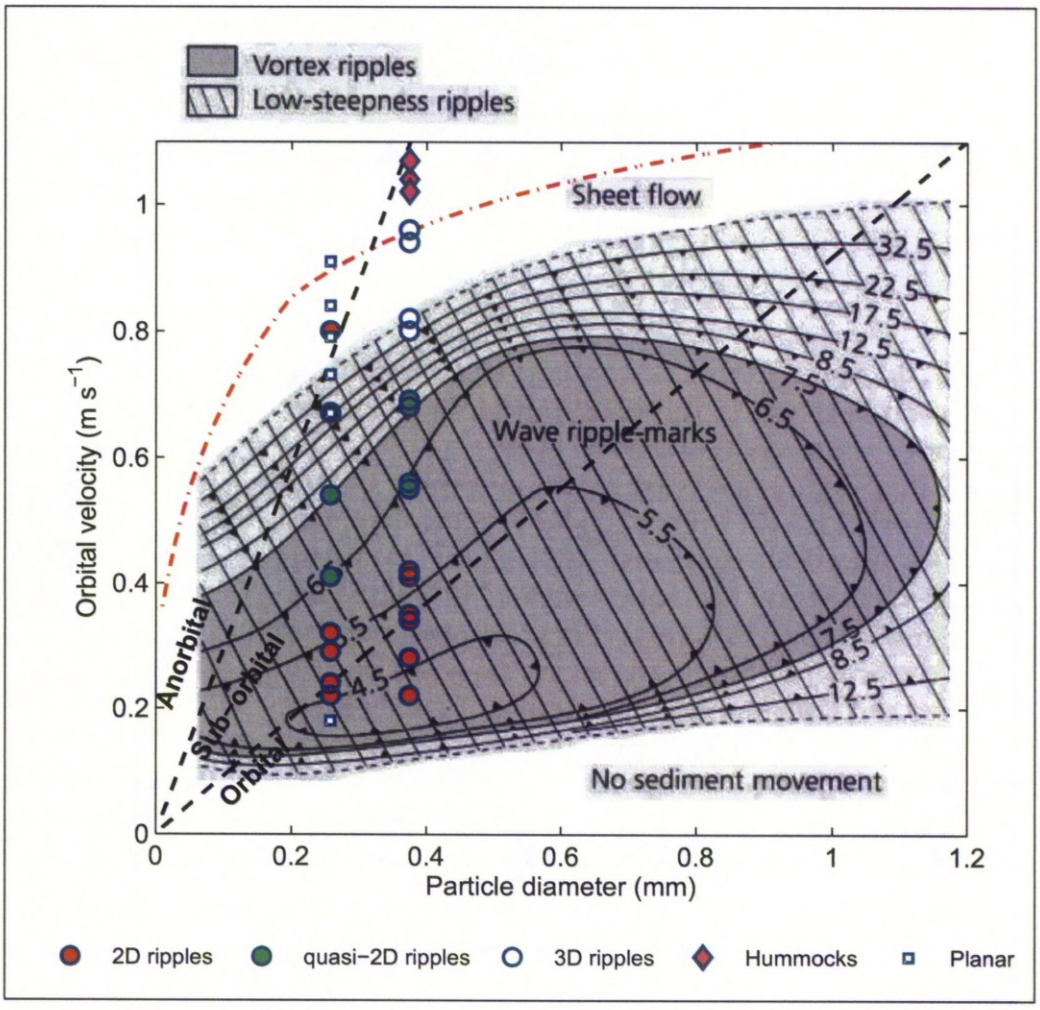

Figure 8.4: The oscillatory bedform phase diagram of Allen (1979) with the results from the irregular wave Deltaflume experiments indicated. The 3D plan-form geometry of the ripples present in each case are indicated. Also shown are the orbital–anorbital boundaries of Clifton (1979) (– –), and the suggested boundary for Hummock formation of Kleinhans (2005) (– · –), for a wave period of 6 seconds.

but also the low-steepness ripple regime. The results within the low-steepness ripple regime are inherited beds from previous, stronger, flows that existed during the waning stage of the storm sequence, as discussed in Chapter 7. The medium-grained bed did not flatten out and the results within the low-steepness ripple and sheet flow regimes are 3D ripples and hummocks. This broadly conforms to the bedform phase diagram of Allen (1979), as the 3D ripples had low steepness and Chapter 7 suggested that sheet flow processes operated while the bed was populated by 3D ripples and hummocks.

Under step changes in the significant wave height, sandy beds broadly respond in a way depicted by the bedform phase of Allen (1979). There are, however, deviations at the edge of boundaries associated with the irregular nature of the flow. The bedform phase diagram of Allen (1979) shows both bedform physicality and process. The ripple regimes are described

in terms of ripple steepness, or form-index, and the plane bed regimes are described in terms of process, with the lower-stage bed described as no sediment movement and the upper-stage described as sheet flow. The process description, which could be considered to be inconsistent with the ripple descriptions, allows for low steepness, three-dimensional, bedforms to broadly fit within this paradigm. This paradigm, depicted by the bedform phase diagram, is lacking in that it does not include plan-from ripple geometry which formed a distinct difference in the response of the two beds.

The bedform phase diagram of Allen (1979) is lacking in that it does not include hummocks. This is because hummocks and mega ripples had not been widely reported in 1979, and they are typically considered to be features that form under combined wave and current flows (e.g. Swift et al., 1983). Since the development of Allen's diagram for waves only, there have been many bedform phase diagrams developed for combined waves and currents (e.g. Amos et al., 1996; Arnott and Southard, 1990) incorporating hummocks and mega ripples. Kleinhans (2005) developed a new bedform phase diagram for waves, bringing together results from a number of workers. Kleinhans argued that the boundary between ripples and dunes developed by Allen and Leeder (1980) for currents, could be used as a boundary beneath waves for the transition from ripples to hummocks. This was because Southard et al. (1990) found hummocks to occur under purely oscillatory flow as well as under combined waves and currents. This boundary is shown in Figure 8.4 by the red line ($- \cdot -$), and predicts the hummocks that formed on the medium-grained Deltaflume bed well. This boundary adds information about the plan-form nature of the bed to the diagram of Allen (1979) and complements its transition to sheet flow, suggesting that sheet flow processes occur over hummocks.

Another paradigm which can be used to discuss the development of ripples during a storm sequence is that first developed by Clifton (1976) where the ripples are classified as orbital, sub-orbital or anorbital, and this was done in Chapter 7. Here, this paradigm is compared with that of the bedform phase diagram. It is possible here to consider the results from the Deltaflume because the peak spectral period was held constant. Thus, taking the wave period as 6 seconds, the approximate regime boundaries of Clifton (1976), and more recently Wiberg and Harris (1994), are shown in Figure 8.4 by the dashed lines. The majority of data fall within the sub-orbital regime. Only data from the fine-grained bed fall within the anorbital regime, and this is where the plane bed conditions were observed. Considering these boundaries and the bedform phase diagram shows that within the sheet flow regime depicted in Figure 8.4 the oscillatory orbital excursions can still influence the formation of sub-orbital ripples, as was the case on the medium-grained bed.

The bedform-phase diagram of Allen (1979) does not consider the presence of relict bedforms. In Chapter 7 the ripple cross-sectional dimensions were seen to vary with the ratio of significant orbital diameter, d_s, to median bed sediment diameter, D_{50}. The variation of mean ripple steepness, $\overline{\eta/\lambda}$, with d_s/D_{50} is presented in Figure 8.5(a), and as a function of the order in which the measurements were collected. Figure 8.5(a) shows that during the waning phases

the ripple steepness failed to reach that of the waxing phases for some time after the peak in the flow. This was physically most distinguishable on the fine-grained bed (squares) where the bed remained planar through experiments 8 - 12. Ripples did reform in experiment 13, which were on average steeper, but were superimposed with long wavelength features that formed in the nominally plane bed conditions (see Chapter 7). In terms of mean steepness, there is a large difference between those measurements taken during the waxing and waning phases on the medium-grained bed (circles). Figure 8.5(a) illustrates that (i) there is a time-lag in the response of bedforms in a waning scenario and (ii) relict bedforms can prevail for long periods after the flow regimes have changed. This behaviour is analogous to that observed by Allen (1973) in a unidirectional flow setting shown in Figure 8.5(b).

Figure 8.5(a) shows that the hummocks formed at the peak in the storm sequence, confirming that they are typically constructed during the early waning stages of storms (Amos et al., 1996). During the waxing and peak phases of storms there is typically considerable reworking of the bedforms with large amounts of sediment entrained. This large sediment volume is typically deposited during the waning stages of a storm, where there are still large orbital excursions, forming large bedforms and hummocks (Amos et al., 1996). As the storm abates there is still deposition, but the orbital excursions have lessened and there is little reworking of the bedforms. This is why there is a time lag in Figure 8.5(a). This has implications for bedform preservation since there is substantial deposition, but little reworking of bedforms during the waning phase. Hence hummocks are often preserved as hummocky cross-stratification (Arnott and Southard, 1990; Southard et al., 1990). This also supports the notion of preferential preservation after extreme events.

Question 4. ***How do time average suspended sediment concentration profiles respond to changes in the wave forcing and bed conditions?***

Suspended sediment concentration (SSC) profiles are characterised by their shape and magnitude, or reference concentration, and are strongly dependant on the strength of the oscillatory flow and the type of bedforms present (Ribberink and Al-Salem, 1994; Vincent et al., 1999; Grasmeijer and Kleinhans, 2004). In Chapter 7, these two characteristics of time average SSC profiles were examined during the simulated passing of a storm event. The systematic stepping up and down of the wave forcing allowed the SSC profiles to be studied during a number of hydrodynamic and bedform conditions. Both the rate at which the SSC profiles decayed and their reference concentrations were found to vary with the flow and bedform dimensions. In the case of the reference concentration the parameter most able to parameterise the magnitude of the suspensions over the range of flow and bed conditions was the ripple modified Shields parameter proposed by Nielsen (1986), as discussed in Chapter 7.

It was found that above ripples the shape of the SSC profile is exponential within a near bed mixing layer approximately equal in thickness to two times the exponential decay length scale, the mixing length, as shown by Figure 7.14. This exponential decay supports the concept

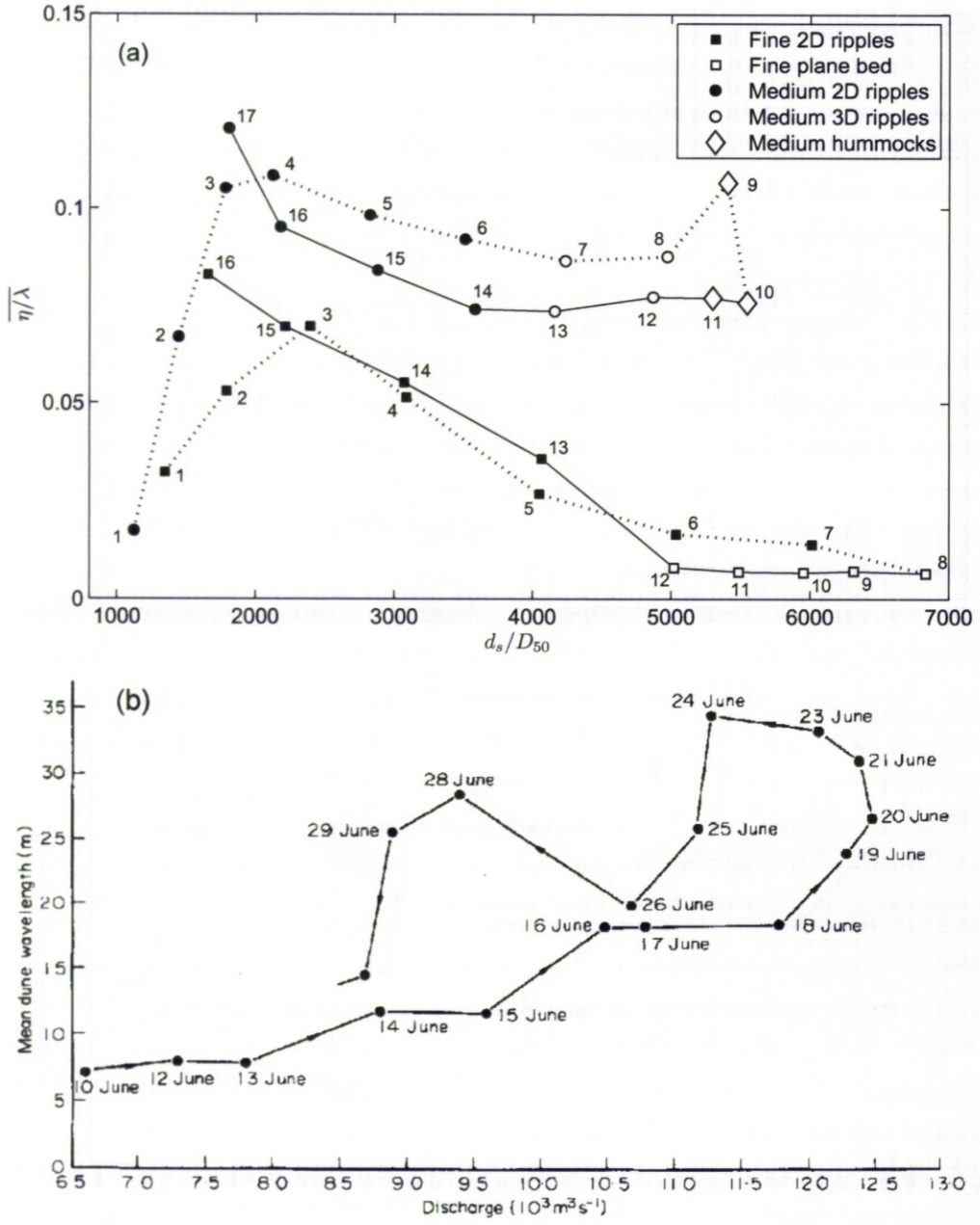

Figure 8.5: (a) Variation in mean ripple steepness, $\overline{\eta/\lambda}$, with the ratio of significant orbital diameter, d_s, and median bed sediment diameter, D_{50}, for oscillatory flow above fine-grained (squares) and medium-grained (circles and diamonds) sand. The order that the measurements were taken and whether they were taken during the waxing ($\cdots$) or waning ($-$) phases are indicated. (b) Variation in mean dune wavelength with discharge of unidirectional flow and as a function of time (from Allen, 1973).

of the sediment diffusivity above ripples being height constant within the near bed mixing layer (Nielsen, 1992; Van Rijn, 1993; Thorne et al., 2009a). Figure 7.14 shows that above this near bed region the mixing length increases with height suggesting that the sediment diffusivity increases with height, as was found to be the case by Thorne et al. (2009a). The exponential mixing length, which is proportional to the sediment diffusivity, has previously been related to the oscillatory flow and the ripple dimensions (e.g. Nielsen, 1992; Van Rijn, 1993). This was confirmed in Chapter 7 where, for the case of 2D ripples, the mixing length was related to the ripple height and steepness and the grain roughness Shields parameter. This relationship did not hold for the 3D ripples and hummocks. Replacing the ripple steepness with the ratio of hydraulic bed roughness to ripple height yielded an expression for the mixing length for all the bedform conditions observed. The expression for the hydraulic roughness included contributions due to ripple form drag and sheet flow processes. In the majority of conditions observed the roughness was dominated by the contribution of the ripples. In the most energetic conditions, however, when large 3D ripples and hummocks formed, the sheet flow contribution dominated the roughness.

These results confirm that both the flow and the bedforms control the magnitude and vertical distribution of time averaged sediment suspensions. There are, however, a wide range of bedform and flow conditions in nature and a common goal is to unite the different processes occurring, at different temporal and spatial scales, in these varied condition within a common framework. The work in Chapter 7 attempts to do this with the use of an enhanced bed roughness.

Question 5. ***Over what timescales do sediment suspension processes operate under irregular waves and what implications does this have for future observations and modelling?***

In the nearshore zone and continental shelf, steep-sided wave formed ripples are common bedforms and the suspension of sediment can be dominated by vortex formation and shedding. Chapter 5 shows that this coherent and repeatable sediment entrainment process can occur, and can strongly contribute to the intra-wave sediment suspension field, beneath irregular waves. It does not, however, have the same repeatability under irregular waves as it does under regular waves, as Figure 8.3 highlights. This initial entrainment process, acting on small spatial and temporal scales, can strongly influence sediment suspensions over larger spatial and temporal scales. Chapter 6 shows that the influence wave groups have on sediment suspensions depends on the availability of entrained sediment within the boundary layer, and this is a function of the bedforms and entrainment process as well as the wave forcing. Chapter 7 shows that the initial entrainment process can influence sediment suspensions over longer timescales still. The near bed mixing length and thickness of the near bed layer were shown to be strongly dependent on a hydraulic roughness with contributions from vortex ripple and sheet flow processes.

Small scale entrainment processes strongly influence the SSC close to the bed under irregular

waves, both instantaneously and in a time average sense. Because there is no true equilibrium under irregular waves, as discussed in Section 8.1, the suspension of sediment at higher elevations is strongly controlled by processes acting at lower frequencies than the wave frequency. Chapter 7 shows that wave groups can lead to the entrainment of sediment to heights >0.8m above the bed. The current related net transport of sediment, at these heights above the bed, could therefore be larger beneath a grouped wave field than a wave field with a higher significant wave height but fewer groups. The time average SSC profile is therefore a function of intra-wave processes close to the bed and lower frequency, wave-group, processes higher up. This goes someway to further explain the scatter above the near bed mixing layer in Figure 7.14, as it depends on the character of the wave groups influencing the time mean SSC profile.

In conclusion, sediment suspensions operate at a variety of different timescales from intra-wave entrainment to sediment-pumping at a frequency associated with wave groups. In terms of experimental design and modelling, it is important to be clear as to the purpose. To truly understand the process of entrainment it is necessary to measure at the smallest scales. This can therefore be fed back into complex process based research model development. A great deal can, however, be inferred about the entrainment process and the sediment transport triad as a whole from time average observations, such as Chapter 7. Finally, the spectral width and character of wave groups can influence the sediment suspensions at intermediate timescales at the order or minutes. It is, therefore, important not only to accurately model intra-wave processes but to consider the wave spectra and the vertical advection of sediment at wave group frequencies.

8.3 Future work

The response to the initial research questions in the previous section raised a number of implications and issues within which there is scope for further research. Some of these points are discussed in more detail below.

Observations of intra-wave sediment entrainment at other points on the ripple cross-sectional profile

In Chapter 5 measurements were made of the SSC field above ripple crests. As outlined in the response to Question 1, it was hard to distinguish whether the advection of vortices induced upstream were contributing to the local SSC field above the crest. With measurements taken at only one point on the ripple cross-sectional profile, it is also challenging to interpret the spatial structure and motion of vortices and small scale turbulent structures. This has previously been addressed by aligning three ABS transceivers across-shore, perpendicular to the ripple crest lines, so that three points on the ripple cross-sectional profile were monitored simultaneously (e.g. Osborne and Vincent, 1996). Others (e.g. Thorne et al., 2003; Van der Werf et al., 2007) have taken continual measurements above a migrating ripple. Assuming the waves to be regular

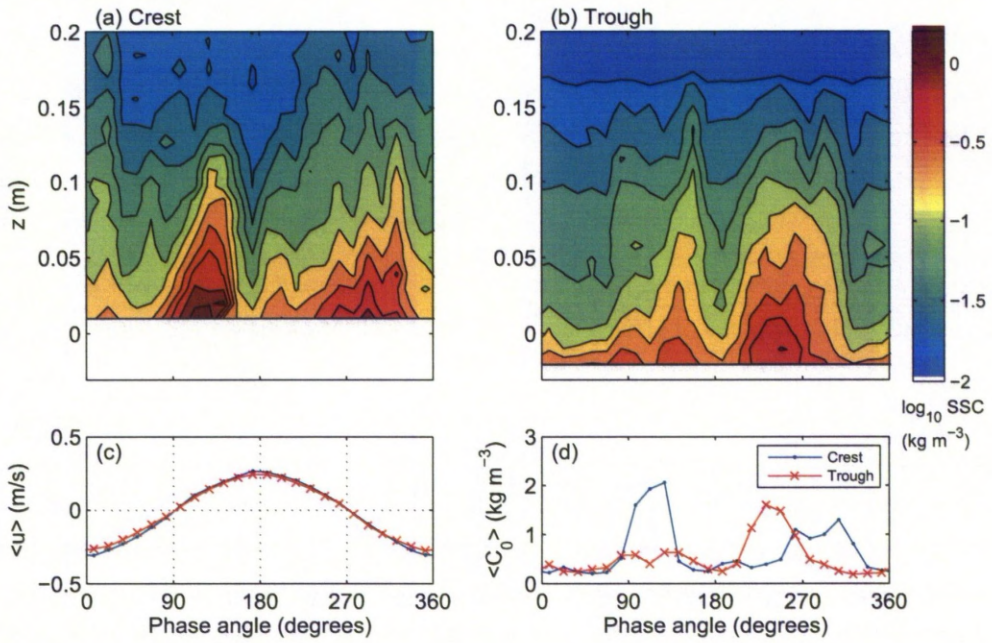

Figure 8.6: Phase ensemble averaged intra-wave suspended sediment concentration, SSC, field above (a) the ripple crest and (b) the ripple trough. The phase ensemble averaged intra-wave velocity and reference concentration are shown in (c) and (d) respectively.

so that the flow is in equilibrium, as in Figure 8.3(a), an impression of the ensemble average spatial structure can be built up. This approach is challenging in the case of irregular waves however.

In the case of the irregular wave Deltaflume experiments studied here, the ABS was mounted on a sliding platform which was periodically moved cross-shore. Figure 8.6 shows the phase ensemble averaged SSC field obtained from the ABS approximately positioned above (a) the ripple crest and (b) the ripple trough. The ABS was in each of these two positions for approximately 10 minutes, approximately 100 wave cycles, beneath irregular waves with $H_s = 0.64$m. The ensemble average reference concentrations are also shown in Figure 8.6(d). Above the ripple crest there are two peaks in the SSC during the wave cycle associated with the advection of vortices at flow reversal. Above the ripple trough, however, there is one major peak at $\sim 235°$ and two minor peaks at $\sim 95°$ and $\sim 130°$. The major peak is associated with the generation of a vortex in the ripple lee during the onshore phase of the wave cycle, and the two smaller peaks are most likely associated with the local generation of a vortex in the lee of a neighbouring ripple and the advection of a vortex generated upstream.

As acoustic technology becomes more reliable and robust and the technology to support such hardware, such as batteries, develops further, the number of transceivers within Acoustic Backscatter Systems will increase. This will allow for high frequency observations to be made over a large surface area of the bed simultaneously, allowing for the tracking of individual vortex structures and entrainment events in three dimensions.

Collocated measurements of sediment concentration and velocity profiles beneath irregular waves

Sediment dynamics is inherently linked to the velocity field within turbulent boundary layers. Whilst turbulence has a stochastic and anisotropic nature, it was shown here that the periodicity within the oscillatory boundary layer can impose some order with the generation of vortices. Making detailed measurements of the velocity field in addition to the SSC field is a crucial further development. It is now possible to make such measurements using Particle Image Velocimetry or Acoustic Doppler Velocity Profilers in conjunction with ABS (e.g. Thorne et al., 2009b). The measurement of the velocity field would enable accurate calculations of sediment flux to be made, such those made by Van der Werf et al. (2007) under regular oscillatory flow.

Net sediment flux calculations above vortex ripples under irregular waves

Van der Werf et al. (2007) made detailed measurements of the near bed velocity field and SSC above vortex ripples. This enabled the cross-shore flux of near bed suspended sediment, due to vortex shedding, to be calculated. These measurements were made under weakly asymmetrical regular oscillatory flow. It is possible to combine such results with those in Chapter 5 here, in order to arrive at estimates of net cross-shore sediment transport due to vortex shedding. One approach might be to take the cross-shore flux of sediment due to vortex shedding beneath regular waves, with orbital diameter d_0, and scale it by $26d_s/\lambda$. This approach is limited by the fact that this work is based on measurements made beneath JONSWAP irregular waves with a peak enhancement factor of $\gamma = 3.3$. Other future work might be to make measurements beneath a range of wave spectra.

Resolving the vertical flux of sediment beneath wave groups

In Chapter 6 the vertical transport of sediment was examined over wave group timescales using the results from the ABS. The evidence was consistent with the wave pumping phenomena previously observed (Villard et al., 2000; Vincent and Hanes, 2002). It is possible that this vertical transport of sediment laden water over wave group timescales could be resolved in the vertical velocity component of the ADV, u_z. u_z was dominated by turbulence, and it was considered beyond the scope of this study to examine the detailed structure of u_z. If there is a residual component to u_z on wave group timescale then it could provide an important quantitative assessment of sediment transport due to wave groups.

Unification of ripple prediction schemes

As outlined in the response to Question 3, there are a number of schemes that can be used to predict the development of ripples including that of the bedform phase diagram (e.g. Allen, 1979) and how the ripple wavelength compares with the orbital diameter (e.g. Clifton, 1976). These schemes are informative in terms of ripple physicality and the processes of sediment

suspension and ripple development. In recent years there has been a surge in the development of schemes to predict the cross-sectional dimensions of ripples (e.g. Wiberg and Harris, 1994; Soulsby and Whitehouse, 2005; Mogridge et al., 1994). There is also some progress towards the prediction of plan-form ripple geometry (e.g. Pedocchi and Garcia, 2009). Integrating these different methodologies into a unified model and classification scheme is the next challenge. Such unification would have an application, not just in coastal science and engineering, but also in the interpretation of preserved ripples. For example, trocoidal shaped ripples with linear plan-form geometry form in different oscillatory-flow and grain size conditions than ripples with curved crests and three-dimensional plan-form geometry. At present, such ripples would fall within the same region on the bedform phase diagram.

Is there merit in the use of one-dimensional vertical models based on regular waves for irregular wave applications?

Modelling the time average, vertical, one-dimensional distribution of suspended sediment is both practical and can reveal some of the underlying physical processes. Examples of such models for use above rippled beds are the *convection-diffusion model* of Nielsen (1992), based on equation (2.12), and the *1DV rippled bed model* of Davies and Thorne (2005). The model of Nielsen (1992) operates in a truly time average sense whereas that of Davies and Thorne (2005) models the intra-wave processes occurring above steep sided ripples under regular waves. Both models require the wave forcing to be parameterised by a regular wave. When using such models to predict sediment suspensions beneath irregular waves it is a valid question to ask what equivalent regular wave should be used. Figure 8.7 shows results from these two models where the equivalent regular waves are parameterised by the peak spectral period and (i) the significant wave height (solid lines), (ii) the mean wave height (dotted lines) and (iii) the mean average height of the top 1/10 waves (dashed lines). The time mean SSC profiles above steep ripples on the medium-grained bed (Figure 8.7(a and b)) and shallow ripples on the fine-grained bed (Figure 8.7(c and d)) were modelled. The 1DV rippled bed model performs well for the case of the steep ripples (Figure 8.7(b)) and poorly in the case of the shallow ripples (Figure 8.7(d)). This is because it accurately describes the process of vortex formation and shedding in the case of steep ripples, but not the processes occurring above shallow ripples. In contrast, the convection-diffusion model performs well in both conditions, but to a lesser degree than the 1DV rippled bed model above the steep ripples. Whilst not representing the process of vortex formation and shedding explicitly, the convection-diffusion appears to perform well in the two different conditions. This is most likely due to the representation of both diffusive *and* convective processes within the model.

Figure 8.7 suggests that there is merit in modelling the time mean SSC profiles under irregular waves with models that require a regular wave parameterisation. There are questions, however, regarding the exact parameterisation and whether there is merit in modelling the intra-wave processes in detail. Nonetheless, the further development of 1DV modelling tech-

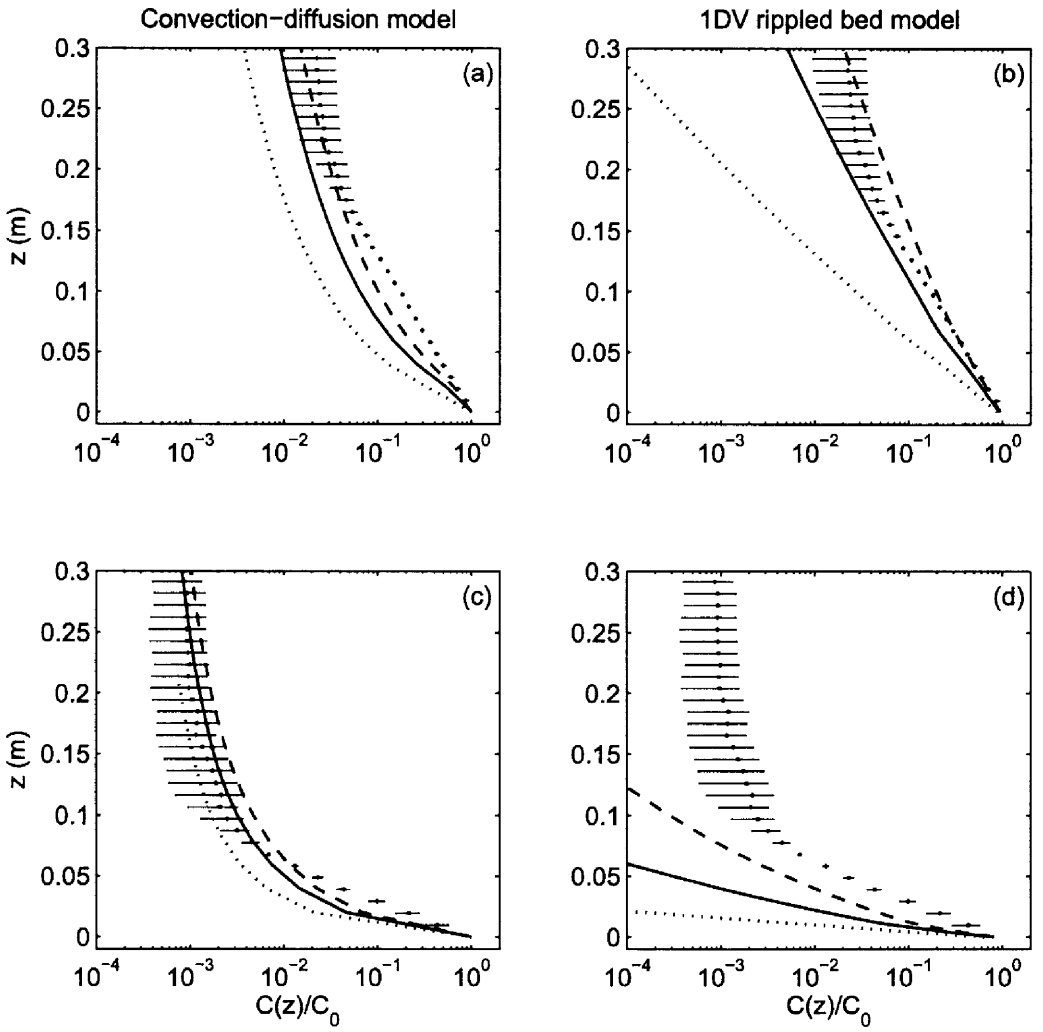

Figure 8.7: The time mean distribution of sediment concentration, $C(z)$, with height above the bed, z, normalised by the reference concentrations at bed level, C_0, from irregular waves experiments where $H_s = 0.64$m and bed sediment was (a, b) upper-medium-grained and (c, d) fine-medium-grained. The lines show results from (a, c) the convection-diffusion model of Nielsen (1992) and (b, d) the 1DV model of Davies and Thorne (2005). The waves were parameterised by the significant wave height (−), mean wave height (· · ·) and mean of the top 1/10 wave heights (− − −).

niques, and well-designed and instrumented field and flume data collection, will lead to improved understanding of sediment transport across different timescales in the coastal zone.

Bibliography

Allen, J. R. L., 1973. Phase differences between bed configuration and flow in natural environments, and their geological relevance. Sedimentology 20 (2), 323–329.

Allen, J. R. L., 1979. A model for the interpretation of wave ripple-marks using their wavelength, textural composition, and shape. Journal of the Geological Society 136 (6), 673–682.

Allen, J. R. L., Leeder, M. R., Apr. 1980. Criteria for the instability of upper-stage plane beds. Sedimentology 27 (2), 209–217.
URL http://doi.wiley.com/10.1111/j.1365-3091.1980.tb01171.x

Allen, P., 1997. Earth Surface Processes. Blackwell Science Ltd.

Allen, T., 1968. Particle size measurment. London: Chapman & Hall.

Amos, C. L., Li, M. Z., Choung, K. S., May 1996. Storm-generated, hummocky stratification on the outer-scotian shelf. Geo-marine Letters 16 (2), 85–94.

Andersen, K. H., 2001. A particle model of rolling grain ripples under waves. Physics of Fluids 13 (1), 58–64.

Ardhuin, F., Drake, T. G., Herbers, T. H. C., 2002. Observations of wave-generated vortex ripples on the north carolina continental shelf. Journal of Geophysical Research-Oceans 107 (C10).

Arnott, R. W., Southard, J. B., Mar. 1990. Exploratory flow-duct experiments on combined-flow bed configurations, and some implications for interpreting storm-event stratification. Journal of Sedimentary Petrology 60 (2), 211–219.

Austin, M. J., Masselink, G., O'Hare, T. J., Russell, P. E., 2007. Relaxation time effects of wave ripples on tidal beaches. Geophysical Research Letters 34 (16).

Bagnold, R. A., 1946. Motion of waves in shallow water: Interaction between waves and sand bottoms. Proc. Royal Society London Series 187 (1008), 1–15.

Bell, P. S., Williams, J. J., 2002. Comprehensive measurements of sediment resuspension processes by waves at full-scale. pol internal document no. 143. Tech. rep., Proudman Oceanographic Laboratory.

Betteridge, K. F. E., Thorne, P. D., Cooke, R. D., 2008. Calibrating multi-frequency acoustic backscatter systems for studying near-bed suspended sediment transport processes. Continental Shelf Research 28 (2), 227–235.

Bijker, E. W., van Hijum, E., Vellinga, P., 1976. Sand transport by waves. In: 15th International Conference on Coastal Engineering. Honolulu, pp. 1149–1167.

Block, M. E., Davies, A. G., Villaret, C., 1994. Suspension of sand in oscillatory flow above ripples: discrete-vortex model and laboratory experiments. In: Blorgey, M., Rajaona, R. D., Sleath, J. F. A. (Eds.), Sediment transport mechanisms in coastal environments and rivers, Euromech 310. World Scientific Publishing Co. Pte. Ltd.

Bosman, J. J., van der Velden, E. T. J. M., Hulsbergen, C. H., 1987. Sediment concentration measurement by transverse suction. Coastal Engineering 11 (4), 353–370.

Boyd, R., Forbes, D. L., Heffler, D. E., 1988. Time-sequence observations of wave-formed sand ripples on an ocean shoreface. Sedimentology 35 (3), 449–464.

Carter, D. J. T., 1982. Prediction of wave height and period for a constant wind velocity using the jonswap results. Ocean Engineering 9 (1), 17–33.

Clifton, H. E., 1976. Wave-formed sedimentary structures - a conceptual model. In: Davis, R. A., Ethington, R. L. (Eds.), Beach and Nearshore Sedimentation. Vol. 24. SEPM Special Publication, pp. 126–148.

Clifton, H. E., Dingler, J. R., 1984. Wave-formed structures and paleoenvironmental reconstruction. Marine Geology 60 (1-4), 165–198.

Davies, A. G., Ribberink, J. S., Temperville, A., Zyserman, J. A., 1997. Comparisons between sediment transport models and observations made in wave and current flows above plane beds. Coastal Engineering 31 (1-4), 163–198.

Davies, A. G., Thorne, P. D., 2002. 1dv-model of sand transport by waves and currents in the rippledbed regime. In: Proceedings of the 28th International Conference on Coastal Engineering. World Scientific, Cardiff, UK, pp. 2599–2611.

Davies, A. G., Thorne, P. D., 2005. Modelling and measurement of sediment transport by waves in the vortex ripple regime. Journal of Geophysical Research 110 (C05017).

Davies, A. G., Thorne, P. D., 2008. Advances in the study of moving sediments and evolving seabeds. Surveys in Geophysics 29 (1), 1–36.

Davies, A. G., van Rijn, L. C., Damgaard, J. S., van de Graaff, J., Ribberink, J. S., 2002. Intercomparison of research and practical sand transport models. Coastal Engineering 46 (1), 1–23.

Davies, A. G., Villaret, A. C., 2002. Prediction of sand transport rates by waves and currents in the coastal zone. Continental Shelf Research 22, 2725–2737.

Davies, A. G., Villaret, C., 1999. Eulerian drift induced by progressive waves above rippled and very rough beds. Journal of Geophysical Research-Oceans 104 (C1), 1465–1488.

Davis, J. P., Walker, D. J., Townsend, M., Young, I. R., 2004. Wave-formed sediment ripples: Transient analysis of ripple spectral development. Journal of Geophysical Research-Oceans 109 (C7).

Dean, R. G., Dalrymple, R. A., 1991. Water wave mechanics for engineers and scientists. World Scientific.

Dohmen-Janssen, C. M., Hanes, D. M., 2005. Sheet flow and suspended sediment due to wave groups in a large wave flume. Continental Shelf Research 25 (3), 333–347.

Dolphin, T., Vincent, C., 2009. The influence of bed forms on reference concentration and suspension under waves and currents. Continental Shelf Research 29 (2), 424–432.

Doucette, J. S., O'Donoghue, T., 2006. Response of sand ripples to change in oscillatory flow. Sedimentology 53 (3), 581–596.

Downing, A., Thorne, P. D., Vincent, C. E., 1995. Backscattering from a suspension in the near field of a piston transducer. Journal of the Acoustical Society of America 97 (3), 1614–1620.

Emery, W. J., Thompson, R. E., 1997. Data analysis methods in Physical Oceanography. Elsevier Science.

Faraci, C., Foti, E., 2002. Geometry, migration and evolution of small-scale bedforms generated by regular and irregular waves. Coastal Engineering 47 (1), 35–52.

Fredsoe, J., Deigaard, R., 1992. Mechanics of coastal sediment transport. World scientific.

Gaunaurd, G. C., Uberall, H., 1983. Rst analysis of monostatic and bistatic acoustic echoes from an elastic sphere. Journal of the Acoustical Society of America 73 (1), 1–12.

Goring, D. G., Nikora, V. I., 2002. Despiking acoustic doppler velocimeter data. Journal of Hydraulic Engineering-Asce 128 (1), 117–126.

Grant, W. D., Madsen, O. S., 1982. Movable bed roughness in unsteady oscillatory flow. Journal of Geophysical Research 87, 469–481.

Grasmeijer, B. T., Kleinhans, M. G., 2004. Observed and predicted bed forms and their effect on suspended sand concentrations. Coastal Engineering 51 (5-6), 351–371.

Green, M. O., 1999. Test of sediment initial-motion theories using irregular-wave field data. Sedimentology 46 (3), 427–441.
URL `http://doi.wiley.com/10.1046/j.1365-3091.1999.00221.x`

Green, M. O., Black, K. P., 1999. Suspended-sediment reference concentration under waves: field observations and critical analysis of two predictive models. Coastal Engineering 38 (3), 115–141.

Hanes, D. M., 1991. Suspension of sand due to wave groups. Journal of Geophysical Research-Oceans 96 (C5), 8911–8915.

Hanes, D. M., Alymov, V., Chang, Y. S., Jette, C., 2001. Wave-formed sand ripples at duck, north carolina. Journal of Geophysical Research-Oceans 106 (C10), 22575–22592.

Hansen, E. A., Fredsoe, J., Deigaard, R., 1994. Distribution of suspended sediment over wave-generated ripples. Journal of Waterway Port Coastal and Ocean Engineering-Asce 120 (1), 37–55.

Hansen, J. L., van Hecke, M., Ellegaard, C., Andersen, K. H., Bohr, T., Haaning, A., Sams, T., 2001. Stability balloon for two-dimensional vortex ripple patterns. Physical Review Letters 87 (20), 4.

Hay, A. E., Sheng, J. Y., 1992. Vertical profiles of suspended sand concentration and size from multifrequency acoustic backscatter. Journal of Geophysical Research-Oceans 97 (C10), 15661–15677.

Heathershaw, A. D., 1974. Bursting phenomena in sea. Nature 248 (5447), 394–395.

Jonsson, I. G., 1980. A new approach to oscillatory rough turbulent boundary layers. Ocean Engineering 7, 109–152.

Kaye, G. W. C., Laby, T. H., 1986. Tables of physical and chemical constants. Longman Inc. New York.

Kleinhans, M. G., 2005. SANDPIT Sand transport and morphology of offshore mining pits (Ed. Van Rijn, L. C. and Soulsby, R. L. and Hoekstra, P. and Davies, A. G.). Aqua Publications, Ch. Part II Q Phase diagrams of bed states in steady, unsteady, oscillatory and mixed flows.

Komar, P. D., 1974. Oscillatory ripple marks and evaluation of ancient wave conditions and environments. Journal of Sedimentary Petrology 44 (1), 169–180.

Larsen, L. H., 1982. A new mechanism for seaward dispersion of midshelf sediments. Sedimentology 29 (2), 279–283.

Lee, G.-h., Dade, W. B., Friedrichs, C. T., Vincent, C. E., 2004. Examination of reference concentration under waves and currents on the inner shelf. Journal of Geophysical Research 109 (C2).

Lee, T. H., Hanes, D. M., 1995. Direct inversion method to measure the concentration profile of suspended particles using backscattered sound. Journal of Geophysical Research 100 (C2), 2649–2657.

Lee, T. H., Hanes, D. M., 1996. Comparison of field observations of the vertical distribution of suspended sand and its prediction by models. Journal of Geophysical Research-Oceans 101 (C2), 3561–3572.

Mackenzie, K. V., 1981. Nine-term equation for sound speed in the oceans. Journal of the Acoustical Society of America 70 (3), 807–812.

Malarkey, J., Davies, A. G., 2002. Discrete vortex modelling of oscillatory flow over ripples. Applied Ocean Research 24 (3), 127–145.

Malarkey, J., Davies, A. G., 2004. An eddy viscosity formulation for oscillatory flow over vortex ripples. Journal of Geophysical Research 109 (C12016).

Marsh, S. W., Vincent, C. E., Osborne, P. D., 1999. Bedforms in a laboratory wave flume: An evaluation of predictive models for bedform wavelengths. Journal of Coastal Research 15 (3), 624–634.

Miller, M. C., Komar, P. D., 1980. Oscillation sand ripples generated by laboratory apparatus. Journal of Sedimentary Petrology 50 (1), 173–182.

Moate, B. D., Thorne, P. D., 2009. Measurements and inversion of acoustic scattering from suspensions having broad size distributions. Journal of the Acoustical Society of America 126 (6), 2905–2917.

Mogridge, G. R., Davies, M. H., Willis, D. H., 1994. Geometry prediction for wave-generated bedforms. Coastal Engineering 22, 255–286.

Nakato, T., Locher, F. A., Glover, J. R., Kennedy, J. F., 1977. Wave entrainment of sediment from rippled beds. Journal of the Waterway Port Coastal and Ocean Division-Asce 103 (1), 83–99.

Nichols, C. S., Foster, D. L., 2007. Full-scale observations of wave-induced vortex generation over a rippled bed. Journal of Geophysical Research-Oceans 112 (C10), 17.

Nielsen, P., 1981. Dynamics and geometry of wave-generated ripples. Journal of Geophysical Research 86, 6467–6472.

Nielsen, P., 1983. Entrainment and distribution of different sand sizes under water waves. Journal of Sedimentary Petrology 53 (2), 423–428.

Nielsen, P., 1986. Suspended sediment concentrations under waves. Coastal Engineering 10, 23–31.

Nielsen, P., 1992. Coastal bottom boundary layers and sediment transport. World Scientific.

O'Donoghue, T., Clubb, G. S., 2001. Sand ripples generated by regular oscillatory flow. Coastal Engineering 44, 101–115.

O'Donoghue, T., Doucette, J. S., van der Werf, J. J., Ribberink, J. S., 2006. The dimensions of sand ripples in full-scale oscillatory flows. Coastal Engineering 53 (12), 997–1012.

O'Hara Murray, R. B., Thorne, P. D., Hodgson, D. M., 2011. Intrawave observations of sediment entrainment processes above sand ripples under irregular waves. Journal of Geophysical Research-Oceans 116 (C01001).

Osborne, P. D., Greenwood, B., 1993. Sediment suspension under waves and currents - time scales and vertical structure. Sedimentology 40 (4), 599–622.

Osborne, P. D., Vincent, C. E., 1993. Dynamics of large and small-scale bedforms on a macrotidal shoreface under shoaling and breaking waves. Marine Geology 115 (3-4), 207–226.

Osborne, P. D., Vincent, C. E., 1996. Vertical and horizontal structure is suspended sand concentrations and wave-induced fluxes over bedforms. Marine Geology 131 (3-4), 195–208.

Pedocchi, F., Garcia, M. H., 2009. Ripple morphology under oscillatory flow: 1. prediction. Journal of Geophysical Research-Oceans 114, 16.

Podgorski, K., Rychlik, I., Machado, U. E. B., 2000. Exact distributions for apparent waves in irregular seas. Ocean Engineering 27 (9), 979–1016.

Ramaswamy, V., Rao, P. S., 2006. Grain size analysis of sediments from the northern andaman sea: Comparison of laser diffraction and sieve-pipette techniques. Journal of Coastal Research 22 (4), 1000–1009.

Ribberink, J. S., Al-Salem, A. A., 1994. Sediment transport in oscillatory boundary layers in cases of rippled beds and sheet flow. Journal of Geophysical Research 99 (C6), 12707–12728.

Sheng, J., Hay, A. E., 1988. An examination of the spherical scatterer approximation in aqueous suspensions of sand. Journal of the Acoustical Society of America 83 (2), 598–610.

Shi, N. C., Larsen, L. H., 1984. Reverse sediment transport induced by amplitude-modulated waves. Marine Geology 54 (3-4), 181–200.

Sleath, J. F. A., 1984. Sea bed mechanics. Wiley.

Sleath, J. F. A., Wallbridge, S., 2002. Pickup from rippled beds in oscillatory flow. Journal of Waterway, Port, Coastal, and Ocean Engineering 128 (6), 228–237.

Soulsby, R. L., 1997. Dynamics of Marine Sands. A manual for practical applications. HR Wallingford.

Soulsby, R. L., Whitehouse, R. J. S., December 2005. Prediction of ripple properties in shelf seas. Tech. rep., HR Wallingford.

Southard, J. B., Lambie, J. M., Federico, D. C., Pile, H. T., Weidman, C. R., Jan. 1990. Experiments on bed configurations in fine sands under bidirectional purely oscillatory flow, and the origin of hummocky cross-stratification. Journal of Sedimentary Petrology 60 (1), 1–17.

Styles, R., Glenn, S. M., 2002. Modeling bottom roughness in the presence of wave-generated ripples. Journal of Geophysical Research-Oceans 107 (C8), 15.

Swift, D. J. P., Figueiredo, A. G., Freeland, G. L., Oertel, G. F., 1983. Hummocky cross-stratification and megaripples - a geological double-standard. Journal of Sedimentary Petrology 53 (4), 1295–1317.

Syvitski, J. P. M., Leblanc, K. W. G., Asprey, K. W., 1991. Pirinciples, methods, and application of particle size analysis (Ed. J. P. M. Syvitski). Cambridge University Press, Ch. 13 Interlaboratory interinstrumental calibration experiment, pp. 174–193.

Thorne, P. D., Agrawal, Y. C., Cacchione, D. A., 2007. A comparison of near-bed acoustic backscatter and laser diffraction measurements of suspended sediments. IEEE Journal of Oceanic Engineering 32 (1), 225–235.

Thorne, P. D., Buckingham, M. J., 2004. Measurements of scattering by suspensions of irregularly shaped sand particles and comparison with a single parameter modified sphere model. Journal of the Acoustical Society of America 116 (5), 2876–2889.

Thorne, P. D., Campbell, S. C., 1992. Backscattering by a suspension of spheres. Journal of the Acoustical Society of America 92 (2), 978–986.

Thorne, P. D., Davies, A. G., Bell, P. S., 2009a. Observations and analysis of sediment diffusivity profiles over sandy rippled beds under waves. Journal of Geophysical Research-Oceans 114, 16.

Thorne, P. D., Davies, A. G., Williams, J. J., 2003. Measurements of near-bed intra-wave sediment entrainment above vortex ripples. Geophysical Research Letters 30 (20).

Thorne, P. D., Hanes, D. M., 2002. A review of acoustic measurement of small-scale sediment processes. Continental Shelf Research 22 (4), 603–632.

Thorne, P. D., Hardcastle, P. J., Soulsby, R. L., 1993. Analysis of acoustic measurements of suspended sediments. Journal of Geophysical Research-Oceans 98 (C1), 899–910.

Thorne, P. D., Hurther, D., Moate, B. D., Cooke, R. D., Chassagne, F. X., 2009b. Acoustic measurments of boundary layer flux profiles over a sandy rippled bed under regular waves. In: 3rd International Conference of Underwater Acoustic Measurements: Technologies and Results. Nafplion, Greece.

Thorne, P. D., Meral, R., 2008. Formulations for the scattering properties of suspended sandy sediments for use in the application of acoustics to sediment transport processes. Continental Shelf Research 28 (2), 309–317.

Thorne, P. D., Williams, J. J., Davies, A. G., 2002. Suspended sediments under waves measured in a large-scale flume facility. Journal of Geophysical Research 107 (C8).

Thosteson, E. D., Hanes, D. M., 1998. A simplified method for determining sediment size and concentration from multiple frequency acoustic backscatter measurements. Journal of the Acoustical Society of America 104 (2), 820–830.

Tomkins, M. R., Nielsen, P., Hughes, M. G., 2003. Selective entrainment of sediment graded by size and density under waves. Journal of Sedimentary Research 73 (6), 906–911.

Traykovski, P., Hay, A. E., Irish, J. D., Lynch, J. F., 1999. Geometry, migration, and evolution of wave orbital ripples at leo-15. Journal of Geophysical Research-Oceans 104 (C1), 1505–1524.

Tunstall, E. B., Inman, D. L., 1975. Vortex generation by oscillatory flow over rippled surfaces. Journal of Geophysical Research-Oceans and Atmospheres 80 (24), 3475–3484.

Van der Werf, J. J., Doucette, J. S., O'Donoghue, T., Ribberink, J. S., 2007. Detailed measurements of velocities and suspended sand concentrations over full-scale ripples in regular oscillatory flow. Journal of Geophysical Research-Earth Surface 112 (F2).

Van der Werf, J. J., Ribberink, J. S., O'Donoghue, T., Doucette, J. S., 2006. Modelling and measurement of sand transport processes over full-scale ripples in oscillatory flow. Coastal Engineering 53 (8), 657–673.

Van Rijn, L. C., 1993. Principles of sediment transport in rivers, estuaries and coastal seas. AQUA Publications.

Van Rijn, L. C., 2007. Unified view of sediment transport by currents and waves. iii: Graded beds. Journal of Hydraulic Engineering-Asce 133 (7), 761–775.

Villard, P. V., Osborne, P. D., 2002. Visualization of wave-induced suspension patterns over two-dimensional bedforms. Sedimentology 49 (2), 363–378.

Villard, P. V., Osborne, P. D., Vincent, C. E., 2000. Influence of wave groups on ssc patterns over vortex ripples. Continental Shelf Research 20 (17), 2391–2410.

Vincent, C. E., 2007. Measuring suspended sand concentrations using acoustic backscatter: a critical look at errors and uncertainties. In: Balson, P., Collins, M. B. (Eds.), Coastal and shelf sediment transport. Geological Society of London, Special Publication, p. 274.

Vincent, C. E., Hanes, D. M., 2002. The accumulation and decay of near-bed suspended sand concentration due to waves and wave groups. Continental Shelf Research 22 (14), 1987–2000.

Vincent, C. E., Marsh, S. W., Webb, M. P., Osborne, P. D., 1999. Spatial and temporal structures of suspension and transport over megaripples on the shore face. Journal of Geophysical Research-Oceans 104 (C5), 11215–11224.

Vincent, C. E., Osborne, P. D., 1993. Bedform dimensions and migration rates under shoaling and breaking waves. Continental Shelf Research 13 (11), 1267–1280.

Wiberg, P. L., Harris, C. K., 1994. Ripple geometry in wave-dominated environments. Journal of Geophysical Research 99 (C1), 775–789.

Wiberg, P. L., Sherwood, C. R., 2008. Calculating wave-generated bottom orbital velocities from surface-wave parameters. Computers and Geosciences 34 (10), 1243–1262.

Williams, J. J., Bell, P., Coates, L. E., Metje, N., Selwyn, R., 2003. Interactions between a benthic tripod and waves on a sandy bed. Continental Shelf Research 23 (3-4), 355–375.

Williams, J. J., Bell, P. S., 2006. Laboratory investigation of bedform dynamics and resuspension of sandy sediments at field scale. Journal of Coastal Research 2, 810–815.

Williams, J. J., Bell, P. S., Thorne, P. D., 2005. Unifying large and small wave-generated ripples. Journal of Geophysical Research 110.

Williams, J. J., Bell, P. S., Thorne, P. D., Metje, N., Coates, L. E., 2004. Measurement and prediction of wave-generated suborbital ripples. Journal of Geophysical Research-Oceans 109 (C2).